



**HAL**  
open science

# The gravity-driven flashing of metastable water in a pool heated from below

Jimmy Martin

► **To cite this version:**

Jimmy Martin. The gravity-driven flashing of metastable water in a pool heated from below: An experimental study. Physics [physics]. Université catholique de Louvain (Louvain-la-Neuve, Belgique); Ecole Polytechnique de Louvain, Institute of Mechanics, Materials and Civil Engineering, Thermodynamics and fluid mechanics division, 2023. English. NNT: . tel-04104513

**HAL Id: tel-04104513**

**<https://irsns.hal.science/tel-04104513>**

Submitted on 24 May 2023

**HAL** is a multi-disciplinary open access archive for the deposit and dissemination of scientific research documents, whether they are published or not. The documents may come from teaching and research institutions in France or abroad, or from public or private research centers.

L'archive ouverte pluridisciplinaire **HAL**, est destinée au dépôt et à la diffusion de documents scientifiques de niveau recherche, publiés ou non, émanant des établissements d'enseignement et de recherche français ou étrangers, des laboratoires publics ou privés.

Copyright



Institute of Mechanics,  
Materials and Civil Engineering

# The gravity-driven flashing of metastable water in a pool heated from below

An experimental study

---

Doctoral dissertation presented by

**Jimmy MARTIN**

in partial fulfillment of the requirements for  
the degree of Doctor in Engineering Sciences

May 2023

## **Thesis committee**

Pr. Yann BARTOSIEWICZ (supervisor, UCLouvain)

Dr. Matthieu DUPONCHEEL (secretary, UCLouvain)

Pr. Masahiro FURUYA (member, Waseda University)

Pr. Hervé JEANMART (president, UCLouvain)

Dr. Pierre RUYER (member, IRSN)

Pr. Benoit STUTZ (member, Université Savoie Mont Blanc)

© 2023  
Jimmy MARTIN  
All Rights Reserved

---

# Abstract

The present doctoral research is focused on the gravity-driven flashing of metastable water, a phenomenon which is usually encountered in natural geysers. Specifically, the emphasis is put on the case of a water pool heated from below, motivated by the absence in the scientific literature of any known report of the phenomenon in this precise configuration. A wealth of data, close to the case of interest and related to genuine geysers or unheated depressurized pools can be identified. But the extrapolation of those available results to the studied case is not straightforward and some questions can be specifically formulated. *Does the phenomenon exist in a pool-type geometry, heated from below? If yes, what are its main characteristics? Are we able to model as simple as possible the studied physics for further macroscopic transient simulations?* Because of a lack of information about the studied case in the scientific literature, providing an answer to the above questions implies performing some new experiments. This has motivated the design of the test device called Aquarius, central to this doctoral research. For defining Aquarius, a novel downscaling methodology, presented in this thesis, has been developed by the present author. The method mainly consists in an operating pressure distortion, which allows conserving a large saturation temperature vertical difference even at a reduced scale, with an appropriate choice of system's pressure. Indeed, in the low-pressure case, because of existing steep variations in water saturation temperature against pressure, a little variation in hydrostatic pressure, provided by a reduced pool level, might be enough for achieving some required large vertical difference. By taking some height, this similarity approach, unmentioned yet in the scientific literature to our knowledge, may be beneficial to other types of applications where the gravity-driven flashing is expected to occur, providing a way to reduce the size and hence the cost of the envisioned experiments and keeping water as the working fluid (*e.g.* for 1D-geysers or the pools constituting a passive cooling capacity for some light water nuclear reactors). Having developed this experimental tool, the phenomenon has been further studied and the obtained results are detailed in this thesis. First of all, it is shown that the test device allows obtaining an upper superheated area, located below the liquid free surface, from which the uprising metastable water may potentially turn into bubbles. In this area, the recorded water temperatures often exceed the local saturation and substantial

superheats ranging from 1 to 5°C are reachable. Next, under certain circumstances, the metastable water spontaneously flashes, as materialized by the emergence of numerous bubbles, thereby validating the proposed downscaling methodology. Most of all, the performed tests highlight the existence of the gravity-driven flashing of metastable water in the configuration of a pool heated from below, which constitutes the main result of the present research. Apart from the heating power, the operating pressure and the initial pool level, it is also shown that the phenomenon is particularly sensitive to the initial amount of dissolved gases in the configuration of the Aquarius experiments. Pointedly, the achieved tests have exhibited that the produced metastable water relaxes through the emergence of bubbles within the liquid bulk and almost never onto some immersed solid walls, contrarily to what can be envisioned on the basis of the scientific literature on flashing flows. A theoretical study of the observed nucleation processes is then conducted and provides an interpretation of this very fact. Nevertheless, the fundamental mechanisms standing behind the observed bulk nucleation are not fully unveiled yet. On the basis of some specifically conducted experiments, it appears that neither the so-called homogeneous nucleation nor the nucleation from gas nuclei entrapped into some suspended solid particles are serious candidates for explaining the bulk processes. Instead, the hypothesis of a main contribution of freely-floating gas nuclei to the observed bubble growths is very likely. But we are however left with the same questions that animate the cavitation and thermal-hydraulic communities for decades regarding the stabilizing mechanisms that may act on those freely-floating nuclei. At last, the characterization of the heat and mass transfers taking place within the liquid pool during a typical experiment is discussed. Precisely, some heat and mass transfer coefficients, derived from the available test data, are presented. Interestingly, the correlations that have been defined from the latter coefficients for the two-phase regime are rather original in their mathematical formulation. Those correlations link the noticed heat and mass transfers intensification in the presence of numerous bubbles to the so-called Gibbs number, which is a dimensionless form of the energetic cost required for a bubble nucleation. Moreover, the pre-factor of those correlations does appear related to the initial pool level, which is clearly surprising and could motivate further studies. At last, with those correlations defined and a lumped-parameter model of the liquid pool written, it has been possible to simulate some pre-selected tests, with moderate discrepancies.

**Keywords:**

Gravity-driven flashing, pool heated from below, non-equilibrium phase change, dissolved gases, natural convection, metastable water.

*"Physics is like sex: sure, it may give some practical results, but that's not why we do it."*

— Richard P. Feynman



---

# Acknowledgments

In the first place, I would like to gratefully thank the French Institut de Radioprotection et de Sûreté Nucléaire (IRSN) which has made possible the present doctoral research by its financial support. My former and current bosses at IRSN, Olivier and Franck Dubois, Nicolas Trégourès, Gaétan Guillard and Fabienne Ribeiro, are to be particularly acknowledged for the trust they placed in me when I asked them to begin on a doctoral research project five years ago, while being still involved in my usual missions. Especially, many thanks are addressed to Nicolas and Fabienne for their moral support throughout the tough last moments of this PhD.

I am also particularly grateful to Professor Yann Bartosiewicz, my PhD supervisor, Matthieu Duponcheel and Pierre Ruyer for the helpful and kind advices they provided me throughout my research. Our frequent discussions about the studied physics significantly improved this thesis while satisfying my desire to learn. A big thank goes too to Jean-Marie Seynhaeve, Frank Hesbois and Julien Vervotte from UCLouvain for their invaluable support during the development and build up of the test device.

Next, I would also like to address my thanks to the members of the jury, Professors Masahiro Furuya, Hervé Jeanmart and Benoît Stutz, who accepted to perform a complete examination of the present PhD thesis. Our constructive exchanges during the private PhD defense and their valuable comments and suggestions were widely appreciated.

The so-called SEREX experimental research department at IRSN Cadarache is to be acknowledged as well for having accepted to host the Aquarius experiment the last year of this PhD research and for its constant and efficient technical support. In this department, many thanks are given to my friendly colleagues Benoît Migot and Olivier Bouygues, among many others, for having made my days so stimulating and funny.

Big thanks as well to Hervé Mutelle, Daniele Vivaldi, Marc Forestier, Tony Glantz, Eric Chojnacki, Jean Baccou, Frédéric Péralès, Andrei Jelea and many others, who all added a lot of fun throughout this crazy journey called "PhD"! A big thank too to my Japanese friends Naofumi and Yuriko Tsukamoto, and especially to Yuriko who kindly accepted to illustrate the first page of the introductory chapter of this thesis in a Manga style.

My everyday sources of inspiration as a young researcher are to be acknowledged here: Professors Georges Pès and Jean-Pierre Roubin, thank you for having taught me during my young age your funny and stimulating way to deal with Physics ! To my extraordinary and wise grandfather who left this world too early, Jorge Martìn Sanchez: gracias por todo abuelo...

I would also like to express my infinite gratitude to my darling wife Alice. All of it would not have been possible without the continuous trust and love she provided me throughout this thesis. I am also very thankful to my son James who expected precisely two days after I sent my PhD manuscript to the jury members for leaving his mother's belly... At last, to my good dog Ruby: woof, woof!

Jimmy MARTIN

Saint-Paul-lez-Durance, May 2023

---

# Contents

<b>List of Symbols</b>	<b>xi</b>
<b>List of Figures</b>	<b>xvii</b>
<b>List of Tables</b>	<b>xxxii</b>
<b>1 Introduction</b>	<b>1</b>
1.1 A first glimpse into the studied physics . . . . .	1
1.2 A partially known phenomenon . . . . .	2
1.3 An unstudied physics in pools heated from below . . . . .	4
1.4 Thesis objectives and outline . . . . .	8
<b>2 The experimental setup and methods</b>	<b>11</b>
2.1 Scaling and design of the experimental device . . . . .	11
2.1.1 The definition of a reference pool . . . . .	11
2.1.2 Downsizing and physical similarity . . . . .	12
2.2 The Aquarius experimental device . . . . .	22
2.2.1 Overview of the installation . . . . .	22
2.2.2 The pool vessel . . . . .	24
2.2.3 The heat source . . . . .	24
2.2.4 The operating pressure control system . . . . .	24
2.2.5 Instrumentation . . . . .	29
2.2.6 Data acquisition and post-processing . . . . .	31
2.3 Measurement uncertainties analysis . . . . .	32
2.3.1 Methodology . . . . .	32
2.3.2 Physical measurements uncertainties . . . . .	33
2.3.3 The uncertainties in the computed physical variables . . . . .	35
2.4 The experimental procedure . . . . .	36
<b>3 A first observation of the gravity-driven flashing in a heated pool</b>	<b>39</b>
3.1 Analysis of a typical experiment . . . . .	39

3.1.1	Definition of the reference test . . . . .	39
3.1.2	The highlighted physical features . . . . .	40
3.1.3	Thermodynamic evolution of the liquid pool . . . . .	52
3.1.4	The repeatability of the reference test . . . . .	58
3.2	An interpretation for the observed fast bubble growth . . . . .	61
3.3	Phenomenon sensitivity to heating, pressure, pool level and dissolved gases . . . . .	69
3.3.1	Variations of the heating power . . . . .	69
3.3.2	Variations of the operating pressure . . . . .	71
3.3.3	Variations of the initial pool level . . . . .	75
3.3.4	The key role played by the presence of dissolved gases . . . . .	79
3.3.5	Summary of the highlighted phenomenon's sensitivity . . . . .	82
3.4	The nucleation forcing mechanisms . . . . .	82
3.4.1	The liquid bulk nucleation in a pool with a localized heat source . . . . .	82
3.4.2	The liquid bulk nucleation within an inclined pool vessel . . . . .	87
3.4.3	The nucleation onto the unheated rough wall . . . . .	87
<b>4</b>	<b>A study of the observed nucleation processes</b>	<b>93</b>
4.1	A review of the different nucleation modes . . . . .	93
4.1.1	Definitions and taxonomy . . . . .	93
4.1.2	Physical mechanisms . . . . .	94
4.2	An interpretation of the observed wall nucleation . . . . .	110
4.2.1	The activation of a gas nucleus pre-existing in a wall crevice . . . . .	110
4.2.2	The bubble formation onto the heated wall . . . . .	115
4.2.3	The bubble formation onto the roughest unheated wall . . . . .	119
4.2.4	The deactivation mechanisms of the gas nuclei entrapped in a wall . . . . .	120
4.3	An interpretation of the observed bulk nucleation . . . . .	123
4.3.1	A study of the liquid bulk de novo nucleation occurrence . . . . .	124
4.3.2	An experimental search for the most probable nucleation mode . . . . .	127
4.3.3	An explanation for the late regime of sporadic and violent bubble nucleation . . . . .	130
<b>5</b>	<b>A characterization of the heat and mass transfers</b>	<b>137</b>
5.1	The estimate of the heat and mass transfer rates . . . . .	137
5.1.1	The wall-to-liquid heat transfer coefficient . . . . .	137
5.1.2	The gas/liquid heat transfer rate . . . . .	143
5.1.3	The dissolved air mass transfer rate . . . . .	148
5.2	Heat and mass transfers correlations . . . . .	154
5.2.1	Methodology . . . . .	154
5.2.2	The liquid-bulk-to-free-surface single-phase transfers . . . . .	156
5.2.3	The heated-wall-to-liquid heat transfer . . . . .	161
5.2.4	The two-phase heat and mass transfers . . . . .	164

---

5.3	A lumped-parameter model of the Aquarius pool . . . . .	172
5.3.1	Model description . . . . .	172
5.3.2	The simulation of the reference case . . . . .	176
5.3.3	The simulation of sensitivity cases . . . . .	181
	<b>Conclusions</b>	<b>189</b>
	<b>Bibliography</b>	<b>197</b>
<b>A</b>	<b>The liquid pool mass determination method</b>	<b>207</b>
<b>B</b>	<b>A modeling of the O<sub>2</sub> and N<sub>2</sub> degassing from a water pool</b>	<b>209</b>
B.1	Problem description . . . . .	209
B.2	The solubility and diffusivity of air, O <sub>2</sub> and N <sub>2</sub> in water . . . . .	211
B.2.1	The Henry's volatility constants . . . . .	211
B.2.2	The water-solute binary diffusivities . . . . .	211
B.3	The molar flux of the dissolved species . . . . .	212
B.3.1	The local multicomponent diffusion equations . . . . .	213
B.3.2	The space-integrated equations . . . . .	216
B.3.3	The estimate of the species-dependent film thicknesses . . . . .	216
B.4	Equivalence between the binary and ternary problems . . . . .	219
B.4.1	The liquid-side interfacial composition . . . . .	219
B.4.2	The liquid bulk composition and degassing fluxes . . . . .	220
B.4.3	The dissolved air diffusivity in water . . . . .	221
<b>C</b>	<b>The test data post-processing code in Python 3</b>	<b>223</b>
<b>D</b>	<b>Measurement uncertainties analysis</b>	<b>233</b>
D.0.1	Methodology . . . . .	233
D.0.2	The uncertainties in the measured physical variables . . . . .	236
D.0.3	The uncertainties in the computed physical variables . . . . .	241
D.0.4	The overall uncertainty budget of the computed physical variables	247
<b>E</b>	<b>The lumped-parameter model of the Aquarius pool in Python 3</b>	<b>251</b>
<b>F</b>	<b>An Euler-implicit solver coded in Python 3</b>	<b>257</b>



---

# List of Symbols

## Geometrical parameters

$L/D$	Length-to-diameter or aspect ratio (-)
$H$	Pool height (m)
$L$	Pool length (m)
$W$	Pool width (m)
$V$	Volume (m <sup>3</sup> )
$V_L$	Liquid pool volume (m <sup>3</sup> )
$H_{SFP}$	Spent-Fuel-Pool height (m)
$H_{mockup}$	Aquarius mock-up pool height (m)
$z$	Vertical length variable (m)
$d$	Heat and mass transfers characteristic length (m)
$r$	Arbitrary bubble radius (m)
$r_{SFP}$	Spent-Fuel-Pool reference bubble radius (m)
$r_{mockup}$	Aquarius mock-up reference bubble radius (m)
$R_a$	Surface roughness arithmetical mean deviation (μm)
$S_p$	Pool free surface area (m <sup>2</sup> )
$d_{bubble}$	Bubble diameter (m)
$d_b$	Bubble length-scale (m)
$r_b$	Radius of a gas nucleus (m)
$l$	Particle mean-free-path (m)
$\theta$	Contact angle (rad)
$\theta'$	Effective contact angle (rad)
$\beta$	Cavity mouth opening semi-angle (rad)
$r_c$	Cavity mouth opening radius (m)
$R_z$	Cavity depth (m)
$r_i$	Gas/liquid interfacial radius (m)
$r^*$	Gas/liquid interfacial critical radius (m)
$z_m$	Liquid meniscus height (m)
$S_h$	Heating area (m <sup>2</sup> )
$S_i$	Overall gas/liquid interfacial area (m <sup>2</sup> )

## Composition and thermodynamic variables

$T_{sat}$	Water saturation temperature (K)
$\Delta T_{sat}(z)$	Water saturation temperature vertical difference (K)
$\Delta T_{sat;h}$	Heated wall superheat (K)
$\Delta T_{sat;w}$	Unheated rough wall superheat (K)
$P$	Local pressure (Pa)
$P_L$	Liquid pressure (Pa)
$\frac{\partial T_{sat}}{\partial P}$	Partial derivative of $T_{sat}$ against pressure (K/Pa)
$\Delta T_L$	Liquid pool temperature difference (K)
$T_L$	Volume-averaged liquid pool temperature (K)
$T_G$	Volume-averaged pool's atmosphere temperature (K)
$P_{sat}(T_L)$	Water saturation pressure at $T_L$ (Pa)
$P_G$	Vessel's atmosphere pressure (Pa)
$\Delta T_{eq}$	Liquid thermal metastability degree (K)
$\Delta T_{eq;\infty}$	Asymptotic value of $\Delta T_{eq}$ (K)
$m_L$	Liquid pool mass (kg)
$C_{O_2}$	Dissolved $O_2$ mass concentration (mg/L or ppm)
$C_{O_2}^{eq}$	Dissolved $O_2$ equilibrium mass concentration (mg/L or ppm)
$C_a$	Dissolved air mass concentration (mg/L or ppm)
$C_a^{eq}$	Dissolved air equilibrium mass concentration (mg/L or ppm)
$z_p$	Pool collapsed level (m)
$T_{SFP}$	Spent-Fuel-Pool reference temperature (K)
$P_{SFP}$	Spent-Fuel-Pool reference pressure (Pa)
$T_{mockup}$	Aquarius mock-up reference temperature (K)
$P_{mockup}$	Aquarius mock-up reference pressure (Pa)
$x_w^G$	Water vapor molar fraction (mol/mol)
$P_w^G$	Water vapor partial pressure (Pa)
$x_{O_2}^G$	$O_2$ molar fraction (mol/mol)
$P_{O_2}^G$	$O_2$ partial pressure (Pa)
$x_{N_2}^G$	$N_2$ molar fraction (mol/mol)
$P_{N_2}^G$	$N_2$ partial pressure (Pa)
$x_w^L$	Liquid water molar fraction (mol/mol)
$x_{O_2}^L$	Dissolved $O_2$ molar fraction (mol/mol)
$x_{N_2}^L$	Dissolved $N_2$ molar fraction (mol/mol)
$T_h$	Area-averaged heated bottom plate temperature (K)
$\Delta T_h$	Area-averaged heated bottom plate temperature difference (K)
$T_{int}$	Area-averaged liquid pool free surface temperature (K)
$\omega_a^L$	dissolved air mass fraction in the liquid (kg/kg)
$\omega_a^{Li}$	dissolved air mass fraction at the liquid free surface (kg/kg)
$\omega_a^{Bi}$	dissolved air mass fraction at the bubbles interface (kg/kg)

## Heat and mass transfers

$\dot{m}_L$	Liquid vaporization rate (kg/s)
$\dot{C}_{O_2}$	Dissolved O <sub>2</sub> degassing rate (mg/L/s or ppm/s)
$\dot{Q}_p$	Heating power (W)
$k_m$	Mass transfer coefficient of the so-called penetration theory (m/s)
$\tau_c$	Exposure time of the so-called penetration theory (s)
$j_a^B$	Bubble-averaged local flux associated with the air degassing (kg/m <sup>2</sup> /s)
$j_w^B$	Bubble-averaged local flux associated with water vaporization (kg/m <sup>2</sup> /s)
$\tau_{diff}$	Characteristic time of mass diffusion of the dissolved species in water (s)
$k_h$	Wall-to-liquid heat transfer coefficient (W/m <sup>2</sup> /K)
$m_h$	Heaters total mass (kg)
$C_h$	Heaters specific heat capacity (J/kg/K)
$k_T^L$	Liquid/gas interfacial heat transfer coefficient (W/m <sup>2</sup> /K)
$k_T^L S_i$	Liquid/gas interfacial heat transfer rate (W/K)
$(k_T^L S_i)_{\infty}$	Asymptotic value of the liquid/gas interfacial heat transfer rate (W/K)
$k_m^L$	Liquid/gas interfacial degassing transfer coefficient (W/m <sup>2</sup> /K)
$k_m^L S_i$	Liquid/gas interfacial degassing transfer rate (W/K)
$(k_m^L S_i)_{\infty}$	Asymptotic value of the liquid/gas interfacial mass transfer rate (W/K)
$\tau_{bubble}$	Bubble lifetime (s)
$U_{bubble}$	Bubble terminal velocity (m/s)
$u_b$	Bubble velocity-scale (m/s)
$\tau_{flight}$	Bubble time-of-flight (s)
$\tau_{heat}$	Characteristic time of the liquid-to-bubble heat transfer (s)

## Dimensionless numbers

$Ra_L$	Liquid-side Rayleigh number at pool scale (-)
$Ja_L$	Jakob number (-)
$Ec$	Eckert number (-)
$Re_b$	Bubble Reynolds number (-)
$Pr_L$ or $Pr$	Liquid water Prandtl number (-)
$Le$	Lewis number (-)
$Pe_b$	Bubble Péclet number (-)
$Fr_b$	Bubble Froude number (-)
$Ra_{Li}$	Liquid-to-free-surface Rayleigh number (-)
$Nu_{Li}$	Liquid-to-free-surface Nusselt number (-)
$Sh_{Li}$	Liquid-to-free-surface Sherwood number (-)
$(Ra_{Li})_\infty$	Asymptotic value of the liquid-to-free-surface Rayleigh number (-)
$(Nu_{Li})_\infty$	Asymptotic value of the liquid-to-free-surface Nu number (-)
$(Sh_{Li})_\infty$	Asymptotic value of the liquid-to-free-surface Sherwood number (-)
$Gb$	Gibbs number (-)
$Ra_h$	Liquid-side Rayleigh number at the heated wall (-)
$Nu_h$	Liquid-side Nusselt number at the heated wall (-)
$(Ra_h)_\infty$	Asymptotic value of the liquid-side Rayleigh number at the hot wall (-)
$(Nu_h)_\infty$	Asymptotic value of the liquid-side Nusselt number at the hot wall (-)
$\Phi_T$	Dimensionless form of the heat transfer rate $k_T^L S_i$ (-)
$\Phi_m$	Dimensionless form of the mass transfer rate $k_m^L S_i$ (-)

## Nucleation variables

$\vec{f}_{buoyancy}$	Buoyancy force applied to a gas nucleus (N)
$\vec{f}_{viscous}$	Viscous force applied to a gas nucleus (N)
$\vec{u}_b$	Velocity vector of a gas nucleus (norm in m/s)
$\tau_b$	Characteristic time of the transform of a gas nucleus (s)
$\Delta F$	Change in thermodynamic system's free energy (J)
$\Delta F_{max}$	Free energy barrier for bubble nucleation (J)
$N(r^*)$	Number of formed molecule clusters of size $r^*$ per unit volume ( $m^{-3}$ )
$N_o$	Number of liquid molecules per unit volume at $T_L$ and $P_L$ ( $m^{-3}$ )
$J_{BN}$	De novo bulk nucleation rate ( $m^{-3}s^{-1}$ )
$J_{SN}$	De novo nucleation rate onto a solid discontinuity ( $m^{-3}s^{-1}$ )
$\lambda$	Collision frequency ( $s^{-1}$ )
$\xi$	Heterogeneity factor for bubble nucleation (-)
$\xi_{flat}$	Heterogeneity factor of a flat solid surface (-)
$\xi_{crevice}$	Heterogeneity factor of a crevice (-)
$\xi_{sphere}$	Heterogeneity factor of a solid sphere (-)
$(\Delta T_{sat})_{crit}$	Critical local superheat for the occurrence of bubble wall nucleation (K)
$(P_a^L)_{crit}$	Dissolved air partial pressure for bubble wall nucleation at a null superheat (K)
$(\Delta T_{sat})_{BN}$	Critical local superheat for the occurrence of bubble bulk nucleation (K)
$(P_a^L)_{crit;BN}$	Dissolved air partial pressure for bubble bulk nucleation at a null superheat (K)

## Physical constants

$g$	Gravitational acceleration ( $m/s^2$ )
$\mathcal{R}$	Perfect gas constant (J/mol/K)
$k_B$	Boltzmann's constant (J/K)
$\hbar$	Planck's constant (J . s)
$\mathcal{N}_A$	Avogadro's number ( $mol^{-1}$ )

## Fluid and transport properties

$\rho_L$	Liquid water density (kg/m <sup>3</sup> )
$\rho_G$	Water vapor density (kg/m <sup>3</sup> )
$\beta_L$	Isobaric thermal expansion coefficient (K <sup>-1</sup> )
$\nu_L$	Liquid water kinematic viscosity (m <sup>2</sup> /s)
$\kappa_L$	Liquid water thermal diffusivity (m <sup>2</sup> /s)
$h_{gsat}(P_G)$	Water vapor specific enthalpy at pressure $P_G$ (J/kg)
$u_L$	Liquid water specific internal energy (J/kg)
$U_L$	Liquid water internal energy (J/kg)
$\mathcal{C}_X$	Generic expression for a given transport $X$ coefficient (m <sup>2</sup> /s)
$\mathcal{L}_w$	Water specific latent heat (J/kg)
$C_{p;L}$	Liquid water specific heat capacity (J/kg/K)
$\lambda_L$	Liquid water thermal conductivity (W/m/K)
$\mathcal{D}_{a;w}^L$	Dissolved air/water diffusivity coefficient (m <sup>2</sup> /s)
$\mathcal{D}_{O_2;w}^L$	Dissolved oxygen/water diffusivity coefficient (m <sup>2</sup> /s)
$\mathcal{D}_{N_2;w}^L$	Dissolved nitrogen/water diffusivity coefficient (m <sup>2</sup> /s)
$\mu_L$	Liquid water dynamic viscosity (Pa . s)
$\mathcal{D}_{brownian}$	Brownian diffusion coefficient (m <sup>2</sup> /s)
$\sigma$	Surface tension (J/m <sup>2</sup> )
$\mathcal{H}_a(T_L)$	Dissolved air Henry's volatility constant at $T_L$ (Pa/mol/mol)
$\mathcal{H}_{O_2}(T_L)$	Dissolved O <sub>2</sub> Henry's volatility constant at $T_L$ (Pa/mol/mol)
$\mathcal{H}_{N_2}(T_L)$	Dissolved N <sub>2</sub> Henry's volatility constant at $T_L$ (Pa/mol/mol)
$m$	Mass of one molecule (kg)
$\mathcal{M}_w$	Water molar mass (kg/mol)
$\mathcal{M}_a$	Air molar mass (kg/mol)
$\nu_L$	Liquid water specific volume (m <sup>3</sup> /kg)
$\nu_G$	Water vapor specific volume (m <sup>3</sup> /kg)

---

## List of Figures

1.1	Front view of the so-called <i>Castle Geyser</i> , located in the Yellowstone National Park, USA. . . . .	3
1.2	Illustration of the gravity-driven flashing of superheated water in a geyser-like system, as it is understood to date. The fresh water supply, usually located at the geyser's bottom-end through the form of a phreatic volume is not represented here, for simplicity. Left-hand-side: Stage 1) Water is heated up at the bottom-end of the channel and starts uprising, Stage 2) Water is superheated by gravity when reaching parts of the channel of reduced hydrostatic pressure, such that its temperature becomes higher than the local saturation temperature, Stage 3) Water starts turning into bubbles as a way to tend toward an equilibrium state of greater stability, a process called relaxation, flashing or bubble nucleation. Right-hand-side: idealized vertical profile of the liquid water and saturation temperatures within the geyser. . . . .	3
1.3	Top view of the spent-fuel-pool of Reactor No.1 at EDF's Blayais nuclear power plant, ©Médiathèque IRSN. . . . .	6
1.4	The accidental gravity-driven flashing as envisioned in a spent-fuel-pool. Left-hand-side: 1) Water is heated up by the spent fuels and keeps sub-cooled, 2) A natural convection flow develops at pool scale, 3) The boiling point is locally exceeded in the upper part of the pool by the uprising water, 4) The superheated water flashes and turns into bubbles. Right-hand-side: idealized vertical profile of the water temperature and of the boiling point within the uprising plume. . . . .	7

1.5	Illustration of the flashing of superheated water in an unheated cylindrical glass vessel suddenly subjected to low pressure conditions, adapted from the work of <i>Saury et al.</i> reported in [103]. Left: <i>Saury's</i> experimental device layout. Right: a photo of the glass vessel taken during a typical experiment of <i>Saury et al.</i> One can notice that the bubbles resulting from the depressurized water are uniformly distributed below the pool free surface, thereby suggesting that the phenomenon originates mainly from the liquid bulk rather than from the container's wall. . . . .	8
2.1	Overview of a typical spent-fuel-pool of a so-called light-water-reactor. . .	12
2.2	Variations of water saturation temperature $T_{sat}$ against pressure $P$ . Those variations are steeper in the low-pressure range than around atmospheric pressure. . . . .	19
2.3	Relationship between the mock-up height and its operating pressure, ensuring the conservation of the 20°C saturation temperature vertical difference of a SFP. . . . .	19
2.4	A map of the reached natural convection regimes as a function of two dimensionless numbers characterizing both the intensity of the studied transfer and the nature of the fluid: respectively the <i>Rayleigh</i> and <i>Prandtl</i> numbers, denoted as $Ra_L$ and $Pr$ . For water, with $Pr \approx 7$ , the turbulent regime is reached once $Ra_L > 10^5$ . Figure adapted from the work of <i>Krishnamurti</i> [68]. . . . .	21
2.5	Variations of the terminal velocity of an air bubble in water against bubble diameter. From a diameter of the order of 1 mm, the bubble terminal velocity gets almost constant and close to 30 cm/s, a value here represented by an horizontal red line. Figure adapted from the work of <i>Clift et al.</i> [26].	22
2.6	Overview of the Aquarius test device designed and operated by IRSN / UCLouvain for investigating the gravity-driven pool flashing phenomenon at a laboratory scale. . . . .	23
2.7	The Aquarius experimental device layout and instrumentation. . . . .	23
2.8	Side-view of the mechanical assembly of four machined stainless steel plates constituting the Aquarius pool vessel. . . . .	25
2.9	Side-view of the Vacuubrand™ RE 8 vacuum pump in use within the Aquarius test device. . . . .	26
2.10	Assessed pumping performance with/without the presence of a so-called precision valve at the pump inlet for finely tuning the flow rate. . . . .	27
2.11	Front-view of the condenser equipping the test device, coated by a rock-wool thermal insulation layer. . . . .	27
2.12	Sketch of the inner volume of the condenser vessel, with the heat exchanger made of an helical bent of a copper tube exhibited (the drawing is not in scale). . . . .	28

---

2.13	Front-view of the Partenair™ FRC-VBE 003 air/water heat pump equipping the test device. . . . .	28
2.14	Overview of the available instrumentation and the location within the test device of each utilized sensor. . . . .	29
2.15	Illustration of the physical principle behind the dissolved oxygen measurement, as performed by the Hamilton™ VisiFerm DO Arc 120 sensor. Figure extracted from Hamilton™ website. . . . .	30
2.16	Frontview of the acquisition modules equipping the test device and installed into its electrical cabinet. . . . .	32
2.17	The uncertainties, respectively in link with the measuring chain and the experimental procedure and boundary conditions, combine and alter the quality of the obtained results. In this example, the depicted overall uncertainty varies arbitrarily with time. . . . .	34
2.18	The retained method in the evaluation of the uncertainties affecting the quality of the experimental results, developed according to [59]. . . . .	34
3.1	Chosen position of the four mobile Pt-100 temperature sensors equipping the pool vessel. . . . .	40
3.2	The two-stage gravity-driven flashing of superheated water observed within the test device, when starting the experiment at thermal saturation and with an excess in dissolved gases. . . . .	41
3.3	A close look at the heated wall of the pool vessel, showing numerous processes of bubble nucleation. . . . .	41
3.4	Temperature records performed within the heated wall over time, for the reference case. One can note that the right heater side is slightly hotter than its left counterpart, which most likely explains that the first occurrence of bottom wall nucleation was observed onto the right side. . . . .	42
3.5	The bubbles that nucleated onto the right-side of the heated surface rapidly seeded the whole liquid pool, through the form of an uprising two-phase plume. The bubbly plume thickened over time, having much bigger and more numerous bubbles. . . . .	42
3.6	Underneath the liquid free surface, some of the bubbles provided by the two-phase plume explosively expanded. Those events were located below the whole surface. . . . .	43
3.7	After about 1 min, some bubble nucleation appeared as well onto the left-side of the heated wall. At that moment, the flow seemed to re-organize through the form of a central bubbly plume, most likely composed of the merge of the plumes generated right on top of the two sides of the heated surface. . . . .	43
3.8	A close look at one mushroom-like shaped centimetric bubble, nucleated onto the heated wall (here located close to the center of the image), at the beginning of the reference test. . . . .	45

3.9	A series of photos published by <i>van Stralen et al.</i> in 1975, showing water boiling under pressures in between 27 and 2 kPa. One may notice the similarity between the hemispherical, mushroom-like shaped bubbles obtained by <i>van Stralen et al.</i> and the ones observed within the Aquarius test device. Images extracted from [119]. . . . .	46
3.10	A series of photos published by <i>van Stralen et al.</i> in 1975, showing the piercing from below of a mushroom-like shaped bubble by a high-speed liquid jet, right after its departure from its nucleation site. Images extracted from [119]. . . . .	47
3.11	A distortion-based bubble collapse, captured during one exploratory test performed within the Aquarius device by means of the FASTCAM <sup>TM</sup> SA3 model 120K-M1 high-speed camera. As one can observe, the bubble collapse was not complete in this sequence and there remained some tiny bubbles afterwards, which seeded the liquid. Those tiny bubbles re-grew explosively when reaching the free surface. Photos taken by <i>M. Duponcheel</i> . . . . .	48
3.12	A distortion-based bubble collapse, captured during one exploratory test performed within the Aquarius device by means of the FASTCAM <sup>TM</sup> SA3 model 120K-M1 high-speed camera, with an emphasis on the bubble piercing from below by the high-speed liquid jet. The images are displayed every 8 ms. Photos taken by <i>M. Duponcheel</i> . . . . .	49
3.13	During the first stage of the test and when the initial strong bubbling originating from the heated wall ceased, water continuously turned into bubbles just below the liquid free surface. . . . .	50
3.14	Around the end of the test, the phenomenon became very sensitive to any perturbation. Here, an air bubble originating from the bottom of the tank led to the violent vaporization of metastable water. Sequence of images recorded by means of the FASTCAM <sup>TM</sup> SA3 model 120K-M1 high-speed camera. Photos taken by <i>M. Duponcheel</i> . . . . .	50
3.15	A series of photos taken during the late stage of the reference test. The pictures are displayed every 4 ms. The series shows the interaction of a falling droplet with the liquid free surface. The interaction leads to the violent nucleation of a bubble. . . . .	51
3.16	Measured fluid temperatures of the reference test (the heights $z$ mentioned in the legend for each liquid measurement $T_L$ correspond to the sensor location, with $z = 0$ being the location of the pool bottom surface). . . . .	54
3.17	Estimated dimensionless Rayleigh number $Ra_L$ of the natural convection heat transfer that developed through the liquid pool during the reference test. . . . .	54
3.18	Reference test. Left: estimated liquid mass $m_L$ . Right: estimated liquid vaporization rate $\dot{m}_L$ . . . . .	55
3.19	Measured vessel's atmosphere pressure $P_G$ during the reference test, plotted together with $P_{sat}(T_G)$ , the saturation pressure estimated at temperature $T_G$ . . . . .	55

3.20	Estimate of the thermal metastability degree of the heated liquid $\Delta T_{eq}$ during the reference test. From $t = 3$ hrs, $\Delta T_{eq}$ stabilized at a value of $4.5^{\circ}\text{C} \pm 0.35^{\circ}\text{C}$ up to the end of the test. . . . .	56
3.21	Reference test. Left: measured dissolved oxygen concentration $C_{O_2}$ . Right: estimated oxygen degassing rate $\dot{C}_{O_2}$ . . . . .	57
3.22	Reference test. The variables reflecting the liquid degassing and heat-up kinetics, $C_{O_2}$ and $\Delta T_{eq}$ , were linearly correlated according to a pair of trends that intersected at a time estimated to 45 min, in consistency with the visualized transition between a nucleation stage and its non-nucleation counterpart. . . . .	57
3.23	Main physical variables of the achieved nine identical tests, having parameters as close as possible to those of the so-called reference test. One can notice the overall good repeatability of the considered physical variables. . . . .	59
3.24	The correlation between the variables reflecting the liquid degassing and heat-up kinetics $C_{O_2}$ and $\Delta T_{eq}$ , found out from the reference test data, was well repeated. . . . .	60
3.25	Bubble nucleation was initiated at the left-hand-side of the heated wall during Test #9. This differs from the right-hand-side-located nucleation observed during the reference case. . . . .	61
3.26	An illustration of the envisioned bubble growth mechanisms in a pool. . . . .	61
3.27	An illustration of the so-called penetration theory, providing an explanation for the bubble growth by mass transfer. . . . .	63
3.28	Main recorded physical parameters of the step-by-step test performed in December 14, 2021, in order to verify the predominance of the liquid vaporization mechanism in the observed fast bubble growth. . . . .	67
3.29	A photo taken during Stage 3 of the step-by-step test performed in December 14, 2021. The image shows the same kind of fast and sometimes explosive bubble growth as during the reference test. . . . .	68
3.30	Sensitivity to heating power variations. Left: estimated liquid thermal metastability degree $\Delta T_{eq}$ . Right: measured dissolved $O_2$ mass concentration $C_{O_2}$ . . . . .	69
3.31	Sensitivity to heating power variations. Final or asymptotic value reached by the liquid thermal metastability degree $\Delta T_{eq}$ as a function of the heating power. . . . .	70
3.32	Sensitivity to heating power variations. Left: estimated liquid vaporization rate $\dot{m}_L$ . Right: estimated oxygen degassing rate $\dot{C}_{O_2}$ . . . . .	70
3.33	Sensitivity to heating power variations. Final or asymptotic value reached by the liquid thermal metastability degree $\Delta T_{eq}$ as a function of the heating power. . . . .	71
3.34	Timeline of the first period of the test conducted at a power of 250 W, a pressure of 22 mbar, an initial pool level of 30 cm and an initial dissolved $O_2$ concentration of 6.5 mg/L. One can notice the absence of any bubble nucleation onto the heated bottom wall of the vessel. . . . .	71

3.35	Sensitivity to operating pressure variations at a heating power of 1000 W. Left: estimated liquid thermal metastability degree $\Delta T_{eq}$ . Right: measured dissolved O <sub>2</sub> mass concentration $C_{O_2}$ . . . . .	72
3.36	Sensitivity to operating pressure variations at a heating power of 250 W. Left: estimated liquid thermal metastability degree $\Delta T_{eq}$ . Right: measured dissolved O <sub>2</sub> mass concentration $C_{O_2}$ . . . . .	73
3.37	Sensitivity to operating pressure variations at a heating power of 1000 W. Left: estimated liquid vaporization rate $\dot{m}_L$ . Right: estimated oxygen degassing rate $\dot{C}_{O_2}$ . . . . .	73
3.38	Sensitivity to operating pressure variations at a heating power of 250 W. Left: estimated liquid vaporization rate $\dot{m}_L$ . Right: estimated oxygen degassing rate $\dot{C}_{O_2}$ . . . . .	73
3.39	Sensitivity to operating pressure variations. Final or asymptotic value reached by the liquid thermal metastability degree $\Delta T_{eq}$ as a function of the heating power, plotted for three distinct pressure levels: 22, 32 and 42 mbar. . . . .	74
3.40	Sensitivity to operating pressure variations. Correlation between the variables reflecting the liquid degassing and heat-up kinetics, $C_{O_2}$ and $\Delta T_{eq}$ . Left: heating power of 1000 W. Right: heating power of 250 W. . . . .	74
3.41	A photo taken during the first minute of the test conducted at a power of 1000 W and a pressure of 42 mbar, exhibiting some strong bubble flashing underneath the liquid free surface. One can notice that at the time of the photo, the bubble nucleation has ceased onto the heated bottom wall of the vessel. . . . .	75
3.42	Sensitivity to the initial pool level, at a heating power of 250 W. Left: estimated liquid thermal metastability degree $\Delta T_{eq}$ . Right: measured dissolved O <sub>2</sub> mass concentration $C_{O_2}$ . . . . .	76
3.43	Sensitivity to the initial pool level, at a heating power of 250 W. Left: estimated liquid vaporization rate $\dot{m}_L$ . Right: estimated oxygen degassing rate $\dot{C}_{O_2}$ . . . . .	76
3.44	Sensitivity to the initial pool level, at a heating power of 250 W. Correlation between the variables reflecting the liquid degassing and heat-up kinetics, $C_{O_2}$ and $\Delta T_{eq}$ . . . . .	77
3.45	Timeline of the first period of the test conducted at a power of 250 W, a pressure of 22 mbar, an initial pool level of 20 cm and an initial dissolved O <sub>2</sub> concentration of 6.5 mg/L. One can notice the absence of any bubble nucleation onto the heated bottom wall of the vessel. . . . .	77
3.46	A photo taken 3 min after the beginning of the test conducted at a power of 250 W, a pressure of 22 mbar, an initial dissolved O <sub>2</sub> concentration of 6.5 mg/L and an initial pool level of 20 cm, exhibiting some strong flashing underneath the liquid free surface. . . . .	78

3.47	Timeline of the first period of the test conducted at a power of 250 W, a pressure of 22 mbar, an initial pool level of 20 cm and an initial dissolved $O_2$ concentration of 6.5 mg/L. One can notice the absence of any bubble nucleation onto the heated bottom wall of the vessel. . . . .	78
3.48	A photo taken 10 s after the beginning of the test conducted at a power of 1000 W, a pressure of 22 mbar, an initial dissolved $O_2$ concentration of 6.5 mg/L and an initial pool level of 20 cm, exhibiting some strong flashing underneath the liquid free surface and a not less intensive bubble nucleation onto the vessel's heated bottom wall. . . . .	79
3.49	Sensitivity to the initial content in dissolved gases. Estimated liquid thermal metastability degree $\Delta T_{eq}$ . Left: heating power of 250 W. Right: heating power of 1000 W. . . . .	80
3.50	Sensitivity to the initial content in dissolved gases. Measured dissolved $O_2$ mass concentration $C_{O_2}$ . Left: heating power of 250 W. Right: heating power of 1000 W. . . . .	80
3.51	Sensitivity to the initial content in dissolved gases. Correlation between $\Delta T_{eq}$ and $C_{O_2}$ . Left: heating power of 250 W. Right: heating power of 1000 W. . . . .	81
3.52	Timeline of the first period of the tests conducted at a power of 1000 W, a pressure of 22 mbar, an initial pool level of 30 cm but two different initial dissolved $O_2$ concentrations: 6.5 and 0.15 mg/L. One can notice the absence of any bubble nucleation process in the pool and onto the vessel's walls when the liquid is initially highly depleted in dissolved gases. . . . .	81
3.53	Two photos taken at time $t = 1$ min after the beginning of two tests conducted for studying the effect of a localized heat source on the phenomenon. One can notice that in the case of a localized heating, the flashing, usually appearing underneath the liquid free surface, is restricted to the area of the latter which is right on top of the heat source. . . . .	84
3.54	Effect of a localized heat source on the phenomenon, at a heating power of 250 W. Temperature records performed within the heated wall over time. One can notice the wide temperature difference between the left and right sides of the bottom wall when the latter is differentially heated. . . . .	84
3.55	Effect of a localized heat source on the phenomenon, at a heating power of 250 W. Measured fluid temperatures (the heights $z$ mentioned in the legend for each liquid measurement $T_L$ correspond to the sensor location, with $z = 0$ being the location of the pool bottom surface). . . . .	85
3.56	Effect of a localized heat source on the phenomenon, at a heating power of 250 W. Left: estimated liquid thermal metastability degree $\Delta T_{eq}$ . Right: measured dissolved $O_2$ mass concentration $C_{O_2}$ . . . . .	85
3.57	Effect of a localized heat source on the phenomenon, at a heating power of 250 W. Left: estimated liquid vaporization rate $\dot{m}_L$ . Right: estimated oxygen degassing rate $\dot{C}_{O_2}$ . . . . .	85

3.58	Effect of a localized heat source on the phenomenon, at a heating power of 250 W. Correlation between the variables reflecting the liquid degassing and heat-up kinetics, $C_{O_2}$ and $\Delta T_{eq}$ . . . . .	86
3.59	A technical comparison between the MIDI and Aquarius similar experimental devices, both designed by the present author and operated at IRSN Cadarache. . . . .	86
3.60	The angular orientation of the vessel influences the natural convection of heat within the liquid bulk, thereby affecting the phenomenon. Left: No discernible macro-circulation, a uniform flashing is observed below the free surface. Right: A macro-circulation is forced from left to right by inclining the test device, the flashing takes place mainly where the liquid uprises. Photos taken by <i>M. Duponcheel</i> . . . . .	87
3.61	A study of the forcing of bubble nucleation onto the unheated rough wall of the vessel. Photo taken right after the beginning of the test conducted at a power of 250 W, a pressure of 22 mbar, an initial dissolved $O_2$ concentration of 9.5 mg/L, an initial pool level of 30 cm and a prior dry out of the unheated rough wall. Numerous bubbles are visible, thereby validating the retained forcing experimental procedure. . . . .	88
3.62	A study of the forcing of bubble nucleation onto the unheated rough wall of the vessel. Left: estimated liquid thermal metastability degree $\Delta T_{eq}$ . Right: measured dissolved $O_2$ mass concentration $C_{O_2}$ . . . . .	89
3.63	A study of the forcing of bubble nucleation onto the unheated rough wall of the vessel. Left: estimated liquid vaporization rate $\dot{m}_L$ . Right: estimated oxygen degassing rate $\dot{C}_{O_2}$ . . . . .	89
3.64	A study of the forcing of bubble nucleation onto the unheated rough wall of the vessel. Correlation between the variables reflecting the liquid degassing and heat-up kinetics, $C_{O_2}$ and $\Delta T_{eq}$ . . . . .	89
3.65	A study of the forcing of bubble nucleation onto the unheated rough wall of the vessel. Photo taken during the bubbling stage of the test conducted at a power of 250 W, a pressure of 22 mbar, an initial dissolved $O_2$ concentration of 9.5 mg/L, an initial pool level of 30 cm and a prior dry out of the unheated rough wall. During the beginning of that stage, bubbles were seen nucleating both within the liquid bulk and onto the pre-dried out wall. . . . .	90
3.66	An illustration of the observed three locations for bubble nucleation within the Aquarius device. . . . .	92
4.1	A proposed classification for the possible bubble nucleation modes based on their energetic cost. Two main categories of very different energetic cost magnitude are recognized: the nucleation from a pre-existing gas nucleus and the <i>de novo</i> nucleation. . . . .	94

4.2	An estimate of the bubble Péclet number $Pe_b$ , given by Equation (4.6), for water against $r_b$ , at an arbitrary liquid temperature $T_L$ of 300 K and at a low pressure such that $\rho_L \gg \rho_G$ . One can notice that $Pe_b > 1$ for a bubble radius $r_b > 0.5 \mu\text{m}$ . . . . .	96
4.3	An illustration of the bubble hydrodynamic stabilization mechanism, based on the Brownian motion of water molecules. This mechanism comes into play for air bubble sizes smaller than $1 \mu\text{m}$ . . . . .	97
4.4	The idealization of a gas nucleus floating freely in water and its associated thermodynamic variables. . . . .	98
4.5	The idealization of a Harvey's nucleus entrapped in a solid wall, here a solid particle suspended in the liquid, and its associated thermodynamic variables. . . . .	101
4.6	The gas capture mechanism during the wetting of some solid particle by a liquid, according to <i>Bankoff</i> [7]. . . . .	102
4.7	Idealized cylindrical wall crevice onto some solid surface and a postulated entrapped gas nucleus within it. . . . .	102
4.8	A microscopic view of artificial Polystyrene particles with a corrugated surface, extracted from [4]. . . . .	103
4.9	The idealization of a bubble nucleation cycle taking place onto a wall. Here this cycle is exemplified for the peculiar case of a disequilibrating heat and/or mass transfer coming from the liquid bulk. . . . .	105
4.10	An illustration of the postulated mechanism behind the de novo formation of a gas nucleus within the liquid bulk. . . . .	106
4.11	Variations of the free energy $\Delta F$ associated with the formation of a gas nucleus against radius $r$ . The position $r = r^*$ is an equilibrium point. But this equilibrium is unstable, since this point is a local maximum and not a local minimum of the free energy. . . . .	107
4.12	An illustration of the postulated mechanism behind the de novo formation of a gas nucleus around a solid discontinuity present within the liquid. The molecules are obviously not in scale with respect to the solid discontinuity. . . . .	109
4.13	Illustration of the two main variables characterizing a solid surface roughness in surface metrology: the arithmetical mean roughness $R_a$ and maximum peak-to-valley height $R_z$ . . . . .	111
4.14	Illustration of the capillary meniscus that is expected to form between the liquid bulk and pool vessel vertical walls. . . . .	112
4.15	Variations of the pressure-dependent term of $(\Delta T_{sat})_{crit}$ against the liquid local pressure $P_L$ . $(\Delta T_{sat})_{crit}$ is a decreasing function of $P_L$ over the studied pressure range (10 - 100 mbar). . . . .	114
4.16	Variations of $(\Delta T_{sat})_{crit}$ against the liquid local pressure $P_L$ and partial pressure of dissolved air $P_a^L$ . Upper map: estimate for the finely-polished solid surface. Lower map: estimate for the rough solid surface. . . . .	115

4.17	Time variations of $(\Delta T_{sat})_{crit}$ and $\Delta T_{sat;h}$ , evaluated at the heated wall, for the four selected tests. The graphs are plotted over only the first 10 min of a test, <i>i.e.</i> when the bubble nucleation process is likely to occur at the heated wall. . . . .	117
4.18	A focus on the time variation of $\Delta T_{sat;h}$ , evaluated at the heated wall, for the four selected tests. The graphs are plotted over only the first 10 min of a test, <i>i.e.</i> when the bubble nucleation process is likely to occur at the heated wall. . . . .	118
4.19	Time variations of the hydrostatic pressure $P_L$ at the bottom of the pool and dissolved air partial pressure $P_a^L$ . The graphs are plotted over only the first 10 min of a test, <i>i.e.</i> when the bubble nucleation process is likely to occur at the heated wall. . . . .	118
4.20	Unheated rough vertical wall of the pool vessel. Upper map: time trend of an interpolation of the unheated wall vertical temperature profile, achieved on the basis of the ten discrete measurements detailed in Table 4.3. Lower map: time trend of an interpolation of the unheated wall vertical superheat profile $\Delta T_{sat;w}$ . . . . .	121
4.21	Comparison of the maximum value of $\Delta T_{sat;w}$ , denoted as $\text{Max}(\Delta T_{sat;w})$ , with its corresponding critical liquid superheat $(\Delta T_{sat})_{crit}$ , at the unheated rough wall of the pool vessel, during the reference case. . . . .	121
4.22	Illustration of a collapsing gas nucleus subjected to a pressure pulse, simulated by <i>Lohse et al.</i> (figure extracted from [16]). At the stressed nucleus interface, a liquid jet forms. The latter is here able to reach and flood the bottom of the cavity, thereby removing any remnant gas. . . . .	124
4.23	Variations of the temperature-dependent term $(P_a^L)_{crit;BN}$ against the liquid local temperature $T_L$ . . . . .	126
4.24	A photography of the Aquarius water pool taken 3 minutes after the test startup. One may note that fewer bubbles were seen nucleating within the liquid when the water was left at rest during 19 days prior to the test. . . .	129
4.25	Time variations of the liquid thermal metastability degree $\Delta T_{eq}$ (left graph) and of the dissolved $O_2$ concentration $C_{O_2}$ (right graph). . . . .	129
4.26	Time variations of the liquid pool mass $m_l$ (left graph) and of the liquid vaporization rate $\dot{m}_l$ (right graph). . . . .	130
4.27	A series of photographs taken during the late stage of the reference test, presented in Chapter 3. The pictures are displayed every 4 ms. The series shows the interaction of a falling droplet with the free surface of the superheated liquid. The interaction leads to the violent growth of a bubble. . . . .	132
4.28	A series of photographs taken during the late stage of the reference test, presented in Chapter 3. The pictures are displayed every 4 ms. The series shows the interaction of a falling droplet with the free surface of the superheated liquid, with an emphasis on the event of a void formation right after the droplet impact. . . . .	133

4.29	A series of photographs of a droplet impact and its resulting void formation, published by <i>Worthington</i> in 1908 and extracted from [127]. . . . .	134
5.1	An idealization of the heat transfer taking place between the heated bottom wall and the liquid bulk. . . . .	138
5.2	Reference test. Left: estimate of the heated wall temperature difference $\Delta T_h$ . Right: estimate of the heated wall heat transfer coefficient $k_h$ . . . . .	139
5.3	Repeated time-trends of $k_h$ , the wall-to-liquid heat transfer coefficient. . . . .	139
5.4	Standard deviation $\sigma_{k_h}$ of the repeated time-trends of $k_h$ . . . . .	140
5.5	Average time-trend of the repeated $k_h$ with its associated estimated uncertainty. . . . .	141
5.6	Sensitivity to heating power variations. Estimate of the heated wall heat transfer coefficient $k_h$ . . . . .	141
5.7	Sensitivity to operating pressure variations. Estimate of the heated wall heat transfer coefficient $k_h$ . . . . .	142
5.8	Sensitivity to initial pool level variations. Estimate of the heated wall heat transfer coefficient $k_h$ . . . . .	142
5.9	Sensitivity to initial content in dissolved gases variations. Estimate of the heated wall heat transfer coefficient $k_h$ . . . . .	143
5.10	An idealization of the heat and mass transfers taking place between the liquid bulk and the overall gas/liquid interfacial area (all bubbles + pool free surface), during the two-phase regime. . . . .	144
5.11	Reference test. Estimate of the gas/liquid heat transfer rate $k_T^L S_i$ . . . . .	145
5.12	Repeated time-trends of $k_T^L S_i$ , the gas/liquid heat transfer rate. . . . .	145
5.13	Standard deviation $\sigma_{k_T^L S_i}$ of the repeated time-trends of $k_T^L S_i$ . . . . .	146
5.14	Average time-trend of the repeated $k_T^L S_i$ with its associated estimated uncertainty. . . . .	146
5.15	Sensitivity to heating power variations. Estimate of the gas/liquid heat transfer rate $k_T^L S_i$ . . . . .	147
5.16	Sensitivity to operating pressure variations. Estimate of the gas/liquid heat transfer rate $k_T^L S_i$ . . . . .	147
5.17	Sensitivity to initial pool level variations. Estimate of the gas/liquid heat transfer rate $k_T^L S_i$ . . . . .	148
5.18	Sensitivity to initial content in dissolved gases variations. Estimate of the gas/liquid heat transfer rate $k_T^L S_i$ . . . . .	148
5.19	Reference test. Estimate of the dissolved air degassing rate $k_m^L S_i$ . . . . .	150
5.20	Repeated time-trends of $k_m^L S_i$ , the dissolved air degassing rate. . . . .	151
5.21	Standard deviation $\sigma_{k_m^L S_i}$ of the repeated time-trends of $k_m^L S_i$ . . . . .	151
5.22	Average time-trend of the repeated $k_m^L S_i$ with its associated estimated uncertainty. . . . .	152
5.23	Sensitivity to heating power variations. Estimate of $k_m^L S_i$ , the dissolved air degassing rate. . . . .	153

5.24	Sensitivity to operating pressure variations. Estimate of $k_m^L S_i$ , the dissolved air degassing rate. . . . .	153
5.25	Sensitivity to initial pool level variations. Estimate of $k_m^L S_i$ , the dissolved air degassing rate. . . . .	154
5.26	Sensitivity to initial content in dissolved gases variations. Estimate of $k_m^L S_i$ , the dissolved air degassing rate. . . . .	154
5.27	An idealization of the heat and mass transfers taking place between the liquid bulk and its free surface during the single-phase regime. . . . .	157
5.28	The Nusselt versus Rayleigh numbers natural convection heat transfer correlation obtained in the single-phase regime from the 24 tests of the regular matrix. This correlation reflects the liquid-bulk-to-free-surface heat transfer behind the free surface evaporation process. . . . .	159
5.29	The tests initiated with a different amount of dissolved oxygen comply as well with the Nusselt versus Rayleigh natural convection heat transfer correlation, obtained in the single-phase regime, from the 24 tests of the regular matrix. This correlation reflects the liquid-bulk-to-free-surface heat transfer behind the free surface evaporation process. . . . .	159
5.30	The Sherwood versus Rayleigh numbers natural convection mass transfer correlation obtained in the single-phase regime from the 24 tests of the regular matrix. This correlation reflects the liquid-bulk-to-free-surface dissolved gases transfer behind the degassing process. . . . .	160
5.31	The tests initiated with a different amount of dissolved oxygen comply as well with the Sherwood versus Rayleigh natural convection mass transfer correlation, obtained in the single-phase regime, from the 24 tests of the regular matrix. This correlation reflects the liquid-bulk-to-free-surface dissolved gases transfer behind the degassing process. . . . .	161
5.32	The Nusselt versus Rayleigh numbers natural convection heat transfer correlation obtained from the 24 tests of the regular matrix. This correlation reflects the heated-wall-to-liquid heat transfer. . . . .	163
5.33	The tests initiated with a different amount of dissolved oxygen comply as well with the Nusselt versus Rayleigh natural convection heat transfer correlation, obtained from the 24 tests of the regular matrix. This correlation reflects the heated-wall-to-liquid heat transfer. . . . .	164
5.34	Plotting of $\Phi_T$ versus $Gb$ , achieved on the basis of the time-series of the tests composing the regular matrix. . . . .	166
5.35	Plotting of $\Phi_T/Gb^{-0.33}$ versus $Gb$ , achieved on the basis of the time-series of the tests composing the regular matrix. . . . .	167
5.36	Plotting of $\Phi_T/Gb^{-0.33}$ versus $Gb$ , with a color scale taking into account the retained initial pool level, achieved on the basis of the time-series of the tests composing the regular matrix. . . . .	168

5.37	Plotting of $\Phi_T/Gb^{-0.33}/Ra_L^{1.5}$ versus $Gb$ , with a color scale taking into account the retained initial pool level, achieved on the basis of the time-series of the tests composing the regular matrix. . . . .	168
5.38	Plotting of $\Phi_T/Gb^{-0.33}/Ra_L^{1.5}$ versus $Gb$ , achieved on the basis of the time-series of the tests initiated with a different amount of dissolved oxygen. . .	169
5.39	Plotting of $\Phi_m$ versus $Gb$ , achieved on the basis of the time-series of the tests composing the regular matrix. . . . .	170
5.40	Plotting of $\Phi_m/Gb^{-0.33}$ versus $Gb$ , achieved on the basis of the time-series of the tests composing the regular matrix. . . . .	170
5.41	Plotting of $\Phi_m/Gb^{-0.33}$ versus $Gb$ , with a color scale taking into account the retained initial pool level, achieved on the basis of the time-series of the tests composing the regular matrix. . . . .	171
5.42	Plotting of $\Phi_m/Gb^{-0.33}/Ra_L^{1.5}$ versus $Gb$ , with a color scale taking into account the retained initial pool level, achieved on the basis of the time-series of the tests composing the regular matrix. . . . .	172
5.43	Plotting of $\Phi_m/Gb^{-0.33}/Ra_L^{1.5}$ versus $Gb$ , achieved on the basis of the time-series of the tests initiated with a different amount of dissolved oxygen. . .	172
5.44	Illustration of the modeled control volume $V_L$ and its associated conservative and state variables. . . . .	174
5.45	Simulation of the reference test. Left: liquid mass $m_L$ . Right: liquid vaporization rate $\dot{m}_L$ . . . . .	177
5.46	Simulation of the reference test. Time-trend of the thermal metastability degree of the heated liquid $\Delta T_{eq}$ . . . . .	178
5.47	Simulation of the reference test. Left: dissolved oxygen mass concentration $C_{O_2}$ . Right: oxygen degassing rate $\dot{C}_{O_2}$ . . . . .	178
5.48	Simulation of the reference test. Left: heated wall temperature difference $\Delta T_h$ . Right: heated wall heat transfer coefficient $k_h$ . . . . .	179
5.49	Simulation of the reference test. Left: interfacial heat transfer rate $k_T^L S_i$ . Right: interfacial mass transfer rate $k_m^L S_i$ . . . . .	179
5.50	Simulation of the reference test. Dimensionless quantities $\Phi_T$ and $\Phi_m$ associated with the interfacial heat and mass transfer rates $k_T^L S_i$ and $k_m^L S_i$ . .	179
5.51	Simulation of the reference test. Correlation between the variables reflecting the liquid degassing and heat-up kinetics, $C_{O_2}$ and $\Delta T_{eq}$ . . . . .	180
5.52	Simulated sensitivity to heating power variations. Left: estimated liquid thermal metastability degree $\Delta T_{eq}$ . Right: measured dissolved $O_2$ mass concentration $C_{O_2}$ . . . . .	182
5.53	Simulated sensitivity to heating power variations. Left: estimated liquid vaporization rate $\dot{m}_L$ . Right: estimated oxygen degassing rate $\dot{C}_{O_2}$ . . . . .	182
5.54	Simulated sensitivity to heating power variations. Left: interfacial heat transfer rate $k_T^L S_i$ . Right: interfacial mass transfer rate $k_m^L S_i$ . . . . .	183

5.55	Simulated sensitivity to operating pressure variations. Left: estimated liquid thermal metastability degree $\Delta T_{eq}$ . Right: measured dissolved O <sub>2</sub> mass concentration $C_{O_2}$ . . . . .	184
5.56	Simulated sensitivity to operating pressure variations. Left: estimated liquid vaporization rate $\dot{m}_L$ . Right: estimated oxygen degassing rate $\dot{C}_{O_2}$ . . . . .	184
5.57	Simulated sensitivity to operating pressure variations. Left: interfacial heat transfer rate $k_T^L S_i$ . Right: interfacial mass transfer rate $k_m^L S_i$ . . . . .	184
5.58	Simulated sensitivity to initial pool level variations. Left: estimated liquid thermal metastability degree $\Delta T_{eq}$ . Right: measured dissolved O <sub>2</sub> mass concentration $C_{O_2}$ . . . . .	185
5.59	Simulated sensitivity to initial pool level variations. Left: estimated liquid vaporization rate $\dot{m}_L$ . Right: estimated oxygen degassing rate $\dot{C}_{O_2}$ . . . . .	186
5.60	Simulated sensitivity to initial pool level variations. Left: interfacial heat transfer rate $k_T^L S_i$ . Right: interfacial mass transfer rate $k_m^L S_i$ . . . . .	186
5.61	Simulated sensitivity to initial content in dissolved gases variations. Left: estimated liquid thermal metastability degree $\Delta T_{eq}$ . Right: measured dissolved O <sub>2</sub> mass concentration $C_{O_2}$ . . . . .	187
5.62	Simulated sensitivity to initial content in dissolved gases variations. Left: estimated liquid vaporization rate $\dot{m}_L$ . Right: estimated oxygen degassing rate $\dot{C}_{O_2}$ . . . . .	187
5.63	Simulated sensitivity to initial content in dissolved gases variations. Left: interfacial heat transfer rate $k_T^L S_i$ . Right: interfacial mass transfer rate $k_m^L S_i$ . . . . .	187
A.1	Aquarius vessel $\Delta P = f(m_L)$ relationship. . . . .	208
B.1	Illustration of the gas/liquid interface separating the studied ternary mixture of water and dissolved O <sub>2</sub> and N <sub>2</sub> from a gas bulk. . . . .	210
B.2	The temperature-dependent Henry's volatility constants of air, O <sub>2</sub> and N <sub>2</sub> in dissolution within water (in Pa/mol/mol) according to the data published in [1] and [47]. . . . .	212
B.3	The temperature-dependent diffusivities of air, O <sub>2</sub> and N <sub>2</sub> in liquid water, empirically determined and reported by <i>Wise and Houghton</i> in [126]. . . . .	213
B.4	Illustration of the postulated heat and mass transfer films where the temperature and composition gradients are non-null, in the vicinity of the gas/liquid interface. . . . .	214
B.5	Temperature dependence of the <i>ratio</i> between the O <sub>2</sub> and N <sub>2</sub> film thicknesses. This quantity is almost constant and equal to 0.95 over the temperature range 10-60°C. . . . .	218
B.6	Temperature dependence of the <i>ratio</i> between the mass and heat transfer film thicknesses. The mass transfer film is 3 to 4 times smaller than the heat transfer film over the temperature range 10-60°C. . . . .	218
B.7	The temperature dependence of $\mathcal{H}_m^*$ , the <i>ratio</i> of the Henry's constants of the dissolved species, defined in Equation (B.44). . . . .	220

B.8	The comparison between the empirical $\mathcal{D}_{a;w}^L$ , reported in [126], and its prediction based on Equation (B.60) and on the values of $\mathcal{D}_{O_2;w}^L$ and $\mathcal{D}_{N_2;w}^L$ given in [126]. . . . .	222
D.1	The uncertainties, respectively in link with the measuring chain and the experimental procedure and boundary conditions, combine and alter the quality of the obtained results. In this example, the depicted overall uncertainty varies arbitrarily with time. . . . .	236
D.2	The followed methodology in the evaluation of the uncertainties affecting the quality of the experimental results, according to the GUM [59]. . . . .	236
D.3	Calibration test of the Pt-100 probes - temperature records. Left: full time scale. Right: time scale restricted to 8 hours. . . . .	238
D.4	Calibration test of the Pt-100 probes - differences between the corrected measurements and the reference temperature. . . . .	240
D.5	Left: variation of $u_{T_{sat}}^{mes}$ against <b>P140Ap</b> . Right: variation of $u_{P_{sat}}^{mes}$ against <b>T120W</b> . The maximum value of those two uncertainties is respectively equal to 0.048°C and 0.076 mbar. . . . .	243
D.6	Main physical variables of the achieved nine identical tests, having parameters as close as possible to those of the so-called reference test. One can notice the overall good repeatability of the considered physical variables. .	248

---

## List of Tables

2.1	Comparison of the reference spent-fuel-pool and Aquarius test device main characteristics. . . . .	24
2.2	The used pressure sensors and their relative accuracy. . . . .	35
2.3	Combined uncertainties attributed to a set of relevant physical variables, with a coverage factor of 95%. . . . .	35
3.1	The achieved nine identical tests for studying the repeatability of the observed phenomena. In the last column of this table is indicated the side of the heated wall where some bubble nucleation was observed at first. . . .	58
3.2	Calculated time-averaged standard deviations associated with each main physical variable, on the basis of the nine repeated tests. . . . .	60
3.3	The series of tests achieved for investigating the effect of the heating power on the phenomenon. . . . .	69
3.4	The series of tests achieved for investigating the effect of the operating pressure on the phenomenon. . . . .	72
3.5	The series of tests achieved for investigating the effect of the initial pool level on the phenomenon. . . . .	75
3.6	The series of tests achieved for investigating the effect of the initial content in dissolved gases on the phenomenon. . . . .	79
3.7	The series of tests achieved for investigating the effect of a localized heat source on the phenomenon. . . . .	83
3.8	The series of tests achieved for investigating the effect of a forcing of bubble nucleation onto the unheated rough wall on the phenomenon. . . . .	88
4.1	The estimate of the characteristic lengths of the finely-polished and rough stainless steel walls of the pool vessel. . . . .	113
4.2	The selected tests for studying bubble nucleation onto the heated wall. . .	116
4.3	Reference of the Pt-100 thermometers embedded in the rough vertical wall of the pool vessel and their vertical position. . . . .	119

5.1	The series of tests composing the so-called regular experimental matrix. . . . .	155
5.2	The series of tests used as a verification basis for the developed heat and mass transfers correlations. . . . .	155
5.3	The series of tests, retained and simulated, for investigating the effect of the heating power on the phenomenon. . . . .	181
5.4	The series of tests, retained and simulated, for investigating the effect of the operating pressure on the phenomenon. . . . .	183
5.5	The series of tests, retained and simulated, for investigating the effect of the initial pool level on the phenomenon. . . . .	185
5.6	The series of tests, retained and simulated, for investigating the effect of the initial content in dissolved gases on the phenomenon. . . . .	186
B.1	The Henry's volatility constants of air, O <sub>2</sub> and N <sub>2</sub> in dissolution within water (in Pa/mol/mol) according to the data published in [1] and [47]. . . . .	211
B.2	The diffusivities of air, O <sub>2</sub> and N <sub>2</sub> in liquid water, empirically determined and reported by <i>Wise and Houghton</i> in [126]. . . . .	212
D.1	Correction factors applied to the Pt-100 thermometers. . . . .	239
D.2	The used pressure sensors and their relative accuracy. . . . .	240
D.3	Propagated standard or relative uncertainties $u_X^{mes}$ or $\epsilon_X^{mes}$ in link with the measuring chain. . . . .	246
D.4	Time-averaged standard or relative uncertainties $u_X^{rep}$ or $\epsilon_X^{rep}$ of the repeated relevant physical quantities $X$ of a pool flashing test. . . . .	247
D.5	The overall uncertainty budget of the computed physical variables. . . . .	249



---

# Introduction



## 1.1 A first glimpse into the studied physics

The gravity-driven flashing of superheated water, topic of the present doctoral thesis, is a non-equilibrium phase change phenomenon which is usually associated with a type of natural marvel called *geyser* (*cf.* Figure 1.1) [77]. The phenomenon is also met in a wealth of industrial thermal systems having some key features in common with this marvel. In order to get a first insight into the studied phenomenon and highlight its key features, let us first focus on its most popular and perhaps funniest occurrence: the geyser. The latter, leading to an upward discharge of both liquid and vapor to the atmosphere, is typically cyclic and comes out according to the three stages illustrated in Figure 1.2. For observing the phenomenon, a heat supply is obviously essential (Stage 1) [2]. If this input is achieved at a low position within the geyser's geometry, as depicted for instance in Figure 1.2, the heated liquid is hence expected to rise toward the upper-end of the channel. During its upward course, the flowing liquid naturally

experiences a decrease in hydrostatic pressure. If the latter is enough, the liquid temperature may exceed the saturation one, associated with the local pressure, at some elevation within the channel (Stage 2). In doing so, the liquid may reach a *metastable equilibrium state*, also largely referred to as *superheated state* in the thermal-hydraulic community and throughout this thesis. Provided there exists a much more stable equilibrium state than the metastable one, corresponding to thermal saturation, a gas phase may spontaneously appear within the liquid as a way to reach this ultimate equilibrium (Stage 3). In details, the energetic cost associated with the formation of this new phase can be directly supported by the heat in excess within the metastable liquid, thereby bringing the latter closer to thermal saturation conditions. This process is classically called *relaxation* in physics [34] or *flashing*, in the thermal-hydraulic community [72], two terms that will be often met in the present doctoral thesis. The formed new phase is merely constituted by bubbles, whose emergence is referred to as *nucleation*. Sometimes, the liquid superheating does not lead to a bubble nucleation. Instead, if some tiny bubbles, largely referred to as *gas nuclei* in this thesis, pre-exist within the liquid, the latter may directly and preferentially relax by vaporizing onto those available gas/liquid interfaces. Anyhow, the presence and growth of those bubbles further reduce the local hydrostatic pressure, thereby enhancing the degree of thermal metastability of the liquid and increasing the vaporization and/or bubble nucleation rate, in a self-sustained fashion that is often explosive [90]. This last case, which is typically unwanted in an industrial context, is precisely the one leading to the spectacular geyser eruptions met in Nature (*cf.* Figure 1.1). In short, this introductory example exhibits three essential features allowing the occurrence of the phenomenon: a heat supply located at the bottom-end of the studied system, a significant vertical variation in saturation temperature favoring a gravity-driven superheating of the uprising hot fluid and an open top-end from which some liquid and vapor can be ejected. Keeping in mind those three key features, let us question the level of knowledge associated with the phenomenon in what follows.

## 1.2 A partially known phenomenon

If the first and second stages of the studied physics are rather well understood [77], in turn, the bubble nucleation process in water keeps unclear more than a century after its first analyses [18]. Indeed, the community has early recognized that superheated water relaxation depends on many extraneous factors such as the presence within the liquid of solid impurities, dissolved gases or chemical surfactants [34], or more exotically, the presence of water molecules ionized by an incoming subatomic particle, like photons or neutrons [36], [67]. For obvious reasons, these molecular-scale or subatomic factors are often if not always difficult to characterize, which justifies the absence of a consensual theory for describing the phenomenon to that date [87]. Bringing more fuzziness to the topic, bubble nucleation appears sensitive to the nature of the solid walls of the water container, with some materials leading to the emergence of bubbles and some others



Figure 1.1: Front view of the so-called *Castle Geyser*, located in the Yellowstone National Park, USA.

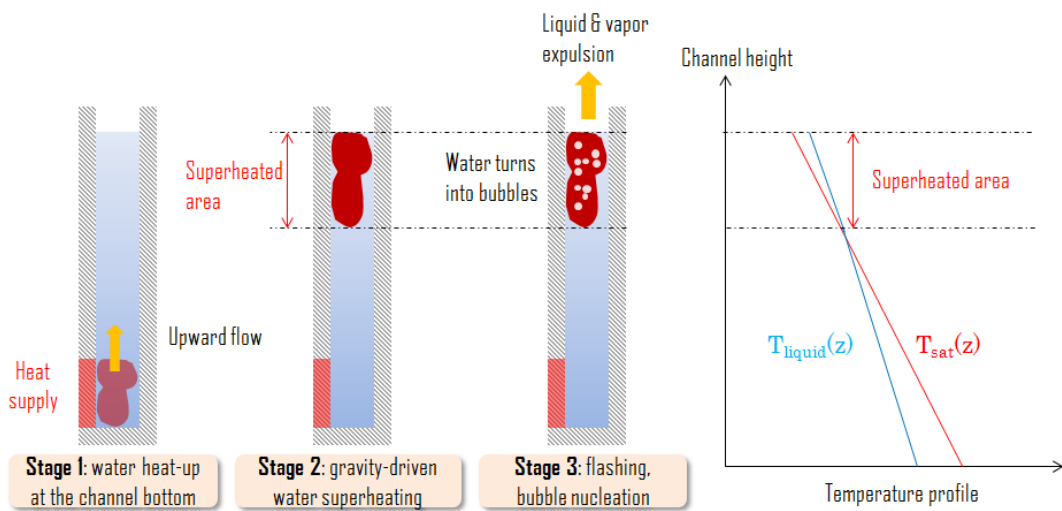


Figure 1.2: Illustration of the gravity-driven flashing of superheated water in a geyser-like system, as it is understood to date. The fresh water supply, usually located at the geyser's bottom-end through the form of a phreatic volume is not represented here, for simplicity. Left-hand-side: Stage 1) Water is heated up at the bottom-end of the channel and starts uprising, Stage 2) Water is superheated by gravity when reaching parts of the channel of reduced hydrostatic pressure, such that its temperature becomes higher than the local saturation temperature, Stage 3) Water starts turning into bubbles as a way to tend toward an equilibrium state of greater stability, a process called relaxation, flashing or bubble nucleation. Right-hand-side: idealized vertical profile of the liquid water and saturation temperatures within the geyser.

not. As early as the nineteenth century, physicists did report this effect, such as the French physicist *A. Guillemin* in [48], who discussed its consequence for the operation and safety of steam engines, or the British physicist *H. Cavendish* who stated in [23]: “*The excess of the heat of water above the boiling point is influenced by a great variety of circumstances*”, those many circumstances being naturally the ones mentioned above. The temperature at which heated water boils, literally at which it turns into bubbles, is from the very beginning of thermometry considered as a reference point for instrument calibration, what unsurprisingly, has continuously raised issues about those nucleation circumstances since then [24]. More importantly, the fuzziness about the relaxation process of superheated water has brought confusion in the academic field when teaching the very nature of water boiling, as argued by the science philosopher *H. Chang* in [25]: “*We all learn at school that pure water always boils at 100°C (212°F), under normal atmospheric pressure. Like surprisingly many things that "everybody knows", this is a myth. We ought to stop perpetuating this myth in schools and universities and in everyday life: not only is it incorrect, but it also conveys misleading ideas about the nature of scientific knowledge. And unlike some other myths, it does not serve sufficiently useful functions.*” As it will be widely discussed later in this thesis, even the pre-existence of gas nuclei in the liquid, promoting its vaporization, is still debated to that date with two competing theories being available but unverified for every envisioned configuration [87]. In sum, the studied physics does appear only partially understood by the community because of all those still-open questions in link with the relaxation of metastable water.

### 1.3 An unstudied physics in pools heated from below

As already mentioned, Nature provides us with some spectacular occurrences of the studied phenomenon through the existence of geysers. Those fascinating systems, that are not yet fully understood for the reasons discussed above, have been widely studied for more than two centuries [100], even regarding their most remote materializations in the solar system [19]. In an industrial context, many types of vertical channel two-phase flows are concerned with the phenomenon, often seen as a destabilizing feature [77]. For instance, in the field of rocket engines, its occurrence is feared, which has motivated many experimental studies the past decades [90]. In the nuclear industry, this type of two-phase instability is also suspected under low pressure, low flow-rate conditions in those envisioned light water nuclear reactors operated passively, by means of natural convection [77]. This has yielded many studies, starting with those of *Jiang et al.* performed in 1995 [60] and *Paniagua et al.* in 1999 [95]. Recently, taking advantage from more modern instrumentation techniques, *Manera et al.* in 2003 and then *Furuya et al.* in 2005 investigated the phenomenon in a set of dedicated experimental devices at TU Delft University [79], [45]. In contrast and to our best knowledge, the scientific literature does not mention to date any similar study in a pool-type geometry heated from below. This is perhaps a legitimate consequence of the only few natural

or industrial occurrences of the phenomenon in this very configuration. Let us briefly review those occurrences, as reported in the literature. First of all, the phenomenon is assumed, with no certainty, to contribute to the often spectacular phreatic volcanic eruptions. Those eruptions are indeed thought as being driven by the decompression, superheating and phase change experienced by some uprising subterranean geothermal water, heated from below in the vicinity of a magma in a phreatic chamber (*i.e.* some sort of liquid pool) [21]. In an industrial context, the gravity-driven flashing of superheated water is considered as one of the phenomena that might occur during a loss-of-cooling accident affecting the storage pools of spent nuclear fuels, also shortly referred to as SFP [93], [94]. Indeed, such pools are usually 10-meter deep as visible in Figure 1.3, which results in a vertical saturation temperature difference of the order of 20°C. Those pools may also contain up to a dozen megawatts of radioactive decay heat. When the cooling system of a SFP is accidentally lost, as this occurred for instance during the Fukushima-Daiichi nuclear accident in March 2011 [113], each stored spent fuel acts as a heat source and generates an upward flow of warm water which can be potentially superheated by a vertical decompression and later vaporize, as illustrated in Figure 1.4. If no countermeasures are taken during this accident, the pool water level will drop down, ultimately leading to the uncovering of the spent fuels and later, to their degradation, as it was feared during the Fukushima-Daiichi accident [93]. Before that very outcome, two specific safety risks have been highlighted as being worth evaluated. First, the raise of the water temperature and the potential presence of bubbles in the pool might hinder the recovery of the SFP cool-down by restarting the normal cooling systems in the course of the accident, if the electric supply of the latter systems is somehow recovered. Indeed, pumping some superheated water, with or without bubbles within it, may represent a technical challenge, with the pumps being potentially prompt to cavitation and/or to loose their suction [94]. Second, the radioactive contamination initially retained in the water of any SFP, in particular under accidental conditions, is expected to leak out and reach the atmosphere on top of the pool. This release process is known as being triggered by the potential bubbling / boiling of the water containing the population of residual radionuclides [122]. These specific issues have motivated the conduction of a research program on SFP accidents at the French *Institut de Radioprotection et de Sûreté Nucléaire* (IRSN) from the past ten years. Among the IRSN's activities on that topic is the present doctoral project, led in collaboration with the *Université catholique de Louvain* (UCLouvain, Belgium) since 2018.

Nevertheless, one may wonder how different is a pool-type configuration from genuine or industrial geyser-like systems and if one can legitimately extrapolate what is known about the latter to the former. For answering these questions, a close look at the available literature on geysers may help, obviously. First of all, many authors, such as for instance *Murphy*, mentioned the importance of the length-to-diameter or “aspect” ratio of the geyser for observing a cyclic expulsion of both vapor and liquid [90]. If one denotes this ratio as  $L/D$ , a cyclic geysering can be empirically reproduced for

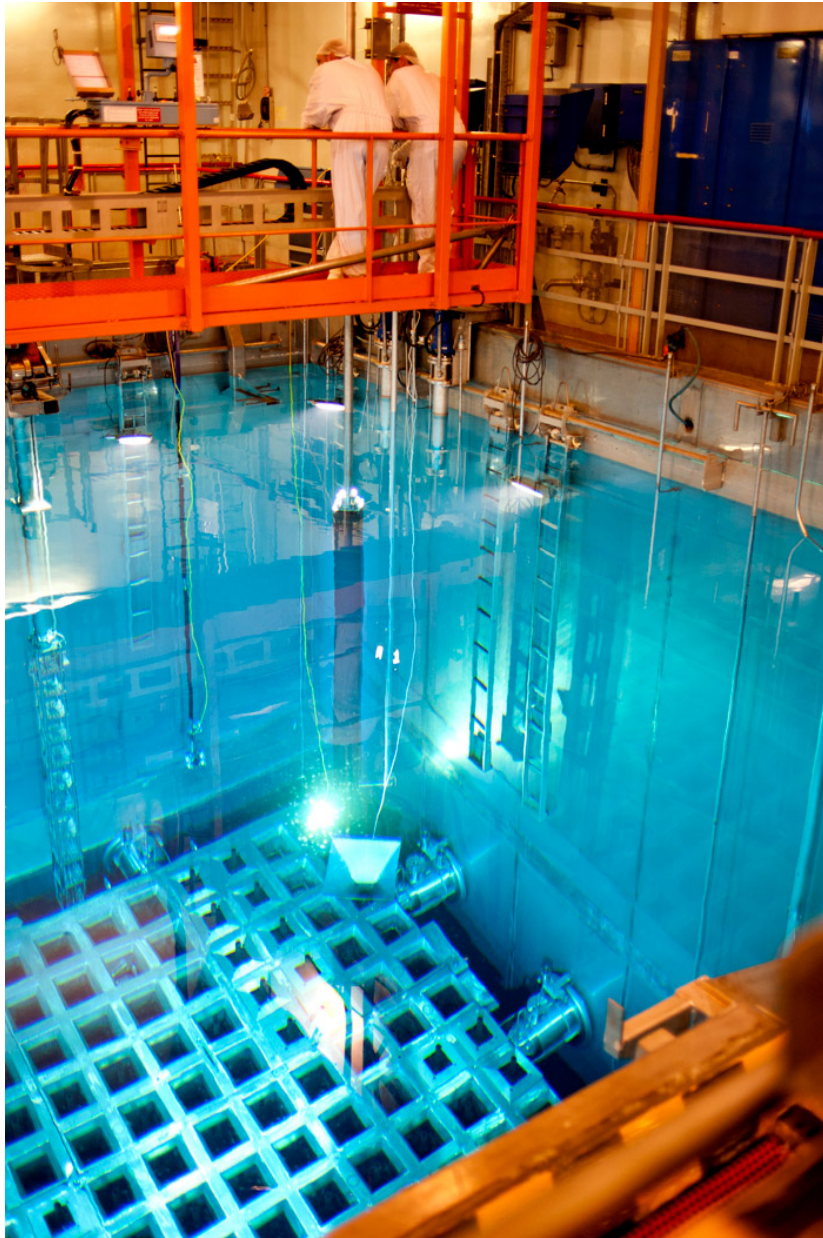


Figure 1.3: Top view of the spent-fuel-pool of Reactor No.1 at EDF's Blayais nuclear power plant, ©Médiathèque IRSN.

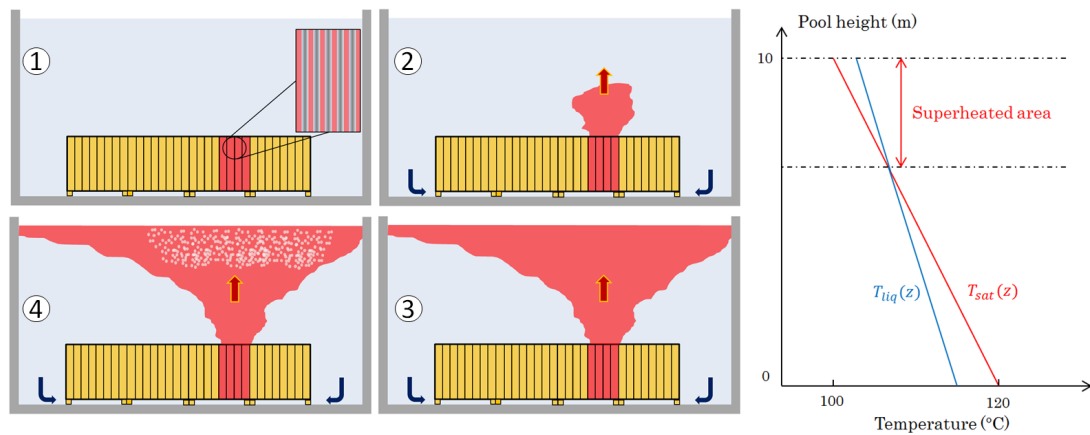


Figure 1.4: The accidental gravity-driven flashing as envisioned in a spent-fuel-pool. Left-hand-side: 1) Water is heated up by the spent fuels and keeps subcooled, 2) A natural convection flow develops at pool scale, 3) The boiling point is locally exceeded in the upper part of the pool by the uprising water, 4) The superheated water flashes and turns into bubbles. Right-hand-side: idealized vertical profile of the water temperature and of the boiling point within the uprising plume.

$1.5 < L/D < 30$ , corresponding to vertical tube configurations [77]. For  $L/D$  smaller than unity and corresponding to pool-type geometries, the phenomenon is hence expected to turn steady and yield a continuous, rather than cyclic, expulsion of vapor and liquid at the geometry's upper-end. In this case, the phenomenon is no longer referred to as geyser. But considering that all the studies mentioned above are mostly focused on the cyclic features of geysers, the extrapolation of what is known about the latter to a heated water pool under steady flashing conditions is useless. Second, the reach of liquid superheats within the upper-part of such pools is clearly questionable. Indeed, the flow topology and in turn the liquid temperature field are to be very different in between a vertical tube and a pool geometry, the  $L/D$  ratio being a key parameter of natural convection flows [116]. At last is the question of the relaxation mechanisms that may emerge from the superheated water. As mentioned earlier in this introduction, bubble nucleation is sensitive to the presence and nature of the solid walls of the water container. Therefore, one may wonder if in a pool-type configuration those solid walls are to play the same role with regards to this process. Indeed, the area of all immersed surfaces is in this case much smaller than the liquid volume when compared with a channel geometry. One may thus expect the impact of these walls on bubble nucleation to be sensibly different. Regarding this feature of the phenomenon, a wealth of studies has been conducted in unheated pool-type geometries for exploring the physics of so-called *flash evaporator systems*, the most significant of them being those of *Huyghe et al.* [56], *Gopalakrishna et al.* [46], *Kim and Lior* [64], or more recently *Saury et al.* [103]. Systematically in all those studies, an initially subcooled liquid is suddenly brought to a superheated, metastable state, by a fast vessel decompression. As illustrated in Figure 1.5 adapted from [103], in this condition the liquid turns into bubbles uniformly within its superheated upper part. By varying largely the experimental con-

control parameters, the cited authors highlighted a weaker sensitivity of bubble nucleation processes to the presence of the container's solid walls. But, the process by which the liquid is brought to a superheated state being here fundamentally different in the absence of any heat supply, this forbids the direct extrapolation of those results to the case of pools heated from below and subjected to a constant atmospheric pressure.

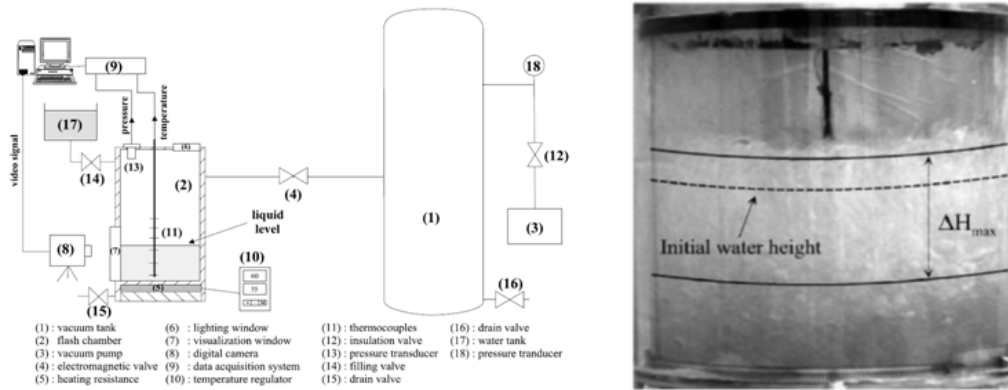


Figure 1.5: Illustration of the flashing of superheated water in an unheated cylindrical glass vessel suddenly subjected to low pressure conditions, adapted from the work of *Saury et al.* reported in [103]. Left: *Saury's* experimental device layout. Right: a photo of the glass vessel taken during a typical experiment of *Saury et al.* One can notice that the bubbles resulting from the depressurized water are uniformly distributed below the pool free surface, thereby suggesting that the phenomenon originates mainly from the liquid bulk rather than from the container's wall.

## 1.4 Thesis objectives and outline

Motivated by the absence of any known report of the phenomenon in the configuration of a pool heated from below and by the emphasized difficulties in extrapolating the results related to genuine geysers or unheated depressurized pools to the studied case, the present doctoral thesis has been conducted with the following objectives:

- Highlight the phenomenon in a pool-type geometry heated from below and characterize it, if it exists in the latter;
- Provide some novel elements regarding the metastable water relaxation mechanisms in this configuration;
- Provide a simple modeling of the studied physics for further macroscopic transient simulations.

Summarizing the activities performed during this doctoral research in order to fulfill the above objectives, the present thesis is organized as follows:

- **Chapter 2** first describes the test device, designed and operated in the frame of this thesis by the present author, in order to investigate the phenomenon at a

laboratory scale. The empirical methods utilized throughout this thesis are also detailed in this chapter;

- **Chapter 3** provides a first insight into the physics of the gravity-driven flashing of metastable water in a pool heated from below. For that purpose, an experiment exhibiting the typical features of the studied phenomenon is introduced. The results of a conducted set of sensitivity tests are also discussed;
- **Chapter 4** is devoted to the analysis of the observed nucleation processes, presented in Chapter 3. The analysis is based on some theoretical concepts and models. In that frame, an interpretation of the noticed bubble nucleation is then proposed;
- **Chapter 5** presents a macroscopic characterization of the heat and mass transfers discussed throughout this thesis, achieved by means of a set of computed transfer coefficients and dimensionless correlations. At last, a lumped-parameter model of the performed experiments is provided and compared with a set of selected tests.



---

# The experimental setup and methods

*“All knowledge of reality starts from experience.”*

— Albert Einstein

## Introduction

This chapter details the experimental setup, called Aquarius, that was designed and operated jointly by UCLouvain and IRSN, in order to investigate the gravity-driven flashing of metastable water in pools heated from below. First, Section 2.1 presents the scaling and design methodology that was followed in order to define the Aquarius mock-up. Then, Section 2.2 provides the main characteristics of the latter test device. Next in Section 2.3, the output of a measurement uncertainties analysis performed prior to the conducted experiments is given. At last, one can find in Section 2.4 the details of the experimental procedure according to which most of the tests discussed in this thesis were conducted.

## 2.1 Scaling and design of the experimental device

### 2.1.1 The definition of a reference pool

Let us remind that two cases are currently reported in the scientific literature as being associated with the studied phenomenon: the so-called phreatic volcanic eruptions and the loss-of-cooling accidents in the storage pools of spent nuclear fuels. As indicated in Chapter 1, the present doctoral research, performed in the frame of IRSN’s missions in nuclear safety, focuses on the latter configuration. Before going deeper in this thesis, let us first provide some more details about the studied case. The spent-fuel-pools, also referred to as SFP, are large storage capacities made of concrete and stainless steel, whose footprint area is of the order of  $100 \text{ m}^2$ . Those pools contain typically  $1000 \text{ m}^3$  of demineralized water and from 100 to 1000 nuclear fuel assemblies. The latter are stored vertically in parallelepipedic disposal cells, as visible in Figure 2.1 and may provide at

most an overall decay heat power of the order of a dozen MW [93]. The footprint area of the heat source constituted by those spent nuclear fuels is of the order of 75% of the overall pool free surface area. Importantly, the height of a classical pool is of the order of 10 m for providing a sufficient radiation shield to any nuclear operator working in the SFP building. As already pointed out, this leads to a 1-bar hydrostatic pressure vertical difference and in turn, to a 20°C vertical difference in saturation temperature within the pool. In this thesis, the below characteristics have been retained as reference values for what is later called the *reference pool*, from which the Aquarius experimental device is to be defined:

- **Pool length:** 11 m;
- **Pool width:** 7.5 m;
- **Nominal pool water level:** 10 m;
- **Pool free surface area:** 82 m<sup>2</sup>;
- **Footprint area of the heat source:** 61 m<sup>2</sup>;
- **Decay heat power:** 10 MW.

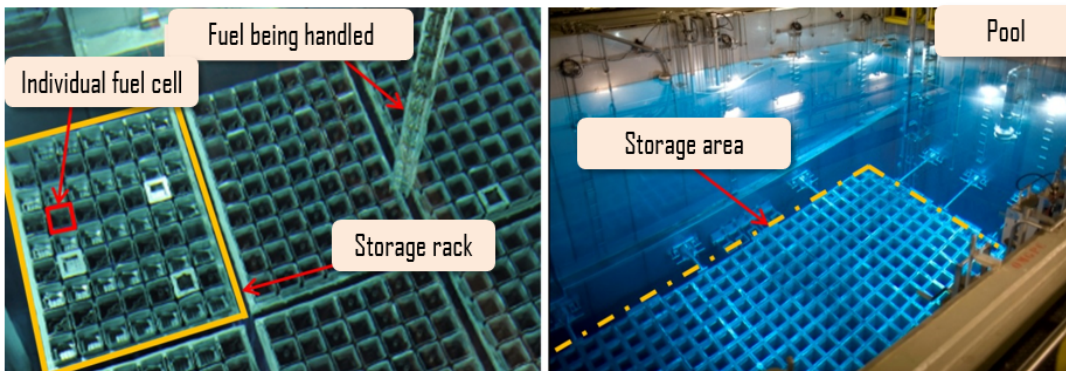


Figure 2.1: Overview of a typical spent-fuel-pool of a so-called light-water-reactor.

### 2.1.2 Downsizing and physical similarity

In Chapter 1, some expected characteristics of the studied phenomenon have been highlighted, such as for instance the gravity-driven water superheating mechanism and the natural convection heat transfer taking place within the pool. In order to get results that are physically similar to the ones expected at the scale of the reference pool, those features are obviously to be reproduced within the experimental device. This key point is investigated in what follows.

**The dimensionless numbers associated with the phenomenon** When defining a small-scale mock-up aiming at reproducing the physics of a full-scale system, an ample use of so-called *heat and mass transfers dimensionless numbers*, having a specific physical meaning, is classically performed [35]. One well-known member of this class of physical quantities is for instance the *Reynolds number* denoted as  $Re$  and useful when dealing with fluid flows [49]. For assessing the physical similarity between the previous two systems, one has to verify whether those numbers are of the same magnitude or not at both scales. Obviously, one has first to define which numbers among the above family are relevant to the treated problem. For doing so, two ways can be followed. First of all, one can derive those numbers from the balance equations associated with the studied case. Indeed, by expressing those equations in a dimensionless fashion, a set of physical dimensionless numbers does appear. For instance, by applying this method to the so-called *Navier-Stokes* equations of a single-phase fluid flow, among the obtained numbers is the  $Re$  mentioned above. In link with the studied flashing phenomenon, many authors applied this methodology to the equations governing gas/liquid two-phase channel flows, such as for instance *Ishii and Kataoka* who derived the scaling laws for systems under 1-D natural circulation [58], or *Yadigaroglu and Zeller* who did the same for a flashing-driven natural circulation loop [128]. But to our knowledge and in consistency with the absence of any known report of the phenomenon in the configuration of a pool heated from below, no publications are available to date in the scientific literature regarding the scaling laws expected in this case. In addition, the phenomenon being for now poorly known in this specific configuration, an *a priori* determination of those relevant dimensionless numbers according to the above process would most likely yield uncertain results. Indeed, the utilized governing equations are usually simplified and/or adapted to the physical mechanisms being treated, in particular regarding their numerous so-called closure relations [35]. In this very case, those mechanisms are precisely uncertain, as it has been discussed in Chapter 1. An efficient and more simple alternative to the previous method is the so-called *dimensional analysis*. When applied, the latter allows obtaining the requested relevant dimensionless numbers by analyzing the mathematical relations that may exist between a pre-identified set of physical variables, with regards to their unit of measure [9]. Importantly, the method does not require any *a priori* knowledge of the involved physical mechanisms. Essentially, it is based on the so-called *Vaschy-Buckingham theorem*, also known as *Pi theorem*. The latter gives the maximum number of dimensionless quantities that one can derive from a dimensional analysis. Precisely, if one investigates a set of  $n$  independent physical variables being associated with  $k$  different units of measure, this maximum number is equal to  $n - k$ . Next, obtaining those  $n - k$  dimensionless numbers is just a matter of mathematical combinations between the  $n$  independent physical variables [35]. Let us now apply the Vaschy-Buckingham theorem to the variables that can be assumed important with regards to the studied phenomenon. In the present research, fourteen supposedly-relevant variables have been considered:

- $g$ , the gravitational acceleration (in  $\text{m/s}^2$ );

- $\beta_L$ , the isobaric thermal expansion coefficient of liquid water (in  $\text{K}^{-1}$ );
- $\Delta T$ , some driving temperature difference (in K);
- $H$ , the liquid pool height (in m);
- $\nu_L$ , the liquid water kinematic viscosity (in  $\text{m}^2/\text{s}$ );
- $\kappa_L$ , the liquid water thermal diffusivity (in  $\text{m}^2/\text{s}$ );
- $C_{p;L}$ , the liquid water specific heat capacity (in  $\text{J}/\text{kg}/\text{K}$  or in  $\text{m}^2/\text{s}^2/\text{K}$ );
- $\mathcal{L}_w$ , the water specific latent heat (in  $\text{J}/\text{kg}$  or in  $\text{m}^2/\text{s}^2$ );
- $d_b$ , some bubble length-scale, here associated with its diameter (in m);
- $u_b$ , some bubble velocity-scale (in  $\text{m}/\text{s}$ );
- $\rho_L$ , the liquid water density (in  $\text{kg}/\text{m}^3$ );
- $\rho_G$ , the water vapor density (in  $\text{kg}/\text{m}^3$ );
- $\dot{Q}_p$ , the pool heating power (in W or in  $\text{kg}\cdot\text{m}^2/\text{s}^3$ );
- $C_a$ , the mass concentration of the dissolved air potentially present in the water pool (in  $\text{kg}/\text{m}^3$ ).

As one can notice, those variables are expressed according to four fundamental units of measure, associated with length, mass, time and temperature. Hence, the Vaschy-Buckingham theorem gives a maximum number of relevant dimensionless quantities that can be obtained from the above variables equal to  $14 - 4 = 10$ . Let us then compute those numbers, denoted as  $\Pi_1 \dots \Pi_{10}$ . For doing so, four repeated physical variables encompassing the involved four fundamental units of measure in an independent way have to be selected among the fourteen listed above [35]. For that purpose,  $C_{p;L}$ ,  $\Delta T$ ,  $\nu_L$  and  $\rho_L$  have been chosen, which yields:

$$\Pi_1 = C_{p;L}^{\alpha_1} \Delta T^{\beta_1} \nu_L^{\gamma_1} \rho_L^{\delta_1} g \quad (2.1)$$

$$\Pi_2 = C_{p;L}^{\alpha_2} \Delta T^{\beta_2} \nu_L^{\gamma_2} \rho_L^{\delta_2} \beta_L \quad (2.2)$$

$$\Pi_3 = C_{p;L}^{\alpha_3} \Delta T^{\beta_3} \nu_L^{\gamma_3} \rho_L^{\delta_3} H \quad (2.3)$$

$$\Pi_4 = C_{p;L}^{\alpha_4} \Delta T^{\beta_4} \nu_L^{\gamma_4} \rho_L^{\delta_4} \kappa_L \quad (2.4)$$

$$\Pi_5 = C_{p;L}^{\alpha_5} \Delta T^{\beta_5} \nu_L^{\gamma_5} \rho_L^{\delta_5} \mathcal{L}_w \quad (2.5)$$

$$\Pi_6 = C_{p;L}^{\alpha_6} \Delta T^{\beta_6} \nu_L^{\gamma_6} \rho_L^{\delta_6} d_b \quad (2.6)$$

$$\Pi_7 = C_{p;L}^{\alpha_7} \Delta T^{\beta_7} \nu_L^{\gamma_7} \rho_L^{\delta_7} u_b \quad (2.7)$$

$$\Pi_8 = C_{p;L}^{\alpha_8} \Delta T^{\beta_8} \nu_L^{\gamma_8} \rho_L^{\delta_8} \rho_G \quad (2.8)$$

$$\Pi_9 = C_{p;L}^{\alpha_9} \Delta T^{\beta_9} \nu_L^{\gamma_9} \rho_L^{\delta_9} \dot{Q}_p \quad (2.9)$$

$$\Pi_{10} = C_{p;L}^{\alpha_{10}} \Delta T^{\beta_{10}} \nu_L^{\gamma_{10}} \rho_L^{\delta_{10}} C_a \quad (2.10)$$

with  $\alpha_1 \dots \alpha_{10}$ ,  $\beta_1 \dots \beta_{10}$ ,  $\gamma_1 \dots \gamma_{10}$ ,  $\delta_1 \dots \delta_{10}$ , some exponents to be determined, while ensuring that the numbers  $\Pi_1 \dots \Pi_{10}$  keep dimensionless. Having found out those exponents and sparing the reader the detailed calculations, one gets:

$$\Pi_1 = g (C_{p;L} \Delta T)^{-3/2} \nu_L \quad (2.11)$$

$$\Pi_2 = \beta_L \Delta T \quad (2.12)$$

$$\Pi_3 = (C_{p;L} \Delta T)^{1/2} \frac{H}{\nu_L} \quad (2.13)$$

$$\Pi_4 = \frac{\kappa_L}{\nu_L} \quad (2.14)$$

$$\Pi_5 = \frac{\mathcal{L}_w}{C_{p;L} \Delta T} \quad (2.15)$$

$$\Pi_6 = (C_{p;L} \Delta T)^{1/2} \frac{d_b}{\nu_L} \quad (2.16)$$

$$\Pi_7 = \frac{u_b^2}{C_{p;L} \Delta T} \quad (2.17)$$

$$\Pi_8 = \frac{\rho_G}{\rho_L} \quad (2.18)$$

$$\Pi_9 = \frac{\dot{Q}_p}{\rho_L \nu_L^2} (C_{p;L} \Delta T)^{-1/2} \quad (2.19)$$

$$\Pi_{10} = \frac{C_a}{\rho_L} \quad (2.20)$$

where one can recognize, either directly or indirectly by rearranging the above quantities, some classical dimensionless numbers in use in the field of fluid mechanics. Those numbers are:

$$\frac{\rho_G}{\rho_L} = \Pi_8 \quad (2.21)$$

the vapor-to-liquid density ratio,

$$Ra_L = \frac{g \beta_L \Delta T H^3}{\nu_L \kappa_L} \quad (2.22)$$

$$= \frac{\Pi_1 \Pi_2 \Pi_3^3}{\Pi_4} \quad (2.23)$$

the so-called *Rayleigh number* of the liquid phase,

$$Ja_L = \frac{C_{p;L} \Delta T}{\mathcal{L}_w} \quad (2.24)$$

$$= \frac{1}{\Pi_5} \quad (2.25)$$

the so-called *Jakob number*,

$$Ec = \frac{u_b^2}{C_{p;L} \Delta T} \quad (2.26)$$

$$= \Pi_7 \quad (2.27)$$

the so-called *Eckert number*,

$$Re_b = \frac{u_b d_b}{\nu_L} \quad (2.28)$$

$$= \frac{\Pi_6}{\Pi_7^{1/2}} \quad (2.29)$$

the so-called bubble's *Reynolds number*,

$$Pr_L = \frac{\nu_L}{\kappa_L} \quad (2.30)$$

$$= \frac{1}{\Pi_4} \quad (2.31)$$

the so-called liquid water *Prandtl number*,

$$Fr_b = \frac{u_b^2}{g d_b} \quad (2.32)$$

$$= \frac{\Pi_7}{\Pi_1 \Pi_6} \quad (2.33)$$

the so-called bubble's *Froude number* and

$$\frac{C_a}{\rho_L} = \omega_a \quad (2.34)$$

$$= \Pi_{10} \quad (2.35)$$

the mass fraction of dissolved air in water. Two more unnamed numbers can be constructed from the obtained  $\Pi_1 \dots \Pi_{10}$ . First is:

$$\underbrace{\frac{H}{u_b}}_{\tau_{flight}} \times \underbrace{\frac{\kappa_L}{d_b^2}}_{1/\tau_{heat}} = \frac{\Pi_3}{\Pi_7^{1/2}} \frac{\Pi_4}{\Pi_6^2} \quad (2.36)$$

that can be seen as the ratio between two time-scales, denoted as  $\tau_{flight}$  and  $\tau_{heat}$ . The first of the previous two time-scales is the time-of-flight of a bubble crossing the entire pool of height  $H$  at an average velocity-scale  $u_b$ . The second time-scale is in turn the characteristic time of the heat transfer that may exist across the liquid boundary layer surrounding the bubble of typical diameter  $d_b$ . Next is:

$$\frac{\dot{Q}_p \kappa_L}{\rho_L H^3 (C_{p;L} \Delta T)^2} = \frac{\Pi_9 \Pi_4}{\Pi_3^3} \quad (2.37)$$

which can be seen as some dimensionless form of the heat source power, provided the above pre-determined relevant physical variables. Overall, one can note that the above ten dimensionless numbers provide a sufficient physical description of the treated problem since none of the envisioned features of the latter seem omitted. Indeed at the first place,  $Pr_L$  being the ratio between two relevant fluid properties (*i.e.* its kinematic viscosity  $\nu_L$  and thermal diffusivity  $\kappa_L$ ), is related to the nature of the fluid. Next,  $Ra_L$

quantifies the intensity of the natural convection flow expected at pool scale whereas  $Ja_L$  provides some dimensionless form of a potential liquid superheat  $\Delta T$ , which is central to the flashing. In turn,  $\rho_G/\rho_L$ ,  $Ec$ ,  $Re_b$ ,  $Fr_b$  and  $\tau_{flight}/\tau_{heat}$  clearly encompass the key features of the bubbles dynamics. At last,  $\dot{Q}_p \kappa_L/\rho_L H^3 (C_{p,L} \Delta T)^2$  allows considering the heat supply in a dimensionless fashion whereas  $\omega_a$  takes into account the potential presence of gases in dissolution within water. The following similarity analysis will hence rely on the above ten numbers, judged as relevant with regards to the treated problem. But before going into more details, let us define some downscaling ratio.

**The definition of the test mock-up scaling ratio** First of all, an important parameter with regards to the phenomenon is the aspect ratio of the studied geometry, as it has been argued in Chapter 1. Hence, the latter parameter should be conserved whatever the chosen scale. Obviously, this imposes to proceed by means of an homothetic transform when downsizing the geometrical parameters of the reference pool. For investigating the phenomenon, the choice of an homothetic scaling ratio of 1:25 has been made, motivated by practical and economical considerations. Indeed, with a SFP nominal water pool level of 10 m, the retained ratio leads to a mock-up height of 40 cm, which is fairly reasonable with the intent to perform a laboratory-scale experiment. But one may wonder if the choice of this scaling ratio allows reproducing properly the studied physics. Let us answer this question in what follows, by tackling the subject in a point-by-point fashion.

**The reproduction of the gravity-driven water superheating mechanism** As already mentioned, the discussed phenomenon is triggered by the existence of a significant vertical variation of the water saturation temperature. In typical SFPs, the latter is of the order of 20°C and results from the 1-bar hydrostatic pressure difference that exists along the 10-meter height of such pools. By considering that in the studied problem the liquid temperature may at most be equal to the saturation one, estimated at the heat source location, those 20°C hence represent the maximum superheat that might be reached within the pool. Obviously, this maximum value can be reached only where the local hydrostatic pressure is at its lowest value, *i.e.* at the liquid free surface. This allows estimating some bounding value for the SFP *Jakob* number, here denoted as  $(Ja_L)_{SFP}$ :

$$(Ja_L)_{SFP} = 0.034 \quad (2.38)$$

For obvious practical reasons, the study of the phenomenon cannot be considered at full scale. It is thus impossible to reproduce that bounding  $(Ja_L)_{SFP}$  by a scale reduction without compromises. Worse, if the mock-up scale is heavily reduced, the vertical saturation temperature difference might not be sufficient for preventing the onset of nucleate pool boiling onto the heating source, which in turn might hamper the gravity-driven flashing.

Interestingly, as found out by the present author, this issue can be solved by taking advantage from the particularity of water properties. Indeed, as one can notice from Figure 2.2, the variations of water saturation temperature against pressure, denoted as  $T_{sat}$ , are much steeper in the low-pressure range than around atmospheric pressure. This remarkable fact allows conserving the 20°C saturation temperature vertical difference of a SFP and hence the  $(Ja_L)_{SFP}$ , even at a reduced scale, with an appropriate choice of system's pressure. Indeed, in the low-pressure case, because of those steep variations in  $T_{sat}$  against pressure, a little variation in hydrostatic pressure, provided by a reduced pool level, might be enough for achieving the required 20°C. In a more general frame, this similarity approach may be beneficial to other types of applications where the gravity-driven flashing is expected to occur, providing a way to reduce the size and hence the cost of the envisioned experiments and keeping water as the working fluid (*e.g.* for 1D-geyser flows or passive system pools). Accordingly, the most suited operating pressure can be determined as follows. If a 20°C saturation temperature vertical difference is to be conserved over some height  $H$ , such as in the present study, then:

$$[\Delta T_{sat}(z)]_{SFP} = [\Delta T_{sat}(z)]_{mock-up} \quad (2.39)$$

$$\Leftrightarrow \left[ \int_0^H \frac{\partial T_{sat}}{\partial P} dP \right]_{SFP} = \left[ \int_0^H \frac{\partial T_{sat}}{\partial P} dP \right]_{mock-up} \quad (2.40)$$

$$\Leftrightarrow \left[ \int_0^H \frac{\partial T_{sat}}{\partial P} \rho_L g dz \right]_{SFP} = \left[ \int_0^H \frac{\partial T_{sat}}{\partial P} \rho_L g dz \right]_{mock-up} \quad (2.41)$$

with  $z$ , the vertical length variable,  $P$ , the local pressure,  $\rho_L$ , the liquid density and  $g$ , the gravitational acceleration. If one assumes that the variations of the water density  $\rho_L$  and the partial derivative of the pressure-dependent saturation temperature  $\frac{\partial T_{sat}}{\partial P}$  can be neglected along the vertical axis:

$$\left[ \frac{\partial T_{sat}}{\partial P} \rho_L g H \right]_{SFP} = \left[ \frac{\partial T_{sat}}{\partial P} \rho_L g H \right]_{mock-up} \quad (2.42)$$

which finally gives:

$$\left[ \frac{\partial T_{sat}}{\partial P} \right]_{mock-up} = \frac{H_{SFP}}{H_{mock-up}} \left[ \frac{\partial T_{sat}}{\partial P} \right]_{SFP} \quad (2.43)$$

By applying the above approach to the retained scaling ratio of 1:25, the conservation of the 20°C vertical difference of the saturation temperature along the downsized pool height of 40 cm imposes to retain a 22-mbar operating pressure, as it can be seen in Figure 2.3. In sum with this method, by construction:

$$(Ja_L)_{SFP} = (Ja_L)_{mock-up} \quad (2.44)$$

$$(Pr_L)_{SFP} = (Pr_L)_{mock-up} \quad (2.45)$$

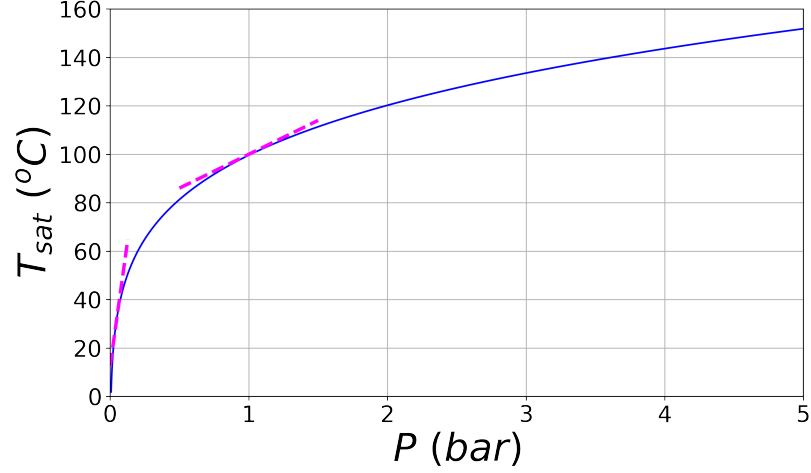


Figure 2.2: Variations of water saturation temperature  $T_{sat}$  against pressure  $P$ . Those variations are steeper in the low-pressure range than around atmospheric pressure.

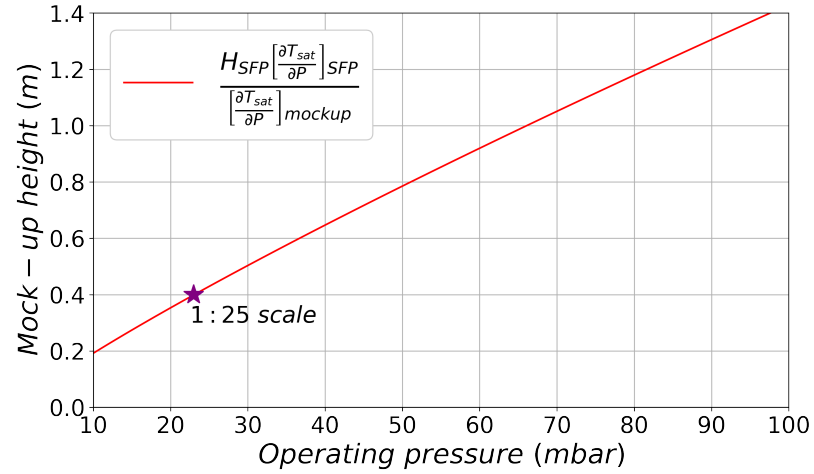


Figure 2.3: Relationship between the mock-up height and its operating pressure, ensuring the conservation of the 20°C saturation temperature vertical difference of a SFP.

But obviously, the operated pressure distortion impacts significantly the vapor-to-liquid density ratio introduced above, as follows:

$$\frac{\left(\frac{\rho_G}{\rho_L}\right)_{SFP}}{\left(\frac{\rho_G}{\rho_L}\right)_{mock-up}} \approx 50 \quad (2.46)$$

which is an unavoidable limitation of the proposed similarity approach. At last, regarding the dimensionless amount of dissolved air  $\omega_a$ , if one can impose at the mock-up scale the expected mass concentration  $C_a$  of the full-scale case and provided that  $\rho_L$  does not vary significantly in between the two retained pressures,  $\omega_a$  can be hence considered as identical at both scales:

$$(\omega_a)_{SFP} = (\omega_a)_{mock-up} \quad (2.47)$$

**A downscaled heat source** Then, the heat source power needs to be downscaled as well. For doing so, one may conserve the already presented dimensionless number characterizing the heat supply:

$$\left( \frac{\dot{Q}_p \kappa_L}{\rho_L H^3 (C_{p;L} \Delta T)^2} \right)_{SFP} = \left( \frac{\dot{Q}_p \kappa_L}{\rho_L H^3 (C_{p;L} \Delta T)^2} \right)_{mock-up} \quad (2.48)$$

Provided  $(\kappa_L/(\rho_L(C_{p;L}\Delta T)^2))_{SFP} \approx (\kappa_L/(\rho_L(C_{p;L}\Delta T)^2))_{mock-up}$  with  $\Delta T = 20^\circ\text{C}$ , this can be achieved by imposing the same power density  $\dot{Q}_p/H^3$  at the reduced scale. With a scaling ratio of 1:25, conserving the typical power density of a SFP, of the order of  $10 \text{ kW/m}^3$ , yields a reduced power of 1 kW. As one can figure out, reproducing the geometrical configuration of a real SFP heat source at such a reduced scale is technically challenging. For this reason, the mock-up heat source geometry has been simplified and consists in a planar surface representing 75% of the pool cross-sectional area.

**A conservation of the turbulent nature of the heat and mass transfers** Regarding the natural convection flow that is expected to develop in the heated pool, one can analyze its similarity at both scales on the basis of an estimate of the already introduced *Rayleigh* number:

$$Ra_L = \frac{g\beta_L\Delta TH^3}{\nu_L\kappa_L} \quad (2.49)$$

As one can notice,  $Ra_L$  varies as the cubic power of the system's height. Hence, a scale reduction of 1:25 affects that number by a factor  $25^3 = 1.5 \times 10^4$ :

$$\frac{(Ra_L)_{mock-up}}{(Ra_L)_{SFP}} = 0.7 \times 10^{-4} \quad (2.50)$$

Fortunately, the  $Ra_L$  characterizing the accidental natural convection flows in a SFP are expected to be of the order of  $10^{13}$ - $10^{15}$  [81], far above the threshold value, equal to  $10^5$  in water, from which the convection is considered turbulent, as seen in Figure 2.4. Thus, with regards to the conservation of the turbulent nature of the studied natural convection, the chosen scaling ratio of 1:25 appears appropriate, with the studied flows being expected to remain turbulent even at the reduced scale of the Aquarius experiment.

**A partially impacting bubble size distortion** Of course, operating at a lower pressure distorts the bubbles typical size and hence their dynamics. Let us detail this effect by comparing two bubbles of radii  $r_{SFP}$  and  $r_{mock-up}$ , having the same number of water vapor moles, both at the SFP and mock-up scales. Bearing in mind that the ideal gas law is a good approximation of the behavior of water vapor for pressures below 50 bar and provided a constant number of moles of gas, this yields:

$$\frac{4}{3}\pi r_{SFP}^3 \frac{P_{SFP}}{\mathcal{R}T_{SFP}} = \frac{4}{3}\pi r_{mock-up}^3 \frac{P_{mock-up}}{\mathcal{R}T_{mock-up}} \quad (2.51)$$

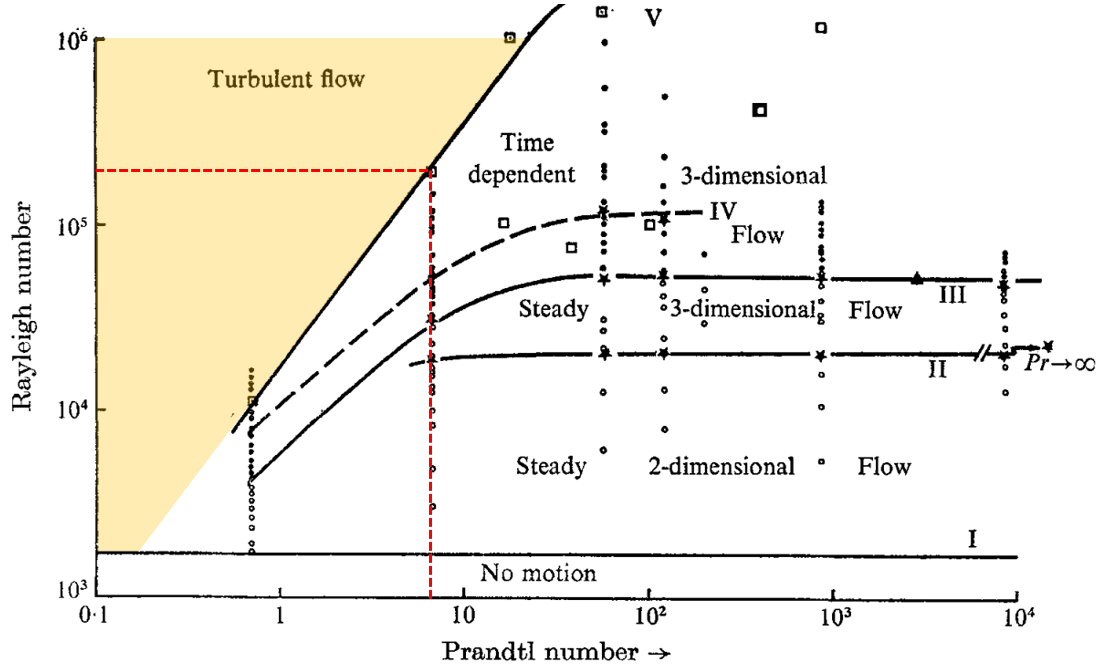


Figure 2.4: A map of the reached natural convection regimes as a function of two dimensionless numbers characterizing both the intensity of the studied transfer and the nature of the fluid: respectively the *Rayleigh* and *Prandtl* numbers, denoted as  $Ra_L$  and  $Pr$ . For water, with  $Pr \approx 7$ , the turbulent regime is reached once  $Ra_L > 10^5$ . Figure adapted from the work of *Krishnamurti* [68].

with  $\mathcal{R}$ , the so-called perfect gas constant. Hence, it comes:

$$\frac{r_{mock-up}}{r_{SFP}} = \left( \frac{P_{SFP} T_{mock-up}}{T_{SFP} P_{mock-up}} \right)^{1/3} \quad (2.52)$$

$$\frac{r_{mock-up}}{r_{SFP}} = 3.4$$

with  $P_{SFP}, T_{SFP} = 1 \text{ bar}, 100^\circ\text{C}$  and  $P_{mock-up}, T_{mock-up} = 22 \text{ mbar}, 20^\circ\text{C}$ . Regarding the bubble typical velocity  $u_b$ , one can legitimately assume that the order of magnitude of the latter is weakly modified by the expected distortion of the bubble size. Indeed, as seen in Figure 2.5, the terminal velocity of a bubble can be approximated as a constant equal to 30 cm/s for bubble diameters bigger than 1 mm (*i.e.* within the expected bubble diameter range, whatever the scale). All in all, one can hence consider that the bubble size distortion should not be significant regarding the following three dimensionless numbers related to bubble dynamics:

$$\frac{(Re_b)_{mock-up}}{(Re_b)_{SFP}} \approx 3.4 \quad (2.53)$$

$$\frac{(Ec)_{mock-up}}{(Ec)_{SFP}} \approx 1 \quad (2.54)$$

$$\frac{(Fr_b)_{mock-up}}{(Fr_b)_{SFP}} \approx 0.29 \quad (2.55)$$

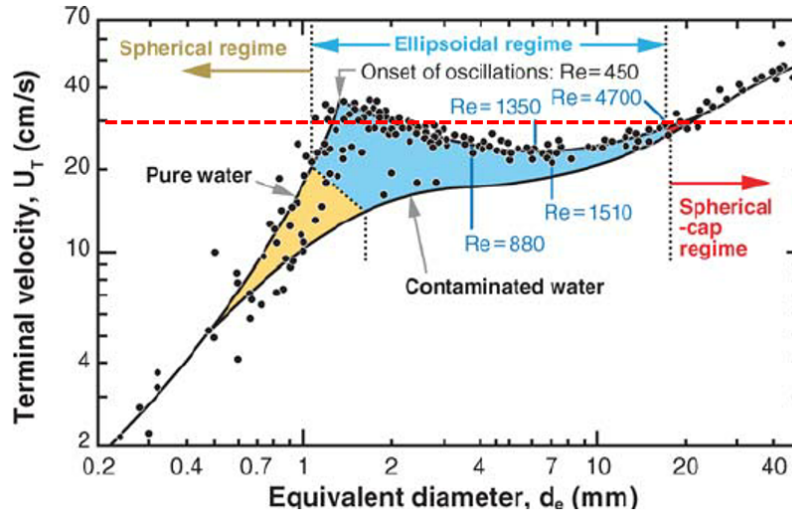


Figure 2.5: Variations of the terminal velocity of an air bubble in water against bubble diameter. From a diameter of the order of 1 mm, the bubble terminal velocity gets almost constant and close to 30 cm/s, a value here represented by an horizontal red line. Figure adapted from the work of *Clift et al.* [26].

The last number in link with this dynamics is however significantly distorted when reducing the pressure, which constitutes the second limitation of the proposed similarity approach:

$$\frac{(\tau_{flight}/\tau_{heat})_{mock-up}}{(\tau_{flight}/\tau_{heat})_{SFP}} \approx 0.0034 \quad (2.56)$$

In details, this significant discrepancy between the  $\tau_{flight}/\tau_{heat}$  at both scales means that under the action of a liquid-to-bubble heat transfer, the bubbles are expected to grow much less within the mock-up than within the reference pool because of the reduced pool's height, in spite of their bigger size.

## 2.2 The Aquarius experimental device

### 2.2.1 Overview of the installation

The experimental device that results from the above downsizing and physical similarity approach, named Aquarius, consists in a 50 L closed vessel of height  $H = 40$  cm, length  $L = 45$  cm and width  $W = 30$  cm, having a heat source located at its bottom-end and providing a maximum 1-kW power. As seen in Section 2.1, operating the experimental device at a reduced pressure around 20 mbar allows reproducing the targeted 20°C saturation temperature vertical difference expected at the SFP scale. For that purpose, the pool vessel is connected to a vacuum pump and a condenser. The resulting experimental setup is illustrated in the below Figures 2.6-2.7. Its main characteristics are compared to those of the defined reference pool in Table 2.1. In what follows are successively detailed the technical features of the Aquarius test device.

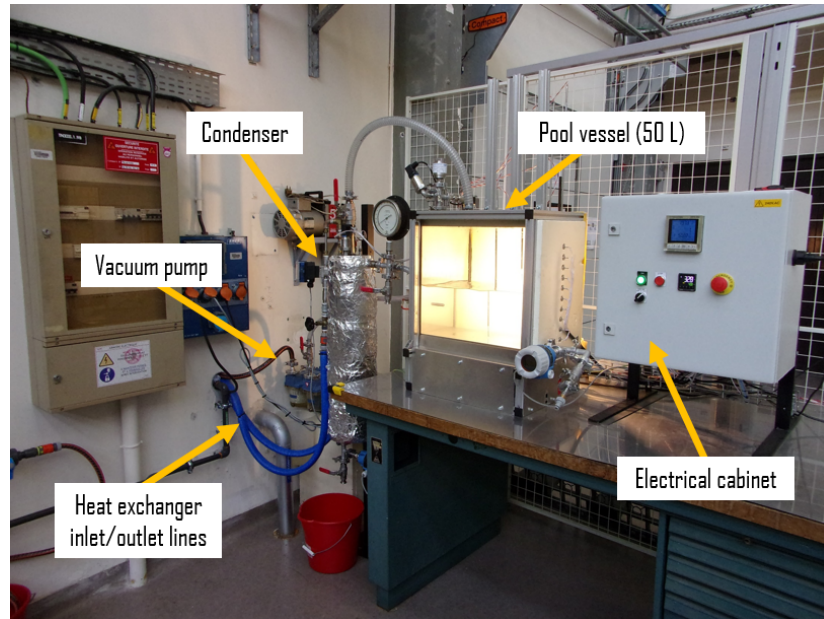


Figure 2.6: Overview of the Aquarius test device designed and operated by IRSN / UCLouvain for investigating the gravity-driven pool flashing phenomenon at a laboratory scale.

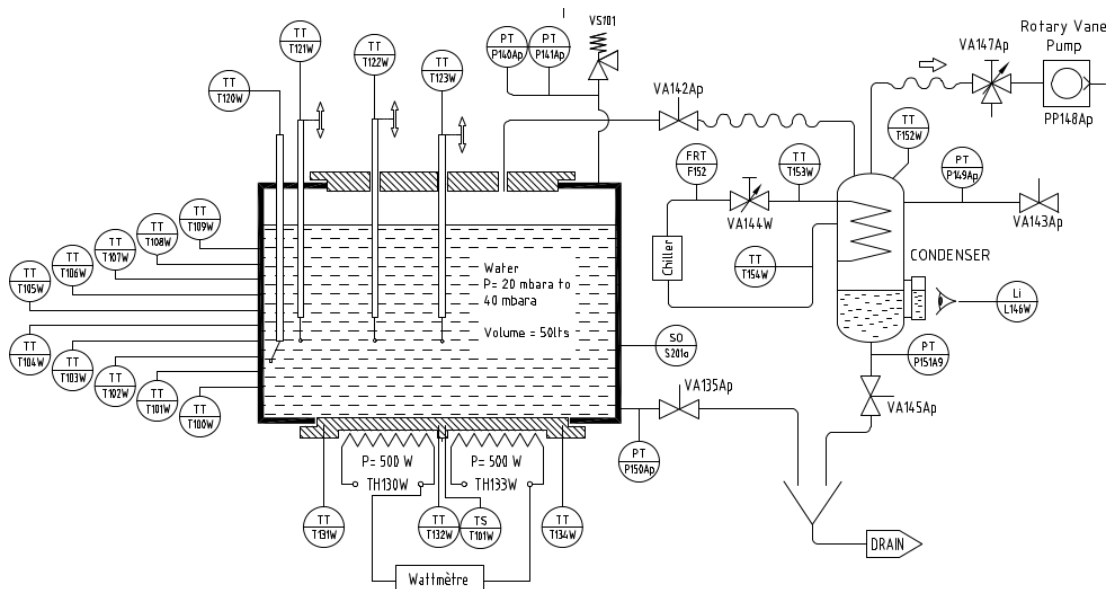


Figure 2.7: The Aquarius experimental device layout and instrumentation.

Table 2.1: Comparison of the reference spent-fuel-pool and Aquarius test device main characteristics.

Parameter	Ref. spent-fuel-pool	Aquarius test device (1:25)
<i>Pool length</i>	11 m	45 cm
<i>Pool width</i>	7.5 m	30 cm
<i>Pool height</i>	10 m	40 cm
<i>Pool volume</i>	825 m <sup>3</sup>	54 L
<i>Pool free surface area</i>	82 m <sup>2</sup>	0.135 m <sup>2</sup>
<i>Heat source footprint area</i>	61 m <sup>2</sup>	0.101 m <sup>2</sup>
<i>Maximum heat power</i>	10 MW	1 kW
<i>Ref. operating pressure</i>	1 bar	22 mbar
<i>Ref. temperature</i>	100°C	20°C

### 2.2.2 The pool vessel

The pool vessel is constituted by a mechanical assembly of four 23-mm-thick machined stainless steel plates, as visible in Figure 2.8. In the introduction of the present thesis, the key role played by the nature of the solid surfaces of the water container with regards to bubble nucleation has been emphasized. Having this phenomenon's sensitivity in mind, two different types of surface roughness have been retained. In details, all vessel's immersed surfaces are finely-polished, with a measured arithmetical mean deviation  $R_a = 0.1 \mu\text{m}$  (*i.e.* an indicator of surface roughness, further explained in Chapter 4), except the right-hand-side vertical wall, made intentionally rough, with a  $R_a$  of  $3 \mu\text{m}$ . At last, two parallel optical windows made of 23-mm-thick Securit™ glass plates are glued onto the front and back sides of the vessel's structure, thereby allowing phenomenological observations.

### 2.2.3 The heat source

A heating element, providing a 1-kW maximum thermal power to the water pool, is located at the bottom of the vessel. This element is constituted by two independent resistive heaters, each providing a maximum power of 500 W. Those heaters are respectively placed at the left and right-hand-sides of the pool, are embedded in the vessel's bottom wall and occupy 75% of the overall bottom surface. They are both supplied with an alternative current, under a voltage of 220 V. The current intensity can be tuned by means of a rheostat, which allows controlling the injected heating power. At last, the bottom surface of the heaters, in contact with the laboratory's atmosphere, is thermally insulated by means of a rockwool layer.

### 2.2.4 The operating pressure control system

The required operating pressure is set up and controlled by means of the combined action of the vacuum pump, shown in Figure 2.9 and the condenser, depicted in Figure 2.11. Let us detail how this is achieved. First of all, the vacuum pump allows imposing



Figure 2.8: Side-view of the mechanical assembly of four machined stainless steel plates constituting the Aquarius pool vessel.

low pressure conditions down to the saturation pressure, denoted as  $P_{sat}(T_L)$ , corresponding to the temperature  $T_L$  of the liquid contained within the vessel. The utilized vacuum pump has the following characteristics:

- **Brand:** Vacuubrand™;
- **Model:** RE 8;
- **Free air displacement rate:** 8.6 m<sup>3</sup>/h;
- **Ultimate vacuum:** 0.1 mbar.

Prior to the experiments described in this thesis, some qualification tests were submitted to the vacuum pump with the intent to assess its pumping performance. Two configurations were considered: with and without the presence of a so-called precision valve at the pump inlet for finely tuning the flow rate. The obtained results are shown in Figure 2.10. Overall, the pumping performance does seem satisfactory, with a reach of  $P_{sat}(T_L)$  achieved in less than a minute with a simple valve at the pump inlet and in less than 5 min with the precision valve. The latter configuration, being judged useless with regards to the only need to reach as fast as possible the required pressure, has been discarded in any further experiment. Next, once those conditions are reached, the condenser keeps a constant pressure within the pool vessel, by turning any steam coming

from the latter into liquid. This is achieved by imposing within the 12-L inner volume of the condenser the circulation of a cold stream of water. The latter circulation is performed within an helical heat exchanger made of a bent copper tube, placed into the condenser vessel, as illustrated in Figure 2.12. The heat exchanger has the following characteristics:

- **Heat exchanger diameter:** 60 mm;
- **Heat exchanger height:** 255 mm;
- **Copper tube outer diameter:** 10 mm;
- **Copper tube inner diameter:** 8 mm;
- **Copper tube total length:** 4 m.

The circulating water temperature is regulated by means of a Partenaire™ FRC-VBE 003 air/water heat pump, illustrated in Figure 2.13 and providing a maximum cooling power of 3.6 kW associated with a minimum outlet water temperature of 5°C. This component comprises its own pump for ensuring the circulation of the chilled water. The heat pump is usually utilized as follows. First, a heat pump water temperature set point is chosen. Next, the flow rate of the water circulating through the condenser heat exchanger is adjusted by means of the manual control valve visible in Figure 2.11 (see the black valve wheel situated at the outlet of the noticeable vertical blue piping). In doing so, one can equilibrate the heat exchanger cooling power with the enthalpy flux associated with the steam entering the condenser. Thus, one can regulate the system's pressure. The heat pump performance was assessed as well prior to the first experimental campaign, which allowed identifying the cooling power corresponding to each pair of heat pump water temperature and water circulation flow rate.



Figure 2.9: Side-view of the Vacuubrand™ RE 8 vacuum pump in use within the Aquarius test device.

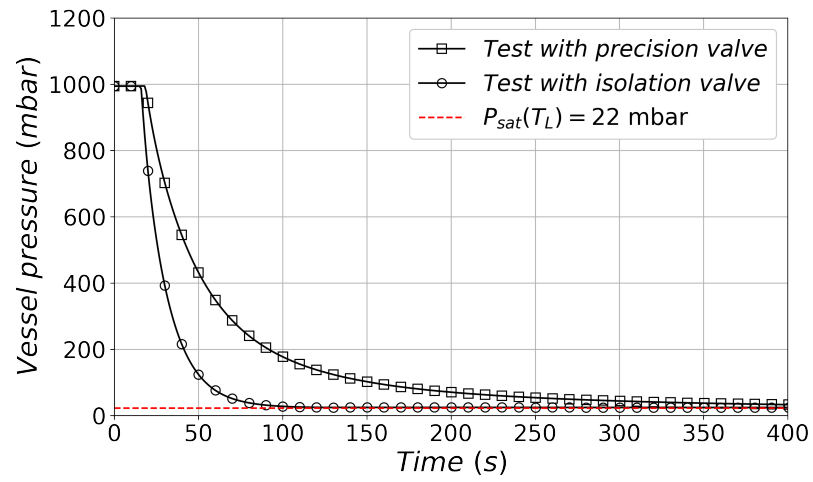


Figure 2.10: Assessed pumping performance with/without the presence of a so-called precision valve at the pump inlet for finely tuning the flow rate.



Figure 2.11: Front-view of the condenser equipping the test device, coated by a rock-wool thermal insulation layer.

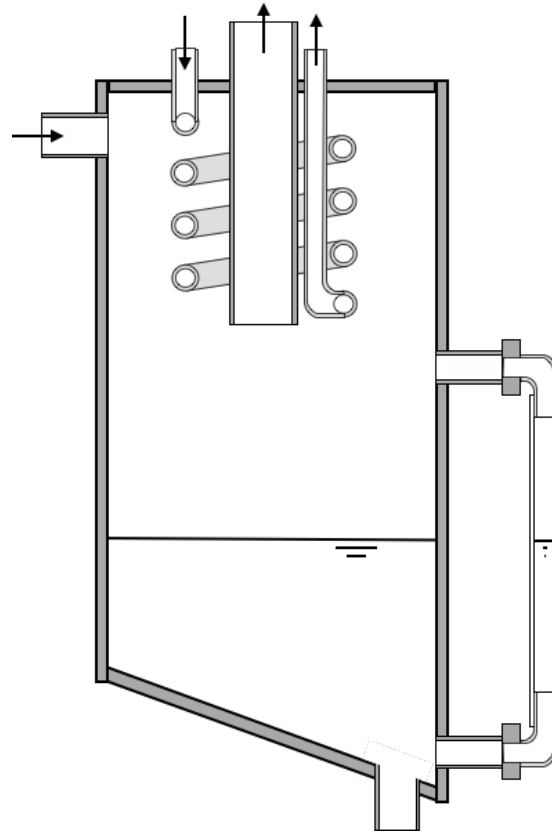


Figure 2.12: Sketch of the inner volume of the condenser vessel, with the heat exchanger made of an helical bent of a copper tube exhibited (the drawing is not in scale).



Figure 2.13: Front-view of the Partenaire™ FRC-VBE 003 air/water heat pump equipping the test device.

### 2.2.5 Instrumentation

Various types of measurements are performed within the Aquarius device during a typical experiment. Those measurements are further detailed in what follows. In support of the next descriptions, Figure 2.14 gives an overview of the available instrumentation and the location within the test device of each utilized sensor.

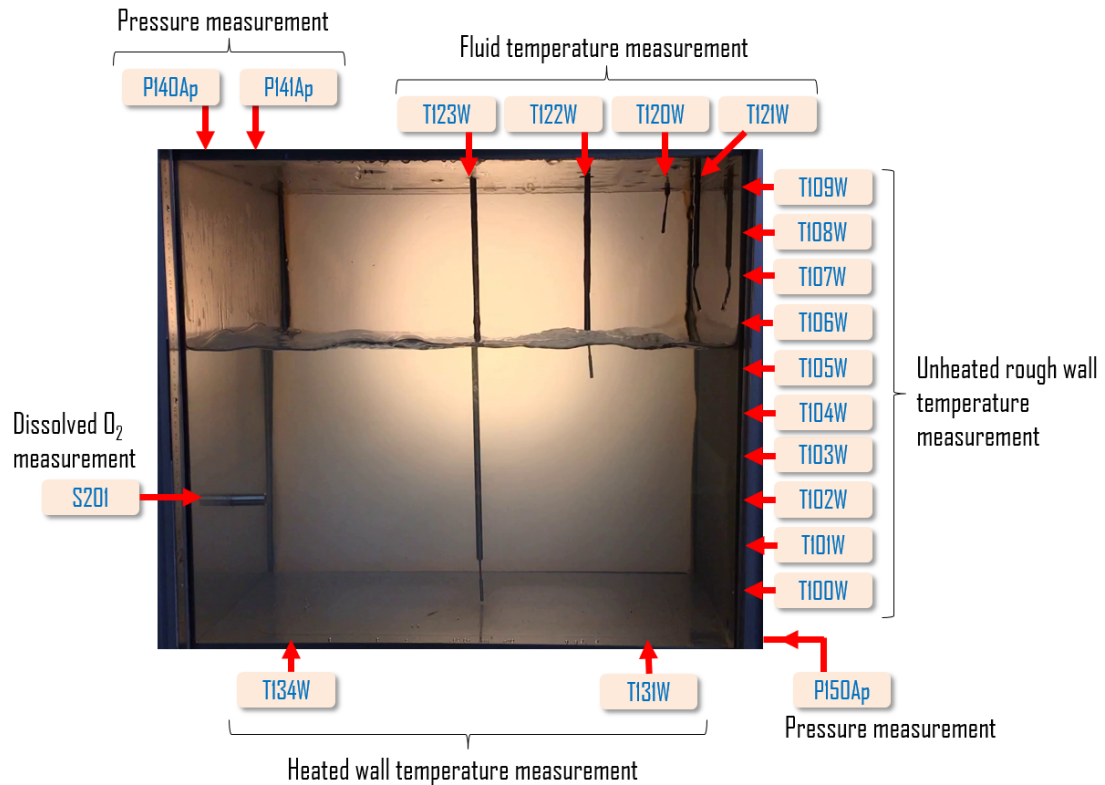


Figure 2.14: Overview of the available instrumentation and the location within the test device of each utilized sensor.

**Thermal measurements** The device is equipped with four Pt-100 class A temperature probes whose position can be manually modified within the vessel. Those probes are referred to as T120W, T121W, T122W, T123W. Ten Pt-100 class A probes, whose reference is T100W, T101W, T102W, T103W, T104W, T105W, T106W, T107W, T108W, T109W, are embedded in the lateral rough wall of the pool vessel. Two more Pt-100 probes of the same class are located within the heated bottom wall, in the vicinity of the liquid pool. Those are referred to as T131W and T134W. Contrarily to the Pt-100 measuring fluid temperatures, those embedded in both the heated and unheated walls cannot be displaced.

**Pressure measurements** Two piezoelectric pressure sensors are located on top of the vessel for monitoring the operating pressure with two complementing accuracy levels. The first of them, referred to as P140Ap, is provided by Endress+Hauser™ (model Cerabar PMC21). It allows measuring pressures within the range 0-110 mbar. The

other sensor, referenced as [P141Ap](#) and sold by Thermibel™ (model AM510), provides pressure measurements in between 0-1600 mbar. Another piezoelectric sensor is installed at the vessel's bottom-end, in order to deduce liquid mass variations throughout the tests according to a methodology described in Appendix A. The sensor, sold by Endress+Hauser™ (model Cerabar M PMC51), is referred to as [P150Ap](#) and gives measurements in the range 0-150 mbar.

**Dissolved oxygen measurement** As mentioned in the introduction of the present thesis, the community recognizes the role played by the presence of gases in dissolution within a liquid when the latter is placed in a flashing configuration. Within water, two dissolved gases are mainly met - the  $O_2$  and  $N_2$  species - and have thus to be monitored. For that purpose, a dissolved oxygen sensor sold by Hamilton™ (model VisiFerm DO Arc 120) and referenced as [S201](#) is placed within the test device, as visible in Figure 2.14. The sensor provides dissolved  $O_2$  measurements for mass concentrations standing in between 4 ppb and 25 ppm, with a response time (98%) smaller than 30 seconds at 25°C. This is achieved by means of an optical, non-intrusive method. The latter, illustrated in Figure 2.15, is based on the oxygen-dependent luminescence quenching of a specific solid material, referred to as luminophore, placed at the forefront of the sensor. This material, once subjected to an incoming blue light, reacts differently whether some oxygen atoms are present or not in its close vicinity. Next, a correlation given by the manufacturer allows estimating from the optical reaction of the luminophore the corresponding amount of dissolved  $O_2$  in water. Provided the measured amount of  $O_2$  the unmeasured amount of dissolved  $N_2$  can be then estimated by means of the analytical method detailed in Appendix B.

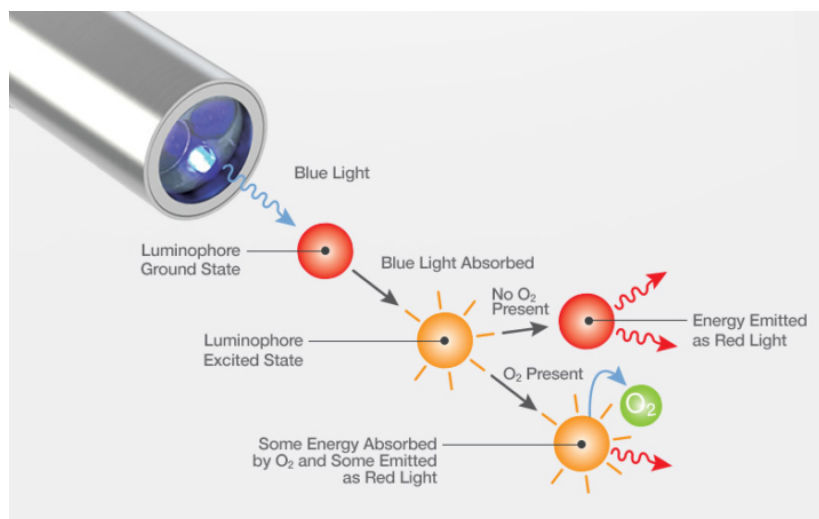


Figure 2.15: Illustration of the physical principle behind the dissolved oxygen measurement, as performed by the Hamilton™ VisiFerm DO Arc 120 sensor. Figure extracted from Hamilton™ website.

**Flow visualization** For visualizing any experiment within the Aquarius device, a use is generally made of an Apple™ Iphone SE 2020 on-board camera. High-speed video records are typically achieved with the latter camera at a rate of 240 frames per second. A FASTCAM™ SA3 model 120K-M1 high-speed camera is occasionally placed in front of one of the two optical windows for finer, high-quality observations.

**Miscellaneous instrumentation** The Aquarius test device is equipped with some more instruments that are devoted to process measurements. Those are detailed below. First, the electric supply of the two resistive heaters is fully monitored through the combined measurement of the input currents and voltage. This allows getting an in-line estimate of the injected electric power and in turn, of its thermal counterpart. Second, the condenser is also instrumented in order to control and monitor the test conditions. It is equipped with two piezoelectric pressure sensors. One is located at its bottom-end and follows changes in its liquid inventory. One is installed at its top-end, in its gaseous volume, together with a temperature measurement. Two more temperature sensors are located at the inlet and outlet of the embedded heat exchanger. At last, a flow-meter provides the water mass flow rate circulating through the latter component.

## 2.2.6 Data acquisition and post-processing

Finally, let us provide some information about the data acquisition system, illustrated in Figure 2.16. First of all, the performed temperature measurements are all recorded by means of a NI-9216 cDAQ™ acquisition module equipping the experimental device. In turn, the dissolved O<sub>2</sub> and pressure measurements are all captured by means of a NI 9205™ acquisition module. The acquired signals are then managed by means of a dedicated LabView™ program. One may note that, unless indicated, the data presented next has been systematically acquired at a frequency of 1 Hz. In addition, the data post-processing is conducted by means of a Python 3 code written by the present author and provided in Appendix C. When post-processing the data, a smoothing of the latter is usually performed along a moving 3-min time interval, whose value has been proven optimal for minimizing as much as possible any data loss by the smoothing while being efficient enough.

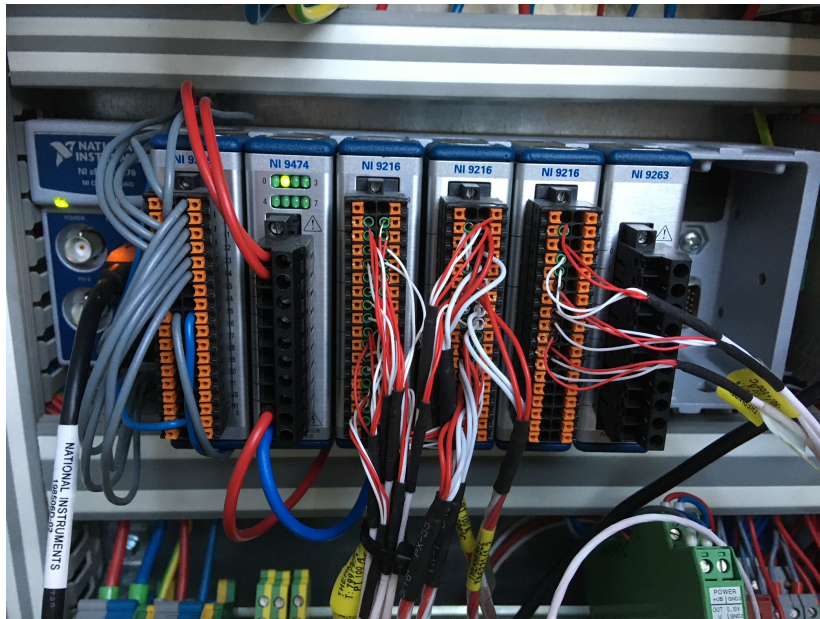


Figure 2.16: Frontview of the acquisition modules equipping the test device and installed into its electrical cabinet.

## 2.3 Measurement uncertainties analysis

### 2.3.1 Methodology

The so-called measurement uncertainties evaluation is an unmissable stage in the development of any experimental device. Such an evaluation was conducted during the presented research and is described in this section. Before detailing the obtained results, let us develop the followed methodology, adapted from the recommendations of the *Guide to the expression of uncertainty in measurement* - or GUM - a reference guideline in metrology [59]. First of all, the overall uncertainty affecting any result of the presented experiments is usually postulated as deriving from two distinct, irreducible and unknown sources of errors [59]. The latter are:

- In link with the measurements performed throughout a test, any measuring chain, including of course those of the present project, being always intrinsically limited and imperfect;
- In link with the experimental procedure and boundary conditions of the test device, applied throughout an experiment. In spite of the care taken in setting up and controlling a typical test, the initial state and boundary conditions of the experimental device, together with the actions taken in the course of a test are expected to differ in some limited but irreducible extent, thereby bringing some more uncertainty to the test results.

The uncertainties which derive from the above first type of errors can be estimated by means of any available information about the utilized measuring chain, such as for

instance, a calibration report or a sensor's technical data-sheet. In doing so, the obtained uncertainty estimates are referred to as *Type B uncertainties*, according to [59]. The uncertainties arising from the second type of errors are however better estimated by means of statistical methods, in which case they are referred to as *Type A uncertainties* [59]. In practice, those Type A uncertainties are highlighted by repeating  $N$  times a chosen reference test, by conserving at every trial:

- The same experimental method;
- The same operator;
- The same equipment;
- The same environmental conditions;
- The same location.

All in all, those differing sources of uncertainties combine and alter the quality of the results in a way which is depicted in Figure 2.17. They must be evaluated separately as-realistically-as possible. The retained process, illustrated in Figure 2.18, was performed during the presented research by:

1. Applying the so-called Type B uncertainty evaluation method recommended in [59] to the primary physical variables that are directly measured throughout an experiment;
- 2.a. Propagating the Type B uncertainties in link with these primary variables into the mathematical expression of some identified relevant physical variables that derive from the measurement of those very primary variables;
- 2.b. Evaluating the uncertainties in link with the experimental procedure and boundary conditions affecting the derived physical variables by repeating 9 times a pre-selected test;
3. Eventually combining the uncertainties obtained at stages 2.a. and 2.b.

In what follows, only the output of the performed uncertainties analysis is given, for more clearness. The interested reader may however find out all the details of the analysis in Appendix D.

### 2.3.2 Physical measurements uncertainties

**Uncertainties in temperature measurements** The temperature measurements performed within the test device are based on 19 Pt-100 4-wire platinum resistance thermometers of class A, as shown in Figure 2.14. The accuracy associated with this latter class is of  $\pm 0.15^\circ\text{C}$  at a reference temperature of  $0^\circ\text{C}$  [118]. In order to improve the accuracy of those measurements, the 19 thermometers were all calibrated in a way

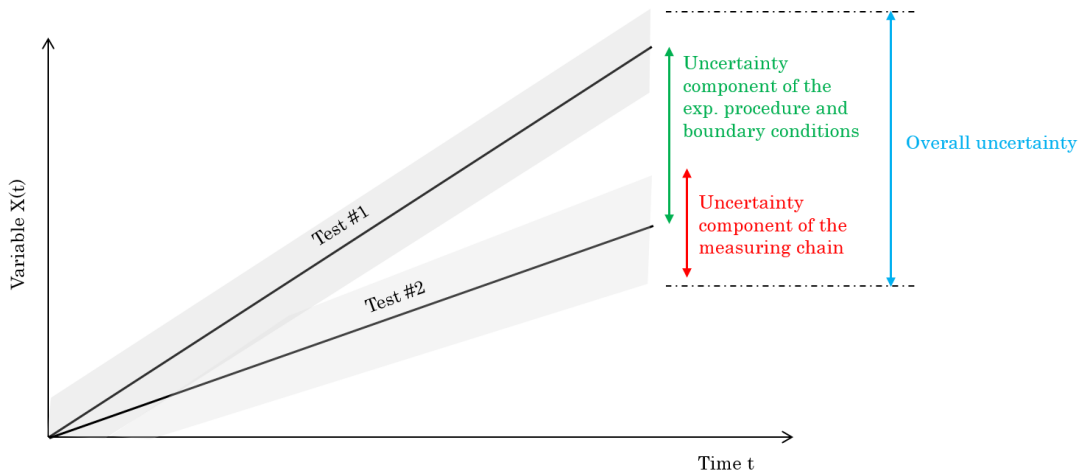


Figure 2.17: The uncertainties, respectively in link with the measuring chain and the experimental procedure and boundary conditions, combine and alter the quality of the obtained results. In this example, the depicted overall uncertainty varies arbitrarily with time.

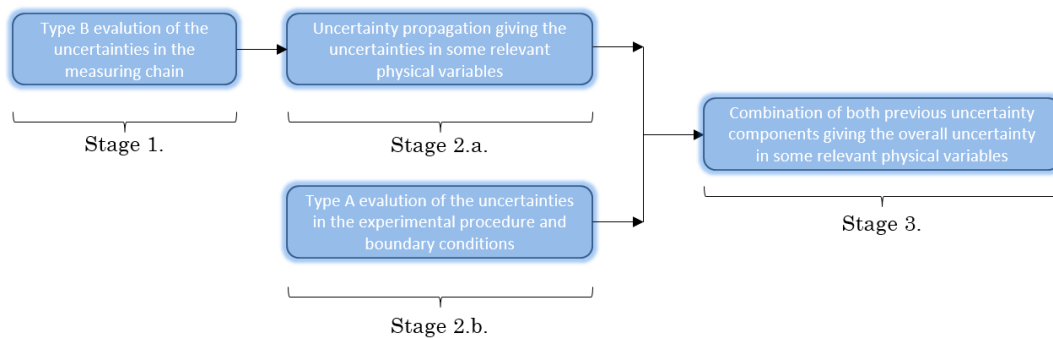


Figure 2.18: The retained method in the evaluation of the uncertainties affecting the quality of the experimental results, developed according to [59].

which is described in Appendix D. In doing so, the uncertainty associated with those temperature measurements was reduced down to  $\pm 0.02^\circ\text{C}$ .

**Uncertainties in pressure measurements** The pressure measurements performed within the test device are based on a set of pressure transducer sensors, as shown in Figure 2.7. Their relative accuracy, defined as a percentage of the measured pressure within the measuring range and specified by the manufacturer after having calibrated those instruments, are given in Table 2.2.

**Uncertainties in dissolved oxygen measurements** As already said, the  $\text{O}_2$  mass concentration in dissolution within water is measured by means of a Hamilton VisiFerm™ DO Arc 120 optical probe. This instrument was adjusted by the manufacturer which

Table 2.2: The used pressure sensors and their relative accuracy.

Sensor ref.	Model	Measurement range	Relative accuracy
P140Ap	E+H Cerabar PMC21	0-110 mbar	$\pm 0.5$ %
P141Ap	Thermibel AM-510	0-1.6 bar	$\pm 0.5$ %
P150Ap	E+H Cerabar M PMC51	0-150 mbar	$\pm 0.01$ %

reported a two-point calibration. Another calibration point was checked by means of the ArcAir™ interface software at the laboratory and yielded satisfactory results. After all, the accuracy of this sensor is estimated to  $\pm 1$  % of the measured  $O_2$  concentration, as described in Appendix D.

### 2.3.3 The uncertainties in the computed physical variables

As it will be seen later in Chapter 3, a limited set of physical variables does appear relevant for characterizing the performed experiments. Those variables, further introduced in Section 3.1.3, are:

- $\Delta T_{eq}$ : the so-called liquid thermal metastability degree;
- $P_G$ : the vessel's atmosphere pressure;
- $m_L$ : the liquid pool mass;
- $\dot{m}_L$ : the liquid vaporization rate;
- $C_{O_2}$ : the dissolved  $O_2$  concentration;
- $\dot{C}_{O_2}$ : the  $O_2$  degassing rate.

The uncertainties attributed to the latter were estimated according to the methodology introduced above and yielded the results given in Table 2.3, with a retained coverage factor of 95%.

Table 2.3: Combined uncertainties attributed to a set of relevant physical variables, with a coverage factor of 95%.

Parameter	Combined uncertainty (coverage factor: 95%)
Liquid thermal metastability degree $\Delta T_{eq}$	0.4°C
Vessel's atmosphere pressure $P_G$	5.5%
Liquid pool mass $m_L$	0.74 kg
Liquid vaporization rate $\dot{m}_L$	0.10 g/s
Dissolved $O_2$ concentration $C_{O_2}$	3.9%
$O_2$ degassing rate $\dot{C}_{O_2}$	6.1%

## 2.4 The experimental procedure

Unless mentioned, the experiments presented in this thesis were typically achieved according to the following standard test procedure, that has proven able to yield repeatable results:

- **Filling stage:** the pool is filled up or partially drained with demineralized and filtered water, depending on the required initial water level ;
- **Bubbling stage:** the liquid pool is bubbled by means of the laboratory compressed air system, in order to reach a targeted and measured initial content in dissolved  $O_2$  (if required) ;
- **Chiller start-up:** the chiller is parameterized and started-up, in order to reach a stationary cold source temperature prior to the test ;
- **Heaters start-up:** the required heat power is fixed by means of a rheostat and the heaters are then electrically fed  $\rightarrow$  progressive increase of the liquid temperature, denoted as  $T_L$ , up to its targeted value ;
- **Depressurization:** once the required initial pool temperature is reached, the depressurization is initiated by starting up the vacuum pump. The vessel pressure naturally tends towards  $P_{sat}(T_L)$ , *i.e.* the saturation pressure corresponding to the initial liquid pool temperature  $T_L$ . At that stage, the pool atmospheric volume is quasi-exclusively filled with steam water and hence highly depleted in air (however, the liquid still contains some dissolved gas) ;
- **Pressure regulation:** the vacuum pump is kept working throughout the test and the condenser heat exchanger valve is regulated by the operator (the cold source temperature set point being kept unchanged), both operations allowing the pool pressure to remain stable along any potential vaporization and/or degassing processes.

This procedure systematically initiates a pool flashing test at thermal saturation conditions, *i.e.*  $T_L(t = 0) = T_{sat}(P_G)$ .

## Conclusions

In this chapter, we have detailed the methodology according to which the so-called Aquarius experimental device was defined. The latter, which is a 1:25-scale mock-up of a typical spent-fuel-pool, is expected to reproduce the gravity-driven flashing of metastable water phenomenon in the configuration of interest. Thanks to some of the Aquarius technical features and to a pre-consolidated test procedure, one can control during any envisioned experiment:

- The initial liquid pool level;

- The heating power;
- The spatial distribution of the heat supply onto the vessel's bottom wall;
- The operating pressure;
- The initial amount of gases in dissolution within the liquid.



---

# A first observation of the gravity-driven flashing in a heated pool

*“The excess of the heat of water above the boiling point is influenced by a great variety of circumstances.”*

— Henry Cavendish

## Introduction

This chapter provides a first insight into the physics of the gravity-driven flashing of metastable water in a pool heated from below. For that purpose, an experiment exhibiting the typical features of the studied phenomenon is introduced in Section 3.1.1. Then, the phenomenology of this experiment is detailed in Section 3.1.2, on the basis of a set of photos taken during the latter. Next is discussed in Section 3.1.3 the corresponding thermodynamic evolution of the pool. One may wonder if those results are repeatable and what causes the typically observed fast bubble growths. These questions are respectively addressed in Sections 3.1.4 and 3.2. With those general results introduced, the phenomenon sensitivity to variations in heating power, operating pressure, initial pool level and content in dissolved gases is later explored in Section 3.3. At last, we provide a set of specific studies of the effect of some bubble nucleation forcing mechanisms on the phenomenon (Section 3.4).

## 3.1 Analysis of a typical experiment

### 3.1.1 Definition of the reference test

Before presenting the typical features of a gravity-driven pool flashing experiment, let us first introduce the characteristics of the test that is retained for that purpose, later referred to as the *reference test*. This test was achieved on April 12, 2022, with the following settings:

- **Thermal power**  $\dot{Q}_p = 1000$  W;
- **Operating pressure**  $P_G = 22$  mbar;
- **Initial liquid temperature**  $T_L(0) = 20^\circ\text{C}$ ;
- **Initial pool level**  $z_p(0) = 30$  cm;
- **Initial content in dissolved oxygen**  $C_{O_2}(0) = 5.8$  mg/L (value in excess at a pressure of 22 mbar).

Naturally, the reference test which is presented next was performed according to the experimental procedure defined in Chapter 2. In addition, we are to mention the chosen position of the four Pt-100 temperature sensors equipping the pool vessel for in-fluid measurements. This is done in Figure 3.1.

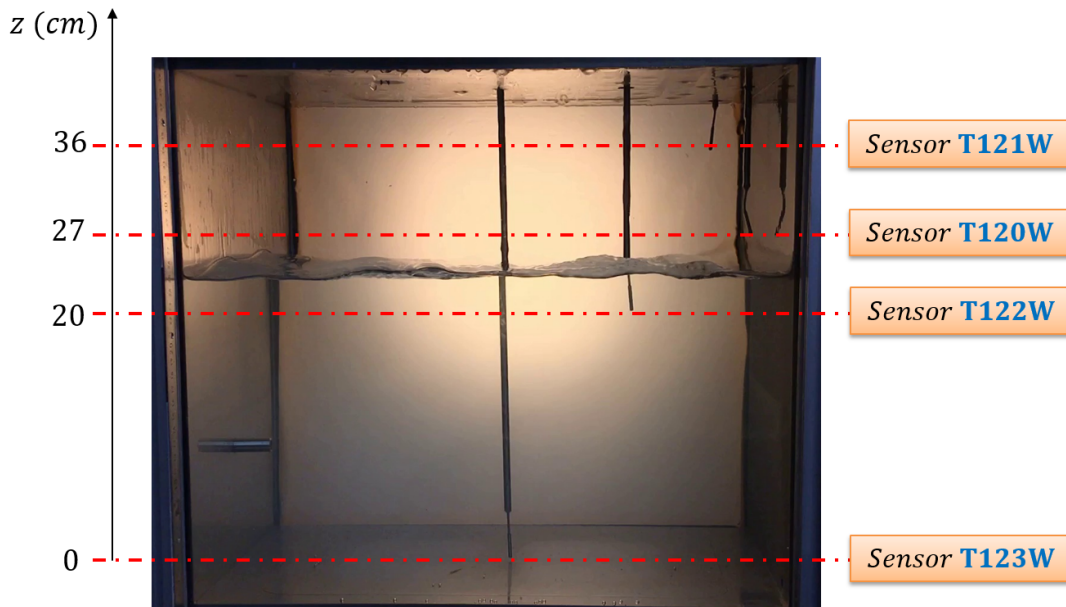


Figure 3.1: Chosen position of the four mobile Pt-100 temperature sensors equipping the pool vessel.

### 3.1.2 The highlighted physical features

Starting the test under thermal saturation conditions and with an excess in dissolved gases, the thermodynamic system constituted by the liquid pool evolved according to a two-stage process, illustrated in Figure 3.2.

During the first stage which lasted approximately 45 min, a strong and continuous bubbling was observed below the water free surface, as shown in Figure 3.2. Particularly under the retained experimental conditions, the strong bubbling also took place momentarily onto the heated bottom wall of the pool vessel and did not last more than 3 min. This particular bubbling and its overall effect are illustrated in the following

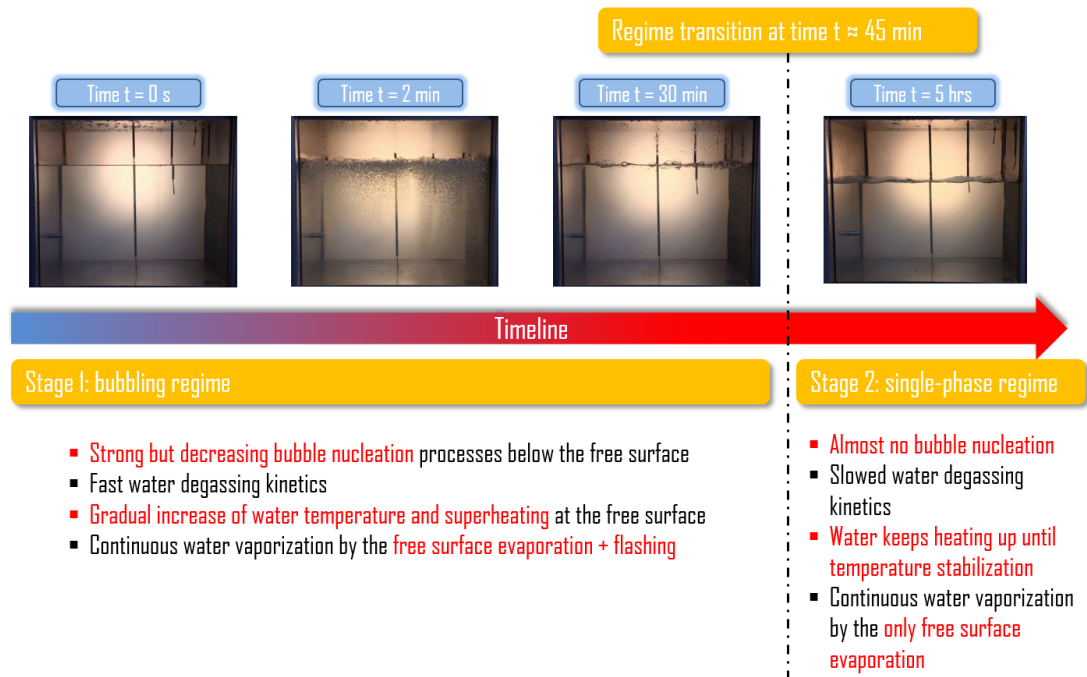


Figure 3.2: The two-stage gravity-driven flashing of superheated water observed within the test device, when starting the experiment at thermal saturation and with an excess in dissolved gases.

figures, which provide a set of photos taken during the first 3 min of the experiment. Initially, some bubble nucleation appeared onto the right-hand-side of the heated wall, as exhibited in Figure 3.3. As it will be discussed later in this chapter, the location of the first occurrence of bubble nucleation onto the heated surface is purely random and is most likely due to some initial temperature differences between the left and right sides of this very surface. In the present case, this hypothesis is consistent with the temperature records performed within the heated wall over time, given in Figure 3.4, with the right heater side being slightly hotter than its left counterpart.



Figure 3.3: A close look at the heated wall of the pool vessel, showing numerous processes of bubble nucleation.

Next, those nucleated bubbles rapidly seeded the whole liquid pool through the form of an uprising two-phase plume, as seen in Figure 3.5. It can be emphasized from

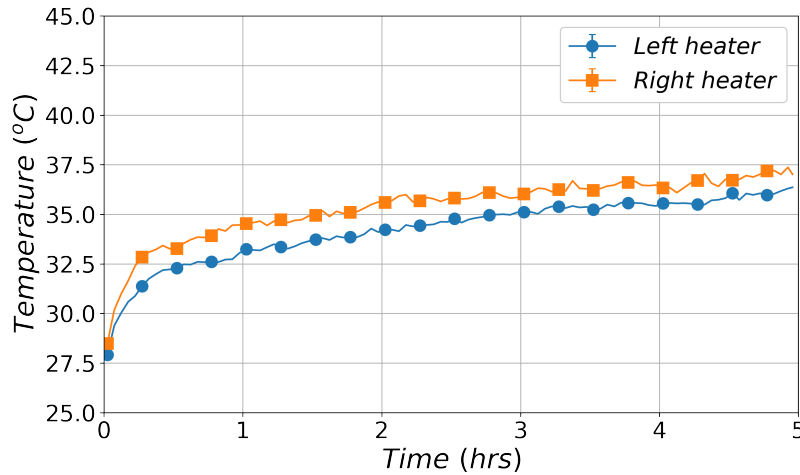


Figure 3.4: Temperature records performed within the heated wall over time, for the reference case. One can note that the right heater side is slightly hotter than its left counterpart, which most likely explains that the first occurrence of bottom wall nucleation was observed onto the right side.

these photos that the bubbly plume thickened over time, having much bigger and more numerous bubbles.

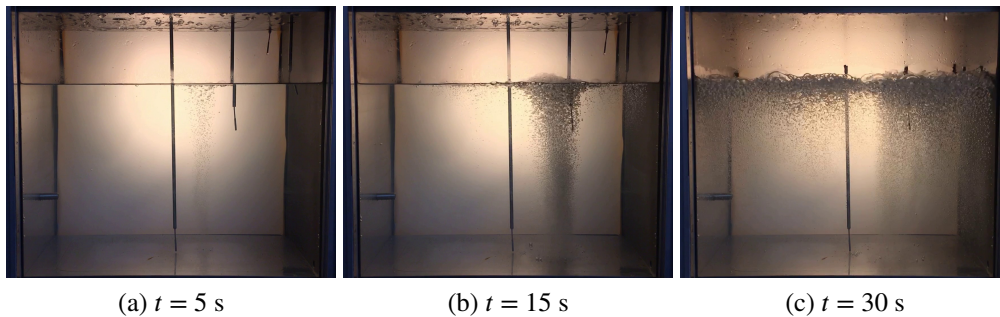


Figure 3.5: The bubbles that nucleated onto the right-side of the heated surface rapidly seeded the whole liquid pool, through the form of an uprising two-phase plume. The bubbly plume thickened over time, having much bigger and more numerous bubbles.

Underneath the liquid free surface, some of the seeding bubbles explosively expanded, as visible in Figure 3.6. It is to be noted that those events were located below the whole surface. After about 1 min, some bubble nucleation appeared as well onto the left-side of the heated wall, as seen in Figure 3.7, thereby contributing to the liquid seeding in bubbles. Singularly, the flow seemed to re-organize through the form of a central bubbly plume, most likely composed of the merge of the plumes generated right on top of the two sides of the heated surface. As seen too, the event further increased the number of bubbles that expanded explosively below the free surface.

Focusing on the heated surface, we identified at least two bubble seeding mechanisms that are worth being mentioned. First of all, at the very beginning of the test,

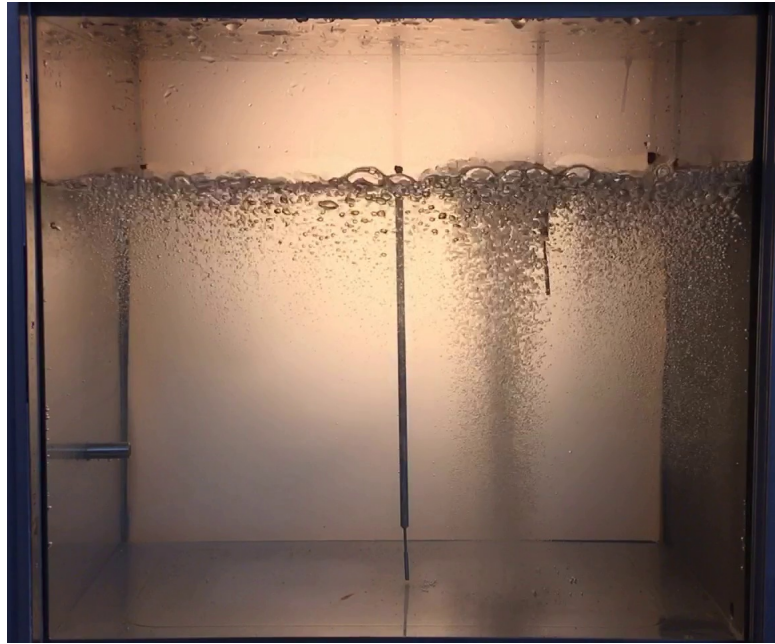


Figure 3.6: Underneath the liquid free surface, some of the bubbles provided by the two-phase plume explosively expanded. Those events were located below the whole surface.



Figure 3.7: After about 1 min, some bubble nucleation appeared as well onto the left-side of the heated wall. At that moment, the flow seemed to re-organize through the form of a central bubbly plume, most likely composed of the merge of the plumes generated right on top of the two sides of the heated surface.

some millimetric bubbles nucleated on this surface. Those bubbles detached, kept unchanged till reaching the free surface and thus seeded the liquid *as is*. This situation is for instance the one seen in the first photo of Figure 3.5. As time went by, the bubbles were nucleated up to a larger size, of the order of half a centimeter around 30 s after the test initiated. Such bubbles are shown in Figure 3.3. After about 1 min, those bubbles got bigger but less numerous, with radii progressively exceeding 1 cm, as it is exhibited in Figure 3.8. Interestingly the latter were, for the largest of them, hemispherical and mushroom-like shaped, as it is expected under reduced pressure conditions. Such shapes have been frequently reported in the literature since the pioneering work of *Cole and Shulman*, performed in 1966 on that topic [28]. For instance, the obtained bubble shapes agree well with the ones recorded and published by *van Stralen et al.* in [119] (*cf.* the series of photos extracted from [119], given in Figure 3.9) and with those recently obtained by *Michaïe* with more modern experimental techniques [84]. Moreover under reduced pressure conditions, this mode of water boiling is known as leading to the formation of a high-speed liquid jet below the formed mushroom-like bubble, right after its departure from its nucleation site. This process is illustrated in Figure 3.10, obtained by *van Stralen et al.* and extracted from [119]. From this series of photos, one can note that the departed bubble is progressively pierced from below by this very liquid jet, though invisible. This event significantly distorts the bubble which may later collapse or not, depending on the strength of the perturbation. Thus, the mechanism can potentially seed the liquid with tinier satellite bubbles. Such a distortion-based bubble collapse was captured during one exploratory test performed within the Aquarius device, by means of the FASTCAM™SA3 model 120K-M1 high-speed camera. The sequence of events is shown in Figure 3.11. As one can observe, the bubble collapse was not complete in this sequence and there remained some tiny bubbles afterwards, which seeded the liquid. Those tiny bubbles re-grew explosively when reaching the free surface, as seen in the last photo of Figure 3.11. Another fast record of this very process is given in Figure 3.12, with an emphasis on the bubble piercing from below by a high-speed liquid jet.

After about 3 min, the bottom wall nucleation described above was no longer visible. From that stage, the water was only turning into bubbles right underneath its free surface. This latter process gradually weakened over time, yielding fewer but bigger bubbles, as visible in Figure 3.13, which is a picture of the pool, taken at time  $t = 30$  min. Then, after about 45 min, a second regime characterized by a quasi-absence of bubble nucleation settled, referred to as single-phase regime in what follows. Around the end of the test, the observation of nucleation became a rare but violent event. At that very moment, the latter occurred randomly and was understood as resulting from some fortuitous element. For instance, in what follows, one can associate the explosive growth of the bubble in Figure 3.14 to the unwanted release of an air bubble that remained temporarily attached to the pool vessel bottom. Another example is given in Figure 3.15, where the collide of a falling liquid droplet with the liquid free surface had the same effect. Most often, the burst of decametric bubbles at the water free surface



Figure 3.8: A close look at one mushroom-like shaped centimetric bubble, nucleated onto the heated wall (here located close to the center of the image), at the beginning of the reference test.

such as the one illustrated herein led to the generation of secondary tiny bubbles by gas entrapment at that very surface, thus sustaining some nucleation during a brief period before the phenomenon vanished. Such secondary bubbles are visible underneath the free surface in the last three photos of Figure 3.14.

At last, it is worth noting that no bubble nucleation was observed at all onto the unheated and roughest vertical wall of the pool vessel, contrarily to our prior expectations. This singular behavior will be discussed in more details in Chapter 4.

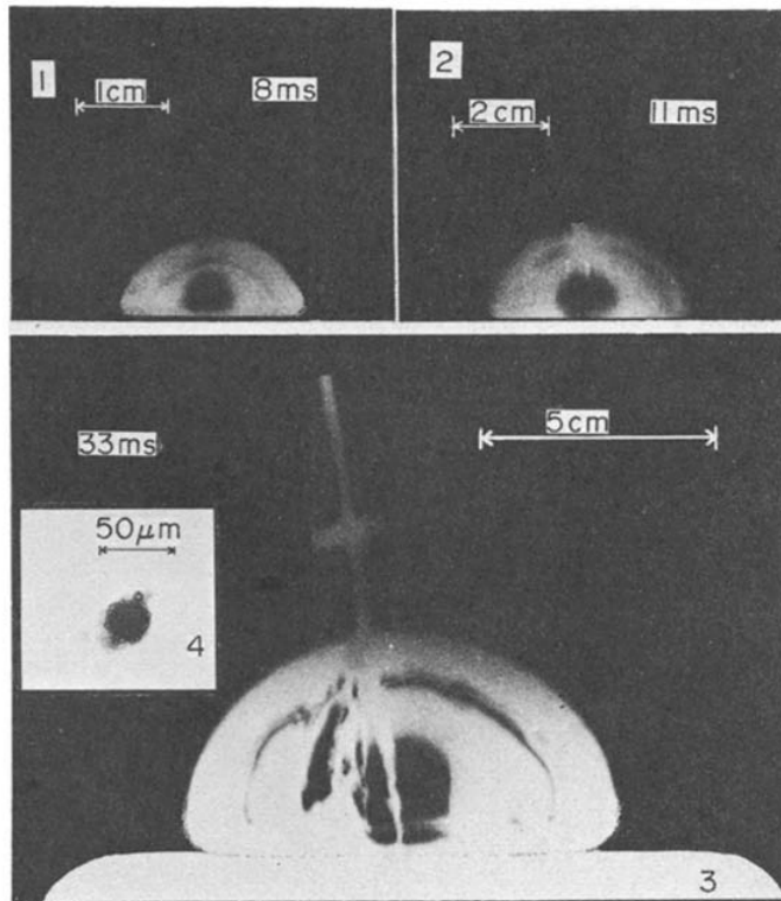


Figure 3.9: A series of photos published by *van Stralen et al.* in 1975, showing water boiling under pressures in between 27 and 2 kPa. One may notice the similarity between the hemispherical, mushroom-like shaped bubbles obtained by *van Stralen et al.* and the ones observed within the Aquarius test device. Images extracted from [119].

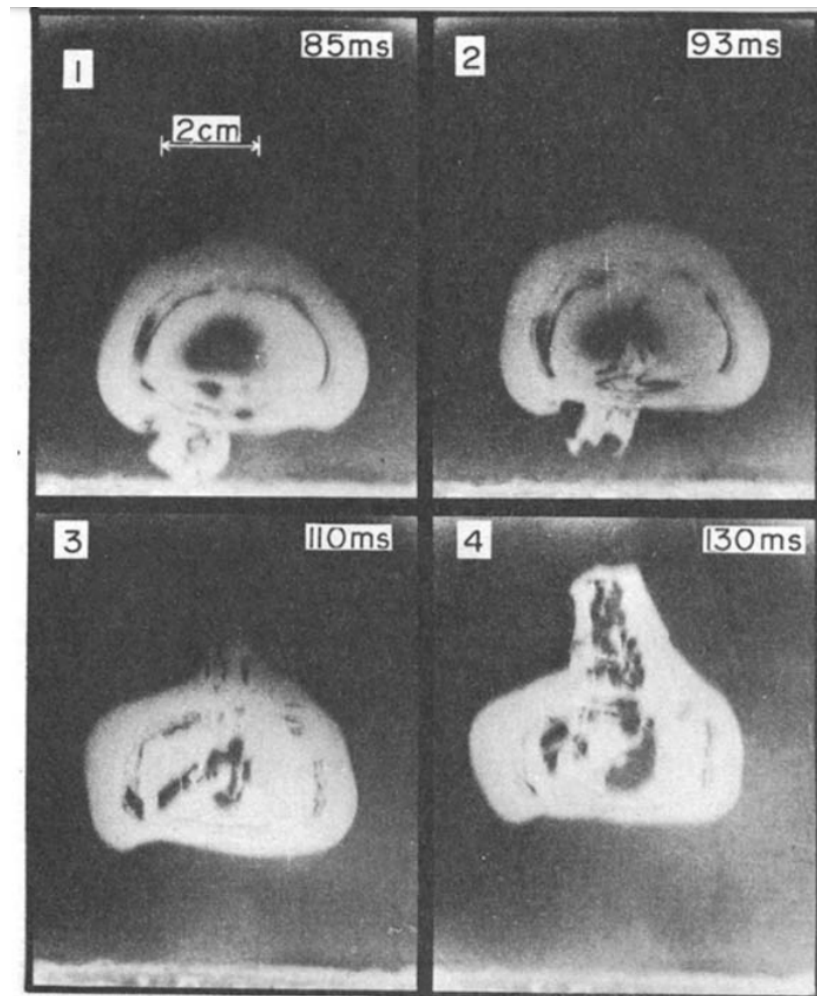


Figure 3.10: A series of photos published by *van Stralen et al.* in 1975, showing the piercing from below of a mushroom-like shaped bubble by a high-speed liquid jet, right after its departure from its nucleation site. Images extracted from [119].

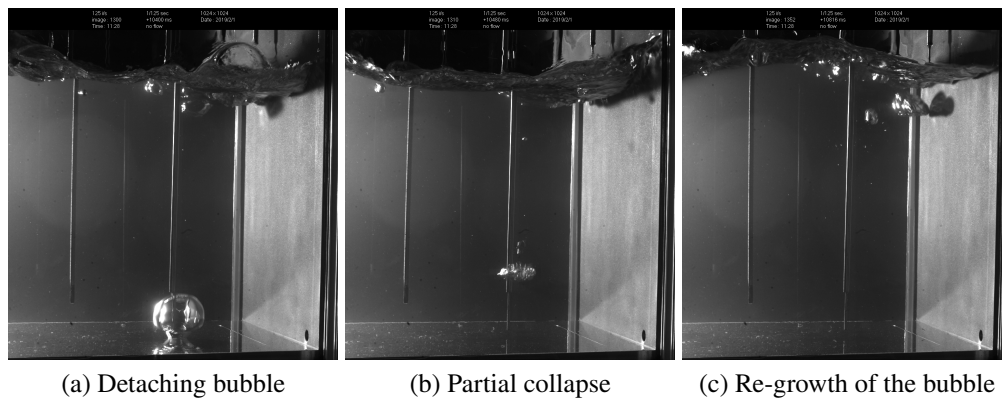


Figure 3.11: A distortion-based bubble collapse, captured during one exploratory test performed within the Aquarius device by means of the FASTCAM™SA3 model 120K-M1 high-speed camera. As one can observe, the bubble collapse was not complete in this sequence and there remained some tiny bubbles afterwards, which seeded the liquid. Those tiny bubbles re-grew explosively when reaching the free surface. Photos taken by *M. Duponcheel*.





Figure 3.13: During the first stage of the test and when the initial strong bubbling originating from the heated wall ceased, water continuously turned into bubbles just below the liquid free surface.

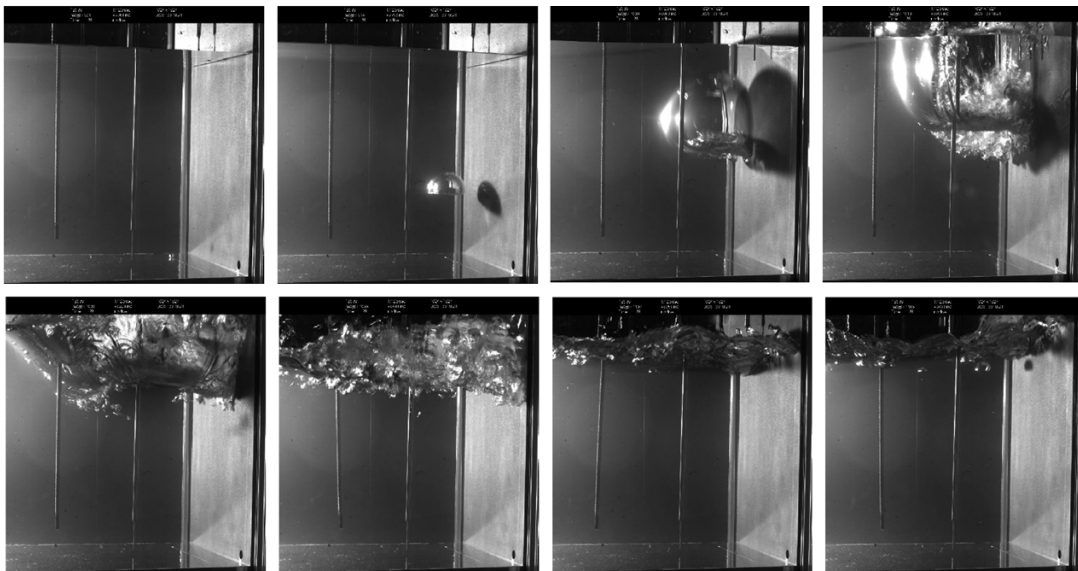


Figure 3.14: Around the end of the test, the phenomenon became very sensitive to any perturbation. Here, an air bubble originating from the bottom of the tank led to the violent vaporization of metastable water. Sequence of images recorded by means of the FASTCAM<sup>TM</sup>SA3 model 120K-M1 high-speed camera. Photos taken by *M. Duponcheel*.



Figure 3.15: A series of photos taken during the late stage of the reference test. The pictures are displayed every 4 ms. The series shows the interaction of a falling droplet with the liquid free surface. The interaction leads to the violent nucleation of a bubble.

### 3.1.3 Thermodynamic evolution of the liquid pool

At the startup of the test as seen in Figure 3.16,  $T_L$ , the measured liquid pool temperature was initially equal to  $T_{sat}(P_G)$ , the saturation temperature, computed from the vessel's atmosphere pressure measurement  $P_G = \text{P140Ap}$ . One may also notice that  $T_G$ , the pool's atmosphere temperature measurement was approximately equal to  $T_{sat}$  throughout the test, thereby indicating that the pool gaseous volume was almost fully filled with water vapor. Indeed, let us denote  $P_w^G$  the water vapor partial pressure and  $x_w^G$  the water vapor molar fraction. If one considers that the water vapor is in thermodynamic equilibrium with its liquid counterpart within the pool's atmosphere (*i.e.* a rather reasonable assumption, owing to the typical large amount of liquid droplets present onto the pool vessel walls in this very volume, in addition to the liquid free surface, providing a large gas/liquid interfacial area), one can show that the latter two thermodynamic quantities are interrelated according to the so-called *Raoult's law* [121]:

$$x_w^G = \frac{P_{sat}(T_G)}{P_G} \quad (3.1)$$

Hence, with  $T_G \approx T_{sat}(P_G)$ , one gets bijectively  $P_{sat}(T_G) \approx P_G$ . Thus,  $x_w^G \approx 1$ , meaning that the pool's atmosphere is almost completely constituted by water vapor. In turn,  $x_{O_2}^G$  the  $O_2$  molar fraction in the vessel's atmosphere is necessarily very close to zero. This implies that the corresponding dissolved  $O_2$  equilibrium mass concentration  $C_{O_2}^{eq}$  at the liquid free surface, fairly well predicted by the so-called *Henry's law* [104], is also close to zero. Therefore in the present experimental conditions, while  $C_{O_2}$ , the dissolved  $O_2$  concentration in the liquid is far from zero, it is expected that the latter species remains in a chemical disequilibrium state with regards to the vessel's atmosphere.

Next, one can observe from Figure 3.16 that, while remaining underwater, the measured liquid temperatures were relatively close to each other. This indicates that the liquid pool was subjected to a strong thermal mixing, throughout the reference test. One may wonder which mechanism stands behind this efficient mixing. First of all, in a two-phase regime, the bubbles are expected to enhance the natural convection heat transfer developed at pool scale [70] and efficiently mix the liquid pool, thereby making uniform its temperature field [91]. This is in agreement with the small variations in temperature, measured at totally different places in the liquid bulk during the first 45 min of the test (*i.e.* throughout the bubbly regime). During the single-phase regime however, the liquid temperature field uniformity can be explained only if the natural convection flow that developed at pool scale was turbulent. Indeed, this bulk temperature uniformity has been early reported as a specific feature of the turbulent regime and it is no longer observed when the regime is laminar [116]. As discussed in Chapter 2, the natural convection heat transfer regime is well represented by the so-called Rayleigh dimensionless number, referred to as  $Ra_L$  in the liquid phase. We recall that this number is defined as:

$$Ra_L = \frac{g\beta_L\Delta T_L d^3}{\nu_L\kappa_L} \quad (3.2)$$

with  $g$ , the gravitational acceleration,  $\beta_L$  the isobaric thermal expansion coefficient,  $\Delta T_L$  the temperature difference driving the natural convection heat transfer,  $d$  the characteristic length along which the heat transfer develops,  $\nu_L$  the kinematic viscosity and  $\kappa_L$  the thermal diffusivity. The larger its value, the more intensive the natural convection heat transfer. As stated in Chapter 2, there exists a threshold value associated with  $Ra_L$  from which the initially laminar heat transfer regime turns turbulent. In the case of water, this value is approximately equal to  $10^5$  [68]. On that basis, let us estimate the values taken by  $Ra_L$  in the liquid pool during the reference test and verify whether the heat transfer was turbulent or not. For doing so, let us first associate the characteristic length  $d$  with the pool collapsed level  $z_p$ . Indeed, in the case of a heat transfer developing between two horizontal planar surfaces of different temperatures, fixing  $d$  equal to  $z_p$  is the most natural choice [116]. The latter collapsed level is defined as:

$$z_p = \frac{m_L}{\rho_L S_p} \quad (3.3)$$

where  $m_L$  is the liquid pool mass,  $\rho_L$  the liquid density and  $S_p$ , the pool free surface area. In what follows, the liquid mass  $m_L$  is determined on the basis of the simultaneous pressure measurements **P140Ap** and **P150Ap**, respectively performed at the pool upper and lower ends, as it is detailed in Appendix A. Next, one has to fix the driving temperature difference  $\Delta T_L$ . Let us first define it as:

$$\Delta T_L = T_h - T_{int} \quad (3.4)$$

where  $T_h$  and  $T_{int}$  are respectively the area-averaged heated bottom plate and liquid free surface temperatures. One can approximate  $T_h$  as:

$$T_h = \frac{1}{2} (\mathbf{T131W} + \mathbf{T134W}) \quad (3.5)$$

with **T131W** and **T134W**, respectively the temperature measurements performed within the left and right sides of the pool heated wall (*cf.* Chapter 2). Further, because  $x_w^G \approx 1$  throughout the reference test, as it has been discussed above, the best guess for the unmeasured  $T_{int}$  is  $T_{int} \approx T_{sat}(P_G)$ . At last, all fluid properties remaining in the expression for  $Ra_L$  are estimated at the arithmetic mean of the measured liquid temperatures  $T_L(z)$ . The results obtained on the basis of the reference test data are visible in Figure 3.17. Two points are worth being mentioned from those results. First, as one can see,  $Ra_L$  was systematically of the order of  $10^9$  throughout the test, as it was envisioned during the scaling of the Aquarius device (*cf.* Chapter 2). Second, the estimates for  $Ra_L$  were always far above the threshold value from which the natural convection is considered turbulent in water. Hence, this is consistent with the observed liquid bulk temperature uniformity during the single-phase regime.

Going further in the analysis of the thermodynamic evolution of the liquid pool, one can notice that at some point of the test, the temperature denoted as  $T_L(z = 27 \text{ cm})$  did not further follow the trend of the other two measured liquid bulk temperatures (*cf.* Figure 3.16). This effect is clearly correlated with the gradual drop in liquid collapsed

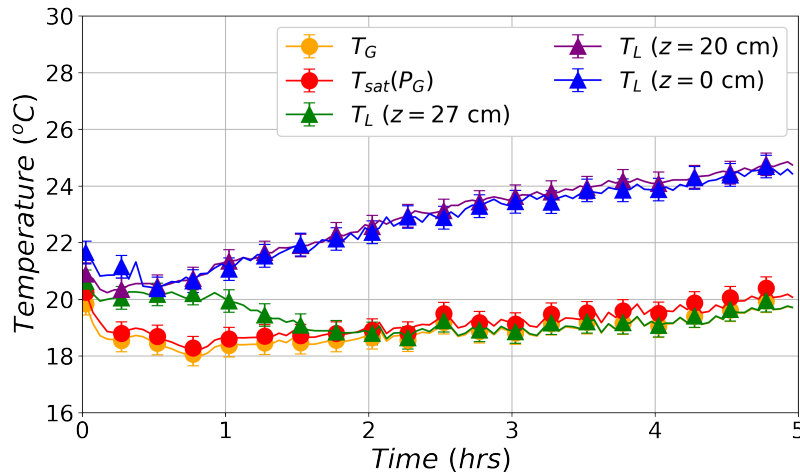


Figure 3.16: Measured fluid temperatures of the reference test (the heights  $z$  mentioned in the legend for each liquid measurement  $T_L$  correspond to the sensor location, with  $z = 0$  being the location of the pool bottom surface).

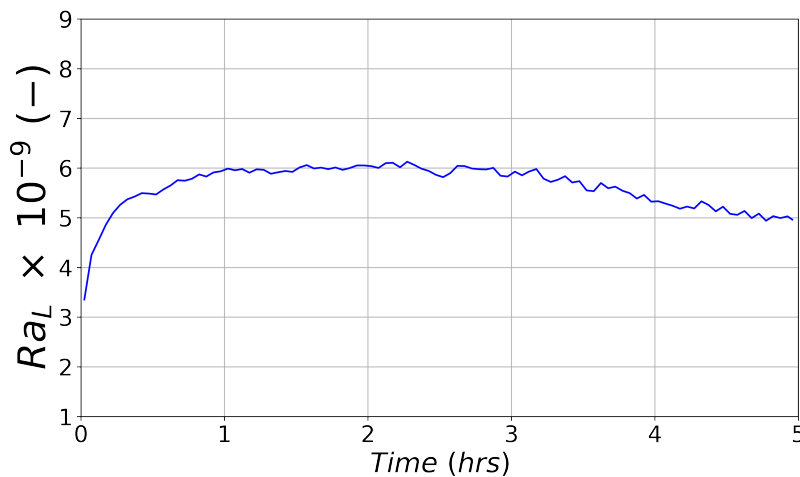


Figure 3.17: Estimated dimensionless Rayleigh number  $Ra_L$  of the natural convection heat transfer that developed through the liquid pool during the reference test.

level  $z_p$ , visible for instance in Figure 3.2. With this in mind, let us study the kinetics of the liquid mass variation. In Figure 3.18 is given, in the left-hand-side, the estimate of the liquid mass, already introduced as  $m_L$ . In the right-hand-side is provided the time-trend of the so-called liquid vaporization rate, denoted as  $\dot{m}_L$  and approximated as:

$$\dot{m}_L \approx \frac{m_L(t + \Delta t) - m_L(t)}{\Delta t} \quad (3.6)$$

with  $t$  being the time variable. At first, one can notice that the variations in liquid mass were almost linear over time, during the reference test. After some brief transient period, those variations were achieved at an almost constant rate of:

$$|\dot{m}_L(t > 30 \text{ min})| \approx 0.4 \text{ g/s} \quad (3.7)$$

Interestingly, this rate is almost equal to  $\dot{Q}_p / h_{gsat}(P_G)$ , the expected value in the case of a complete energetic equilibrium between the provided heat power  $\dot{Q}_p$  and the enthalpy flux associated with water vaporization  $|\dot{m}_L| \times h_{gsat}(P_G)$ . It also shows that the water vaporization process was most likely here the main heat sink mechanism. This fact is the positive consequence of the pressure-based similarity approach proposed in this study. Indeed, working here at such a reduced pressure of 22 mbar imposes to the system a mild level of working temperatures, of the order of 22°C (*cf.* Figure 3.16), thereby minimizing the heat losses at pool's boundaries. Most important, during the single-phase stage of the test and in agreement with the absence of any sustained bubble nucleation, one may assert that the free surface evaporation of the liquid was the only vaporization mode allowing to energetically compensate for the heat supplied at the bottom of the pool. It is worth mentioning that throughout the test duration, the vessel's atmosphere pressure  $P_G$  varied slightly and negligibly, as seen in Figure 3.19.

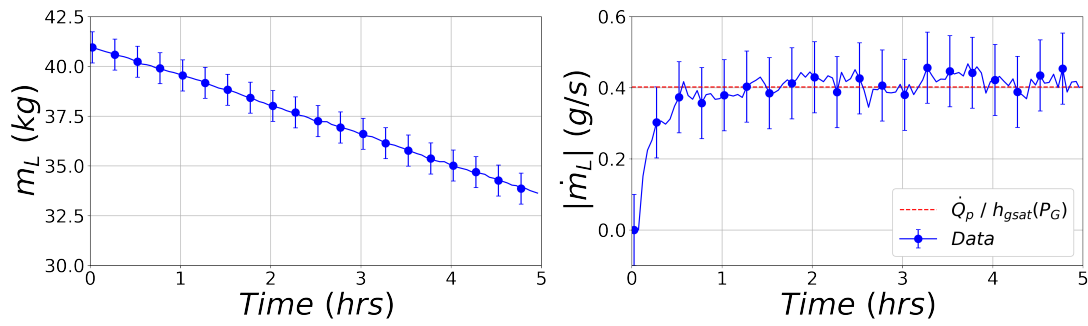


Figure 3.18: Reference test. Left: estimated liquid mass  $m_L$ . Right: estimated liquid vaporization rate  $\dot{m}_L$ .

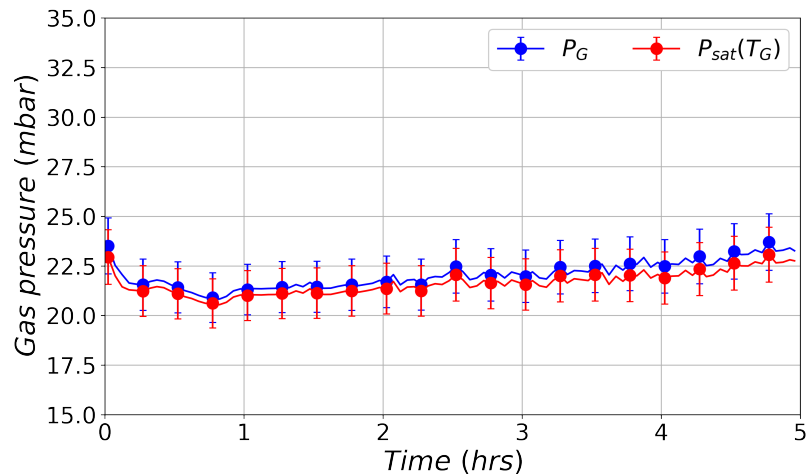


Figure 3.19: Measured vessel's atmosphere pressure  $P_G$  during the reference test, plotted together with  $P_{sat}(T_G)$ , the saturation pressure estimated at temperature  $T_G$ .

Another point is to be emphasized. As one can notice from Figure 3.16, the liquid pool temperatures significantly deviated over time from the saturation temperature

$T_{sat}(P_G)$ . Obviously, this reveals that the liquid state, initially at thermodynamic stable equilibrium (*i.e.* at thermal saturation) entered more and more into its metastable domain as time went by. It is interesting to determine up to which metastable state the liquid evolved. For doing so, let us introduce a variable  $\Delta T_{eq}$  that is later referred to as the *liquid thermal metastability degree*. This degree is defined as:

$$\Delta T_{eq} = \langle T_L \rangle - T_{sat}(P_G) \quad (3.8)$$

with  $\langle T_L \rangle$  the arithmetic mean of the measured liquid bulk temperatures. The application of Equation (3.8) to the reference test data is illustrated in Figure 3.20. One can observe that the liquid metastability degree did not increase indefinitely during the test. Indeed, it appears that from  $t = 3$  hrs,  $\Delta T_{eq}$  stabilized at an approximate value of  $4.5^\circ\text{C} \pm 0.35^\circ\text{C}$  up to the end of the test. Pointedly, this so-called *asymptotic state* of the metastable liquid maintained during a relatively long period of 2 hrs, in spite of the sporadic and violent events of bubble nucleation that have been mentioned earlier in this chapter.

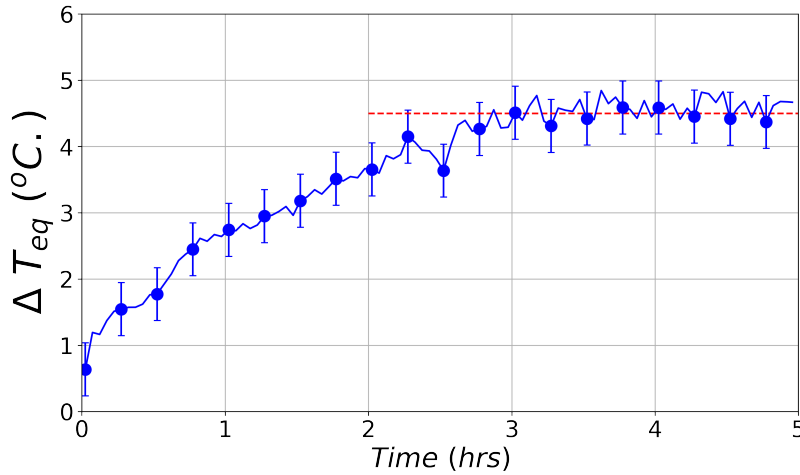


Figure 3.20: Estimate of the thermal metastability degree of the heated liquid  $\Delta T_{eq}$  during the reference test. From  $t = 3$  hrs,  $\Delta T_{eq}$  stabilized at a value of  $4.5^\circ\text{C} \pm 0.35^\circ\text{C}$  up to the end of the test.

At last, let us study the time-variations of the amount of gases dissolved in the liquid pool. For that purpose, the left-hand-side graph of Figure 3.21 represents the direct measurement of the dissolved oxygen concentration within the liquid  $C_{O_2}$ . The latter is a good indicator for the amount of dissolved air, in spite of the lacking measurement of the other main contributor to the air composition - the  $\text{N}_2$  species - as stated in Chapter 2 and justified in Appendix B. The right-hand-side graph of this very figure is an estimate of the  $\text{O}_2$  degassing rate  $\dot{C}_{O_2}$ , given by:

$$\dot{C}_{O_2} \approx \frac{C_{O_2}(t + \Delta t) - C_{O_2}(t)}{\Delta t} \quad (3.9)$$

First of all one can observe that, as expected, the dissolved  $\text{O}_2$  concentration, initially in excess, decreased over time, as a system's way for reaching a chemical equilibrium state with regards to this same species. Then, it is worth pointing out that the

$O_2$  degassing flux, which was almost null initially, peaked temporarily at a value of approximately 17 mg/L/s., before dropping back to low values, from  $t = 60$  min. This suggests the existence of a substantial dissolved  $O_2$  mass transfer within the liquid pool, during the initial stage of the test. This result is in agreement with the pool visualization performed at some key moments of the test, which revealed an initial strong bubbling process (Figures 3.2-3.13). The bubbling being known as efficiently promoting the heat and mass transfers in a liquid [73], it is hence a significant candidate for explaining the observed trend in  $\dot{C}_{O_2}$ . To conclude, it is interesting to notice that the time-variations of  $\Delta T_{eq}$  and  $C_{O_2}$  were correlated, as seen in Figure 3.22. This graph exhibits two linear trends, which intersect for  $C_{O_2} = 0.55$  mg/L. Finding from Figure 3.21 the time corresponding to the reach of  $C_{O_2} = 0.55$  mg/L yields approximately 45 min, *i.e.* more or less the observed duration for the bubbling regime. This clear and abrupt change in the two linear trends slope is hence interpreted up to that point as reflecting the transition between the bubbling/non-bubbling regimes that was evidenced above.

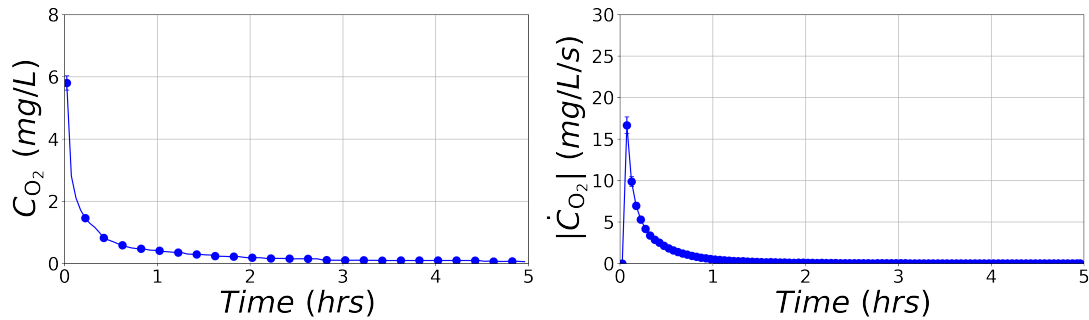


Figure 3.21: Reference test. Left: measured dissolved oxygen concentration  $C_{O_2}$ . Right: estimated oxygen degassing rate  $\dot{C}_{O_2}$ .

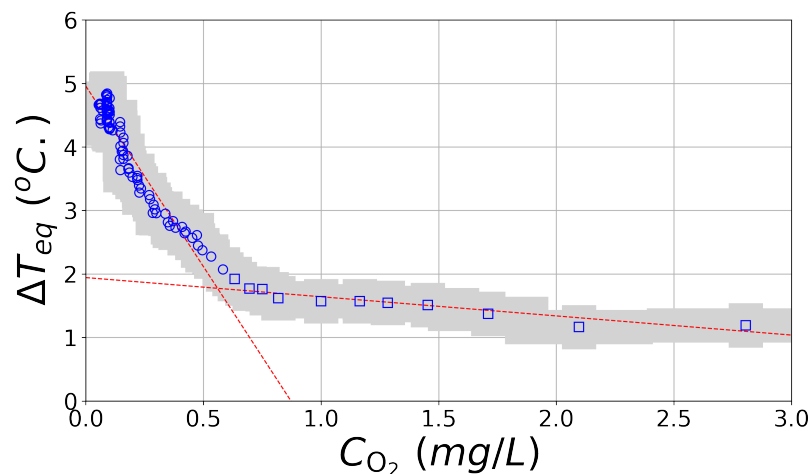


Figure 3.22: Reference test. The variables reflecting the liquid degassing and heat-up kinetics,  $C_{O_2}$  and  $\Delta T_{eq}$ , were linearly correlated according to a pair of trends that intersected at a time estimated to 45 min, in consistency with the visualized transition between a nucleation stage and its non-nucleation counterpart.

### 3.1.4 The repeatability of the reference test

Let us check now if the results deduced from the reference test were repeatable. In order to do so, nine identical tests, having parameters as close as possible to those of the so-called reference test, were conducted. Those tests are listed in Table 3.1 and their common characteristics are given below:

- Thermal power  $\dot{Q}_p = 1000$  W;
- Operating pressure  $P_G = 22$  mbar;
- Initial liquid temperature  $T_L(0) = 20^\circ\text{C}$ ;
- Initial pool level  $z_p(0) = 30$  cm;
- Initial content in dissolved oxygen  $C_{O_2}(0) = 6.5$  mg/L (value in excess at a pressure of 22 mbar).

Table 3.1: The achieved nine identical tests for studying the repeatability of the observed phenomena. In the last column of this table is indicated the side of the heated wall where some bubble nucleation was observed at first.

Test No.	Date	Side of the heated wall where nucleation occurred
1	November 25, 2021	Left side
2	February 25, 2022	Left side
3	February 28, 2022	Right side
4	March 1, 2022	Both sides
5	March 14, 2022	Left side
6	March 21, 2022	Both sides
7	March 23, 2022	Both sides
8	March 25, 2022	Left side
9	April 5, 2022	Left side

A comparison of the most relevant physical quantities characterizing these tests is provided in Figure D.6. Those quantities are the ones that have been presented in the previous Section 3.1.3:

- $\Delta T_{eq}$ : the so-called liquid thermal metastability degree;
- $P_G$ : the vessel's atmosphere pressure;
- $m_L$ : the liquid pool mass;
- $\dot{m}_L$ : the liquid vaporization rate;
- $C_{O_2}$ : the dissolved  $O_2$  concentration;
- $\dot{C}_{O_2}$ : the  $O_2$  degassing rate.

At first, one can notice the overall good repeatability of those physical variables. The observed time trends were all repeatable, with a relatively small level of discrepancy from one test to another. The calculated time-averaged standard deviations, associated with the differences in each variable  $X$  value from test to test, are referred to as  $\bar{\sigma}_X$ . They are further given in Table 3.2.

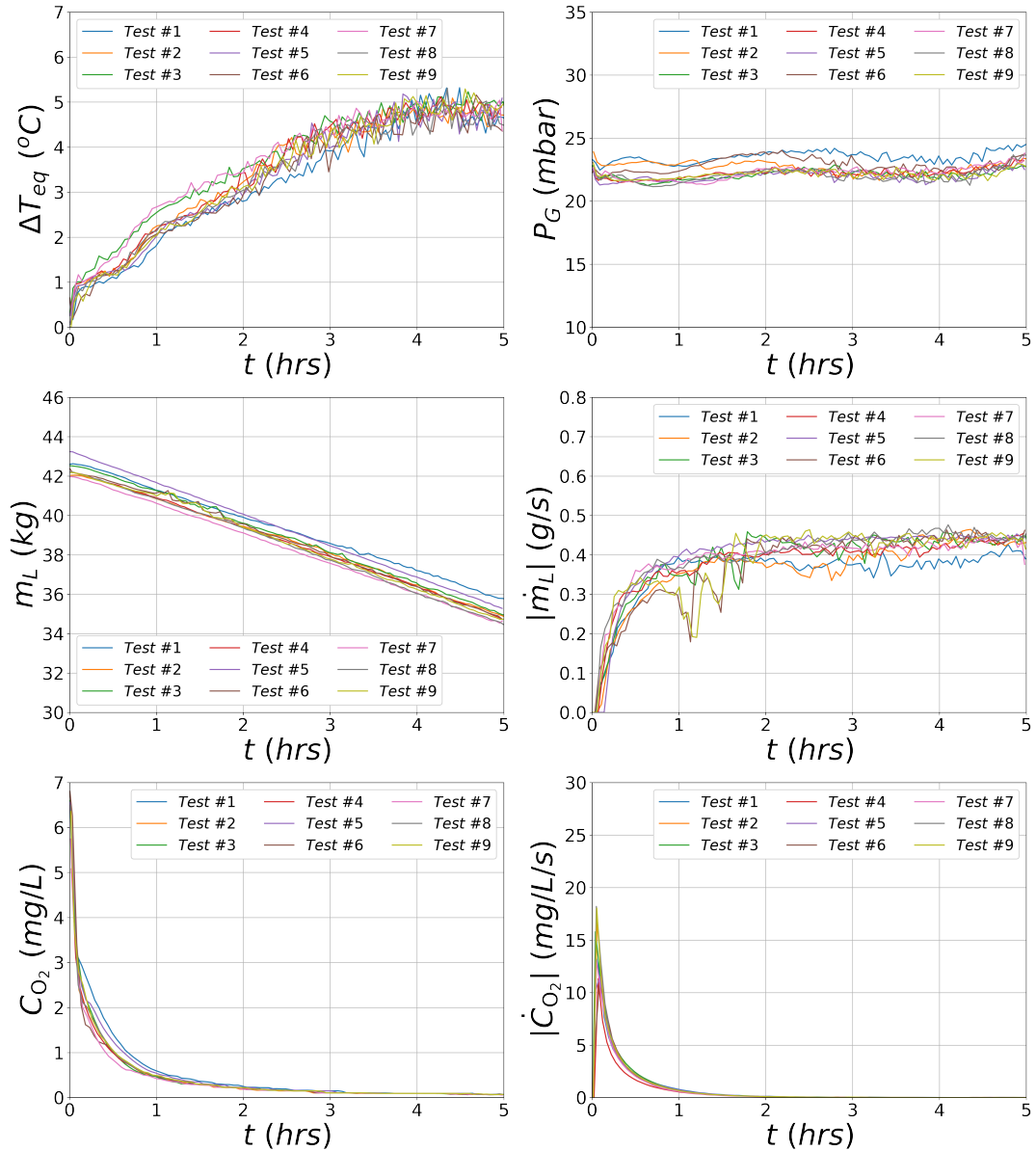


Figure 3.23: Main physical variables of the achieved nine identical tests, having parameters as close as possible to those of the so-called reference test. One can notice the overall good repeatability of the considered physical variables.

Obviously, with such a good repeatability of the computed  $\Delta T_{eq}$  and measured  $C_{O_2}$ , the correlation that has been found between the latter two variables in Section 3.1.3 is to be repeatable as well. This is indeed verified in Figure 3.24. The  $C_{O_2}$  threshold value, postulated as reflecting the transition between the bubbling/non-bubbling regimes and equal to 0.55 mg/L for the reference test, is actually much closer to 0.45 mg/L when

Table 3.2: Calculated time-averaged standard deviations associated with each main physical variable, on the basis of the nine repeated tests.

Parameter	Time-averaged standard deviation	Value
Liquid thermal metastability degree	$\bar{\sigma}_{\Delta T_{eq}}$	0.17°C
Vessel's atmosphere pressure	$\bar{\sigma}_{P_G}$	0.53 mbar
Liquid pool mass	$\bar{\sigma}_{m_L}$	0.32 kg
Liquid vaporization rate	$\bar{\sigma}_{\dot{m}_L}$	0.03 g/s
Dissolved O <sub>2</sub> concentration	$\bar{\sigma}_{C_{O_2}}$	0.09 mg/L
O <sub>2</sub> degassing rate	$\bar{\sigma}_{\dot{C}_{O_2}}$	0.19 mg/L/s

considering more data. The overall phenomenology, described in Section 3.1.2, was also repeatable with some slight discrepancies that are detailed below. First of all, whatever the repeated test, bubbles nucleated onto the bottom heated surface and below the liquid free surface, without exception. The bubbling regime invariably lasted around 45 min. However, the location at the bottom wall of the onset of bubble nucleation was not always the same. This is illustrated in Figure 3.25 which is a close look of the heated wall surface at the beginning of Test #9. As one can see, the bottom wall bubble nucleation here initiated at the left-hand-side, which differs from the right-hand-side-located nucleation observed during the reference case (*cf.* Figure 3.5). All noted first occurrences of the bottom wall bubble nucleation are listed in Table 3.1. From this listing, it seems that the left-hand-side of the heated wall is a preferred place for the onset of this very process, although this specificity is not yet understood.

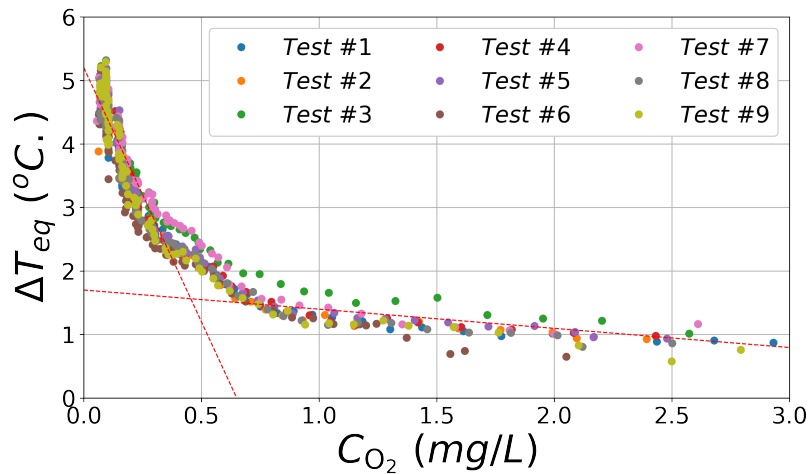


Figure 3.24: The correlation between the variables reflecting the liquid degassing and heat-up kinetics  $C_{O_2}$  and  $\Delta T_{eq}$ , found out from the reference test data, was well repeated.

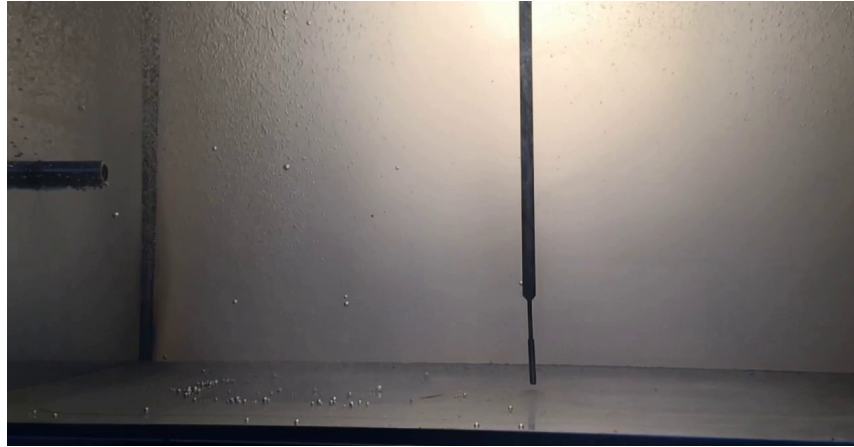


Figure 3.25: Bubble nucleation was initiated at the left-hand-side of the heated wall during Test #9. This differs from the right-hand-side-located nucleation observed during the reference case.

### 3.2 An interpretation for the observed fast bubble growth

Having explored the main features of a typical gravity-driven pool flashing experiment and its associated thermodynamic evolution, one may wonder what causes the observed fast, sometimes explosive, bubble growth following the nucleation events. Three mechanisms, illustrated in Figure 3.26, can be postulated as underlying this exaggerated growth. Those are successively detailed in what follows.

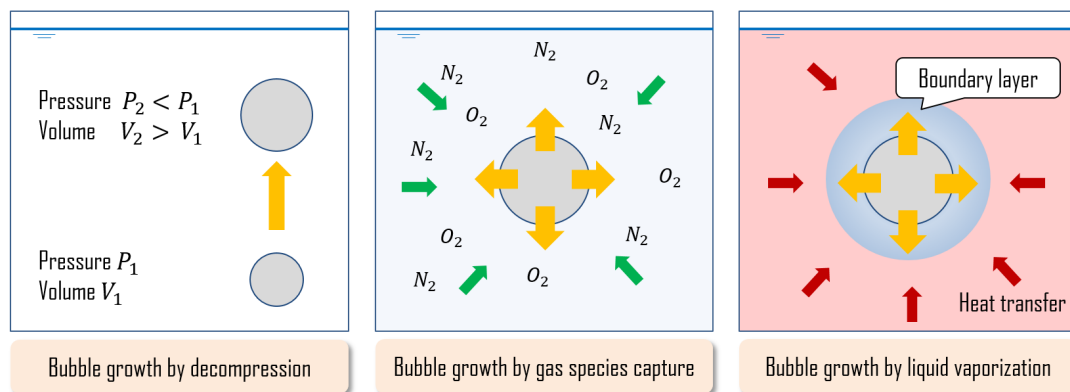


Figure 3.26: An illustration of the envisioned bubble growth mechanisms in a pool.

Assuming that some bubble has nucleated at a low position within the pool, the latter, when rising through the liquid, is obviously subjected to a change in hydrostatic pressure, referred to as decompression. If this thermodynamic transform does not involve any mass change and is isothermal, the decrease of bubble pressure  $P$  leads to its volume  $V$  expansion. The process is well described by the so-called *Boyle-Mariotte's law*, provided the gas can be assumed as ideal [121]. This law allows estimating the

change in bubble volume as follows:

$$\frac{P_1}{P_2} = \frac{V_2}{V_1} \quad (3.10)$$

with the subscript {1 ; 2} referring to the stage of the thermodynamic transform, as depicted in the first inset of Figure 3.26. On that basis, let us now estimate the order of magnitude of the bubble volume variation, here expressed as the ratio  $V_2/V_1$ , induced by decompression under the conditions that are typical to the reference test. In order to get an upper-bound of this ratio, let us assume that some bubble that nucleated onto the vessel's bottom wall detaches and rises through the whole liquid pool, *i.e.* over a total length of 30 cm. In these conditions and if the inner bubble pressure is close enough to those of the liquid (this is typically true for air bubbles in water larger than 1 mm, *cf.* Laplace-Young's law [33]):

- $P_2 = P_G = 22 \text{ mbar}$ ;
- $P_1 = P_2 + \rho_L g z_p$ .

With  $\rho_L$ , the volume-averaged liquid density taken equal to  $1000 \text{ kg/m}^3$  and  $z_p = 30 \text{ cm}$ , this yields  $P_1 = 52 \text{ mbar}$ . Hence:

$$\frac{V_2}{V_1} \approx 2.4$$

With the volume of a sphere being:

$$V_{sphere} = \frac{4}{3} \pi r_{sphere}^3 \quad (3.11)$$

the corresponding bubble radius ratio is:

$$\frac{r_2}{r_1} = \left( \frac{V_2}{V_1} \right)^{1/3} \approx 1.3$$

Noticing that bubbles typically grew fast from millimetric to centimetric sizes underneath the liquid free surface (hence a  $\times 10$  radius change, *cf.* Section 3.1.2 and for instance, Figure 3.7), this mechanism, though relevant, does not fully explain the observation. Two other mechanisms are thought as being in a better agreement with the observation: the bubble growth by either dissolved gases capture or liquid vaporization, as represented in the second and third insets of Figure 3.26. Indeed, it has been already highlighted that the liquid pool was both supersaturated in dissolved gases and superheated in its upper part, throughout the reference test (*cf.* Section 3.1.3). Under such disequibrated conditions, a bubble rising through the liquid is expected to overcome two combined mass transfers and hence, to expand by change of mass, as a system's way to relax its supersaturation and superheating. Let us now estimate the change of mass that may result from the above transfers. For doing so, let us first introduce some key concepts.

The problem of a bubble growing by change of mass when rising through a liquid phase has long been studied both experimentally and theoretically since the first times of chemical engineering, the latter phenomenon being widely encountered in many practical applications in that field [47]. In the past, many researchers have highlighted the mechanisms underlying this phenomenon: the mass transfer taking place between the liquid phase and the rising bubble is unsteady. Indeed, because of its up-rising movement, the bubble continuously encounters some fresh liquid at its top end, having the bulk composition and/or temperature. When some liquid flows around the bubble surface, a mass transfer develops between the bubble and the liquid, and the latter overcomes a change in its properties in link with this transfer (*i.e.* composition and/or temperature). This configuration being continuously renewed as long as the bubble rises, the mass transfer is hence never steady in the present case [104]. We illustrate the process in Figure 3.27.

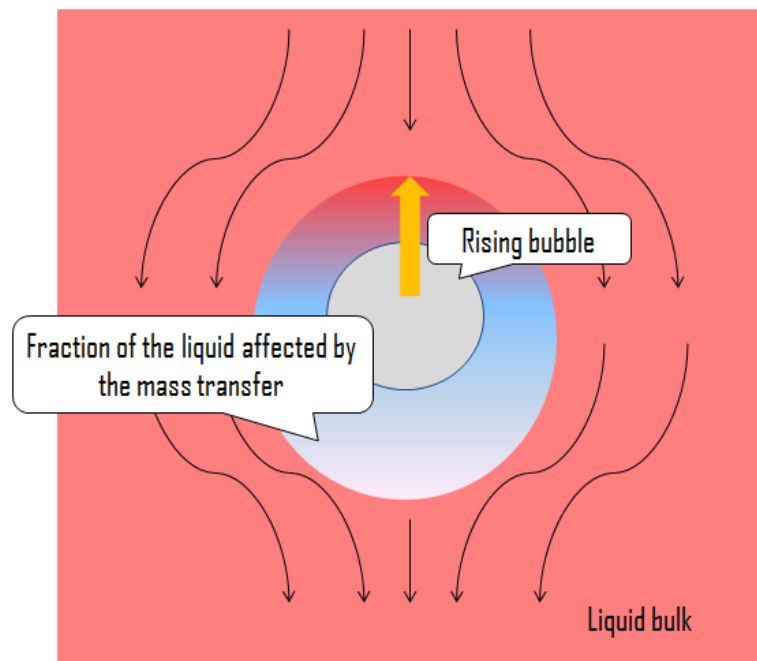


Figure 3.27: An illustration of the so-called penetration theory, providing an explanation for the bubble growth by mass transfer.

Further, a model known as the *penetration theory*, deriving from *Fick's second law of diffusion* [32], was first introduced by *Higbie* in 1935 [52]. This model, once applied to a bubble geometry, postulates that the latter overcomes an unsteady mass transfer, whose transfer coefficient denoted as  $k_m$  and given in m/s, is obviously time-dependent. Starting from *Fick's second law of diffusion*, one can show that this coefficient reads [13]:

$$k_m = 2\sqrt{\frac{\mathcal{D}_X}{\pi \tau_c}} \quad (3.12)$$

where  $\mathcal{C}_X$  denotes the transport coefficient corresponding to the considered transfer  $X$  and  $\tau_c$  is the so-called *exposure time* which characterizes the renewed contact between the bubble and some fresh liquid. With  $d_{bubble}$  and  $v_{bubble}$  being respectively the bubble diameter and terminal velocity, this characteristic time can be approximated as [13]:

$$\tau_c \approx \frac{d_{bubble}}{v_{bubble}} \quad (3.13)$$

On that basis, denoting respectively the bubble-averaged local fluxes associated with the air degassing and liquid vaporization processes illustrated in Figure 3.26 as  $j_a^B$  and  $j_w^B$  (in kg/m<sup>2</sup>/s), one can estimate  $j_a^B$  as [13]:

$$j_a^B = 2 \sqrt{\frac{\mathcal{D}_{a;w}^L v_{bubble}}{\pi d_{bubble}}} (C_a(z) - C_a^{eq}(z)) \quad (3.14)$$

and by analogy  $j_w^B$ , according to the work done by *Fritz and Ende* in 1936 [44], [98], [72]:

$$j_w^B = \frac{1}{\mathcal{L}_w} \sqrt{\frac{(\lambda_L)^2 v_{bubble}}{\pi \kappa_L d_{bubble}}} (T_L(z) - T_{sat}(z)) \quad (3.15)$$

with  $\mathcal{D}_{a;w}^L$  the dissolved air/water diffusivity coefficient,  $C_a(z)$  the dissolved air local mass concentration,  $C_a^{eq}(z)$  its equilibrium value at local liquid temperature  $T_L(z)$  and pressure  $P_L(z)$ ,  $\mathcal{L}_w$  the water specific latent heat,  $\lambda_L$  the water thermal conductivity,  $\kappa_L$  the water thermal diffusivity and  $T_{sat}(z)$  the local saturation temperature, estimated at pressure  $P_L(z)$ .

Next, let us compare the two mass fluxes generated by the air degassing and liquid vaporization processes. For doing so, we further consider the ratio:

$$\frac{j_a^B}{j_w^B} = \frac{2\mathcal{L}_w \mathcal{D}_{a;w}^L \sqrt{Le}}{\lambda_L} \left( \frac{C_a(z) - C_a^{eq}(z)}{T_L(z) - T_{sat}(z)} \right) \quad (3.16)$$

where both the bubble diameter  $d_{bubble}$  and terminal velocity  $v_{bubble}$  have canceled out and with  $Le$ , the so-called Lewis number, equal to:

$$Le = \frac{\kappa_L}{\mathcal{D}_{a;w}^L} \quad (3.17)$$

Let us now apply Equation (3.16) to the thermodynamic specificities of the reference test (*cf.* Section 3.1.3). First of all, for a liquid temperature around 20°C, with a water thermal diffusivity  $\kappa_L$  of the order of 10<sup>-7</sup> m<sup>2</sup>/s and a dissolved air/water mass diffusivity around 10<sup>-9</sup> m<sup>2</sup>/s,  $Le \approx 100$ . Then,  $\mathcal{L}_w$  and  $\lambda_L$  being respectively of the order of 2.4 × 10<sup>6</sup> J/kg and 0.6 W/m/K under the studied conditions, one gets:

$$\frac{2\mathcal{L}_w \mathcal{D}_{a;w}^L \sqrt{Le}}{\lambda_L} \approx 10^{-7} \text{ m}^3 \text{ K/kg}$$

Therefore, unless  $(T_L(z) - T_{sat}(z))$  is smaller than at least  $10^{-7}$  K, the mass flux induced by the liquid vaporization is expected to be completely dominant when compared to its air degassing counterpart. This is obviously true for local liquid superheats around or bigger than unity as the ones obtained during the reference test (*cf.* Section 3.1.3), whatever the quantity  $(C_a(z) - C_a^{eq}(z))$ . Thus, throughout a typical experiment, the liquid vaporization is postulated as being the main process leading to the observed fast bubble growth, the bubble growth induced by decompression or by air degassing being practically negligible. Especially, going back to the phenomenological features described in Section 3.1.2, the bubble growth following the observed nucleation events is thought as being the signature of the flashing of some superheated water.

In order to verify in an experimental way the above theoretical considerations, we set up a specific test that was performed in December 14, 2021. The retained experimental parameters were:

- Thermal power  $\dot{Q}_p = 500$  W;
- Operating pressure  $P_G = 80$  mbar;
- Initial liquid temperature  $T_L(0) = 14.5^\circ\text{C}$ ;
- Initial pool level  $z_p(0) = 30$  cm;
- Initial content in dissolved oxygen  $C_{O_2}(0) = 7$  mg/L (value in excess at a pressure of 80 mbar).

In this test, we brought the liquid into its chemical and thermal metastability domains in a step-by-step way that allowed isolating the air-degassing-induced bubble growth process from its liquid vaporization counterpart. Those stages are detailed below:

- **Stage 1 (from 0 to 3 hrs):** The liquid pool was first depressurized by means of the vacuum pump down to 80 mbar. The pressure was then manually regulated by acting on the inlet valve of the pump. During that stage, the heaters were left off. The gases in dissolution within the liquid were hence in a chemical disequilibrium state with regards to the vessel's atmosphere. At a pressure of 80 mbar and a temperature of  $14.5^\circ\text{C}$ , the liquid was however subcooled (*i.e.* below its saturation temperature).
- **Stage 2 (from 3 to 7 hrs):** The heaters were then started and the liquid gradually heated up toward its saturation temperature. In the interval, while the liquid was still subcooled, the dissolved gases remained in a chemical disequilibrium state.
- **Stage 3 (from 7 to 7 hrs 40 min):** After reaching its saturation temperature, the liquid turned superheated.
- **Stage 4 (from 7 hrs 40 min to 9 hrs):** The heaters were shut down and the vessel was repressurized up to one atmosphere.

According to the above step-by-step procedure, the liquid was thus brought exclusively into its chemical metastability domain during Stages 1 and 2, and into both its chemical and thermal metastability ones during Stage 3. The obtained results are shown in Figure 3.28. First of all during Stage 1, as one can see from this figure, the liquid did not degas significantly, in spite of the large gases supersaturation imposed by the initial pressure drop from 1 bar to 80 mbar. Indeed, under these conditions and without any heat supply within the pool, the liquid may be considered at rest and the dissolved gases in excess can thus only escape from the liquid through the free surface by a purely diffusional process. Let us estimate the characteristic time  $\tau_{diff}$  of this diffusion. With  $S_p$  denoting the liquid free surface area, equal to  $0.135 \text{ m}^2$ , and  $\mathcal{D}_{a,w}^L$ , the dissolved air/water diffusivity coefficient, of the order of  $10^{-9} \text{ m}^2/\text{s}$ , one gets:

$$\tau_{diff} = \frac{S_p}{\mathcal{D}_{a,w}^L} \approx 1560 \text{ days}$$

which is an excessively long time period, thereby explaining the observed stable  $C_{O_2}$  value throughout Stage 1. During this same stage, some bubbles started to shyly nucleate onto the bottom wall surface. However, those bubbles were not seen growing significantly during the period and kept in place. When the heaters were started at the beginning of Stage 2, a natural convection flow developed within the liquid pool. With the liquid becoming agitated that way, the dissolved gases in excess started to escape toward the vessel's atmosphere with a significant and increasing kinetics, as visible in the third graph of Figure 3.28. The heated liquid started to evaporate too, through its free surface, as shown in the fifth graph of this figure providing the time-trend of the liquid mass  $m_L$ . The air bubbles attached to the bottom wall started to grow. Occasionally, some of them detached and rose up to the free surface, with however, no noticeable fast growth, contrarily to the observations discussed in Section 3.1.2. With the liquid being still subcooled, the degassing kinetics was relatively moderate. Indeed, the dissolved  $O_2$  concentration decreased only by about  $1.8 \text{ mg/L}$  during 4 hrs. Then, when the liquid became superheated, a clear and abrupt change occurred within the pool. At that moment, bubbles nucleated within the liquid and grew as explosively as for the reference test. This is illustrated in Figure 3.29 which is a photo taken during Stage 3. One can hence confidently state that the latter mode of bubble growth was the almost exclusive signature of flashing, in consistency with the above theoretical considerations.

Moreover, with more numerous and much bigger bubbles present in the liquid, the latter was expected to be more agitated [70] and there was a much larger available gas/liquid interfacial area for the degassing process. This is consistent with the observation of a sharper  $C_{O_2}$  drop over time during Stage 3 (*cf.* third graph of Figure 3.28). The liquid mass variation also increased significantly, revealing the same combined effect of a more agitated liquid and a bigger interfacial area for liquid vaporization.

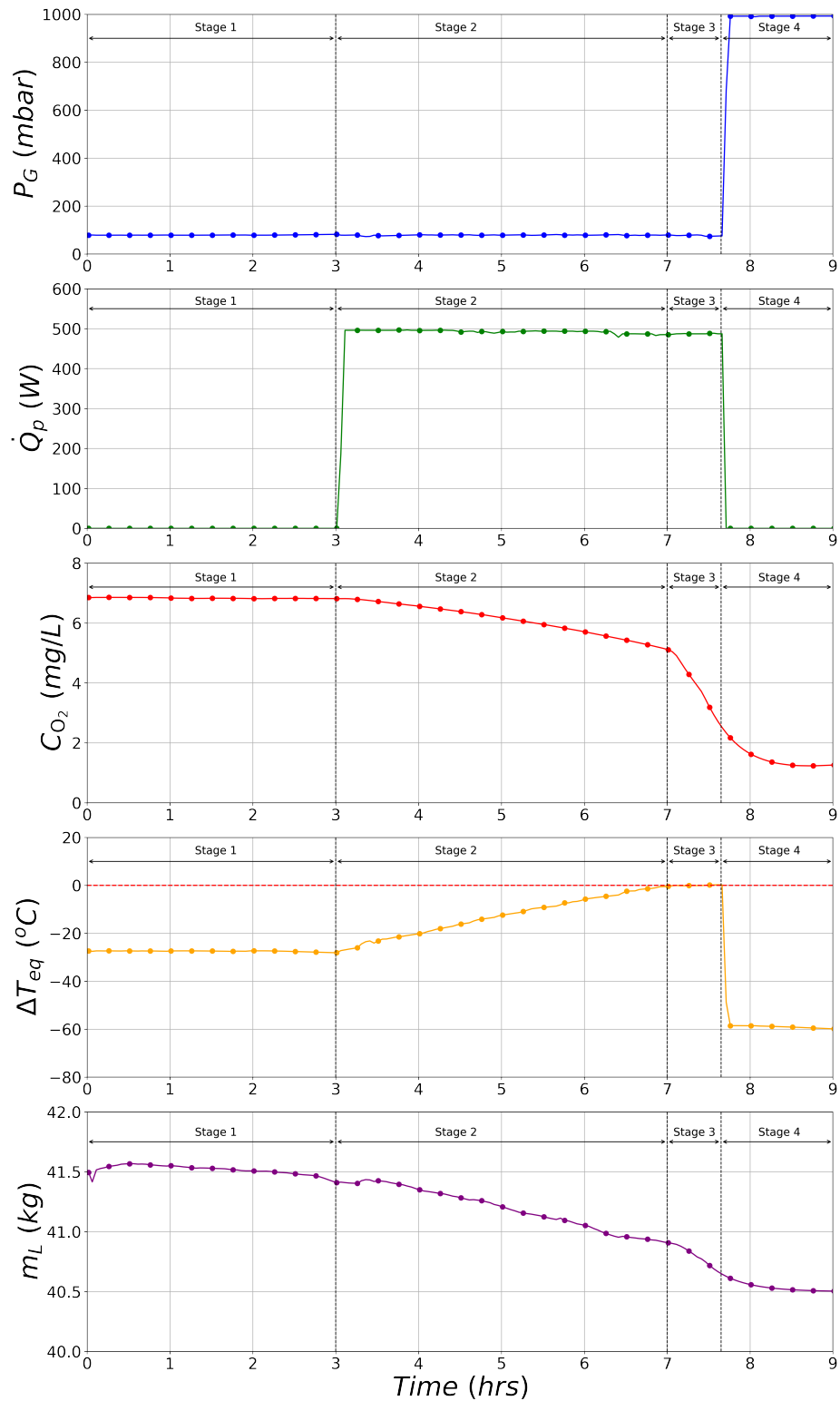


Figure 3.28: Main recorded physical parameters of the step-by-step test performed in December 14, 2021, in order to verify the predominance of the liquid vaporization mechanism in the observed fast bubble growth.



Figure 3.29: A photo taken during Stage 3 of the step-by-step test performed in December 14, 2021. The image shows the same kind of fast and sometimes explosive bubble growth as during the reference test.

### 3.3 Phenomenon sensitivity to heating, pressure, pool level and dissolved gases

#### 3.3.1 Variations of the heating power

In order to study the effect of the heating power on the phenomenon, a series of four tests was achieved. The characteristics of those tests are detailed in Table 3.3. One can remark that the latter were all initiated at identical values of  $P_G$ ,  $z_p(0)$  and  $C_{O_2}(0)$ , with the intent to separate the potential effects of those parameters from the one, expected, of the heating power.

Table 3.3: The series of tests achieved for investigating the effect of the heating power on the phenomenon.

Date of achievement	$\dot{Q}_p$ (W)	$P_G$ (mbar)	$z_p(0)$ (cm)	$C_{O_2}(0)$ (mg/L)
October 21, 2021	1000	22	30	6.5
January 14, 2022	750	22	30	6.5
January 7, 2022	500	22	30	6.5
November 10, 2021	250	22	30	6.5

Let us first study the thermodynamic evolution followed during those tests by the liquid pool. From the left-hand-side of Figure 3.30 representing the plot of the time-trends of  $\Delta T_{eq}$ , one can notice that the heating power had clearly a kinetic effect on the liquid superheating process. Indeed,  $\Delta T_{eq}$  tended faster toward its so-called asymptotic value, denoted as  $\Delta T_{eq;\infty}$ , when the power was large and vice versa. The observed value for  $\Delta T_{eq;\infty}$  did appear as an increasing function of the heating power: the bigger the heating power, the larger the final thermal metastability degree reached by the pool (*cf.* Figure 3.31). The heating power played the same role regarding the monitored  $O_2$  degassing kinetics, with  $C_{O_2}$  dropping faster when the power was large (*cf.* Figure 3.30, right-hand-side graph).

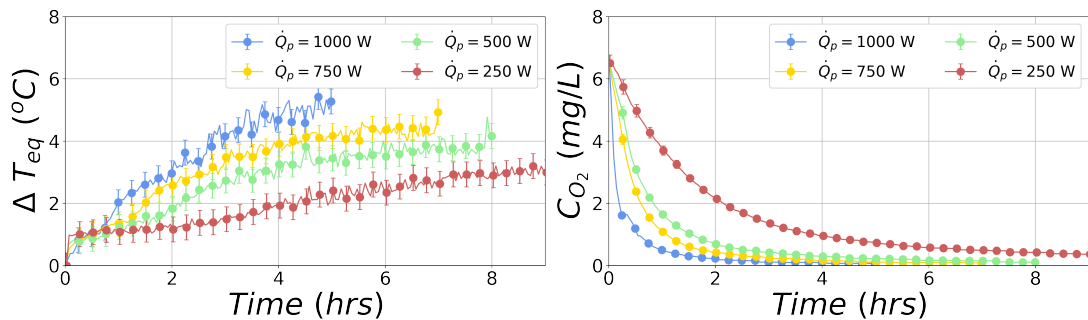


Figure 3.30: Sensitivity to heating power variations. Left: estimated liquid thermal metastability degree  $\Delta T_{eq}$ . Right: measured dissolved  $O_2$  mass concentration  $C_{O_2}$ .

Identically and as visible in Figure 3.32, the vaporization and degassing rates, respectively denoted as  $\dot{m}_L$  (left graph) and  $\dot{C}_{O_2}$  (right graph), were maximum at the

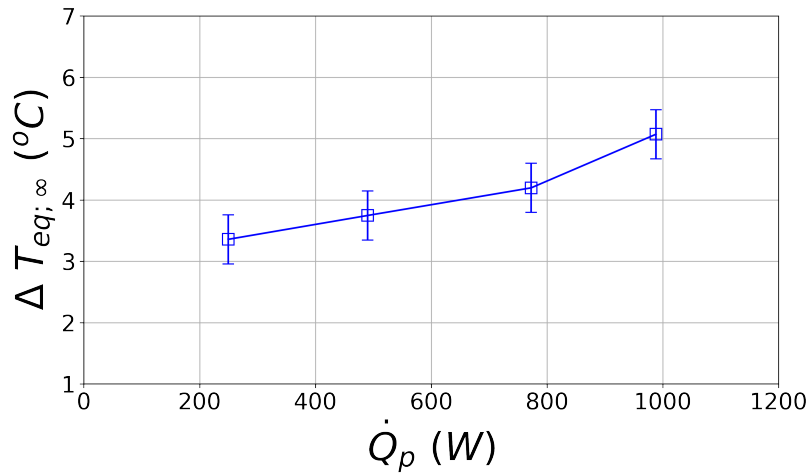


Figure 3.31: Sensitivity to heating power variations. Final or asymptotic value reached by the liquid thermal metastability degree  $\Delta T_{eq}$  as a function of the heating power.

largest heating power, with however, an opposite time variation. Indeed, if the vaporization intensified over time and ultimately stabilized, the degassing process gradually decreased according to the progressive liquid depletion in dissolved gases, here exhibited by the time-trend of  $C_{O_2}$  (*cf.* Figure 3.30, right-hand-side graph).

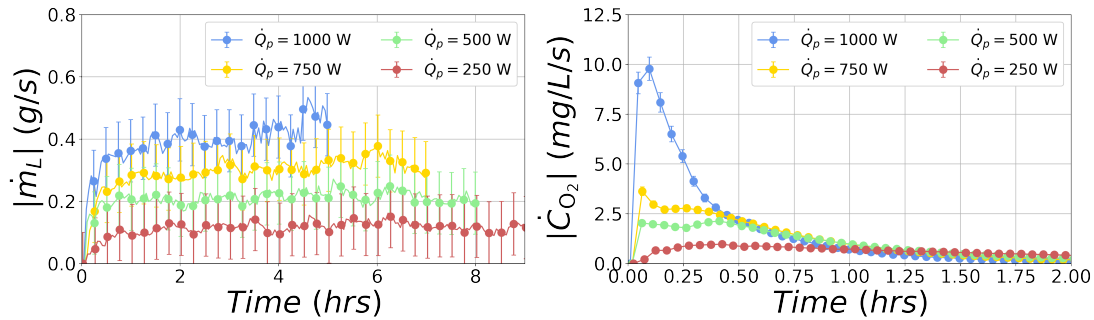


Figure 3.32: Sensitivity to heating power variations. Left: estimated liquid vaporization rate  $\dot{m}_L$ . Right: estimated oxygen degassing rate  $\dot{C}_{O_2}$ .

At last, when plotting the thermal metastability degree  $\Delta T_{eq}$  against the dissolved  $O_2$  concentration, as it has been done in Section 3.1.3, one can observe the same type of correlation than the one reported above. Singularly, the correlation seems dependent to the imposed heating power, since a slight shift appears between the individual correlations obtained for each  $\dot{Q}_p$ .

Next, the potential change in phenomenology induced by variations of the heating power is to be discussed. Overall, the phenomenology was reproduced whatever the retained heating power. Indeed, starting from thermal saturation conditions and an excess in dissolved gases, the liquid pool systematically gradually superheated and degassed, in a two-stage process as the one observed during the reference case (*cf.* Section 3.1.2, Figure 3.2): the pool was always subjected to a strong bubbling during the initial stage of the experiment. However, the duration of this bubbling was seen as being heating-

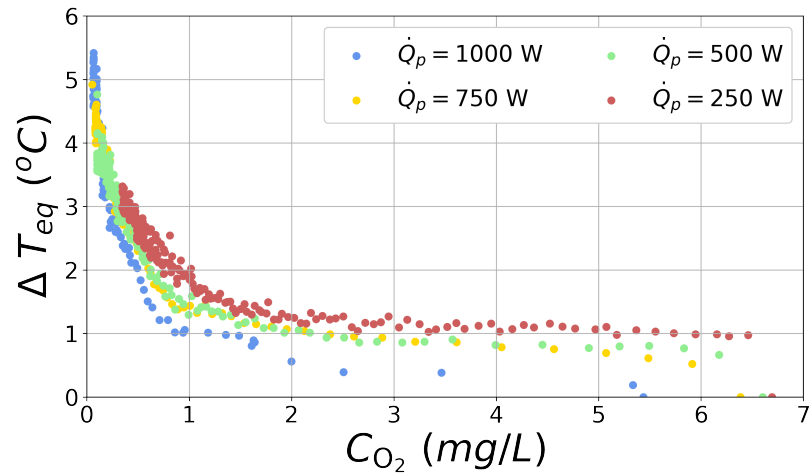


Figure 3.33: Sensitivity to heating power variations. Final or asymptotic value reached by the liquid thermal metastability degree  $\Delta T_{eq}$  as a function of the heating power.

power-dependent: the larger the heating power, the shorter the bubbling duration, and vice versa. Furthermore, if the bubble nucleation was mainly seen underneath the liquid free surface during all tests, the one conducted at a power of 250 W did not lead to the occurrence of an initial nucleation onto the heated bottom wall, contrarily to what was observed during the reference test (*cf.* Section 3.1.2, Figure 3.6). This is visible in Figure 3.34 giving the timeline of the first period of this very test, with a timing identical to the one considered in Figure 3.5. Finally, it is worth pointing out that none of those tests led to the occurrence of bubble nucleation onto the rough and unheated vessel's wall.

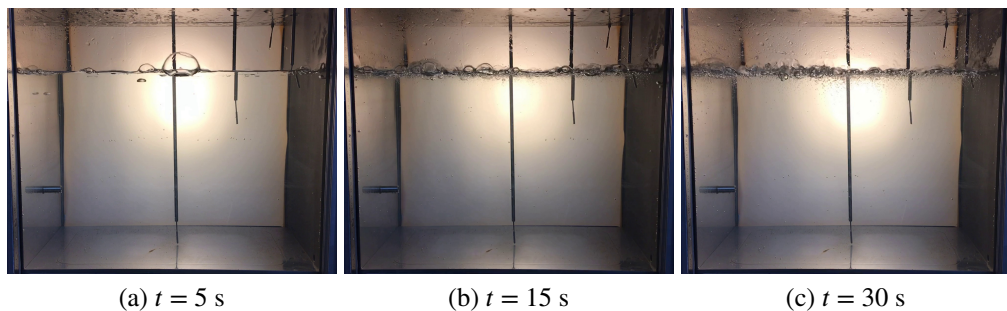


Figure 3.34: Timeline of the first period of the test conducted at a power of 250 W, a pressure of 22 mbar, an initial pool level of 30 cm and an initial dissolved  $O_2$  concentration of 6.5 mg/L. One can notice the absence of any bubble nucleation onto the heated bottom wall of the vessel.

### 3.3.2 Variations of the operating pressure

In order to study the effect of the operating pressure on the phenomenon, a series of twelve tests was achieved. The characteristics of those tests are detailed in Table 3.4.

Four values for  $\dot{Q}_p$  were retained *i.e.* 250, 500, 750 and 1000 W. However,  $z_p(0)$  and  $C_{O_2}(0)$  were respectively fixed to 30 cm and 6.5 mg/L. At last, three values for  $P_G$  complying with the experimental limitations of the Aquarius device were further considered: 22, 32 and 42 mbar.

Table 3.4: The series of tests achieved for investigating the effect of the operating pressure on the phenomenon.

Date of achievement	$\dot{Q}_p$ (W)	$P_G$ (mbar)	$z_p(0)$ (cm)	$C_{O_2}(0)$ (mg/L)
October 21, 2021	1000	22	30	6.5
February 14, 2022	1000	32	30	6.5
October 29, 2021	1000	42	30	6.5
January 14, 2022	750	22	30	6.5
February 15, 2022	750	32	30	6.5
January 26, 2022	750	42	30	6.5
January 7, 2022	500	22	30	6.5
February 16, 2022	500	32	30	6.5
February 3, 2022	500	42	30	6.5
November 10, 2021	250	22	30	6.5
February 17, 2022	250	32	30	6.5
November 19, 2021	250	42	30	6.5

In what follows, we study the thermodynamic evolution of the liquid pool throughout those tests, restricting to the upper and lower bounding values of the heating power, for more clarity (*i.e.* 250 and 1000 W). First of all, Figures 3.35 and 3.36 show the time-trends of  $\Delta T_{eq}$  and  $C_{O_2}$  at a respective heating power of 1000 and 250 W. One can notice that the chosen operating pressure does impact the kinetics of the liquid superheating and degassing processes, although this effect is much clearer at a low power of 250 W than at 1000 W. The graphs given in Figures 3.37 and 3.38, respectively associated with the tests conducted at a heating power of 1000 and 250 W, show the vaporization and degassing rates  $\dot{m}_L$  and  $\dot{C}_{O_2}$ . As one can figure out, the effect of the operating pressure is only visible for the degassing rate  $\dot{C}_{O_2}$ .

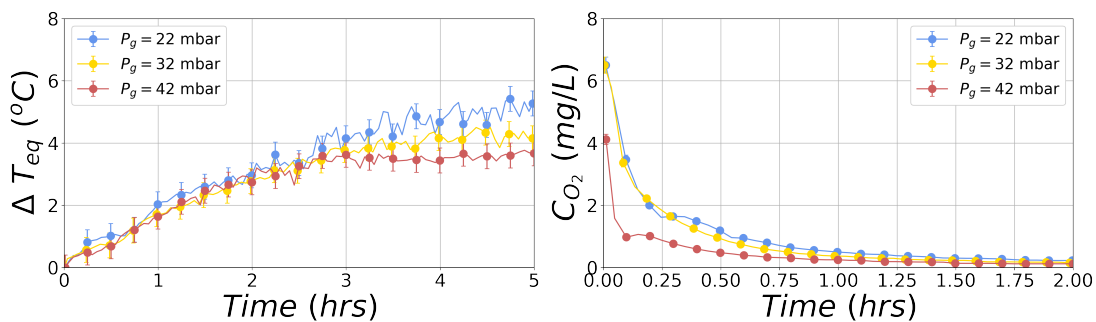


Figure 3.35: Sensitivity to operating pressure variations at a heating power of 1000 W. Left: estimated liquid thermal metastability degree  $\Delta T_{eq}$ . Right: measured dissolved  $O_2$  mass concentration  $C_{O_2}$ .

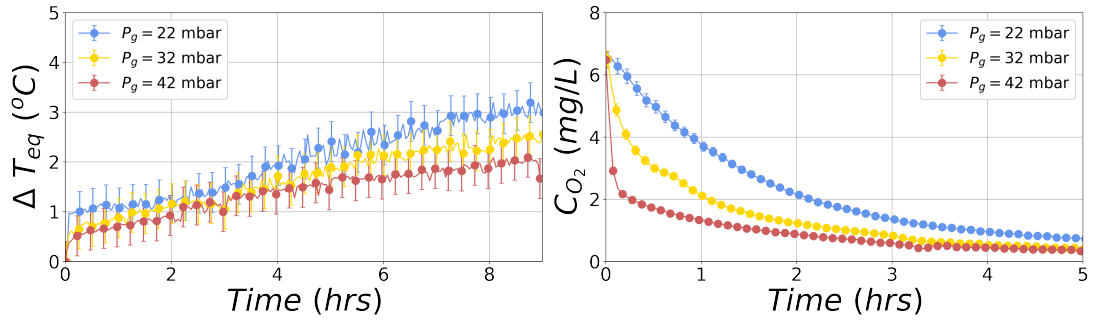


Figure 3.36: Sensitivity to operating pressure variations at a heating power of 250 W. Left: estimated liquid thermal metastability degree  $\Delta T_{eq}$ . Right: measured dissolved  $\text{O}_2$  mass concentration  $C_{\text{O}_2}$ .

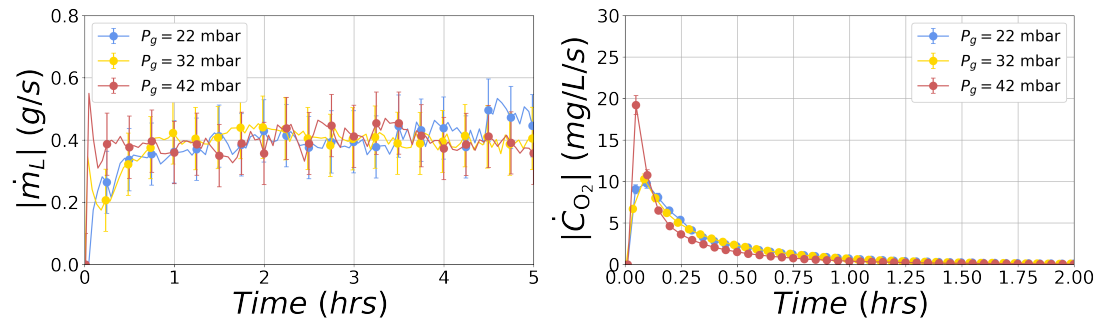


Figure 3.37: Sensitivity to operating pressure variations at a heating power of 1000 W. Left: estimated liquid vaporization rate  $\dot{m}_L$ . Right: estimated oxygen degassing rate  $\dot{C}_{\text{O}_2}$ .

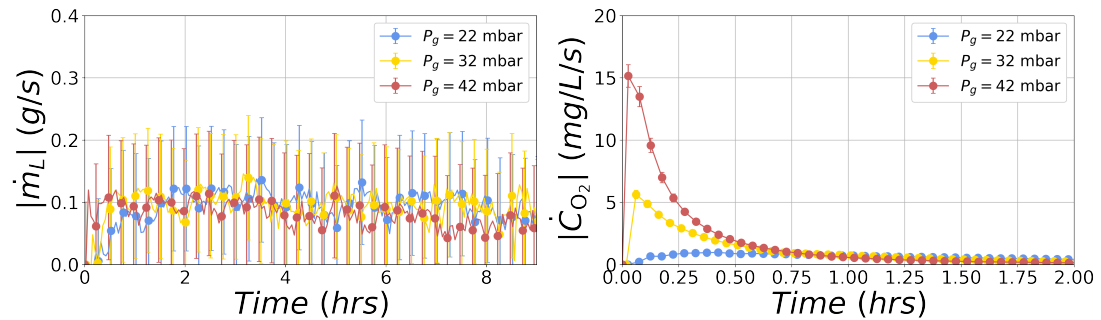


Figure 3.38: Sensitivity to operating pressure variations at a heating power of 250 W. Left: estimated liquid vaporization rate  $\dot{m}_L$ . Right: estimated oxygen degassing rate  $\dot{C}_{\text{O}_2}$ .

Next, in Figure 3.39 are reported the observed values for  $\Delta T_{eq;\infty}$  against the heating power, for the three considered operating pressure levels. First, the exercise shows the same positive dependence of  $\Delta T_{eq;\infty}$  to the heating power as the one highlighted in the previous section (*cf.* Figure 3.31). Second,  $\Delta T_{eq;\infty}$  seems to vary oppositely from an increase in operating pressure: the higher the operating pressure, the lower the final thermal metastability degree reached by the pool.

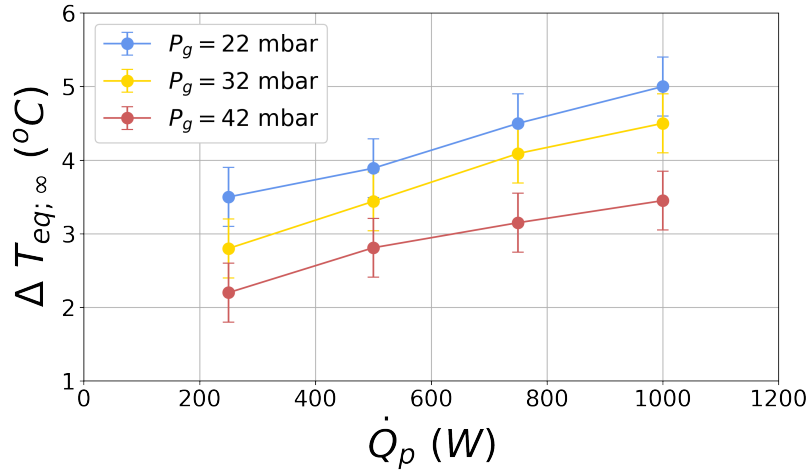


Figure 3.39: Sensitivity to operating pressure variations. Final or asymptotic value reached by the liquid thermal metastability degree  $\Delta T_{eq}$  as a function of the heating power, plotted for three distinct pressure levels: 22, 32 and 42 mbar.

In addition, when plotting the thermal metastability degree  $\Delta T_{eq}$  against the dissolved  $O_2$  concentration, as it has been done in Section 3.1.3, one can observe the same type of correlation than the one reported above. Singularly, the correlation seems dependent to the imposed operating pressure, since a clear shift appears between the individual correlations obtained for each retained pressure.

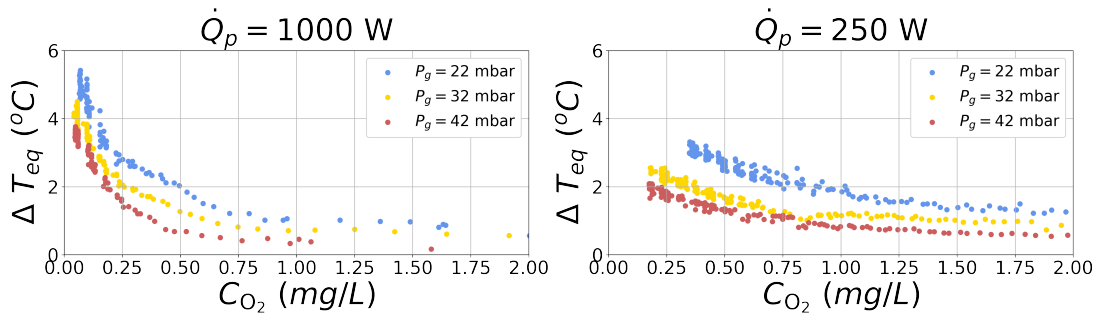


Figure 3.40: Sensitivity to operating pressure variations. Correlation between the variables reflecting the liquid degassing and heat-up kinetics,  $C_{O_2}$  and  $\Delta T_{eq}$ . Left: heating power of 1000 W. Right: heating power of 250 W.

Next, we discuss in what follows the potential change in phenomenology induced by variations of the operating pressure. Overall, the phenomenology was reproduced whatever the retained operating pressure, within the range 22 - 42 mbar. Indeed, starting from thermal saturation conditions and an excess in dissolved gases, the liquid pool systematically superheated and degassed, in a two-stage process as the one observed during the reference case (*cf.* Section 3.1.2, Figure 3.2): the pool was always subjected to a strong bubbling during the initial stage of the experiment. This is for instance visible in Figure 3.41, which is a photo taken during the first minute of the test conducted at a power of 1000 W and a pressure of 42 mbar. However, the duration of this bubbling was seen as being operating-pressure-dependent: the larger the operating pressure, the

shorter the bubbling duration, and vice versa. Finally, it is worth pointing out that none of those tests led to the occurrence of bubble nucleation onto the rough and unheated vessel's wall.



Figure 3.41: A photo taken during the first minute of the test conducted at a power of 1000 W and a pressure of 42 mbar, exhibiting some strong bubble flashing underneath the liquid free surface. One can notice that at the time of the photo, the bubble nucleation has ceased onto the heated bottom wall of the vessel.

### 3.3.3 Variations of the initial pool level

The effect of a variation of the initial pool level is then explored. For doing so, let us consider a series of two tests performed at an operating pressure of 22 mbar, an initial mass concentration in dissolved  $O_2$  of 6.5 mg/L and two distinct values for the initial pool level: 20 and 30 cm. A heating power of 250 W was chosen for conducting those tests. Indeed, in the previous sections, it has been shown that this low power yields a longer bubbling stage when compared with its high-powered counterpart. Thus, it seems beneficial to retain such a low power for exhibiting with ease the effect induced by a differing initial pool level, if there exists any. The parameters of the studied tests are summarized in Table 3.5.

Table 3.5: The series of tests achieved for investigating the effect of the initial pool level on the phenomenon.

Date of achievement	$\dot{Q}_p$ (W)	$P_G$ (mbar)	$z_p(0)$ (cm)	$C_{O_2}(0)$ (mg/L)
November 10, 2021	250	22	30	6.5
November 16, 2021	250	22	20	6.5

The obtained results are successively plotted in Figures 3.42-3.44. First of all, from the left-hand-side of Figure 3.42 representing the time-trend of  $\Delta T_{eq}$ , one can notice that the initial pool level had a very slight effect on the liquid superheating kinetics. Indeed,  $\Delta T_{eq}$  tended a little bit faster toward its so-called asymptotic value, denoted as  $\Delta T_{eq;\infty}$ , when the initial pool level was low and vice versa. However, initial differences in pool level did not lead to differences in the observed asymptotic values  $\Delta T_{eq;\infty}$ . The initial pool level played the same role regarding the monitored  $O_2$  degassing kinetics, with  $C_{O_2}$  dropping faster when the latter was fixed at a low value (*cf.* Figure 3.42, right-hand-side graph). It is worth pointing out that those differences are much clearer from the side of the degassing process.

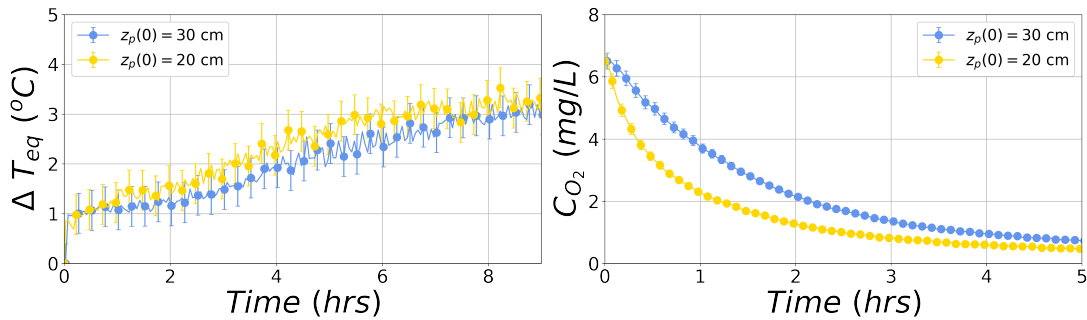


Figure 3.42: Sensitivity to the initial pool level, at a heating power of 250 W. Left: estimated liquid thermal metastability degree  $\Delta T_{eq}$ . Right: measured dissolved  $O_2$  mass concentration  $C_{O_2}$ .

The same effect is obviously noticeable from the right-hand-side graph of Figure 3.43, showing  $\dot{C}_{O_2}$ , the dissolved  $O_2$  degassing rate. But as for the operating pressure, the initial pool level had no impact on the time-trend of the liquid vaporization rate  $\dot{m}_L$ , plotted in the left-hand-side of this same figure. The correlation between the thermal metastability degree  $\Delta T_{eq}$  and the dissolved  $O_2$  concentration  $C_{O_2}$ , plotted in Figure 3.44 appears insensitive to the initial pool level, as one can observe.

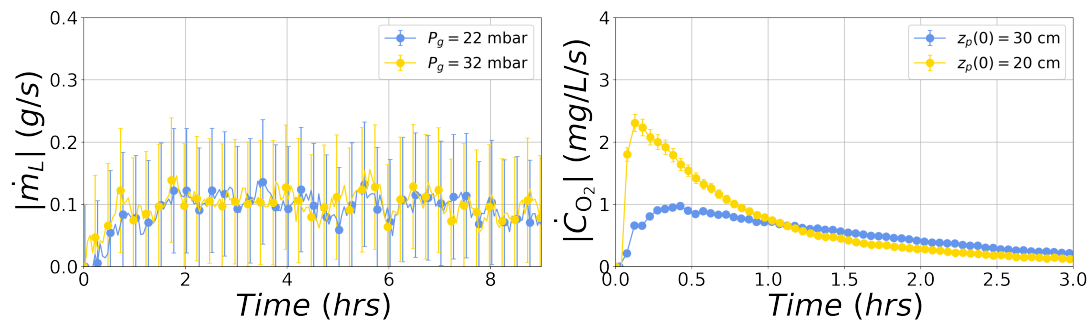


Figure 3.43: Sensitivity to the initial pool level, at a heating power of 250 W. Left: estimated liquid vaporization rate  $\dot{m}_L$ . Right: estimated oxygen degassing rate  $\dot{C}_{O_2}$ .

Phenomenologically, the observations done at a low initial pool level of 20 cm were similar to the ones presented in the previous section for a level of 30 cm, a pressure of 22 mbar and a power of 250W. Interestingly, in spite of the reduced hydrostatic pressure

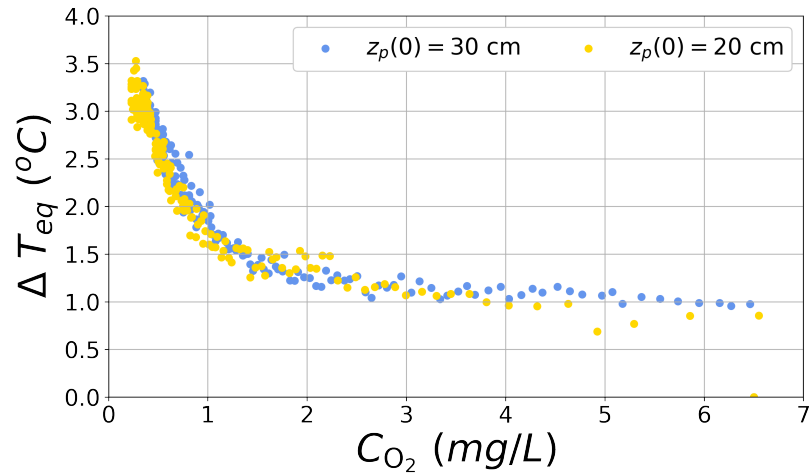


Figure 3.44: Sensitivity to the initial pool level, at a heating power of 250 W. Correlation between the variables reflecting the liquid degassing and heat-up kinetics,  $C_{O_2}$  and  $\Delta T_{eq}$ .

head when the level was set to 20 cm, the gravity-driven flashing was still observed underneath the liquid free surface, as one can see from Figure 3.46. Furthermore, no bubble nucleation was identified onto the heated bottom wall of the vessel, as one can observe from the timeline given in Figure 3.45. It is also worth pointing out that the bubbling stage duration was shorter at a low initial pool level. Finally, we are to mention that during this test, there was no occurrence of bubble nucleation onto the rough and unheated vessel's wall too.

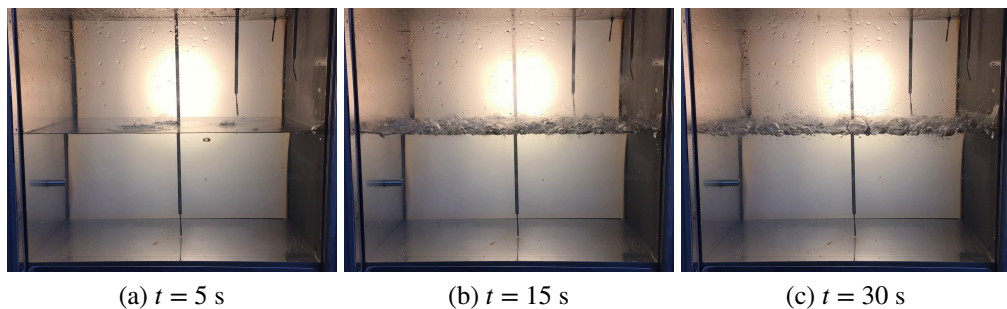


Figure 3.45: Timeline of the first period of the test conducted at a power of 250 W, a pressure of 22 mbar, an initial pool level of 20 cm and an initial dissolved  $O_2$  concentration of 6.5 mg/L. One can notice the absence of any bubble nucleation onto the heated bottom wall of the vessel.

Keeping in mind those results, one may wonder what is the intensity of the bubble nucleation onto the heated bottom wall when observed, in case of a reduced initial pool level of 20 cm. In order to address this question, we made some photographical observations during a dedicated test performed at a heating power of 1000 W, which was expected to yield some bubble nucleation onto the bottom wall. Those observations are illustrated in the following Figures 3.47 and 3.48. Comparing those observations



Figure 3.46: A photo taken 3 min after the beginning of the test conducted at a power of 250 W, a pressure of 22 mbar, an initial dissolved  $O_2$  concentration of 6.5 mg/L and an initial pool level of 20 cm, exhibiting some strong flashing underneath the liquid free surface.

with the ones made for the reference test (*cf.* Section 3.1.2), one can figure out the increased intensity of the bubble nucleation and growth processes when the initial pool level was fixed to a reduced value of 20 cm.

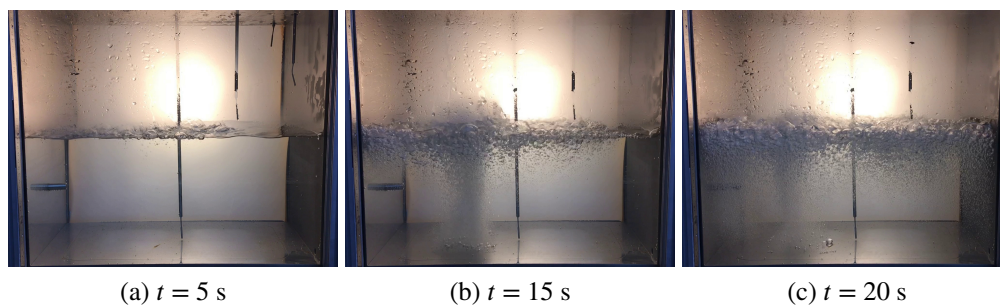


Figure 3.47: Timeline of the first period of the test conducted at a power of 250 W, a pressure of 22 mbar, an initial pool level of 20 cm and an initial dissolved  $O_2$  concentration of 6.5 mg/L. One can notice the absence of any bubble nucleation onto the heated bottom wall of the vessel.



Figure 3.48: A photo taken 10 s after the beginning of the test conducted at a power of 1000 W, a pressure of 22 mbar, an initial dissolved  $O_2$  concentration of 6.5 mg/L and an initial pool level of 20 cm, exhibiting some strong flashing underneath the liquid free surface and a not less intensive bubble nucleation onto the vessel's heated bottom wall.

### 3.3.4 The key role played by the presence of dissolved gases

At last, we discuss the phenomenon sensitivity to the initial content in dissolved gases on the basis of the series of tests described in the below Table 3.6.

Table 3.6: The series of tests achieved for investigating the effect of the initial content in dissolved gases on the phenomenon.

Date of achievement	$\dot{Q}_p$ (W)	$P_G$ (mbar)	$z_p(0)$ (cm)	$C_{O_2}(0)$ (mg/L)
October 21, 2021	1000	22	30	6.5
November 22, 2021	1000	22	30	1.25
October 26, 2021	1000	22	30	0.15
November 10, 2021	250	22	30	6.5
November 15, 2021	250	22	30	1.25
November 9, 2021	250	22	30	0.15

In Figure 3.49, we first show the time-trend of  $\Delta T_{eq}$  obtained for the three selected initial dissolved  $O_2$  concentrations, 6.5, 1.25 and 0.15 mg/L, respectively at a heating power of 250 (left graph) and 1000 W (right graph). For each case, a similar increase of the thermal metastability degree till an asymptotic value was observed. But interestingly, for a same power, the kinetics of this increase was clearly affected by the initial content in dissolved gases, with differences spanning over several hours. Having in mind the sensitivities to the operating pressure and to the initial pool level that have

been previously highlighted, one can state that the initial content in dissolved gases is the major parameter governing the superheating kinetics, for a given heating power. Further on, this effect was more significant at the lowest investigated heating power in the present test series, in consistency with what has been evidenced in the two previous sections. Interestingly, the value of the asymptotic metastability degree was insensitive to the initial content in dissolved gases and solely depended on the imposed heating power, as exhibited in Figure 3.49. In a similar way, we exhibit the time-trend of  $C_{O_2}$  in Figure 3.50. It is worth noting that the  $O_2$  degassing kinetics depended on the initial amount of dissolved gases, as one may expect. Indeed, at a given operating pressure, the larger the initial  $C_{O_2}$ , the higher the initial dissolved  $O_2$  chemical disequilibrium, and hence, the faster the corresponding degassing kinetics. In consistency with these observations, one can note from Figure 3.51 that the correlation between  $\Delta T_{eq}$  and  $C_{O_2}$ , first presented in Section 3.1.3, appears insensitive to the initial amount of  $O_2$  dissolved in the liquid. One has to note that in this figure, the cases with an initial concentration of 0.15 mg/L are however not represented since the above two variables are no longer correlated when the depletion in dissolved  $O_2$  is almost completed.

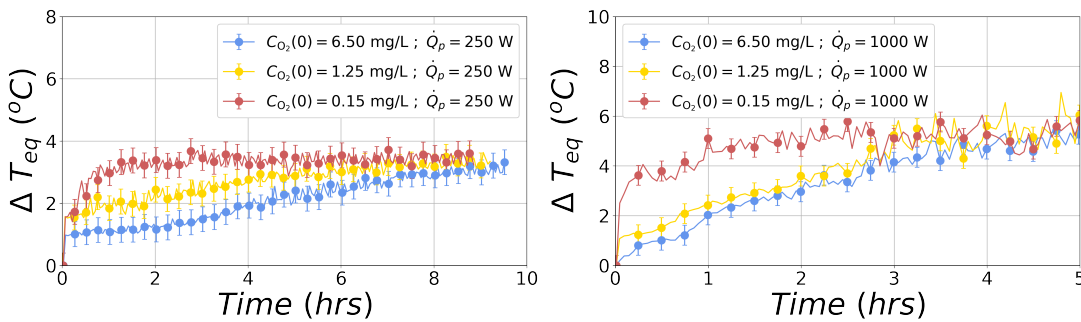


Figure 3.49: Sensitivity to the initial content in dissolved gases. Estimated liquid thermal metastability degree  $\Delta T_{eq}$ . Left: heating power of 250 W. Right: heating power of 1000 W.

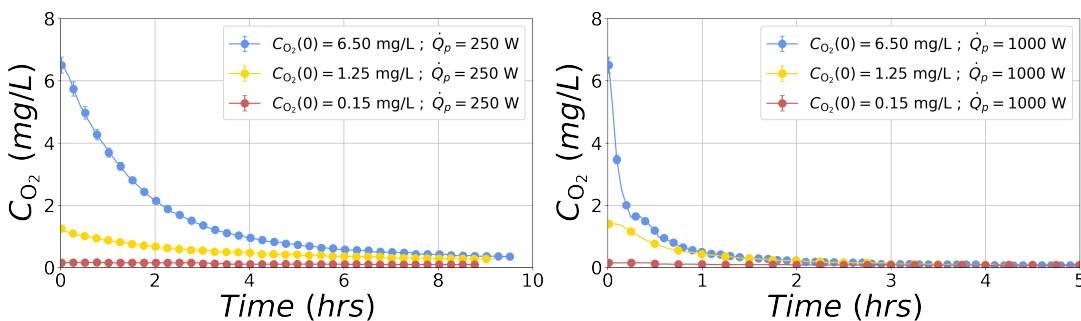


Figure 3.50: Sensitivity to the initial content in dissolved gases. Measured dissolved  $O_2$  mass concentration  $C_{O_2}$ . Left: heating power of 250 W. Right: heating power of 1000 W.

Moreover, the photographic observations achieved during those tests highlighted some significant features of the sensitivity to dissolved gases. Indeed, starting a test

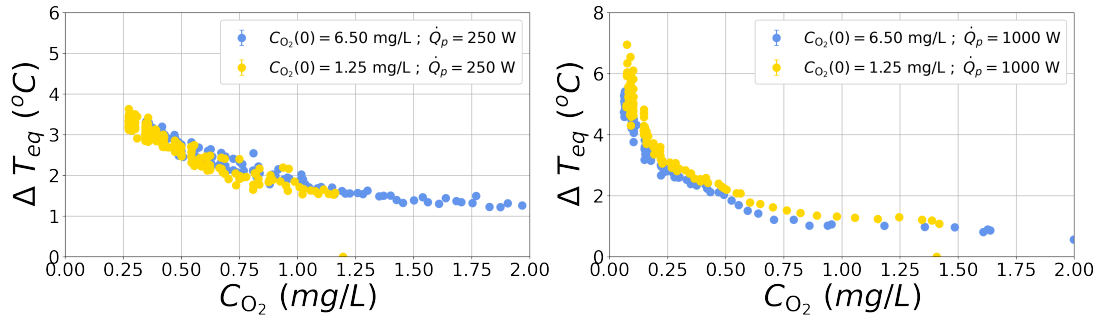


Figure 3.51: Sensitivity to the initial content in dissolved gases. Correlation between  $\Delta T_{eq}$  and  $C_{O_2}$ . Left: heating power of 250 W. Right: heating power of 1000 W.

with water at thermal saturation but with less dissolved gases, with an  $O_2$  concentration  $C_{O_2}(0) = 1.25$  mg/L, clearly led to a weaker and shorter bubble production stage. In the extreme case of  $C_{O_2}(0) = 0.15$  mg/L, no bubbling was observed at all in the pool, apart from sporadic events such as the ones described in Section 3.1.2, during the single-phase stage of the reference test. This situation is exhibited in Figure 3.52, showing a set of photos taken at the beginning of the two tests conducted at a heating power of 1000 W, an operating pressure of 22 mbar, an initial pool level of 30 cm but two different initial dissolved  $O_2$  concentrations: 6.5 and 0.15 mg/L.

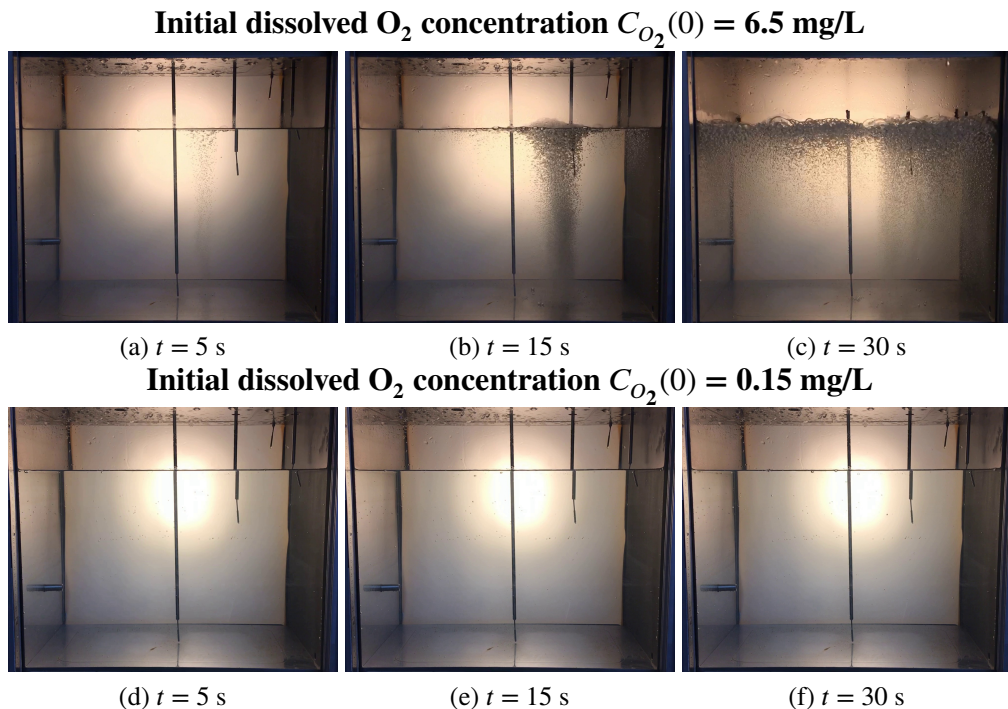


Figure 3.52: Timeline of the first period of the tests conducted at a power of 1000 W, a pressure of 22 mbar, an initial pool level of 30 cm but two different initial dissolved  $O_2$  concentrations: 6.5 and 0.15 mg/L. One can notice the absence of any bubble nucleation process in the pool and onto the vessel's walls when the liquid is initially highly depleted in dissolved gases.

This observation is also consistent with the time-trends of  $\Delta T_{eq}$  given in Figure 3.49. Indeed, with fewer bubbles in presence in the liquid, the latter could not easily flash as a way to reach a stable thermodynamic equilibrium and its superheating kinetics was less temperate. Hence, the point from which the temperature difference between the liquid and its free surface was enough to compensate the heating power by the only free surface evaporation was reached earlier, thereby leading to a faster stabilization of the liquid superheat around  $\Delta T_{eq;\infty}$ .

### 3.3.5 Summary of the highlighted phenomenon's sensitivity

In this section we provide a brief summary of the phenomenon's sensitivities that have been highlighted above. Those sensitivities are described in what follows:

- **All control parameters trigger the degassing and superheating kinetics:** Those kinetics strongly depended on the heating power  $\dot{Q}_p$ , the operating pressure  $P_G$  and initial content in dissolved oxygen  $C_{O_2}(0)$  and slightly depended on the initial pool level  $z_p(0)$ , during the presented tests;
- **Confirmation of the existence of a  $C_{O_2}$  threshold from which no bubbling is observed, in spite of the liquid superheating:** when the test started from a highly depleted state in dissolved gases ( $C_{O_2}(0) = 0.15\text{mg/L}$ ), the liquid metastability degree reached faster its asymptotic value  $\Delta T_{eq;\infty}$  from which the free surface evaporation could fully compensate the heat supply, with no observable bubbling;
- **Two parameters govern the asymptotic value  $\Delta T_{eq;\infty}$ :** The latter variable appeared highly sensitive to the heating power  $\dot{Q}_p$  and operating pressure  $P_G$ ; the initial water level  $z_p(0)$  seemed to play no role at all.

## 3.4 The nucleation forcing mechanisms

In this last section, we give an overview of some additional tests that were conducted with the intent to force the bubble nucleation processes in a specific location within the liquid pool. This was achieved by varying the experimental procedure and/or setup. As it will be detailed, those mechanisms highlighted some more features of the phenomenon that are worth being mentioned.

### 3.4.1 The liquid bulk nucleation in a pool with a localized heat source

Unless indicated, all the tests presented in this thesis were conducted with a so-called homogeneous heat source. In details, this means that the two resistive heaters equipping the Aquarius device were systematically utilized conjointly. But the device offers the

possibility to operate them independently and one may wonder what would be the corresponding effect on the phenomenon. In order to address this question, we conducted a series of two tests, that are described in Table 3.7. One can note that those tests were achieved at a heating power of 250 W, in order to maximize the chance to observe an effect of the localized heat source, if there exists any. Indeed, at such a low power, we have already noticed in the previous sections that the superheating and degassing kinetics are sufficiently slow for yielding a sensible bubbling stage duration. Moreover, each resistive heater being sized for supporting a maximum 500 W (*cf.* Chapter 2), one cannot achieve tests with a localized heat power bigger than 500 W and fixing the latter to 250 W complies with this technical limitation.

Table 3.7: The series of tests achieved for investigating the effect of a localized heat source on the phenomenon.

Date of achievement	$\dot{Q}_p$ (W)	$P_G$ (mbar)	$z_p(0)$ (cm)	$C_{O_2}(0)$ (mg/L)	Heat source distribution
December 8, 2021	250	22	30	9.5	Homogeneous
December 9, 2021	250	22	30	9.5	Localized (right-side)

Let us focus on the phenomenological features of those tests. The latter are illustrated in Figure 3.53, representing two photos each taken 1 min after the beginning of the studied tests. First of all, as one can see, the test conducted with a localized heating did not lead to bubble nucleation onto the heated surface, in spite of the doubled heat flux at this very place. Remarkably, in the present case, one can observe that the flashing, usually appearing underneath the liquid free surface, was restricted to the area of the latter which was right on top of the heat source. Hence, there is a clear impact of the heat source spatial distribution on the bubble nucleation processes and one may thus wonder if this impact may be observed too with regards to the main thermodynamic parameters characterizing the pool. Let us investigate it next.

In Figure 3.54 are first shown the temperature records performed within the heated wall for both tests. A wide temperature difference of approximately 8°C was observed between the left and right sides of the bottom wall when the heat source was localized, whereas for the homogeneous case there was no noticeable temperature difference, as expected. When looking at the fluid temperatures for the localized heating case, the differences are less significant between the sensors located underneath the free surface, being of the order of 0.5°C (*cf.* Figure 3.55).

Interestingly, the thermodynamic parameters that have been shown relevant for describing the studied experiments in Section 3.1.3 did not differ from each other, whatever the retained spatial distribution of the heat source (*cf.* Figures 3.56-3.58).

It is worth noting that the same observation has been done within the so-called MIDI facility, designed by the present author [81] and operated at IRSN for studying the phenomenon, in the frame of the IRSN's DENOPI project on spent-fuel-pool accidents [83]. The latter is briefly described and compared to the Aquarius device in Figure 3.59. It is a similar small-scale basin, heated from below, reproducing the main features of a spent-fuel-pool. MIDI is however of larger dimensions, operated under at-

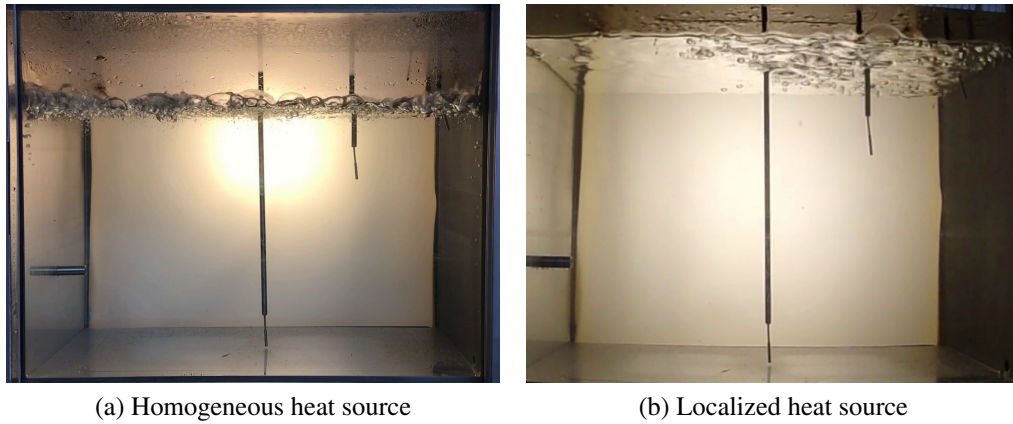


Figure 3.53: Two photos taken at time  $t = 1$  min after the beginning of two tests conducted for studying the effect of a localized heat source on the phenomenon. One can notice that in the case of a localized heating, the flashing, usually appearing underneath the liquid free surface, is restricted to the area of the latter which is right on top of the heat source.

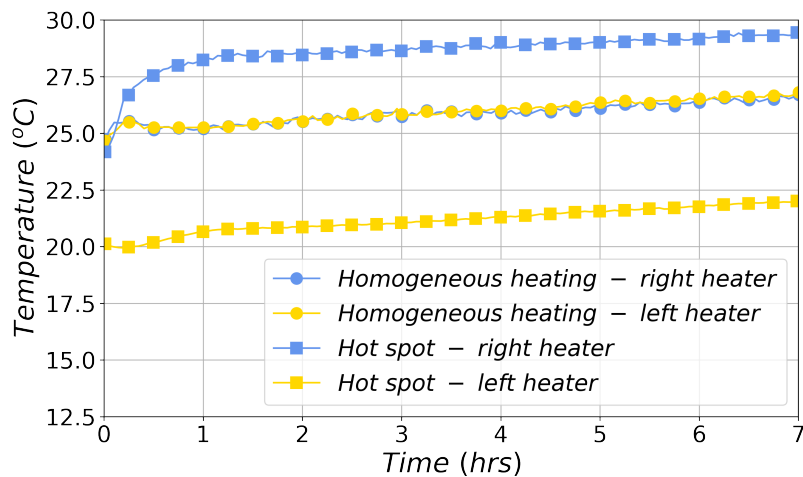


Figure 3.54: Effect of a localized heat source on the phenomenon, at a heating power of 250 W. Temperature records performed within the heated wall over time. One can notice the wide temperature difference between the left and right sides of the bottom wall when the latter is differentially heated.

mospheric pressure and is equipped with a more realistic heat source with regards to the specificities of the spent nuclear fuel storage [85]. In a similar fashion, when locating the heat source in a specific area of the MIDI's pool, we observed a localized bubble nucleation occurrence, as the one depicted for Aquarius, in the right-hand-side of Figure 3.53. But, as for the results shown above, the main thermodynamic parameters of the MIDI's pool did not show much differences [82]. This intriguing observation is worth being further investigated, which constitutes a potential perspective of the present work.

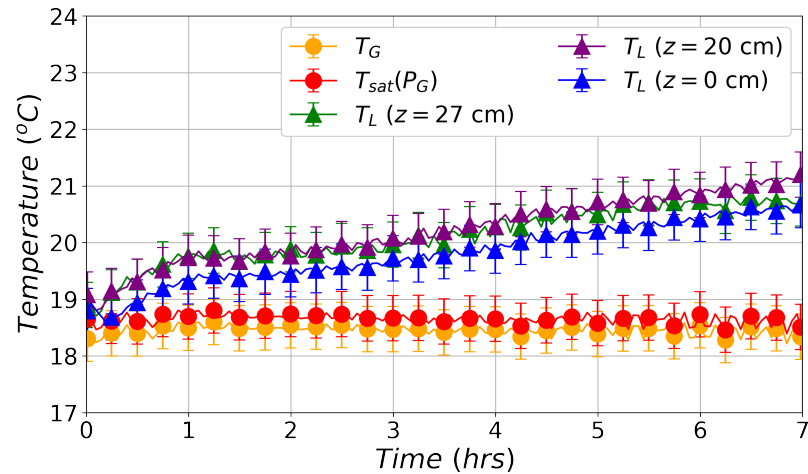


Figure 3.55: Effect of a localized heat source on the phenomenon, at a heating power of 250 W. Measured fluid temperatures (the heights  $z$  mentioned in the legend for each liquid measurement  $T_L$  correspond to the sensor location, with  $z = 0$  being the location of the pool bottom surface).

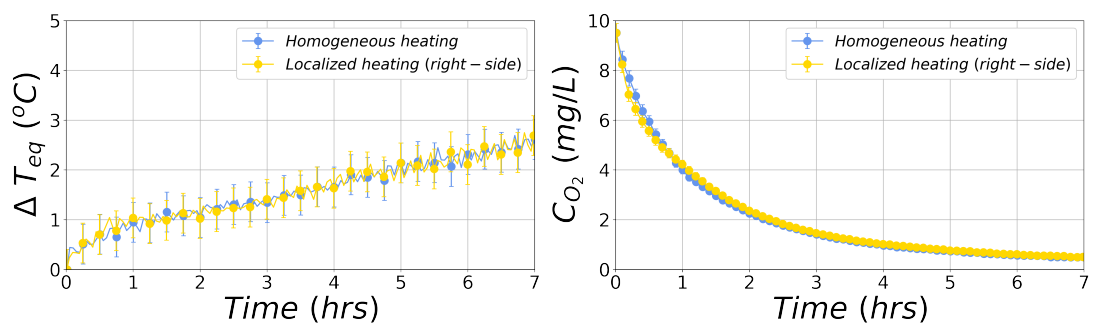


Figure 3.56: Effect of a localized heat source on the phenomenon, at a heating power of 250 W. Left: estimated liquid thermal metastability degree  $\Delta T_{eq}$ . Right: measured dissolved  $O_2$  mass concentration  $C_{O_2}$ .

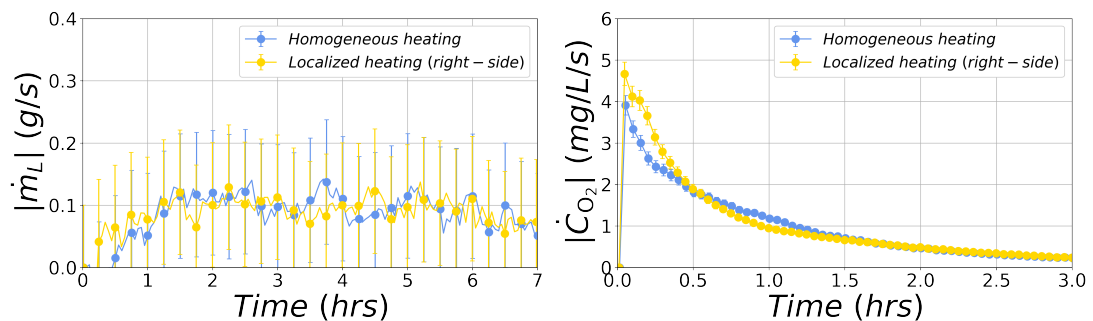


Figure 3.57: Effect of a localized heat source on the phenomenon, at a heating power of 250 W. Left: estimated liquid vaporization rate  $\dot{m}_L$ . Right: estimated oxygen degassing rate  $\dot{C}_{O_2}$ .

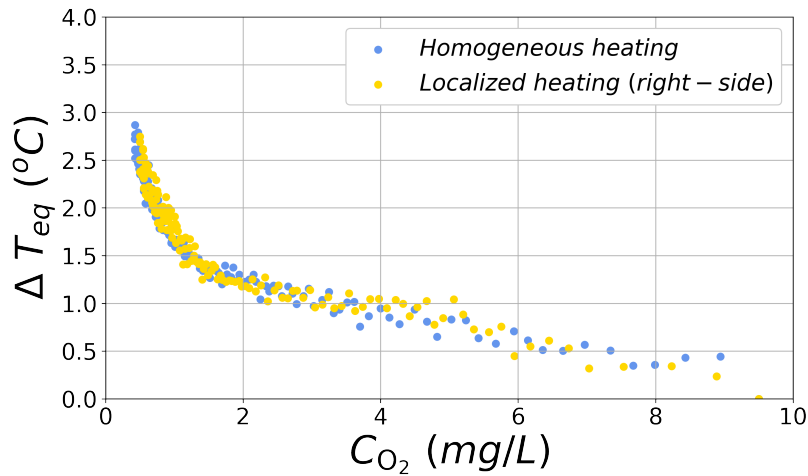


Figure 3.58: Effect of a localized heat source on the phenomenon, at a heating power of 250 W. Correlation between the variables reflecting the liquid degassing and heat-up kinetics,  $C_{O_2}$  and  $\Delta T_{eq}$ .

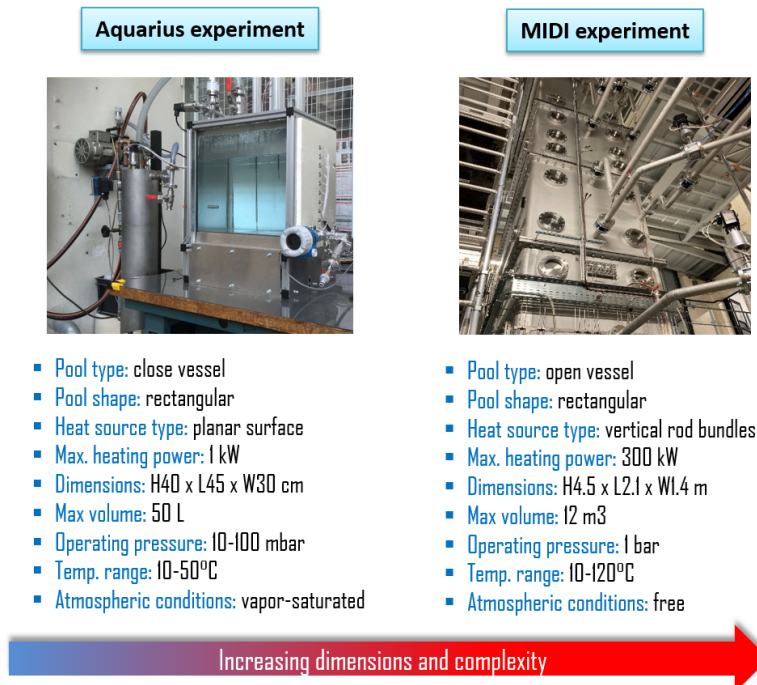


Figure 3.59: A technical comparison between the MIDI and Aquarius similar experimental devices, both designed by the present author and operated at IRSN Cadarache.

### 3.4.2 The liquid bulk nucleation within an inclined pool vessel

An effect identical to the one evidenced by the test conducted with a localized heating was highlighted, by inclining the vessel from the horizontal plane by about 5°. The obtained results are visible in Figure 3.60.

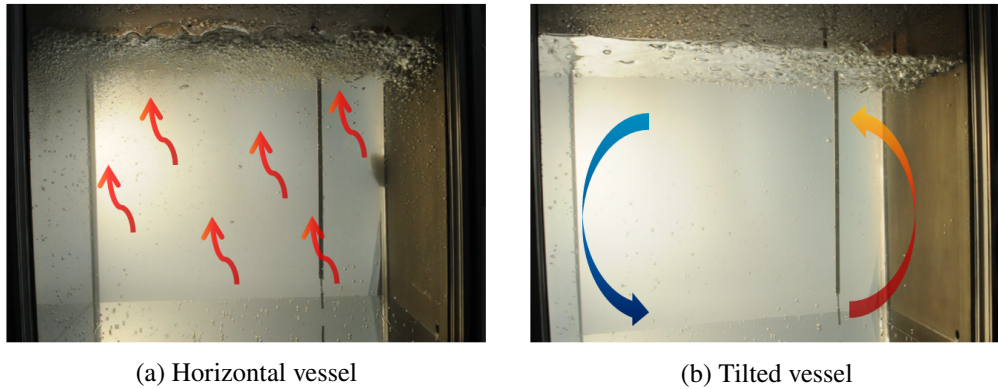


Figure 3.60: The angular orientation of the vessel influences the natural convection of heat within the liquid bulk, thereby affecting the phenomenon. Left: No discernible macro-circulation, a uniform flashing is observed below the free surface. Right: A macro-circulation is forced from left to right by inclining the test device, the flashing takes place mainly where the liquid uprises. Photos taken by *M. Duponcheel*.

This latter setup is understood as resulting in a forcing of the natural convection flows developing in the pool, in consistency with numerous reports done in the thermal-hydraulic literature for decades [97]. With this achieved forcing, higher temperatures and thus a higher superheating might be reached on top of the uprising hot water. In doing so, more flashing would be expected at that very location, in agreement with the observation. As a perspective of the present thesis, it could be interesting to further investigate this effect, taking benefit from advanced flow visualization techniques and 3D numerical simulations.

### 3.4.3 The nucleation onto the unheated rough wall

A last nucleation forcing effect was investigated: the bubble formation onto the unheated rough wall of the pool, a process that was never observed during all the sensitivity tests performed in the frame of this study, as largely mentioned in Section 3.3. This effect is detailed in what follows. In order to force this nucleation process onto the same surface, we proceeded to a partial dry out of the rough wall prior to the launch of a test, with the intent to entrap some air into the wall's crevices when refilling the vessel with water. Only 13 cm of this wall kept underwater, thereby ensuring that the dissolved  $O_2$  sensor did not uncover at all during this preparatory stage. The dry out was obtained by blowing some air stream onto the wall. In doing so, the wall was visibly dry after about 2 hrs and the vessel was then filled with fresh water, up to a pool level of 30 cm. After that wall preparation, some air was then bubbled through the liquid till a

dissolved  $O_2$  concentration of 9.5 mg/L was reached. Next, the liquid was heated up, till a temperature of 19°C, yielding an operating pressure of 22 mbar once imposing some vacuum in the vessel. The experimental parameters of this test are given in Table 3.8, together with those of another test performed in the same conditions but with no prior wall preparation and hence, no nucleation forcing, for further comparisons.

Table 3.8: The series of tests achieved for investigating the effect of a forcing of bubble nucleation onto the unheated rough wall on the phenomenon.

Date of achievement	$\dot{Q}_p$ (W)	$P_G$ (mbar)	$z_p(0)$ (cm)	$C_{O_2}(0)$ (mg/L)	Prior wall preparation
December 8, 2021	250	22	30	9.5	No
December 6, 2021	250	22	30	9.5	Yes

At first, we are to mention that right after the pool depressurization, many bubbles appeared onto the unheated rough wall of the vessel, as visible in Figure 3.61. This observation fully validates the retained forcing experimental procedure. The lowest position of the wall that was previously dried out is clearly visible in this figure: it corresponds to the level from which bubbles are no longer observed.



Figure 3.61: A study of the forcing of bubble nucleation onto the unheated rough wall of the vessel. Photo taken right after the beginning of the test conducted at a power of 250 W, a pressure of 22 mbar, an initial dissolved  $O_2$  concentration of 9.5 mg/L, an initial pool level of 30 cm and a prior dry out of the unheated rough wall. Numerous bubbles are visible, thereby validating the retained forcing experimental procedure.

Phenomenologically, we observed a combination of bubble nucleation in the liquid bulk, as usual for a test at a power of 250 W (*cf.* Section 3.3) and onto the pre-dried out wall. However, the latter nucleation mode did not last more than a few minutes, before completely vanishing. At that moment, only the liquid bulk nucleation maintained. At last, in spite of this forcing, the thermodynamic parameters that have been shown relevant for describing this phenomenology in Section 3.1.3 did not differ that much

from each other when comparing the two studied tests, except for the dissolved  $O_2$  concentration which dropped a little bit faster in the forced case (*cf.* Figures 3.62-3.64).

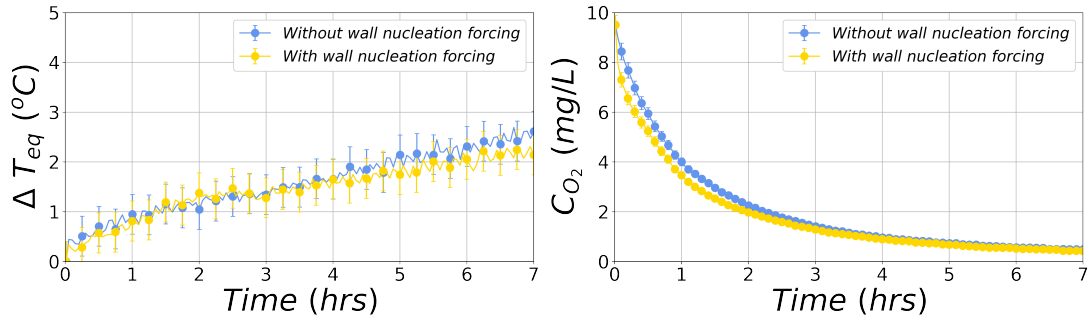


Figure 3.62: A study of the forcing of bubble nucleation onto the unheated rough wall of the vessel. Left: estimated liquid thermal metastability degree  $\Delta T_{eq}$ . Right: measured dissolved  $O_2$  mass concentration  $C_{O_2}$ .

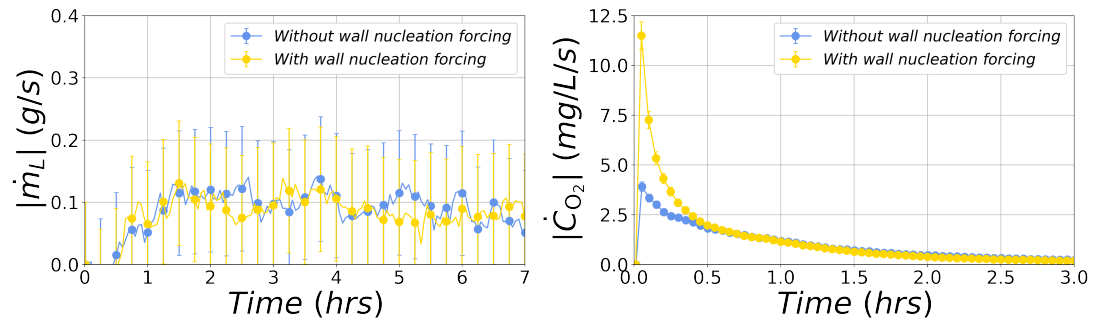


Figure 3.63: A study of the forcing of bubble nucleation onto the unheated rough wall of the vessel. Left: estimated liquid vaporization rate  $\dot{m}_L$ . Right: estimated oxygen degassing rate  $\dot{C}_{O_2}$ .

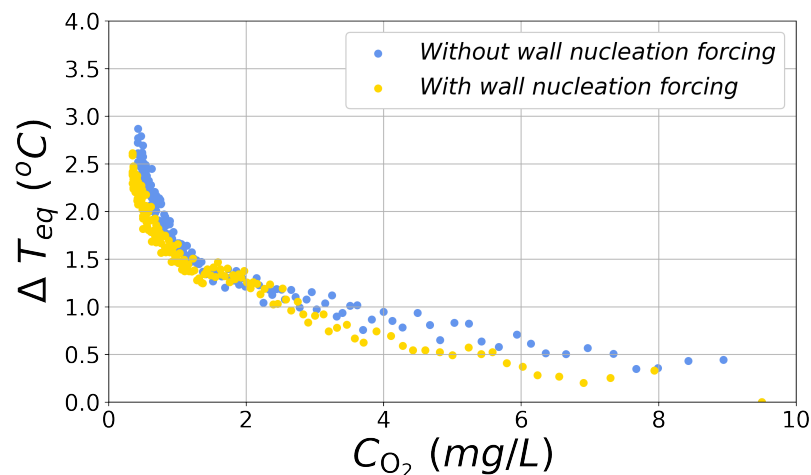


Figure 3.64: A study of the forcing of bubble nucleation onto the unheated rough wall of the vessel. Correlation between the variables reflecting the liquid degassing and heat-up kinetics,  $C_{O_2}$  and  $\Delta T_{eq}$ .



Figure 3.65: A study of the forcing of bubble nucleation onto the unheated rough wall of the vessel. Photo taken during the bubbling stage of the test conducted at a power of 250 W, a pressure of 22 mbar, an initial dissolved  $O_2$  concentration of 9.5 mg/L, an initial pool level of 30 cm and a prior dry out of the unheated rough wall. During the beginning of that stage, bubbles were seen nucleating both within the liquid bulk and onto the pre-dried out wall.

## Conclusions

In this chapter, we have provided a first insight into the physics of the gravity-driven flashing of water in a pool heated from below. This insight has been given through the analysis of a typical experiment, whose results were fairly well repeatable. The latter has highlighted some features that appear specific to the phenomenon. First of all, we have shown that the liquid pool usually evolves according to a two-stage process. During the first stage, the pool has been seen subjected to a strong and continuous bubbling. In this interval, numerous bubbles have been identified nucleating from three distinct locations, illustrated in Figure 3.66:

- Within the liquid bulk, underneath the free surface;
- At the heated bottom wall;
- At the unheated and rough vertical wall.

For those experiments conducted with an initially large chemical disequilibrium in dissolved gases, the so-called bulk nucleation is always present, whatever the retained heating power, initial pool level or operating pressure, over the studied parameters range. Later, the bubbles nucleating that way typically grow in a fast and often explosive fashion. A theoretical analysis, further confirmed by means of a dedicated experiment, has allowed one to associate this exaggerated growth with the so-called flashing process. Indeed, our developments have evidenced that the other two potential mechanisms that may lead to a bubble growth, *i.e.* the decompression felt by an uprising bubble and the capture of dissolved gases, are practically negligible when compared to the flashing. Next, the nucleation onto the vessel's heated wall has been observed only for those tests conducted with a heating power bigger than 250 W. At last, we have shown that when the vessel's rough and unheated wall is not pre-dried out prior to a test, the occurrence of bubble nucleation onto this very surface is never reached.

The second phenomenological stage that has been discussed is referred to as single-phase stage. The latter is characterized by a quasi-absence of bubble nucleation. During this same stage, the observation of nucleation has been indeed shown as a rare and violent event, randomly initiated by some external perturbation (*e.g.* a falling droplet, a detaching bubble).

Then, we have conducted a sensitivity analysis regarding four control parameters of the Aquarius tests. The analysis has allowed emphasizing some more features of the phenomenon. By paraphrasing *Henry Cavendish*, cited at the forefront of this chapter: in a pool heated from below, having a large vertical variation of the saturation temperature, the excess of the heat of water above the boiling point (*i.e.* our proposed thermal metastability degree  $\Delta T_{eq}$ ) is influenced by a great variety of circumstances. Those circumstances being in the present study and by order of importance, the initial amount of dissolved gases and the heating power, the operating pressure, the initial pool level. Importantly, those observations validate the experimental similarity approach, proposed

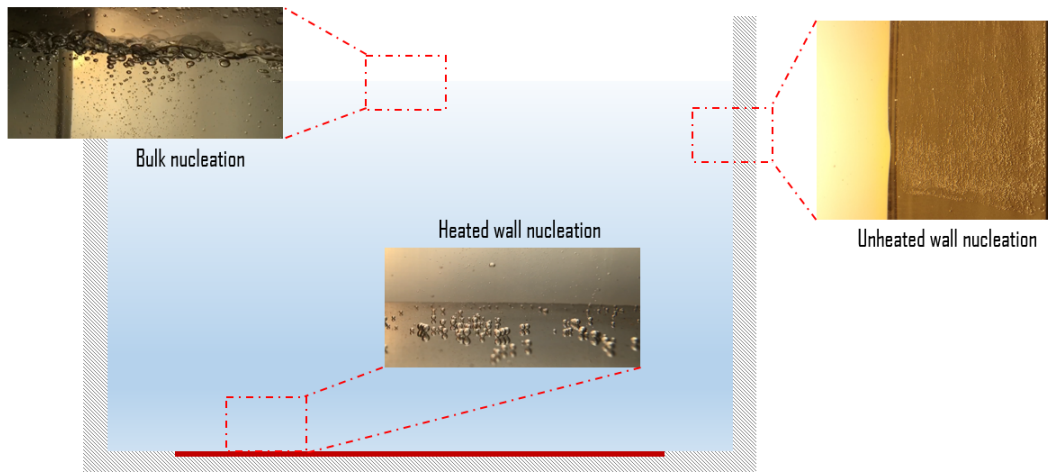


Figure 3.66: An illustration of the observed three locations for bubble nucleation within the Aquarius device.

in Chapter 2, the studied flashing phenomenon, envisioned in large pools, being observed at the small scale of the Aquarius device. It is also worth pointing out that the emergence of bubbles has appeared steady in the present experiments. This is in complete agreement with what is reported in the scientific literature about the relationship between the so-called system's aspect ratio and the steadiness of the phenomenon: for aspect ratios smaller than unity, the superheated water vaporization process is no longer cyclic as in geysers (*cf.* Chapter 1).

Eventually, we have provided an overview of some additional tests that were conducted with the intent to force the bubble nucleation processes in a specific location within the liquid pool. Localizing the heat source onto the heated bottom wall and later, inclining the pool from the horizontal plane, has led to a localized bulk nucleation, thereby highlighting a significant link between the latter process and the natural convection flow taking place within the continuous liquid.

---

# A study of the observed nucleation processes

*“It doesn’t matter how beautiful your theory is, it doesn’t matter how smart you are. If it doesn’t agree with experiment, it’s wrong.”*

— Richard P. Feynman

## Introduction

This chapter is devoted to the analysis of the observed nucleation processes, presented in Chapter 3. The analysis is based on a set of theoretical concepts and models introduced in Sections 4.1.1 and 4.1.2. Next, on that basis, an interpretation of the nucleation of bubbles onto the unheated and heated walls of the pool vessel is proposed in Section 4.2. At last, a similar interpretation is given in Section 4.3 regarding the observed bulk nucleation.

## 4.1 A review of the different nucleation modes

### 4.1.1 Definitions and taxonomy

As already discussed, the term *bubble nucleation* refers to the physical process leading to the spontaneous formation of a bubble into a metastable liquid [34]. This process is of particular importance in the frame of this study. Indeed, the latter fixes the kinetics at which the metastable liquid may relax toward thermal and/or chemical saturation [69]. Bubble nucleation is also a so-called *activated process* [34]. This means that its occurrence is only possible when a *free energy barrier* is overcome by the metastable liquid.

In what follows, we discuss all the potential nucleation mechanisms that may come into play during a gravity-driven pool flashing. For that aim, we first propose a phenomenological taxonomy based on the energetic cost for bubble nucleation. This cost is really highly different whether a *gas nucleus* (*i.e.* some tiny bubble) pre-exists or not within the metastable liquid. Therefore, we can classify the various existing nucleation

mechanisms into the two categories depicted in Figure 4.1: the nucleation from a pre-existing gas nucleus and the *de novo* nucleation. The latter denomination is inspired from the work of *Urban*, who introduced the latin word *de novo* for referring to the spontaneous formation of a gas nucleus within the metastable liquid, by a purely random process of thermal and/or chemical fluctuations [117]. The process can be indefinitely renewed as long as the free energy barrier is exceeded, hence the term *de novo*, which literally means *renewed* in latin. The free energy barrier that is to be overcome for a bubble nucleation is obviously smaller when a gas nucleus pre-exists. The latter may be either floating freely in the liquid or entrapped in some solid crevice (be it located in a wall of the pool vessel or in a suspended solid particle). Then comes the *de novo* nucleation which requires an extra energetic cost for the *a priori* formation of a gas nucleus. This formation is at its highest cost when taking place within the liquid bulk. The cost is however energetically reduced in the presence of some solid foreign body or discontinuity within the liquid phase. All those mechanisms are further detailed in the next subsection.

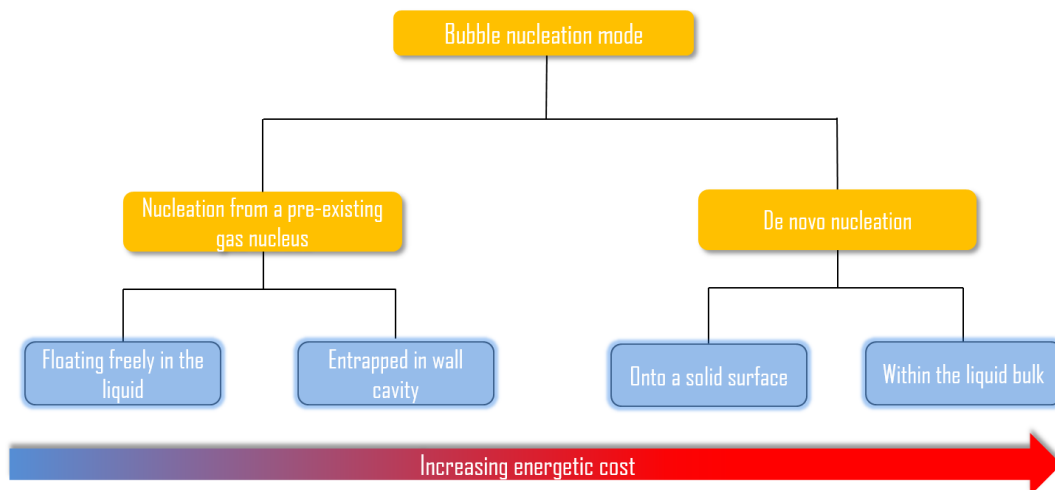


Figure 4.1: A proposed classification for the possible bubble nucleation modes based on their energetic cost. Two main categories of very different energetic cost magnitude are recognized: the nucleation from a pre-existing gas nucleus and the *de novo* nucleation.

### 4.1.2 Physical mechanisms

**The nucleation from a free-floating pre-existing gas nucleus** In the field of water boiling, flashing or cavitation, because of its relatively small energetic cost, the nucleation from a pre-existing gas nucleus is expected as the dominant mode for metastable water relaxation [129] and in particular, the nucleation from free-floating nuclei. The approach postulates that some tiny bubbles of air are always significantly present within water in any engineering application [18]. Those micro-bubbles may, for instance, originate from the filling stage of the studied water container at atmospheric pressure by air entrainment. For investigating the mechanisms by which a metastable volume of water

may turn into bubbles, let us first study the existence and stability conditions governing the postulated free-floating nuclei. The first of these conditions is hydrodynamic. A bubble being always lighter than its carrying liquid is subjected to a so-called buoyancy force, which provides it with an upward movement. This force  $\vec{f}_{buoyancy}$  reads:

$$\vec{f}_{buoyancy} = \frac{4}{3}\pi r_b^3(\rho_L - \rho_G)\vec{g} \quad (4.1)$$

with  $\rho_L$  and  $\rho_G$ , respectively the liquid and gas densities,  $\vec{g}$  the gravitational acceleration and  $r_b$ , the bubble radius. In its uprising movement, the bubble is also subjected to viscous forces  $\vec{f}_{viscous}$  counteracting the buoyancy force. For sufficiently small bubbles, such as the gas nuclei of the present study, the bubble movement is expected to be a so-called low-Reynolds number flow [26]. Under these conditions, the viscous force can be fairly well approximated by the so-called Stokes' formula, which reads, for bubble Reynolds numbers up to unity:

$$\vec{f}_{viscous} = -6\pi\mu_L r_b \vec{u}_b \quad (4.2)$$

with  $\mu_L$ , the liquid dynamic viscosity and  $\vec{u}_b$  the bubble velocity. By strictly counterbalancing  $\vec{f}_{buoyancy}$  and  $\vec{f}_{viscous}$ , one can thus estimate the bubble terminal velocity, also called Stokes' velocity, still for Reynolds numbers up to unity:

$$u_b^{stokes} = \frac{2(\rho_L - \rho_G)gr_b^2}{9\mu_L} \quad (4.3)$$

As one can notice, this rising velocity  $u_b^{stokes}$  is an increasing function of the bubble size, through the variable  $r_b$ . Consequently, at very small sizes, this velocity may potentially reach the order of magnitude of the so-called Brownian velocity of the water molecules. If this condition is met, the bubble is then expected to stop rising up to the liquid free surface. Instead, the small bubble may follow the Brownian motion of the water molecules. In order to estimate whether or not some bubble of radius  $r_b$  may be hydrodynamically stabilized within the liquid, one can introduce a bubble Péclet number  $Pe_b$  [49], which reads:

$$Pe_b = \frac{2 u_b^{stokes} r_b}{\mathcal{D}_{brownian}} \quad (4.4)$$

with  $\mathcal{D}_{brownian}$ , the Brownian diffusion coefficient, equal to [49]:

$$\mathcal{D}_{brownian} = \frac{k_B T_L}{6\pi\mu_L r_b} \quad (4.5)$$

and  $k_B$  and  $T_L$ , respectively the Boltzmann's constant and the liquid temperature. Inserting Equations (4.3) and (4.5) into (4.4) eventually yields:

$$Pe_b = \frac{8(\rho_L - \rho_G)g\pi r_b^4}{3 k_B T_L} \quad (4.6)$$

The possibility for an hydrodynamic stabilization of a gas nucleus floating freely in the liquid can then be done according to the following considerations:

- If  $Pe_b \leq 1$ , the bubble flow is dominated by the Brownian motion of the water molecules: hydrodynamic stabilization;
- If  $Pe_b \gg 1$ , the Brownian motion of the water molecules has no significant impact on the bubble flow. The bubble will rise up to the liquid free surface and escape.

In Figure 4.2 is plotted the variation of Equation (4.6) against  $r_b$  at an arbitrary liquid temperature  $T_L$  of 300 K and at a low pressure such that  $\rho_L \gg \rho_G$ .

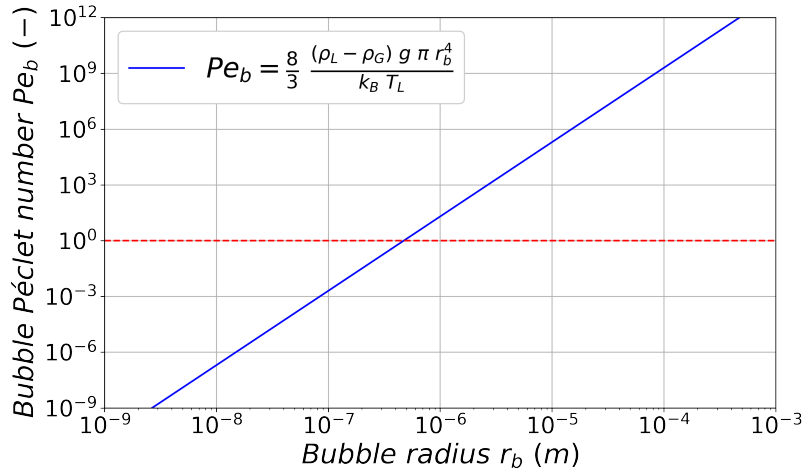


Figure 4.2: An estimate of the bubble Péclet number  $Pe_b$ , given by Equation (4.6), for water against  $r_b$ , at an arbitrary liquid temperature  $T_L$  of 300 K and at a low pressure such that  $\rho_L \gg \rho_G$ . One can notice that  $Pe_b > 1$  for a bubble radius  $r_b > 0.5 \mu\text{m}$ .

As one can observe from that figure,  $Pe_b > 1$  for a bubble radius  $r_b > 0.5 \mu\text{m}$  and becomes much bigger than unity for  $r_b > 1 \mu\text{m}$ . Therefore, one can consider that only air bubbles whose radius  $r_b$  is smaller than  $1 \mu\text{m}$  can be hydrodynamically stabilized within the liquid phase by the Brownian motion of water molecules, thereby preventing them from rising up to the free surface and later escaping (*cf.* Figure 4.3). However, it is worth pointing out that the random motion of such tiny bubbles brings some of them toward the liquid free surface according to a probability which is not null. Hence, over very long time periods, even the hydrodynamically stabilized gas nuclei are expected to escape from a liquid pool. It is possible to estimate this time period on the basis of a simple physics reasoning that is detailed in what follows. At first, the small bubble subjected to the Brownian motion is expected to displace according to a time-dependent length-scale referred to as the particle mean free path and denoted  $l$ . This length is defined as [49]:

$$l = \sqrt{\mathcal{D}_{\text{brownian}} t} \quad (4.7)$$

with  $t$ , the time variable. Getting an estimate of the time period for a significant escape of the stabilized gas bubbles consists in finding the period  $\tau$  from which the particle

mean free path is of the order of magnitude of the vessel length-scale. Let us then apply Equation (4.7) to this problem, with  $l$  being of the order of the typically considered pool water levels, *i.e.* 0.30 m, and the Brownian diffusion coefficient  $\mathcal{D}_{brownian}$  being of the order of  $2 \times 10^{-13} \text{ m}^2/\text{s}$ , at a temperature  $T_L$  of 300 K and with a bubble size  $r_b$  of 1  $\mu\text{m}$ . The numerical application yields:

$$\tau \approx 13,000 \text{ years} \quad (4.8)$$

which is an excessively long time period. A similar numerical application made with a bubble size of the order of 1 nm yields an approximate time period of 40 days, which is still much bigger than the typical duration of a pool flashing test (including its preparatory stage). Therefore, if some gas nuclei sizing below 1  $\mu\text{m}$  are present within water, one can consider them as absolutely remaining in this very liquid, at least according to hydrodynamic considerations.

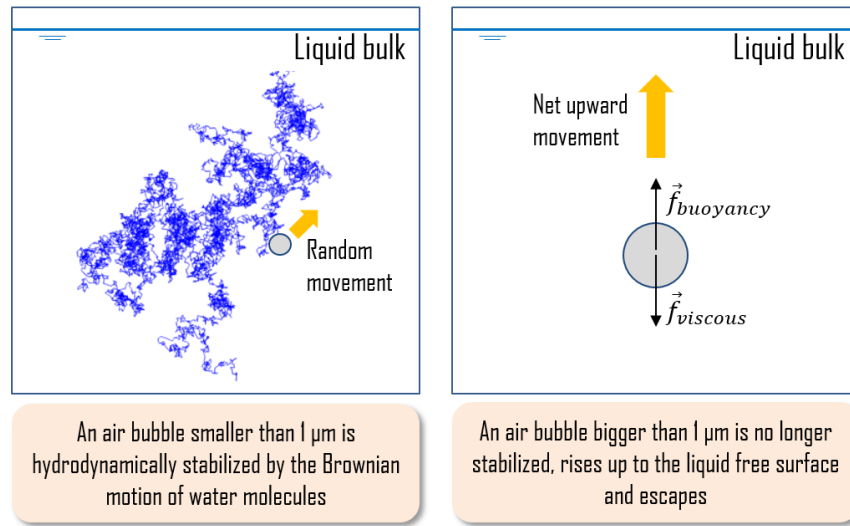


Figure 4.3: An illustration of the bubble hydrodynamic stabilization mechanism, based on the Brownian motion of water molecules. This mechanism comes into play for air bubble sizes smaller than 1  $\mu\text{m}$ .

The second stability criterion associated with a free-floating gas nucleus is thermodynamic. The latter is far more restrictive than the hydrodynamic one that has been discussed above. For understanding this point, let us first assume that, within a liquid at temperature  $T_L$  and pressure  $P_L$ , there exists some gas nucleus of radius  $r_b$ , inner pressure  $P_G$  and temperature  $T_G$ , composed of air (*i.e.* a mixture of  $\text{O}_2$ ,  $\text{N}_2$  and water vapor). This postulated nucleus is illustrated in Figure 4.4. The liquid contains some dissolved  $\text{O}_2$  and  $\text{N}_2$ , whose molar fraction is respectively denoted as  $x_{\text{O}_2}^L$  and  $x_{\text{N}_2}^L$ . These molar fractions obviously combine with those of water, denoted  $x_w^L$ , as:

$$x_{\text{O}_2}^L + x_{\text{N}_2}^L + x_w^L = 1 \quad (4.9)$$

The bulk of the gaseous nucleus is similarly characterized by the molar fractions  $x_{\text{O}_2}^G$ ,  $x_{\text{N}_2}^G$  and  $x_w^G$ , which obviously combine as:

$$x_{\text{O}_2}^G + x_{\text{N}_2}^G + x_w^G = 1 \quad (4.10)$$

The gas bulk is often considered as a so-called ideal mixture of gases, with each gaseous species being an ideal gas [121]. This thermodynamic representation allows connecting the above molar fractions to another set of important variables: the partial pressures of the  $O_2$ ,  $N_2$  and water species, denoted as  $P_{O_2}^G$ ,  $P_{N_2}^G$  and  $P_w^G$ . In this frame, the partial pressures combine according to the so-called *Dalton's law* [121]:

$$P_{O_2}^G + P_{N_2}^G + P_w^G = P_G \quad (4.11)$$

and

$$x_k^G = \frac{P_k^G}{P_G} \quad (4.12)$$

with  $k \in \{O_2; N_2; w\}$ .

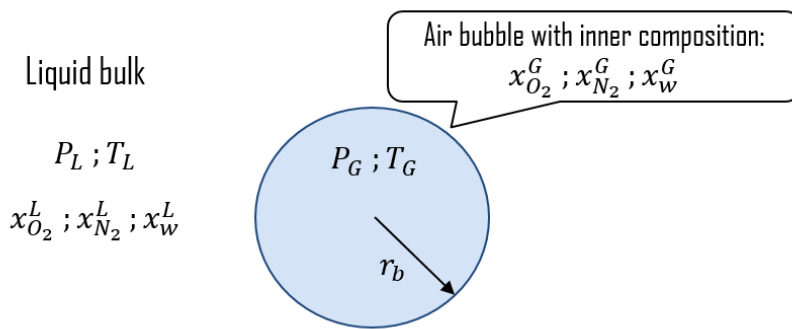


Figure 4.4: The idealization of a gas nucleus floating freely in water and its associated thermodynamic variables.

Next, for being achieved, the thermodynamic equilibrium of the studied bubble requires the simultaneous completion of:

- A *thermal equilibrium* between the gas and liquid phases;
- A *mechanical equilibrium* of the gas/liquid interface;
- A *chemical equilibrium* between the species composing the liquid and those contained in the bubble.

The thermal equilibrium is the easiest to introduce. Indeed, it simply consists in the following equality:

$$T_L = T_G \quad (4.13)$$

Next comes the mechanical equilibrium. At the gas/liquid interface, the intermolecular forces that bind the water molecules together can be macroscopically associated with a so-called surface tension, later denoted as  $\sigma$  [18]. In 1805, *Laplace* showed that this variable can be linked with the pressures of the liquid bulk  $P_L$  and of the bubble  $P_G$  according to a law known as the *Laplace-Young equation* [33]. This law reads, for a spherical interface:

$$P_G - P_L = \frac{2\sigma}{r_b} \quad (4.14)$$

and implies that, because of the curvature of the bubble, the bubble inner pressure  $P_G$  is higher than its liquid counterpart  $P_L$ . At last, one can express the chemical equilibrium of the involved species, *i.e.*  $O_2$ ,  $N_2$  and water, according to two well-known laws that are described below. First of all, one can show that the gas-side water molar fraction is related to the bubble pressure  $P_G$  and temperature  $T_G$  by the so-called *Raoult's law* [121]:

$$x_w^G = \frac{P_{sat}(T_G)}{P_G} \quad (4.15)$$

with  $P_{sat}(T_G)$ , the water saturation pressure at temperature  $T_G$ . Further on, one can show that, within the studied low pressure range, the liquid-side  $O_2$  and  $N_2$  molar fractions are related to their gaseous counterpart by the so-called *Henry's law of solubility* which reads, for each species [104]:

$$x_{O_2}^G = \frac{x_{O_2}^L \mathcal{H}_{O_2}(T_L)}{P_G} \quad (4.16)$$

$$x_{N_2}^G = \frac{x_{N_2}^L \mathcal{H}_{N_2}(T_L)}{P_G} \quad (4.17)$$

where  $P_G$  is the gas total pressure within the nucleus,  $\mathcal{H}_{O_2}(T_L)$  and  $\mathcal{H}_{N_2}(T_L)$  are respectively the  $O_2$  and  $N_2$  Henry's volatility constant (in Pa/mol/mol), at temperature  $T_L = T_G$ . Finally, for a given radius  $r_b$ , the thermodynamic equilibrium of the free-floating bubble is achieved only if the conditions expressed by Equations(4.13-4.17) are simultaneously fulfilled, which is rather restrictive. Thus, any change of any thermodynamic variable characterizing the liquid bulk, such as  $P_L$ ,  $T_L$ ,  $x_{O_2}^L$  or  $x_{N_2}^L$  would then either lead to the expansion or shrinkage of the gas bubble, as a system's attempt to reach another equilibrium. The energetic cost for nucleation is hence null in the present case, since any positive departure from the initial state of the liquid would then lead to the nucleus activation and expansion. However, all those equilibria are intrinsically unstable [43]. In case of a free-floating air bubble, the characteristic time of the variations in bubble radius when any liquid bulk thermodynamic parameter varies can be reasonably estimated by means of the air diffusion model proposed by *Epstein and Plesset* [18]. Integrating the air diffusion equation over the geometry of a postulated bubble gives the following equation [38]:

$$\frac{dr_b}{dt} = -\mathcal{D}_{a,w}^L \frac{C_a^{eq} - C_a}{\rho_G} \left( \frac{1}{\sqrt{\pi \mathcal{D}_{a,w}^L t}} + \frac{1}{r_b} \right) \quad (4.18)$$

with  $\mathcal{D}_{a,w}^L$  the air diffusion coefficient in liquid water,  $C_a$  and  $C_a^{eq}$ , respectively the air mass concentration in water and at saturation. If one neglects as a first order approximation the role played by surface tension, Equation (4.18) admits an analytical solution for the bubble radius variations characteristic time  $\tau_b$ :

$$\tau_b = \frac{r_{bo}^2}{2\mathcal{D}_{a,w}^L} \frac{\rho_G}{|C_a^{eq} - C_a|} \quad (4.19)$$

with  $r_{bo}$ , the initial radius of the gas nucleus under transformation. This equation allows understanding the phenomenological aspects of such a gas nucleus expansion or shrinkage. First of all,  $\tau_b$  is an increasing function of the initial bubble radius  $r_{bo}$ . Hence, the smaller the bubble the faster its transformation. Similarly,  $\tau_b$  is a decreasing function of  $|C_a^{eq} - C_a|$ . Therefore, the higher the chemical disequilibrium of the non-condensable gaseous species in presence within water, the faster the bubble transformation, as expected. More importantly, because  $\tau_b$  varies linearly with  $\rho_G$ , this effect is expected to be even faster at a reduced pressure when compared with atmospheric conditions.

Let us now apply Equation (4.19) to the classical experimental conditions reached at the very beginning of a gravity-driven pool flashing test. For that aim, we postulate the existence of a 1  $\mu\text{m}$  gas nucleus, the latter size being the maximum one below which a bubble hydrodynamic stabilization can be envisioned. Let us next consider a liquid pressure of 20 mbar, yielding a gas density  $\rho_G$  of 0.02  $\text{kg}/\text{m}^3$ . The liquid bulk is further assumed containing some dissolved air at a mass concentration  $C_a$  of 0.024  $\text{kg}/\text{m}^3$ , which is the saturation value under standard atmospheric conditions (*i.e.* the ones imposed to the liquid prior to the vessel depressurization). Because of the initial pool vessel depressurization, the gas volume of the vessel is always almost fully depleted in air, as seen in Chapter 3. Thus, the saturation value of the dissolved air mass concentration  $C_a^{eq}$  is expected to be quasi-null. At last, a value of  $2.5 \times 10^{-9} \text{ m}^2/\text{s}$  is retained for the dissolved air diffusion coefficient  $\mathcal{D}_{a,w}^L$ . Eventually, the numerical application yields a bubble transformation time  $\tau_b$  of the order of 0.2 ms, which is a rather small value. As a comparison,  $\tau_b$  is typically of the order of one second for millimetric bubbles at atmospheric pressure [43].

Having explored the hydrodynamic and thermodynamic stability conditions of a free-floating air bubble, the postulated pre-existence of numerous gas nuclei in water seems rather unlikely, unless some ontological solution is envisioned for stabilizing those gas nuclei [18]. Indeed, the above hydrodynamic study have shown that only bubbles whose typical size is smaller than 1  $\mu\text{m}$  can remain freely in the liquid phase, without escaping under the action of their own buoyancy. However, those tiny bubbles are precisely expected to dissolve very fastly, according to the calculations made by means of Equation (4.19). Such an ontological solution has been proposed by *Fox and Herzfeld* in [42]. These researchers postulated the presence of an organic skin around those nuclei, made of surfactant chemicals that are usually contained in water. Pointedly, this organic skin was postulated impermeable to gas diffusion. Therefore, it was expected that the latter only plays a role on the bubble mechanical equilibrium discussed above, by modifying the value of the surface tension  $\sigma$ . Adding some surfactant agents to the water would then drop the value for  $\sigma$ . In turn, reasoning at a fixed nucleus size  $r_b$ , this would reduce the pressure difference  $P_G - P_L$  between the gas and liquid phases and hence, would relax the metastability conditions to be fulfilled by the liquid for allowing the gas nucleus to exist. However, this reduced surface tension does not change the unstable feature of the existence of such a nucleus. Since then, *Fox and Herzfeld's* assumption has been widely explored in an empirical way [31], with

the experiments made by *Sirotyuk* in 1970 [108], *Yount* in 1978 [131] and *Johnson and Cooke* [61] in 1981 being particularly significant and in good agreement with *Fox and Herzfeld's* views. This approach is now known as the stabilized skin model with variable permeability [87]. The stabilized skin model is currently widely admitted as relevant for explaining a wealth of bulk cavitation experiments in water [5], with however still some debates about the predominance of freely-floating gas nuclei in this very type of experiments [22].

**The nucleation from a pre-existing gas nucleus entrapped in a wall cavity** The second source of pre-existing gas nuclei that is often postulated by the community is known as *Harvey's nucleus*, after the pioneering work of *Harvey et al.* done in 1944 [50], [51]. This approach considers as plausible the presence of gas nuclei entrapped in some of the solid surfaces in contact with the liquid, as depicted in Figure 4.5. Those solid surfaces can be either an imperfectly wetted impurity in suspension within the liquid, also called *mote* [3] or the walls of the liquid container [130].

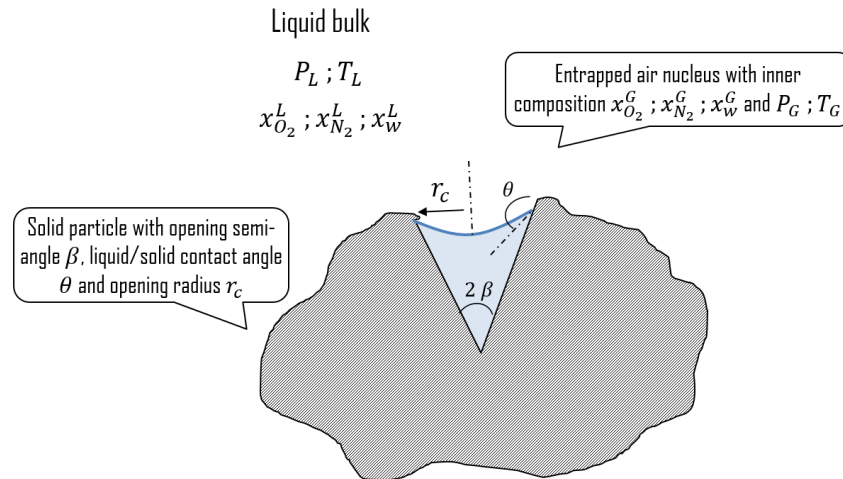


Figure 4.5: The idealization of a Harvey's nucleus entrapped in a solid wall, here a solid particle suspended in the liquid, and its associated thermodynamic variables.

As for the postulated free-floating gas nuclei, we investigate in what follows the existence and stability conditions to be fulfilled by an entrapped nucleus. First of all, the existence of such nuclei is most often attributed to the gas entrapment process that may arise from the filling stage of the water container [8]. Let us consider, to illustrate this process, that a conical cavity as the one shown in Figure 4.5 pre-exists in some solid surface. This cavity is geometrically characterized by some opening radius  $r_c$  and semi-angle  $\beta$ . The solid wettability is further represented by a contact angle  $\theta$  [33]. According to *Bankoff* and then *Lorenz et al.* who studied this mechanism respectively in 1958 and 1974, there exists a geometrical criterion to be fulfilled by the postulated cavity in order to allow entrapping some gas during the filling stage of the water container [7], [76]. This criterion can be expressed by the following relation, for a conical crevice [74]:

- $\theta > 2\beta \rightarrow$  a gas entrapment is possible (cf. Figure 4.6);
- $\theta < 2\beta \rightarrow$  the liquid completely wets the crevice.

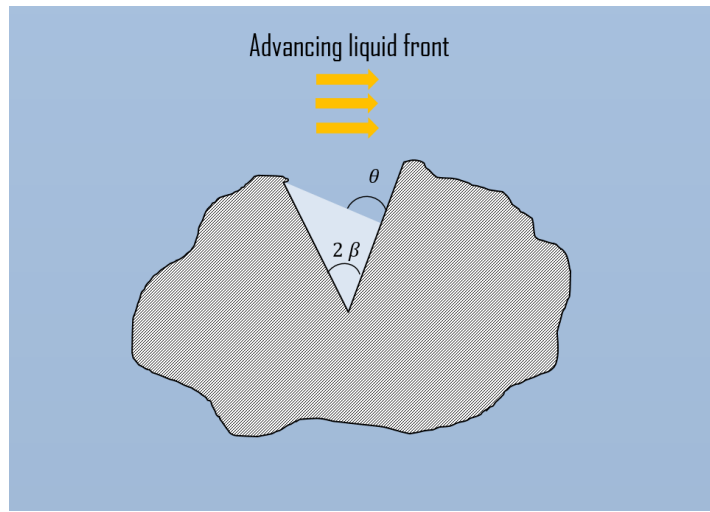


Figure 4.6: The gas capture mechanism during the wetting of some solid particle by a liquid, according to *Bankoff* [7].

A second type of wall cavity idealization is often considered: the cylindrical crevice [107], whose opening radius is still denoted  $r_c$  and whose depth is referred to as  $R_z$  in what follows. This idealized cavity is illustrated in Figure 4.7.

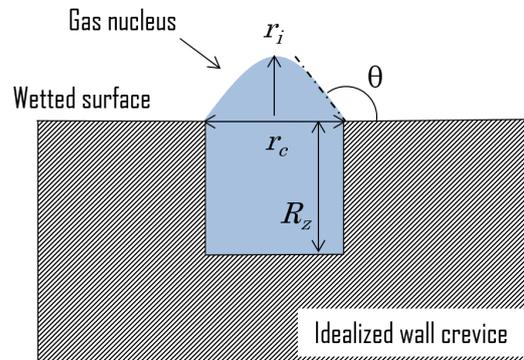


Figure 4.7: Idealized cylindrical wall crevice onto some solid surface and a postulated entrapped gas nucleus within it.

As *Bankoff* and *Lorenz et al.*, *Yan* studied the geometrical conditions allowing gas entrapment for such cylindrical crevices and came up with the following criterion [129]:

- $R_z > \frac{2r_c}{\tan \theta} \rightarrow$  a gas entrapment is possible (cf. Figure 4.7 showing a gas nucleus, once entrapped);
- $R_z < \frac{2r_c}{\tan \theta} \rightarrow$  the liquid completely wets the crevice.

At that stage, one can argue that not all solid surfaces are prompt to entrap some gas nuclei. Only those having crevices whose geometry complies with the above criteria

can do so. Regarding this compliance, another point is to be discussed. If it is clear that solid walls are typically rough enough for complying with these very criteria [29], the question is to be asked for the envisioned solid particles suspended in the liquid. For a long while since *Harvey et al.* work, those particles were postulated as having cracks and crevices. The hypothesis has been tested only very recently, taking benefit from high-resolution microscopy, after some fine observations of real particles. Such an observation, extracted from [4], is given in Figure 4.8. It shows the surface details of some artificial Polystyrene particles. The latter appear corrugated and do not seem to contain any real crack or crevice. Actually, many solid particles naturally present in water, of micrometric size, exhibit the same surface type [88], such as the one first exhibited by *Crum* in [30]. But this very feature is not incompatible with *Harvey's* views. Indeed, according to *Borkent et al.*, gas nuclei may be entrapped onto corrugated surfaces as well. But in this case, the host solid surface is to be hydrophobic [15].

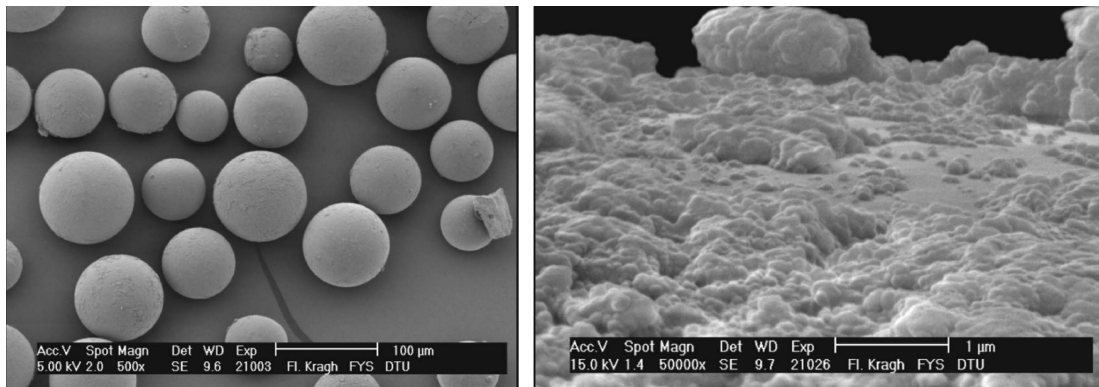


Figure 4.8: A microscopic view of artificial Polystyrene particles with a corrugated surface, extracted from [4].

The next condition governing the existence and stability of entrapped gas nuclei is thermodynamic. The latter has been widely studied since the work of *Harvey et al.* in 1944 [50]. Very early, a modeling based on the developments shown in the previous part on free-floating nuclei has been proposed. It has been improved and proven accurate enough for predicting the onset of cavitation or boiling by many authors since then, including *Strasberg* [110], *Apfel* [3], *Winterton* [125], *Crum* [30] and more recently, *Atchley and Prosperetti* [5]. Those last authors have come up with the most advanced modeling for bubble nucleation from a solid crevice. In details, the model links the gas/liquid interface radius, denoted  $r_i$  as an illustration in Figure 4.7, with the geometrical parameters of the host cavity (which depend on the type of geometry: conical, cylindrical) and the contact angle  $\theta$  [31]. Neglecting the so-called hysteresis effect of the contact angle, *Yan* proposed the simplified set of relations between those very parameters that is detailed below [129]. First, for an hydrophilic liquid/solid contact in a cylindrical cavity:

$$r_i = \frac{r_c}{\cos \theta} \quad (4.20)$$

whereas, for a conical cavity:

$$r_i = \frac{r_c}{\cos(\theta - \beta)} \quad (4.21)$$

with  $\beta$ , the cavity opening semi-angle introduced above. Second, for an hydrophobic liquid/solid contact, be the cavity conical or cylindrical:

$$r_i = \frac{r_c}{\cos(\theta - \frac{\pi}{2})} \quad (4.22)$$

From the above equations, it appears that the geometrical features of the postulated wall cavities do play a role on the required degree of metastability within the liquid, through Equation (4.14) linking  $r_i$  to the pressure difference term  $P_G - P_L$ . The equilibrium of a gas nucleus entrapped that way is however equally unstable. Indeed, as for the free-floating gas nuclei, any departure from the initial state of the liquid would lead to either the nucleus shrinkage or expansion. At last, one can similarly estimate the characteristic time of the variations in bubble radius when any liquid bulk thermodynamic parameter varies, based on the classically admitted bubble wall nucleation mechanism. This mechanism is based on the early observation of bubbles nucleating onto a rough solid surface. The latter typically shows a cyclic bubble production and release process from a pre-identified nucleation site [62], as depicted in Figure 4.9, whatever the type of liquid metastability. For instance, *Burman* highlighted this very process in a liquid solution supersaturated in carbon dioxide [20]. *Hsu and Graham* did the same for a boiling superheated liquid [55]. The cycle is understood as follows. As a first stage, it is considered that some heat and/mass transfer develops at the level of the postulated entrapped nucleus. This transfer may either develop through the liquid bulk, as depicted in Figure 4.9 - stage 1, or from the wall itself, when the latter is heated up. That way, the liquid in contact with the nucleus deviates from its initial state, which activates the nucleus growth (*cf.* stage 2, Figure 4.9). Further on, the progressive growth of the nucleus leads to some local return to the initial state within the surrounding liquid, as shown in stage 3 in the same figure. At some point, the now hydrodynamically-unstable big bubble detaches from the wall, leaving some liquid layer at its vicinity under the initial state (*cf.* stage 4). The cycle may then continue as long as the heat and/or mass transfer may renew some local thermodynamic disequilibrium. Its kinetics is typically separated into two distinct stages: the so-called waiting time and growing time [63]. If the growing time of an entrapped nucleus is really close to the solution derived above for a free-floating nucleus [86] (*i.e.* the same order of magnitude for this time period can be kept in mind), the waiting time deserves more attention. As depicted in the conceptual Figure 4.9, this period is basically associated with the disequilibrating heat and/or mass transfer. And the latter is kinetically very different whether it comes from the wall or from the liquid bulk, as evidenced by *Shin and Jones* [105]. Many models are available for estimating this waiting time. Among them, the most significant are

those of *Hsu*, for a boiling liquid (*i.e.* with a heat transfer coming from the wall) [54] and *Shin and Jones* [105] and later, *Yan and Giot* [129], for a flashing liquid. The use of these models yields a waiting time which is of the order of magnitude of the growing time, in case of a boiling liquid. Conversely, for a flashing flow, the waiting time may be several orders of magnitude bigger than its growing counterpart [98].

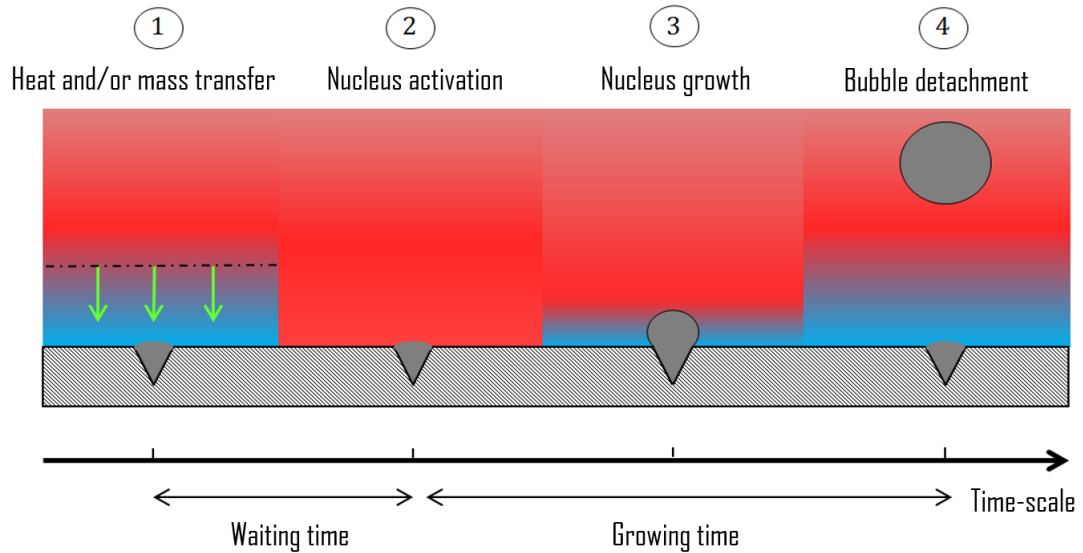


Figure 4.9: The idealization of a bubble nucleation cycle taking place onto a wall. Here this cycle is exemplified for the peculiar case of a disequilibrating heat and/or mass transfer coming from the liquid bulk.

**The de novo nucleation within the liquid bulk** Having explored the possible mechanisms behind the nucleation from pre-existing gas nuclei, we now cover the so-called de novo process, by starting with the most costly mode: the bulk nucleation.

By definition, this nucleation mode relies on the *a priori* formation of a gas nucleus within the metastable liquid (*cf.* Section 4.1.1). The thermal fluctuations occurring naturally within any liquid are consensually considered as a plausible mechanism for this *a priori* formation [14] (there are however some other considered and more exotic mechanisms, such as the cosmic-ray or natural-radiation-induced formation of gas nuclei, that are not treated in what follows [36]). Within such a fluctuating liquid, there exists in turn local density variations. All in all, some region of the liquid may statistically host a bunch of molecules in a gas-state-like-energy, thereby forming the embryo of a gas nucleus, also called proto-nucleus (*cf.* the illustration provided in Figure 4.10).

Obviously, the mechanism is not costless. The formation of this very proto-nucleus is associated with some energetic cost, well represented by the so-called free energy thermodynamic function-of-state, later denoted as  $F$ . With this in mind, the spontaneous formation of a proto-nucleus by thermal fluctuations changes the system's free energy by about some  $\Delta F$ . The latter decomposes into a surface energy component, linked with the capillary forces at the gas/liquid interface, and a mechanical work of

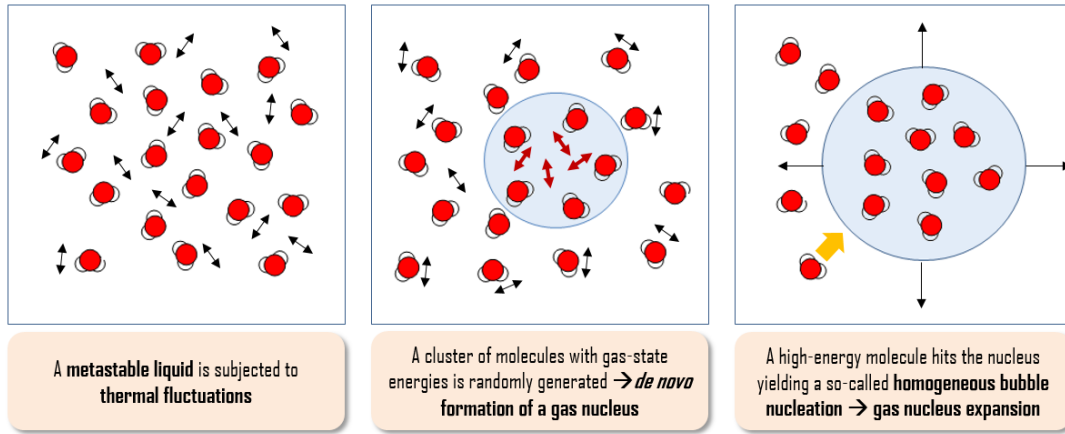


Figure 4.10: An illustration of the postulated mechanism behind the de novo formation of a gas nucleus within the liquid bulk.

the pressure forces component, as follows [80]:

$$\Delta F = \underbrace{4\pi r^2 \sigma}_{\text{surface energy}} - \underbrace{\frac{4}{3}\pi r^3 (P_G - P_L)}_{\text{work of pressure forces}} \quad (4.23)$$

where  $r$  denotes the proto-nucleus radius. When plotted against  $r$ ,  $\Delta F$  exhibits a very specific bell-like shape, as illustrated in Figure 4.11. The curve has a maximum value, denoted  $\Delta F_{max}$ , reached at a specific nucleus radius  $r^*$ . Let us briefly derive from this curve some considerations about the stability of the spontaneously formed nucleus. Let us assume that a proto-nucleus randomly appears within the liquid at a radius  $r$ , different from  $r^*$ . A thermodynamic system being at stable equilibrium if and only if the free energy is at a local minimum in the phase space and the local derivative of  $\Delta F$  against  $r$  being not null everywhere but at  $r = r^*$ , any perturbation of the nucleus radius  $r$  would then lead to either its shrinkage or sudden expansion, as a system's way for minimizing its free energy and tending toward some stable equilibrium. Obviously, the way the proto-nucleus may evolve in these conditions depends on its radius  $r$ : with  $r < r^*$ , the nucleus is expected to collapse whereas with  $r > r^*$ , it is expected to expand. The position  $r = r^*$  is really peculiar. Indeed, at this very location on the curve, the derivative of  $\Delta F$  against  $r$  is strictly null, which means that the position  $r = r^*$  is an equilibrium point. But this equilibrium is unstable, since this point is a local maximum and not a local minimum. Furthermore, thus formed, a nucleus of radius  $r^*$  is considered at equilibrium if and only if it fulfills the mechanical, thermal and chemical conditions detailed above for the free-floating nuclei (*cf.* Equations(4.13-4.17)).

The bubble nucleation process being by definition the spontaneous materialization of a bubble from a preceding gas nucleus, one understands that the random creation of a proto-nucleus can lead to nucleation only if the later spontaneously expands and takes the form of a bubble. This requires that the free energy variation  $\Delta F$  brought by the thermal fluctuations exceeds the maximum value  $\Delta F_{max}$ , hence the notion of an energy

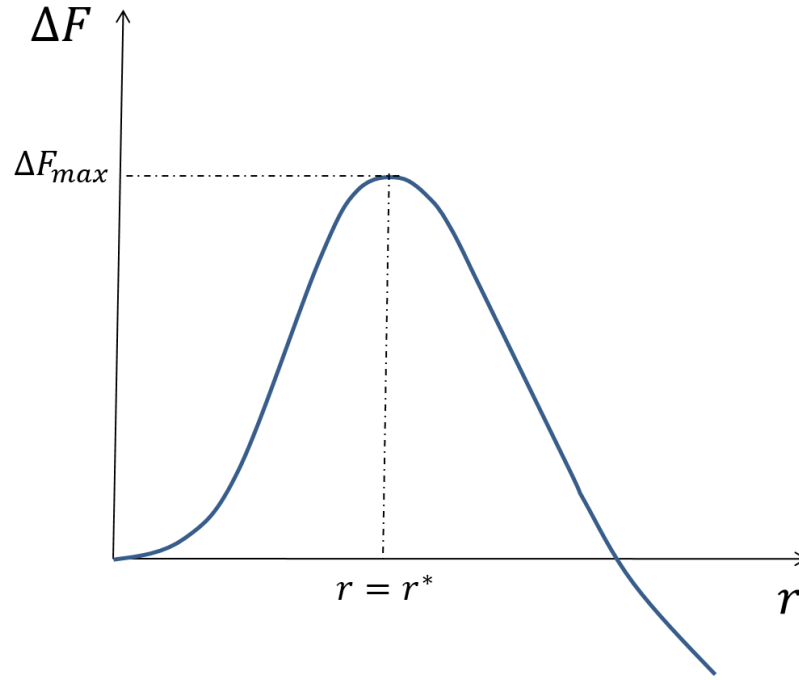


Figure 4.11: Variations of the free energy  $\Delta F$  associated with the formation of a gas nucleus against radius  $r$ . The position  $r = r^*$  is an equilibrium point. But this equilibrium is unstable, since this point is a local maximum and not a local minimum of the free energy.

barrier. Combining Equation (4.23) with (4.14) allows determining an expression for  $\Delta F_{max}$  [14]:

$$\Delta F_{max} = \frac{16}{3} \frac{\pi \sigma^3}{(P_G - P_L)^2} \quad (4.24)$$

At last, as long as the thermal fluctuations lead to some local free energy variation  $\Delta F > \Delta F_{max}$ , the bubble nucleation can take place again and again, hence the term de novo.

In order to go further in the study of the liquid bulk de novo nucleation, let us estimate the system-dependent rate at which such a phenomenon may be observed. For doing so, let us first consider those thermal fluctuations yielding exactly  $\Delta F = \Delta F_{max}$ . Statistical physics allows defining the probability of the spontaneous formation of a proto-nucleus of size  $r^*$ , taking benefit from Boltzmann's equation which describes the size distribution of the cluster of molecules randomly formed that way [29]. With  $N(r^*)$ , the number of randomly formed molecular clusters of size  $r^*$  per unit volume:

$$N(r^*) = N_o \exp\left(\frac{-\Delta F_{max}}{k_B T_G}\right) \quad (4.25)$$

with  $k_B$ , the Boltzmann's constant, already introduced in what precedes,  $T_G = T_L$  at thermodynamic equilibrium and  $N_o$ , a pre-factor usually associated to the number of liquid molecules per unit volume at temperature  $T_L$  and pressure  $P_L$  [14]. Next, from

this unstable equilibrium, it is usually considered that the proto-nucleus will start expanding at least by the collision of one further high-energy molecule [29], as it is illustrated in the third inset of Figure 4.10. If one denotes the so-called collision frequency as  $\lambda$ , one can further define the de novo bulk nucleation rate  $J_{BN}$ , expressed in  $\text{m}^{-3}\text{s}^{-1}$ , as [29]:

$$J_{BN} = \lambda N_o \exp\left(\frac{-\Delta F_{max}}{k_B T_G}\right) \quad (4.26)$$

In [29], *Collier and Thome* discuss the available modelings for estimating the collision frequency  $\lambda$ . For doing so, *Westwater* proposed in 1958 the following equation:

$$\lambda = \frac{k_B T_G}{\hbar} \quad (4.27)$$

with  $\hbar$ , the so-called Planck's constant [124]. *Bernath* proposed in 1952 another expression for  $\lambda$ :

$$\lambda = \frac{2\sigma}{\pi m} \quad (4.28)$$

with  $m$ , the mass of one molecule [12]. When applied to water, both models yield however collision frequencies ranging in between  $10^{12}$  and  $10^{13} \text{ s}^{-1}$  [29]. Further, a close look at Equation (4.26) shows that  $J_{BN}$  is strongly sensitive to the local metastability degree of the liquid, here represented by the pressure difference ( $P_G - P_L$ ). Thus, the bigger the liquid metastability degree, the more probable the de novo bulk nucleation, as phenomenologically expected. As the rule of thumb, this nucleation mode is considered significant when  $J_{BN}$  becomes bigger than 1 bubble/ $\text{m}^3/\text{s}$  [14].

Eventually, one may wonder if this very nucleation mode is likely to be observed in the present study. According to the literature and because of its relatively high energetic cost, this mechanism is never observed in pure and degassed water [29]. Instead, the nucleation frequently takes place onto immersed solid surfaces, from entrapped nuclei [130], [105], [66]. However, a theoretical study of the occurrence conditions for this type of nucleation shows that the phenomenon is likely in the presence of very large amounts of dissolved gases in the liquid phase [111]. It has been further observed experimentally in this very case for three types of liquid, *i.e.* Freon 22, Propane and Isobutane, but not in water, by *Mori et al.* in 1976 [89]. Therefore, in the present study where high dissolved gases supersaturations are reached within the water pool, the question of the occurrence of the de novo bulk nucleation is worth being explored.

**The de novo nucleation onto a solid surface** For a given metastability degree represented by the quantity ( $P_G - P_L$ ) and in the presence of a solid discontinuity in the liquid such as an immersed particle or a wall, it is usually recognized that the energy barrier  $\Delta F_{max}$  for a de novo nucleation is reduced [34]. Thus, at a fixed ( $P_G - P_L$ ), the de novo nucleation is more likely to occur onto or around the solid discontinuities than within the liquid bulk (*cf.* Figure 4.12). The degree of molecular affinity of the liquid/solid couple, also called wettability, matters for this energetic cost reduction. For instance,

*Bankoff* reported in [6] that the energy barrier for a de novo nucleation is a decreasing function of the liquid/solid contact angle for a flat solid surface. The geometry of the solid discontinuity matters too. Indeed, the presence of crevices onto this very surface further reduces the energy barrier [29]. Moreover, if the solid surface is spherical, as expected for some suspended particle, the energetic cost reduction function has a very specific pattern, which depends on the solid particle radius and liquid/solid contact angle [27]. This pattern yields cost reductions only for hydrophobic particles, *i.e.* with  $\theta > 90^\circ$  [129].

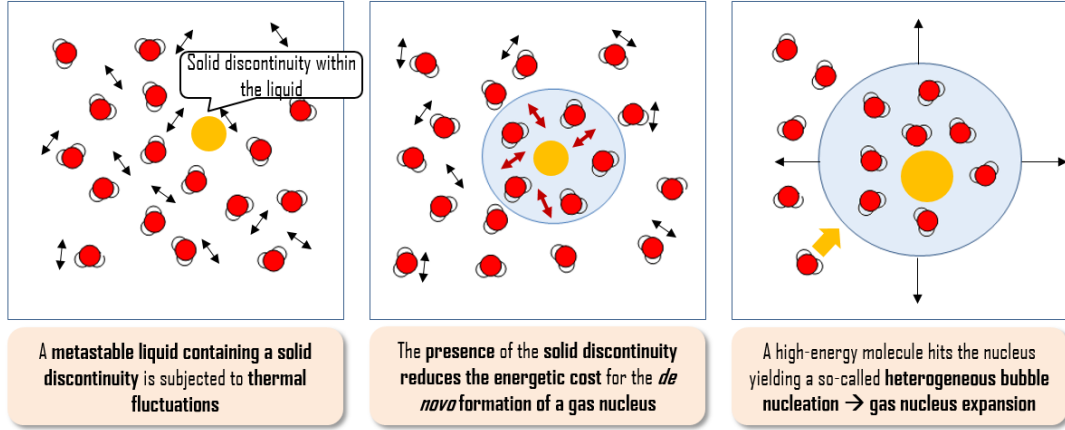


Figure 4.12: An illustration of the postulated mechanism behind the de novo formation of a gas nucleus around a solid discontinuity present within the liquid. The molecules are obviously not in scale with respect to the solid discontinuity.

The energy barrier reduction is usually expressed by a so-called heterogeneity factor  $\xi$ , which is a multiplicative term for the energy cost  $\Delta F_{max}$  given in Equation (4.24) [29]. With  $J_{SN}$  the de novo nucleation rate onto or around a solid discontinuity, this yields:

$$J_{SN} = \lambda N_o \exp\left(\frac{-\xi \Delta F_{max}}{k_B T_G}\right) \quad (4.29)$$

Many researchers investigated the potential expressions for  $\xi$ . Among them is *Bankoff*, who provided the community with an expression for the heterogeneity factor in case of a flat solid surface in 1957, denoted as [6]:

$$\xi_{flat} = \frac{2 + 2 \cos \theta + \cos \theta \sin^2 \theta}{4} \quad (4.30)$$

In case of a solid crevice, idealized as a conical cavity with an opening semi-angle  $\beta$ , as already shown in Figure 4.5, the heterogeneity factor  $\xi_{crevice}$  is still given by Equation (4.30), by replacing  $\theta$  with its so-called effective value  $\theta'$ , given by [29]:

$$\theta' = \frac{\pi}{2} + \theta - \beta \quad (4.31)$$

thus,

$$\xi_{crevice} = \frac{2 + 2 \cos \theta' + \cos \theta' \sin^2 \theta'}{4} \quad (4.32)$$

At last, in case of a spherical solid particle of radius  $r_p$ , for contact angles bigger than  $90^\circ$  (*i.e.* corresponding to an hydrophobic contact, the only one leading to a de novo nucleation from a solid sphere), its corresponding heterogeneity factor  $\xi_{sphere}$  can be approximated as [36]:

$$\xi_{sphere} \approx 1 - \left( \frac{r_p}{r^*} \right)^2 \cos \theta \quad (4.33)$$

with the critical radius  $r^*$  given by Equation (4.14), with  $r_b = r^*$ , and whatever  $\theta$ . Even if all those situations lead to an energy barrier reduction when compared with the liquid bulk de novo nucleation, it is frequently admitted that they are less probable than the ones based on the pre-existence of an entrapped gas nucleus, which are virtually costless [130]. But in the present study where high dissolved gases supersaturations are reached within the water pool, the question of the occurrence of this peculiar de novo nucleation mode is worth being explored, as it has been already discussed for its bulk counterpart.

## 4.2 An interpretation of the observed wall nucleation

As mentioned in Chapter 3, the observed wall nucleation, be the walls heated or unheated, is most likely originating from pre-existing gas nuclei entrapped in some crevices or cracks. The present section aims at verifying the above hypothesis, on the basis of the theoretical developments regarding the existence and stability of entrapped gas nuclei that have been exposed in Section 4.1.2.

### 4.2.1 The activation of a gas nucleus pre-existing in a wall crevice

**An estimate of the characteristic lengths of the walls crevices** At first, let us assume as an idealization, the presence of numerous cylindrical crevices onto the walls of the pool where some bubble nucleation was occasionally observed. The wide spectrum of geometrical features characterizing those cavities is here reduced to a mean cavity height, assumed equal to the  $R_z$  of the wall surface. In surface metrology, we recall that  $R_z$  is namely, for a given solid surface, the area-averaged maximum peak-to-valley height [39], depicted in Figure 4.13.

The idealized cavity is also described by  $r_c$ , a mean cavity radius and its geometry is illustrated in Figure 4.7. As already discussed, another classical type of idealization consists in associating the crevices with conical cavities [129]. However, the latter implies knowing one more geometrical parameter, *i.e.* the conical cavity opening angle.

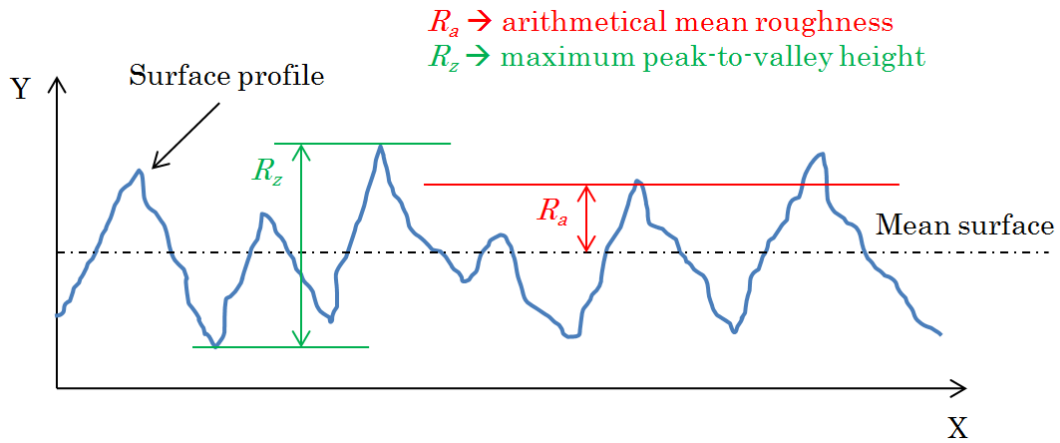


Figure 4.13: Illustration of the two main variables characterizing a solid surface roughness in surface metrology: the arithmetical mean roughness  $R_a$  and maximum peak-to-valley height  $R_z$ .

The order of magnitude of this very angle being unknown in the present case and by the way, being hard to estimate from the available surface metrology data, the conical cavity idealization is therefore more uncertain than the cylindrical one and is thus discarded in what follows. The liquid/wall wettability is quantified by the so-called contact angle  $\theta$ . The liquid/wall  $\theta$  was estimated *a priori*. First of all, for the very polished heated surface, located at the bottom of the pool vessel,  $\theta = 77^\circ$  was retained as an appropriate value for the pair of materials “stainless steel/water” [109]. For the roughest unheated vertical wall of the pool vessel and the same pair of materials, the expected value for  $\theta$  is to be smaller than  $77^\circ$  because of the surface roughness, according to *Wenzel* [123]. Many models are available for estimating the wall roughness effect on the contact angle, such as the ones discussed in [33]. However, in order to get a more reliable estimate of  $\theta$  for the roughest wall, an empirical way was retained. The contact angle between the rough wall and water was deduced from the measurement of the height  $z_m$  at which the meniscus forming in between the liquid free surface and the unheated wall usually stabilizes when the test device is initially filled up with water, as represented in Figure 4.14.

Next, by assuming that the meniscus is only subjected to capillary and hydrostatic pressure forces, one can express the forces balance at its level as follows [33]:

$$\sigma \sin \theta + \frac{1}{2} \rho_L g z_m^2 = \sigma \quad (4.34)$$

where  $\rho_L$  and  $\sigma$  are respectively the liquid density and gas/liquid surface tension and  $g$ , the gravitational acceleration. This equation is often rearranged as [17]:

$$\rho_L g z_m^2 = 2\sigma (1 - \sin \theta) \quad (4.35)$$

For an observed meniscus mean height  $z_m$  of approximately 2 mm (value obtained on the basis of five observations), a liquid density  $\rho_L = 1000 \text{ kg/m}^3$ , a surface tension

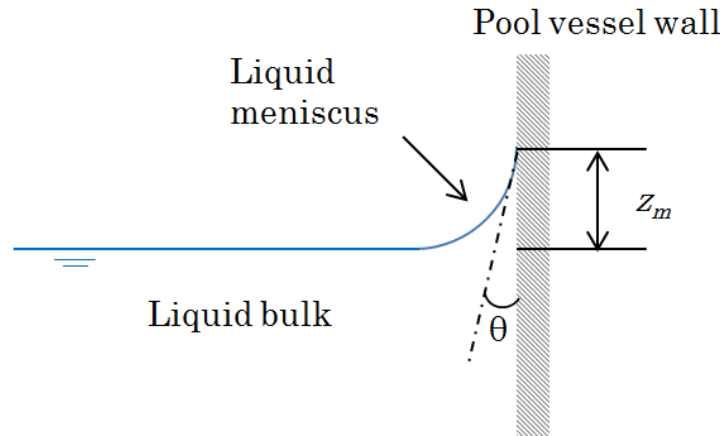


Figure 4.14: Illustration of the capillary meniscus that is expected to form between the liquid bulk and pool vessel vertical walls.

$\sigma = 0.072 \text{ J/m}^2$  the application of Equation (4.35) yields  $\theta = 60^\circ$ , which corresponds to an hydrophilic liquid/solid contact, smaller but close to the one expected between a finely-polished stainless steel surface and water (hydrophilic too), in agreement with *Wenzel's* observations [123].

Further on, according to *Yan* [129], only the hydrophilic cylindrical cavities whose height  $R_z$  complies with the following geometrical criterion can capture a gaseous nucleus during the filling stage of the pool vessel and later act as a nucleation site:

$$R_z > \frac{2 r_c}{\tan \theta} \quad (4.36)$$

On the basis of those geometrical features, the radius of curvature  $r_i$  of the gas/liquid interface of the nucleus entrapped in such a cavity can be deduced from the geometrical relation [129]:

$$r_i = \frac{r_c}{\cos \theta} \quad (4.37)$$

At last, one can thus apply the above equations to the particular parameters of the finely-polished and rough stainless steel surfaces of the pool vessel. The obtained values, listed in Table 4.1 for both types of solid surfaces, are central to the occurrence study of the wall nucleation. Indeed, one way to assess the potential activation of the nucleation sites idealized herein consists in comparing the interfacial radius  $r_i$  of the postulated pre-existing gaseous nucleus with its expected so-called critical radius  $r^*$ , a threshold value from which the nucleus deviates from equilibrium and starts to grow. As already developed, its value depends on local thermodynamic parameters, which allows determining the thermal requirements for the observation of a wall bubble nucleation.

**The local liquid superheat required for gas nucleus activation** In order to express the thermodynamic stability conditions of a gas nucleus entrapped in the walls as a local

Table 4.1: The estimate of the characteristic lengths of the finely-polished and rough stainless steel walls of the pool vessel.

Parameter	Finely-polished surface	Rough surface
$R_a$	0.1 $\mu\text{m}$	3 $\mu\text{m}$
$R_z$	0.3 $\mu\text{m}$	12.5 $\mu\text{m}$
$\theta$	77°	60°
Bounding $r_c$	0.6 $\mu\text{m}$	11 $\mu\text{m}$
Bounding $r_i$	2.7 $\mu\text{m}$	22 $\mu\text{m}$

liquid superheat, denoted as  $(\Delta T_{sat})_{crit}$ , one can make use of the so-called *Clausius-Clapeyron equation*:

$$\left(\frac{dP}{dT}\right)_{sat} = \frac{\mathcal{L}_w}{T_{sat}(v_G - v_L)} \quad (4.38)$$

where  $\mathcal{L}_w$  is the water specific latent heat and  $v_G$  and  $v_L$  are respectively the steam and liquid water specific volumes. Under low pressure conditions such as the ones studied in the Aquarius experiment,  $v_G \gg v_L$ , which yields:

$$\left(\frac{dP}{dT}\right)_{sat} \approx \frac{\mathcal{L}_w}{T_{sat}v_G} \quad (4.39)$$

Under these very conditions, the steam behaviour is well predicted by the so-called *perfect gas law*:

$$P_{sat}\mathcal{M}_wv_G = \mathcal{R}T_{sat} \quad (4.40)$$

with  $\mathcal{M}_w$ , the water molar mass and  $\mathcal{R}$ , the perfect gas constant. Next, substituting the perfect gas law into Equation (4.39) gives:

$$\frac{1}{P_{sat}}dP_{sat} \approx \frac{\mathcal{L}_w\mathcal{M}_w}{\mathcal{R}T_{sat}^2}dT_{sat} \quad (4.41)$$

which for small local variations of either  $P_{sat}$  or  $T_{sat}$  yields:

$$\Delta T_{sat} \approx \frac{\mathcal{R}T_{sat}^2}{P_{sat}\mathcal{L}_w\mathcal{M}_w}\Delta P_{sat} \quad (4.42)$$

At last, substituting Equation (4.51) into (4.14) and retaining as the local saturation conditions:

- $P_{sat} = P_L$ ;
- $T_{sat} = T_{sat}(P_L)$ .

gives:

$$(\Delta T_{sat})_{crit} \approx \frac{\mathcal{R}T_{sat}^2(P_L)}{P_L\mathcal{L}_w\mathcal{M}_w} \left( \frac{2\sigma}{r_i} - P_a^L \right) \quad (4.43)$$

which is the critical local liquid superheat retained in what follows when estimating the occurrence of bubble nucleation. From Equation (4.43), one can notice that  $(\Delta T_{sat})_{crit}$

is a decreasing function of  $r_i$ : small gas nucleus radii require large local liquid superheats for stability and vice versa. The amount of dissolved gases present within the liquid, here represented as the air partial pressure term  $P_a^L$ , plays the same role. The required superheat is indeed reduced when more gases are dissolved within the liquid bulk. Interestingly, there exists a singular amount of dissolved gases from which  $(\Delta T_{sat})_{crit}$  may become negative. This value, denoted as  $(P_a^L)_{crit}$ , is obviously equal to:

$$(P_a^L)_{crit} = \frac{2\sigma}{r_i} \quad (4.44)$$

and is gas-nucleus-radius-dependent, as one might expect. A numerical application of Equation (4.44) to the finely-polished and rough solid surfaces of the pool vessel yields:

- $(P_a^L)_{crit} = 533$  mbar, for the finely-polished surface;
- $(P_a^L)_{crit} = 65$  mbar, for the rough surface.

Thus, a positive superheat may be no longer required for activating the growth of a gas nucleus entrapped in the walls when  $P_a^L > (P_a^L)_{crit}$ , provided there pre-exists such nucleus at that very location. Apart from this change of sign of  $(\Delta T_{sat})_{crit}$  for large values of  $P_a^L$ , Equation (4.44) also exhibits a local liquid pressure dependence, reflected through the term  $\mathcal{R}T_{sat}^2(P_L)/P_L \mathcal{L}_w \mathcal{M}_w$ . This dependence is plotted in Figure 4.15, against the local liquid pressure  $P_L$ , ranging in between 10 and 100 mbar. As one can observe,  $(\Delta T_{sat})_{crit}$  is a decreasing function of  $P_L$  in the studied pressure range.

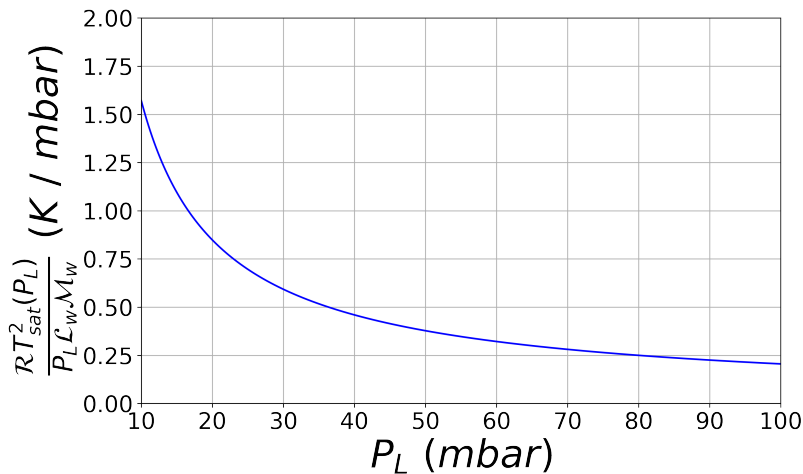


Figure 4.15: Variations of the pressure-dependent term of  $(\Delta T_{sat})_{crit}$  against the liquid local pressure  $P_L$ .  $(\Delta T_{sat})_{crit}$  is a decreasing function of  $P_L$  over the studied pressure range (10 - 100 mbar).

At last, we plot in a more synthetic way in Figure 4.16 the overall variations of  $(\Delta T_{sat})_{crit}$  against the partial pressure of dissolved air  $P_a^L$ , centered around its critical value  $(P_a^L)_{crit}$ , and the liquid local pressure  $P_L$ , for both types of pool vessel solid

surfaces. As discussed in the next sections, the understanding of these variations is central to the interpretation of the observed bubble nucleation processes onto the pool vessel walls.

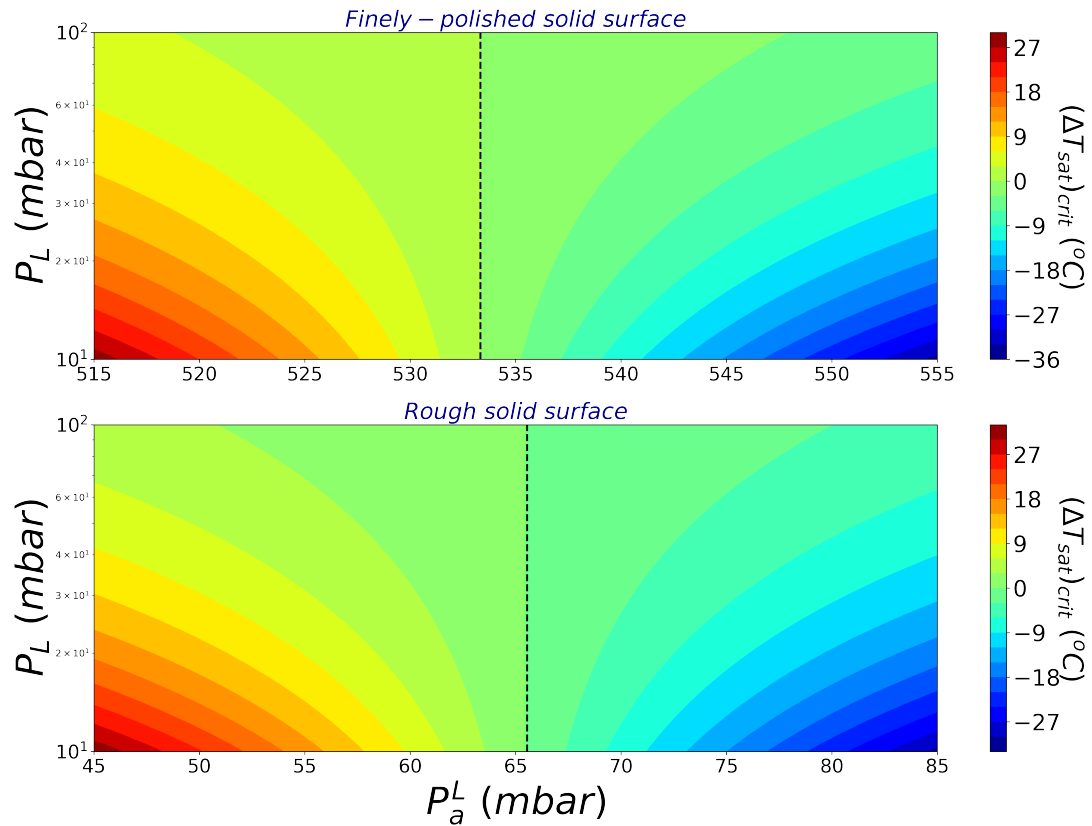


Figure 4.16: Variations of  $(\Delta T_{sat})_{crit}$  against the liquid local pressure  $P_L$  and partial pressure of dissolved air  $P_a^L$ . Upper map: estimate for the finely-polished solid surface. Lower map: estimate for the rough solid surface.

## 4.2.2 The bubble formation onto the heated wall

In what follows, we further analyze the strong but time-limited bubble formation process that was observed onto the heated wall during some of the pool flashing experiments, as discussed in Chapter 3. The tests that are considered for that purpose are described in Table 4.2. The first of those tests consists in the reference case, already presented in Chapter 3. Then are chosen three additional tests which are each differing from the reference case by a variation of either the initial pool level, operating pressure or initial content in dissolved gases. All of them were performed at a fixed heating power  $\dot{Q}_p$  of 1000 W, which was suited for observing a bubble formation process onto the heated wall.

For assessing the likelihood of a gas nucleus activation onto this very surface, a time-dependent local wall superheat denoted as  $\Delta T_{sat;h}$  is first computed for all of those

Table 4.2: The selected tests for studying bubble nucleation onto the heated wall.

Test type	$\dot{Q}_p$ (W)	$P_G$ (mbar)	$z_p(0)$ (cm)	$C_{O_2}(0)$ (mg/L)
Reference test	1000	22	30	6.5
Sensitivity to initial pool level	1000	22	<b>20</b>	6.5
Sensitivity to operating pressure	1000	<b>42</b>	30	6.5
Sensitivity to initial content in dissolved gases	1000	22	30	<b>0.15</b>

tests. This quantity reads:

$$\Delta T_{sat;h} = T_h - T_{sat}(z = 0) \quad (4.45)$$

with  $T_h$ , the estimated mean wall temperature of the heat source, defined as:

$$T_h = \frac{1}{2} (\text{T131W} + \text{T134W}) \quad (4.46)$$

and  $T_{sat}(z = 0)$ , the saturation temperature estimated at the location of the heaters, from the measurement of the pool bottom pressure **P150Ap**.  $\Delta T_{sat;h}$  is then compared with the estimate of the critical liquid superheat  $(\Delta T_{sat})_{crit}$ , defined by Equation (4.43). In this equation,  $P_L$  is obviously replaced by the measured pool bottom pressure **P150Ap**. The radius of curvature of the postulated pre-existing gas nucleus  $r_i$  is equal to  $2.7 \mu\text{m}$  (*cf.* Table 4.1) and  $P_a^L$ , the dissolved air partial pressure, is derived from the dissolved  $O_2$  concentration measurement, as detailed in Chapter 2. On that basis, the activation of a gas nucleus onto the heated wall is judged likely if  $\Delta T_{sat;h} > (\Delta T_{sat})_{crit}$  and unlikely otherwise.

The results obtained for the selected tests are plotted in Figure 4.17. First of all, in the upper-left graph is showed the time-trend of  $\Delta T_{sat;h}$  and  $(\Delta T_{sat})_{crit}$  over the initial 10 min of the reference test. One can notice that  $\Delta T_{sat;h}$  keeps higher than  $(\Delta T_{sat})_{crit}$  during roughly the first 4 min. Along this period, the bubble formation from some postulated pre-existing gas nuclei entrapped in the heated wall was hence a likely process and was actually observed during such a short period, as seen in Chapter 3. Next, when the initial pool level is reduced down to 20 cm, this period reduces accordingly, as seen in the upper-right graph. This is consistent with the phenomenological observation of a faster bubble nucleation process onto the heated surface with a reduced initial pool level (*cf.* Chapter 3). Varying the operating pressure up to 42 mbar leads to the same but more intensive effect of a shortened period for bubble nucleation, as visible in the lower-left graph. At last, in agreement with the noticed absence of bubble nucleation when starting a test with a high depletion in dissolved gases within the liquid pool, the time trends of  $\Delta T_{sat;h}$  and  $(\Delta T_{sat})_{crit}$  do not intersect at all during the fourth test, as observed in the lower-right graph.

Interestingly, a focus on the only  $\Delta T_{sat;h}$  variable provided in Figure 4.18 shows that for both the reference case and the sensitivity test to the initial pool level, the heated wall superheat was actually negative whereas the liquid boiled off onto this very surface during the first minutes of the experiments. This observation may seem counter-intuitive at first glance. It is however consistent with the theoretical developments achieved in Section 4.2.1 and the experimental work of *Mori et al.* [89]. Further on, when compared

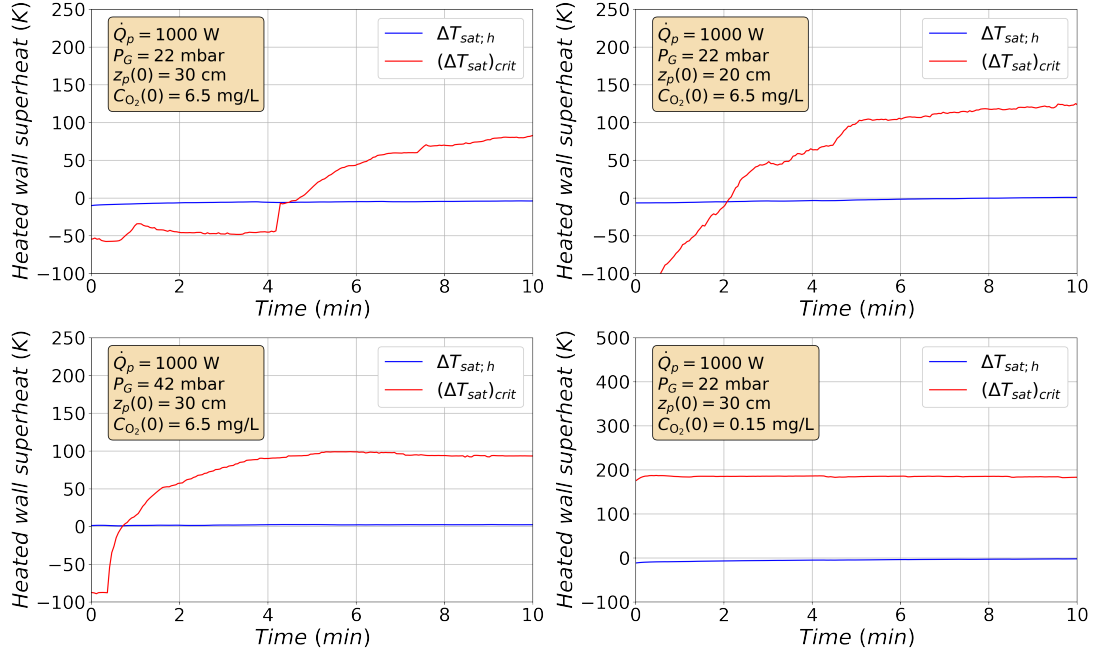


Figure 4.17: Time variations of  $(\Delta T_{sat})_{crit}$  and  $\Delta T_{sat,h}$ , evaluated at the heated wall, for the four selected tests. The graphs are plotted over only the first 10 min of a test, *i.e.* when the bubble nucleation process is likely to occur at the heated wall.

with the reference case, the obtained  $\Delta T_{sat,h}$  for the sensitivity tests to the operating pressure and initial pool level are higher, which is phenomenologically consistent. Indeed, at a smaller initial pool level and an unchanged operating pressure, the measured hydrostatic pressure **P150Ap** is obviously smaller, so does  $T_{sat}(z = 0)$ .  $T_h$  being primarily dependent to the imposed heating power  $\dot{Q}_p$ , as a first order approximation, and this power being identical for all tests, a lower initial pool level thus implies a bigger  $\Delta T_{sat,h}$ . Raising the operating pressure up to 42 mbar has the same reduction effect on the measured pressure **P150Ap** and hence on  $T_{sat}(z = 0)$ , as already discussed in Chapter 2. For the same reasons, it is therefore expected to reach a higher  $\Delta T_{sat,h}$  at a higher operating pressure, when compared with the reference case.

Eventually, one may wonder why the critical liquid superheat  $(\Delta T_{sat})_{crit}$  varies so strongly from one considered test to another, yielding in turn a varying bubble formation duration. A close look at Equation (4.43) allows answering this question. Indeed, according to the proposed theoretical developments and for a fixed radius of curvature  $r_i$ ,  $(\Delta T_{sat})_{crit}$  is a function of the only hydrostatic pressure  $P_L$  and dissolved air partial pressure  $P_a^L$ . As seen in Figure 4.19,  $P_a^L$  is the variable which shows the strongest variation along the studied 10-min period and is hence the main contributor to the observed strong variation of  $(\Delta T_{sat})_{crit}$ . Hence, this highlights the key role played by the degassing phenomenon on the duration of the bubble nucleation process onto the heated surface, under the presented experimental configuration.

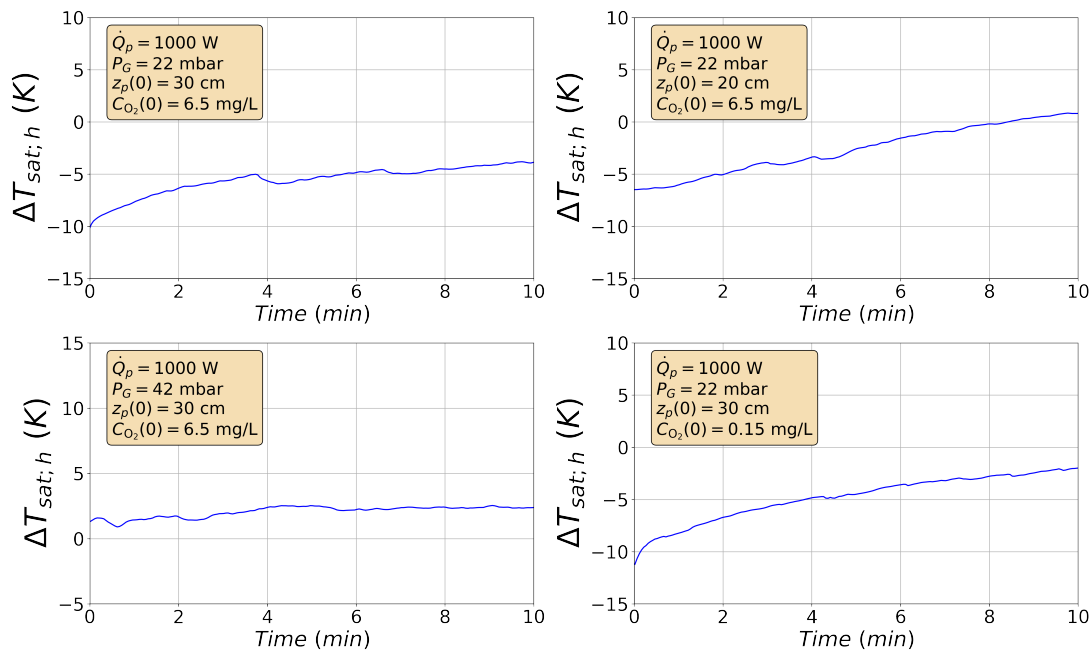


Figure 4.18: A focus on the time variation of  $\Delta T_{sat,h}$ , evaluated at the heated wall, for the four selected tests. The graphs are plotted over only the first 10 min of a test, *i.e.* when the bubble nucleation process is likely to occur at the heated wall.

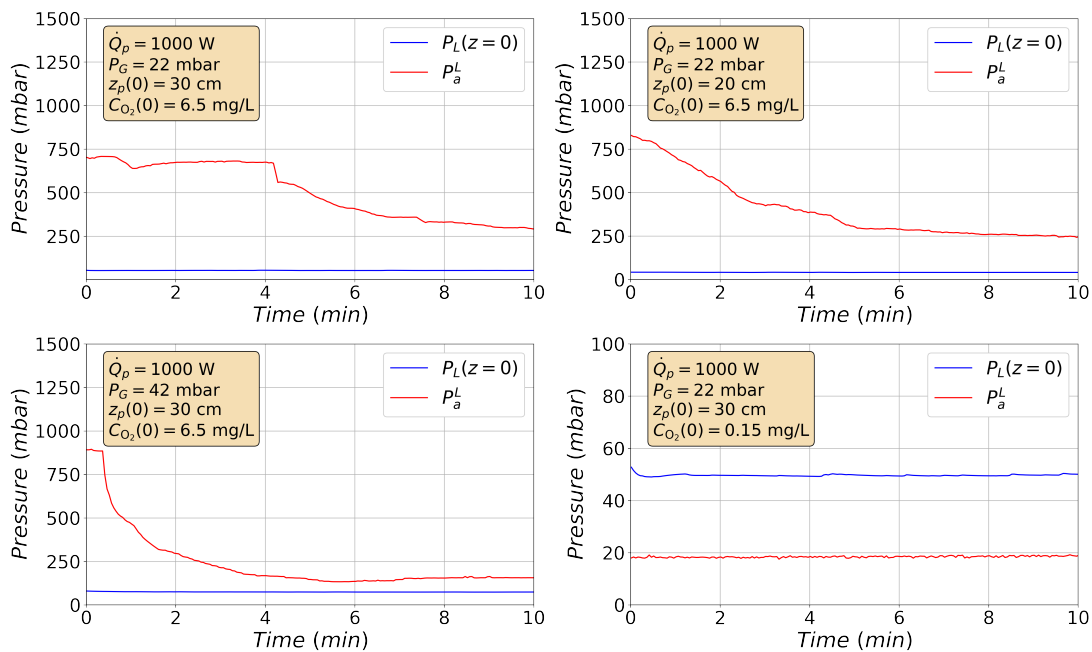


Figure 4.19: Time variations of the hydrostatic pressure  $P_L$  at the bottom of the pool and dissolved air partial pressure  $P_a^L$ . The graphs are plotted over only the first 10 min of a test, *i.e.* when the bubble nucleation process is likely to occur at the heated wall.

### 4.2.3 The bubble formation onto the roughest unheated wall

In this section, as for the heated wall nucleation, we analyze the energetic conditions for a bubble formation onto the roughest unheated wall (*cf.* Chapter 3). For doing so, we focus on the reference test, already presented in Chapter 3. A time-dependent local unheated wall superheat denoted as  $\Delta T_{sat;w}$  is first computed. This quantity reads:

$$\Delta T_{sat;w} = T_w(z) - T_{sat}(z) \quad (4.47)$$

where  $T_w(z)$  is the measured unheated wall temperature and  $T_{sat}(z)$  is the estimated local saturation temperature at position  $z$ , which depends on the local pressure  $P_L(z)$ , equal to  $P_G$  for a sensor located above the liquid free surface position and to its hydrostatic value otherwise:

$$P_L(z) = P_G + \rho_L g (z_p - z) \quad (4.48)$$

with  $\rho_L$ , the liquid density, estimated at temperature  $T_L$ ,  $z$  the temperature sensor's location and  $z_p$ , the pool collapsed level, computed as:

$$z_p = \frac{m_L}{\rho_L S_p} \quad (4.49)$$

where  $m_L$  is the liquid pool mass and  $S_p$ , the pool free surface area. For estimating  $\Delta T_{sat;w}$ , the ten temperature sensors embedded in the roughest unheated wall are later considered. Their reference and positioning are listed in Table 4.3.  $\Delta T_{sat;w}$  is then compared with an estimate of the critical liquid superheat  $(\Delta T_{sat})_{crit}$ , computed from Equation (4.43). In the latter,  $P_L$  is estimated at each temperature sensor location provided in Table 4.3. The radius of curvature of the postulated pre-existing gas nucleus  $r_i$  is equal to 22  $\mu\text{m}$  (*cf.* Table 4.1) and  $P_a^L$ , the dissolved air partial pressure, is derived from the dissolved  $\text{O}_2$  concentration measurement, as justified in Appendix B. On that basis, the activation of a gas nucleus onto the unheated rough wall is judged likely if  $\Delta T_{sat;w} > (\Delta T_{sat})_{crit}$  and unlikely otherwise.

Table 4.3: Reference of the Pt-100 thermometers embedded in the rough vertical wall of the pool vessel and their vertical position.

Sensor reference	z-position (cm)
T100W	2.0
T101W	5.5
T102W	9.0
T103W	12.5
T104W	16.0
T105W	19.5
T106W	23.0
T107W	26.5
T108W	30.0
T109W	33.5

The results obtained for the reference case are exhibited in Figure 4.20. In the latter, the upper map represents the time trend of an interpolation of the unheated wall vertical temperature profile, achieved on the basis of the ten discrete measurements detailed in Table 4.3. In this map is also plotted the estimate of the pool collapsed level  $z_p$ , which is useful to figure out the vertical extent of the liquid pool over time. As expected, the unheated wall temperatures get more and more hotter when time goes by. Those temperatures stabilize somehow from 3.5 hours, in agreement with the already noticed trend of the liquid pool temperature in Chapter 3. Interestingly, one can notice the almost complete uniformity of the vertical temperature profiles over time. The observed temperature differences from one sensor to another are indeed smaller than their associated measurement uncertainty (*i.e.* around  $0.5^\circ\text{C}$ , *cf.* Chapter 2). Consequently, at any time, there is most likely no significant heat conduction along the vertical axis of the unheated wall, thereby discarding the latter phenomenon in the mechanism leading to bubble nucleation.

Next, the lower map of Figure 4.20 represents the time trend of an interpolation of the unheated wall vertical superheat profile  $\Delta T_{sat;w}$ . This map shows, as expected, an increase in  $\Delta T_{sat;w}$  as the vertical position gets closer to the liquid free surface. During the first half of the test,  $\Delta T_{sat;w}$  keeps negative at any location. The latter starts becoming positive and of the order of  $2^\circ\text{C}$  during the second half of the test. However, as discussed for the heated wall, negative or only slightly positive local superheats do not necessarily prevent the bubble nucleation process from occurring, as long as there are enough dissolved gases in presence within the liquid. Let us further investigate this possibility by comparing the maximum value of  $\Delta T_{sat;w}$ , denoted as  $\text{Max}(\Delta T_{sat;w})$ , with its corresponding critical liquid superheat  $(\Delta T_{sat})_{crit}$ . As seen in the lower map of Figure 4.20, the maximum of  $\Delta T_{sat;w}$  being always reached close to the liquid free surface, one can hence retain  $P_L(z) = P_G$  in the computation of  $(\Delta T_{sat})_{crit}$ . The obtained results are given in Figure 4.21. As one can notice,  $\text{Max}(\Delta T_{sat;w})$  is higher than  $(\Delta T_{sat})_{crit}$  during the first hour of the reference test. Along this period, the bubble formation from some postulated pre-existing gas nuclei entrapped in the unheated rough wall was hence a likely process. The latter was however not observed during the reference test, as shown in Chapter 3. Its observation was only possible with a complete drainage, dry out of the inner walls and refill of the pool vessel, prior to a test, as already discussed, which was not part of the followed typical procedure. Hence, this questions the potential deactivation of pre-existing and entrapped gas nuclei that may result from the experimental procedure retained in this study. This point is the topic of the next section.

#### 4.2.4 The deactivation mechanisms of the gas nuclei entrapped in a wall

Because the stability of a postulated gas nucleus entrapped in a wall cavity is not unconditional (*cf.* Section 4.1.2), the presence of such nuclei is thus sensitive to the pressure-

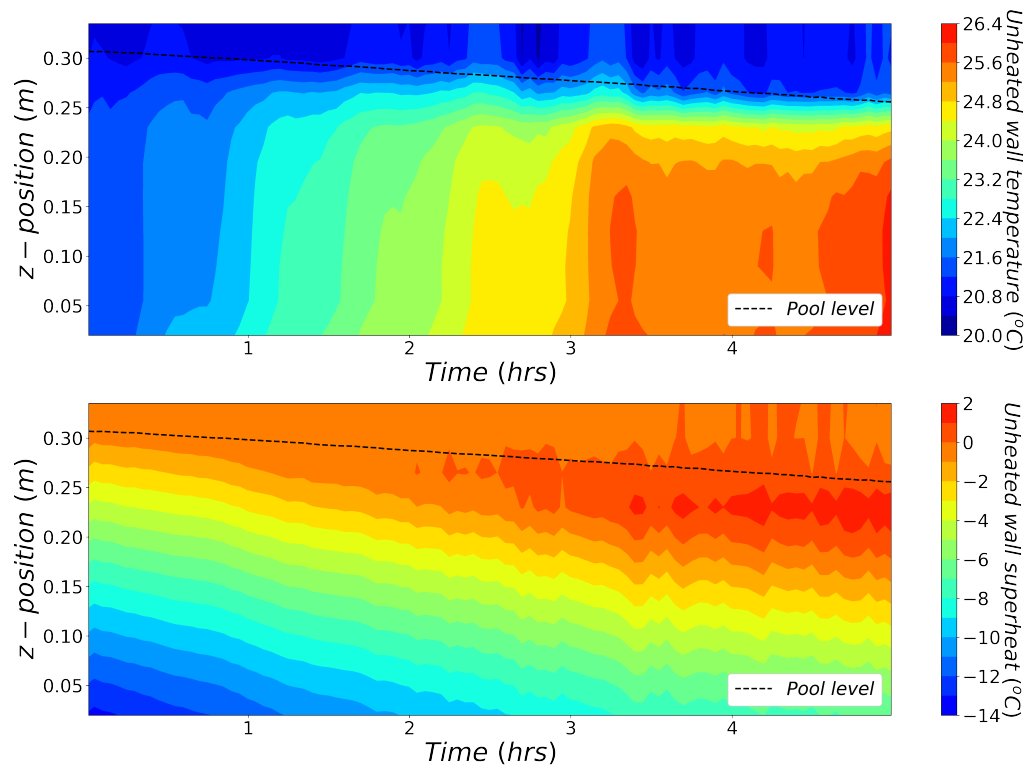


Figure 4.20: Unheated rough vertical wall of the pool vessel. Upper map: time trend of an interpolation of the unheated wall vertical temperature profile, achieved on the basis of the ten discrete measurements detailed in Table 4.3. Lower map: time trend of an interpolation of the unheated wall vertical superheat profile  $\Delta T_{sat;w}$ .

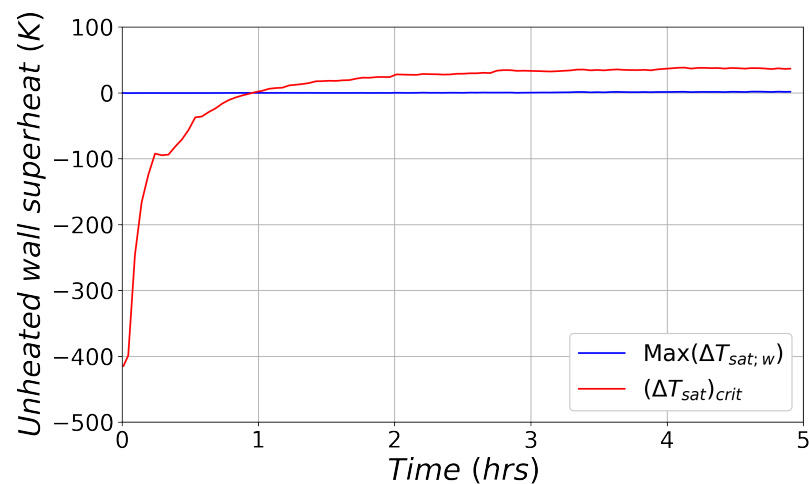


Figure 4.21: Comparison of the maximum value of  $\Delta T_{sat;w}$ , denoted as  $\text{Max}(\Delta T_{sat;w})$ , with its corresponding critical liquid superheat  $(\Delta T_{sat})_{crit}$ , at the unheated rough wall of the pool vessel, during the reference case.

temperature history of the studied system. This sensitivity is actually observed. Indeed, in the thermal-hydraulic community, *Kottowski* mentioned in [67] the deactivation of wall nucleation sites during the normal operation of nuclear reactors, as a consequence

of changes in pressure and/or temperature. Regarding the nucleation within liquid metals, *Holtz* performed a study of this effect in [53]. For water boiling, one can mention for instance the work of *Faw et al.* in 1986 [40]. In the field of water cavitation, the phenomenon is also well-known [115]. The first work on the topic dates back to the pioneering research of *Harvey et al.* performed in 1944. In their study, *Harvey et al.* pre-pressurized a sample of water up to 1090 bar during 15-30 min. The sample was then subjected to the atmospheric pressure and heated up to the onset of boiling. The pre-pressurized water did not boil up before reaching 202°C, which was a first evidence of a pressure history effect on the presence of gas nuclei within the liquid, be it onto its container walls or onto some suspended solid particle [51]. Since then, the effect was further explored by many authors, like *Knapp*, in 1958 [65] or more recently *Ma*, in 1994 [78] and *Ohl et al.*, in 2007 [15].

From one test to another performed within the *Aquarius* experimental device, a substantial part of the unheated rough wall of the pool vessel, the one located below the liquid free surface, remains underwater. The other part of the wall keeps typically fully wetted in between two consecutive tests, because of the retained test procedure (*cf.* Chapter 2). In the interval, the liquid in contact with the unheated rough wall is subjected to a wide pressure-temperature transient. Let us briefly recall this procedure. At the end of the first test, the liquid is at its higher temperature, under the retained low operating pressure and almost fully depleted in dissolved gases. In between the two tests, the liquid pool keeps isolated from the outer atmosphere by remaining under vacuum conditions (this period typically lasts a night). The heat power is also shut down and the liquid gradually cools down, while keeping almost free from dissolved gases. Next, just before the second test, the still gas-free liquid is re-pressurized at one atmosphere. Clearly, this imposes a large thermodynamic disequilibrium to the non-condensable gases nuclei that could remain stabilized up to that point and the latter are thus expected to re-dissolve in water, with a relatively fast kinetics whose characteristic time can be estimated by means of Equation (4.19). Then, some fresh and cold water supply is achieved in order to meet a required initial pool level. The vapor content of those same nuclei can be subjected to a similar process in the interval and recondense. Then, some air is bubbled through the liquid pool until a requested initial dissolved O<sub>2</sub> concentration is reached. At last, the liquid heating is launched and the latter gradually warms up to some desired level. From that point, the second test starts by depressurizing the pool vessel down to its expected operating pressure. Having in mind the above extensive set of experimental evidence in favor of an impact of pressure-temperature transients on the stability of entrapped gas nuclei, the deactivation of the gas nuclei entrapped in rough wall crevices in between two consecutive tests appears as a likely process. However, one may wonder why only the unheated rough wall seems sensitive to pressure-temperature-history effects. Some authors like *Faw et al.* and *Singer and Holtz* studied theoretically the thermodynamic conditions for a complete collapse of an initially-stable entrapped gas nucleus. Their modeling highlighted the impact of the cavity size on the tolerance to gas nucleus deactivation by collapse [40], [106]: the big-

ger the cavity size, the lower its tolerance to thermodynamic disequilibrium conditions, and vice versa. Hence, the differences in cavity size between the unheated rough wall and its heated counterpart, with the crevices of the rough wall being larger (*cf.* Table 4.1), may reasonably explain the observed differential gas nuclei deactivation. We are to mention that a numerical estimate of these differences based on the models evocated above is not straightforward, since it requires knowing much more information about the postulated wall cavities and the exact pressure-temperature history in between two consecutive tests.

Another mechanism can be hypothesized for the deactivation of the entrapped gas nuclei. This mechanism has been recently mentioned in the cavitation literature by *Lohse et al.* in [16]. In details, *Lohse et al.* postulated that, under some pulsed pressure variations, some pre-existing gas nucleus may collapse according to the mechanism simulated in Figure 4.22 by the authors (figure extracted from [16]). Under the action of a pressure pulse, it is hypothesized that a liquid jet forms at the stressed nucleus interface. The latter is conditionally energetic enough for completely reaching the bottom of the wall crevice and wetting it, thereby removing any remnant gas. For investigating this point, the authors made use of an interface-resolved method based on the so-called boundary-integral approach [11]. Provided this mechanism, and for a given positive excursion of the liquid pressure  $P_L$ , the energy of the liquid jet is to be sensitive to the inner pressure of the gas nucleus. However, this pressure is a decreasing function of the gas nucleus interfacial radius  $r_i$ , as expressed by Equation (4.14). Therefore, larger gas nuclei appear more prompt to collapse than smaller ones, under the action of a pressure pulse. Reminding that, during the gravity-driven pool flashing experiments of the present research, there systematically exists some regime of sporadic bubble nucleation yielding large pulsatile variations of the liquid pressure (the latter being observed lately in a test, when the liquid superheat is high and the dissolved gas depletion is almost complete, *cf.* Chapter 3), the mechanism proposed by *Lohse et al.* appears as another serious candidate for explaining the observed deactivation of the unheated wall gas nuclei. In this very case, the deactivation would hence occur lately during a test and not in between two consecutive experiments. The real cause for the gas nuclei deactivation is most likely in between those two hypothesis. We however leave more in-depth studies of the latter as a perspective of the present work.

### 4.3 An interpretation of the observed bulk nucleation

Contrarily to the wall nucleation, the causes leading to the observed bulk nucleation are more uncertain. Indeed, based on the observations and measurements exposed in Chapter 3, it is not straightforward to identify the most probable mode for a bulk nucleation. In what follows, we further analyze the likelihood of all the envisioned bulk nucleation mechanisms, starting with the so-called *de novo* process. Then, a set of experiments that was performed for the specific purpose of exploring the underlying mechanisms of the bulk nucleation is presented.

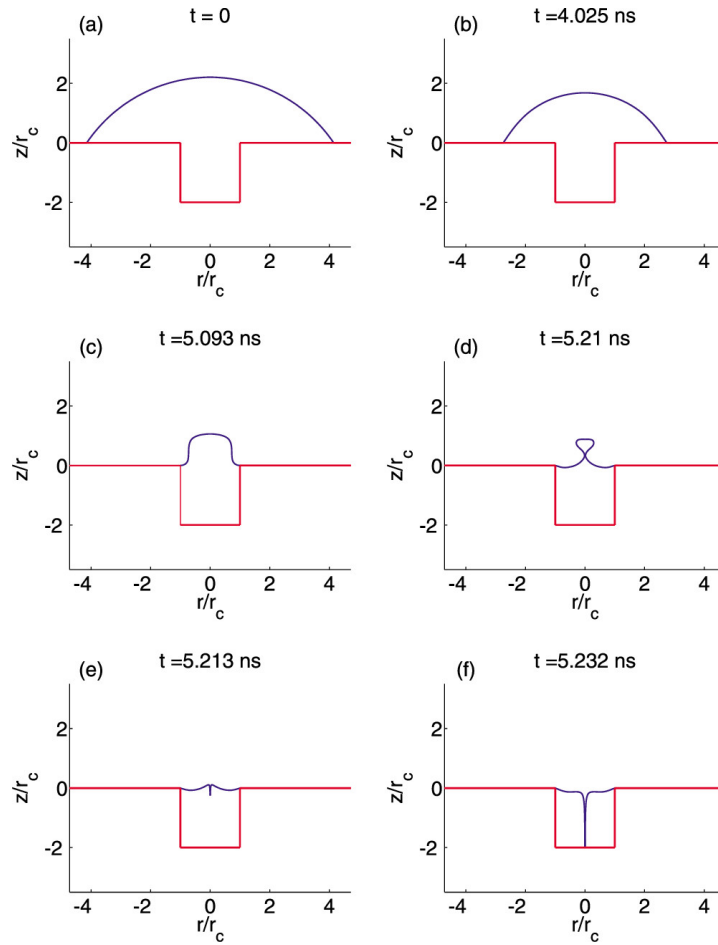


Figure 4.22: Illustration of a collapsing gas nucleus subjected to a pressure pulse, simulated by *Lohse et al.* (figure extracted from [16]). At the stressed nucleus interface, a liquid jet forms. The latter is here able to reach and flood the bottom of the cavity, thereby removing any remnant gas.

### 4.3.1 A study of the liquid bulk de novo nucleation occurrence

In order to study the likelihood of a de novo bubble nucleation within the liquid bulk, let us express the local liquid superheat  $(\Delta T_{sat})_{BN}$  required for observing this very nucleation mode. For that purpose, let us recast Equation (4.26) as follows:

$$P_G - P_L = \left( \frac{16}{3} \frac{\pi \sigma^3}{k_B T_G \ln \left( \frac{\lambda N_a}{J_{BN}} \right)} \right)^{1/2} \quad (4.50)$$

Next, on the basis of the Clausius-Clapeyron equation, we have shown in Section 4.2 that:

$$\Delta T_{sat} \approx \frac{\mathcal{R} T_{sat}^2}{P_{sat} \mathcal{L}_w \mathcal{M}_w} \Delta P_{sat} \quad (4.51)$$

which, with:

- $T_L = T_G$ ;

- $P_G = P_{sat}(T_L) + P_a^L$ ;
- $\Delta P_{sat} = P_{sat}(T_L) - P_L$ .

(cf. Section 4.1.2), yields:

$$(\Delta T_{sat})_{BN} \approx \frac{\mathcal{R}T_{sat}^2(P_L)}{P_L \mathcal{L}_w \mathcal{M}_w} \left( \left( \frac{16}{3} \frac{\pi \sigma^3}{k_B T_L \ln \left( \frac{\lambda N_o}{J_{BN}} \right)} \right)^{1/2} - P_a^L \right) \quad (4.52)$$

by retaining as the local saturation conditions:

- $P_{sat} = P_L$ ;
- $T_{sat} = T_{sat}(P_L)$ .

From Equation (4.52), one can notice that, as for the estimate of the critical local wall superheat introduced above,  $(\Delta T_{sat})_{BN}$  is a function of pressure  $P_L$  through the term  $\mathcal{R}T_{sat}^2(P_L)/P_L \mathcal{L}_w \mathcal{M}_w$ . Hence, having studied yet the variations of  $\mathcal{R}T_{sat}^2(P_L)/P_L \mathcal{L}_w \mathcal{M}_w$  against pressure  $P_L$  in Figure 4.15, one can argue that the local liquid superheat required for a de novo nucleation is a decreasing function of  $P_L$  over the studied pressure range (10 - 100 mbar). All other parameters fixed, the de novo nucleation is hence more likely to occur at higher pressures. Next,  $(\Delta T_{sat})_{BN}$  is similarly a decreasing function of the amount of dissolved gases present within the liquid, here represented by the air partial pressure term  $P_a^L$ . Interestingly again, there exists a singular amount of dissolved gases from which  $(\Delta T_{sat})_{BN}$  may become negative. This value, denoted as  $(P_a^L)_{crit;BN}$ , is obviously equal to:

$$(P_a^L)_{crit;BN} = \left( \frac{16}{3} \frac{\pi \sigma^3}{k_B T_L \ln \left( \frac{\lambda N_o}{J_{BN}} \right)} \right)^{1/2} \quad (4.53)$$

and is temperature-dependent, through the presence of  $T_L$  in this very equation. And around  $(P_a^L)_{crit;BN}$ , the liquid bulk de novo nucleation is to be likely at liquid superheats of a few degrees. Let us estimate this possibility. A numerical application of Equation (4.53) over the temperature range 10 - 100°C is provided in Figure 4.23. For that purpose, we retain for  $J_{BN}$  its minimum value from which one can consider the de novo nucleation as significant, *i.e.* 1 bubble/m<sup>3</sup>/s (cf. Section 4.1.2). The collision frequency term  $\lambda$  is equal to 10<sup>12</sup> s<sup>-1</sup> and the number of water molecules per unit volume  $N_o$  is estimated by means of the below equation:

$$\begin{aligned} N_o &= \mathcal{N}_A \frac{\rho_L}{\mathcal{M}_w} \\ &= 3.35 \times 10^{28} \text{ molecules/m}^3 \end{aligned} \quad (4.54)$$

with  $\mathcal{N}_A$ , the so-called Avogadro's number, equal to  $6.022 \times 10^{23} \text{ mol}^{-1}$ . As seen from Figure 4.23,  $(P_a^L)_{crit;BN}$  is always excessively high over the studied temperature range and of the order of  $10^6$  mbar. This means that, taking  $P_a^L = 1000$  mbar as a reference value for the dissolved air partial pressure of a gas-saturated volume of water in contact with the standard atmosphere, supersaturations bigger than 1000 would be required in order to observe a liquid bulk de novo nucleation for a few degrees of liquid superheat. Such gas supersaturations being by far unreachable within the Aquarius test device, the liquid bulk de novo nucleation mode can be hence confidently discarded.

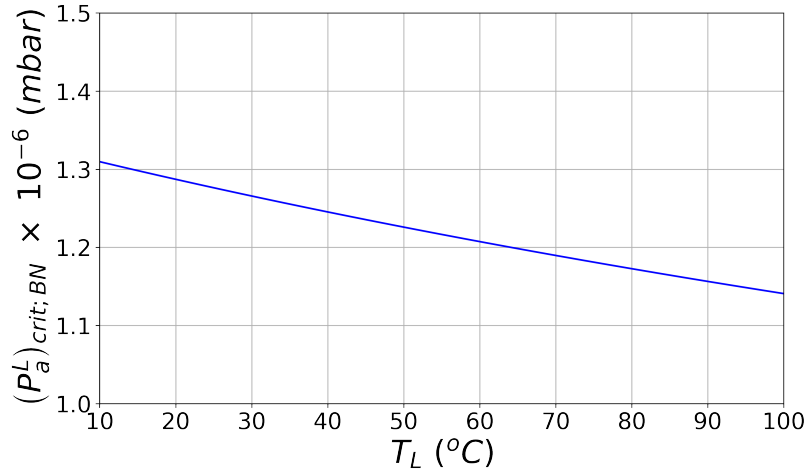


Figure 4.23: Variations of the temperature-dependent term  $(P_a^L)_{crit;BN}$  against the liquid local temperature  $T_L$ .

Let us now estimate the order of magnitude of the required  $(\Delta T_{sat})_{BN}$  in case of a fully gas-depleted water volume, under the conditions of an Aquarius experiment. The term  $\left(\frac{16}{3} \pi \sigma^3 / k_B T_L \ln\left(\frac{\lambda N_o}{J_{BN}}\right)\right)^{1/2}$  being of the order of  $10^6$  mbar in between 10 and  $100^\circ\text{C}$  and  $\mathcal{R}T_{sat}^2(P_L)/P_L \mathcal{L}_w \mathcal{M}_w$  being of the order of 1 K / mbar, one comes up with the unreasonably high value of  $10^6$  K, which by far exceeds the thermodynamic limit of the water superheat, estimated to  $322.75^\circ\text{C}$  [129].

At last, one is left with the de novo nucleation onto a suspended solid particle as the only de novo nucleation mode that can be envisioned up to that point. We recall that, in the presence of such a particle within the metastable liquid, the energy barrier associated with the formation of a proto-nucleus  $\Delta F_{max}$  can be reduced by a factor  $\xi_{sphere}$  which is approximately equal to  $1 - (r_p/r^*)^2 \cos \theta$  for an hydrophobic particle (*i.e.* the only type of wettability leading theoretically to some nucleation, *cf.* Section 4.1.2). A close look at this equation shows that  $\xi_{sphere}$  tends toward zero only for high contact angles close to the limiting value of  $180^\circ$  and large particle sizes  $r_p$ . The utilized water being certainly exempt from almost fully hydrophobic and large (hence, visible) suspended particles, this heterogeneous de novo nucleation is thus judged unlikely as well. At that stage of the analysis, we are left with the nucleation onto pre-existing gas nuclei as the most probable mode within the liquid bulk. But the stability mechanism

behind the postulated pre-existing nuclei, *i.e.* a stabilizing skin or an entrapment within a wall crevice, is still to be determined (*cf.* Section 4.1.2). This point is the topic of the next section.

### 4.3.2 An experimental search for the most probable nucleation mode

In this section, we present a set of experiments that were designed in order to provide some elements for distinguishing the two nucleation modes based on pre-existing gas nuclei. As it has been seen in Section 4.1.2, two nucleation modes may explain the observed liquid bulk nucleation. Those are:

- The nucleation from freely-floating gas nuclei;
- The nucleation from gas nuclei that remain entrapped onto a suspended solid particle.

As already detailed, those modes are each associated with some specific gas nuclei existence and stability conditions. Let us briefly recall them. The gas nuclei postulated entrapped onto some suspended particle (into its corrugated parts and not into some crevice, as it has been discussed in Section 4.1.2) are only subjected to thermodynamic equilibrium conditions. In addition to those conditions, the postulated freely-floating gas nuclei have to fulfill hydrodynamic stability requirements. Indeed, we have demonstrated in Section 4.1.2 that the persistence of such nuclei in water is hydrodynamically possible for the smallest of them, thanks to the Brownian agitation of the liquid molecules. But if one leaves the water resting over a long time period, even stabilized by the Brownian motion, some of those nuclei are prompt to diffuse toward the liquid free surface and escape. This feature is obviously an only characteristic of the freely-floating nuclei.

Therefore, proceeding that way before performing a gravity-driven pool flashing test appears as an interesting tentative for distinguishing the two envisioned nucleation modes. Indeed, assume first that some water volume has been resting for a sufficient time period, with its thermodynamic parameters being almost left unchanged. If the latter, once flashed, yields less bubbles and reaches its so-called asymptotic state with a significantly different kinetics when compared to its reference counterpart (*i.e.* with no preliminary resting period), one might argue that at the beginning of the resting period, there pre-existed some freely-floating nuclei in water of a small size, that partially escaped in the interval. In this very case, the nucleation from those free nuclei would then appear as the main mechanism. And vice versa in favor of the nucleation from gas nuclei entrapped in suspended solid particles, if no main differences are observed.

Based on those considerations, we designed the two tests that are described below. Both tests were performed according to the following set of experimental parameters:

- $\dot{Q}_p = 250 \text{ W}$ ;

- $P_G = 22$  mbar;
- $T_L(0) = 20^\circ\text{C}$ ;
- $z_p(0) = 30$  cm
- $C_{O_2}(0) = 8.8$  mg/L.

Taking advantage from the upcoming Christmas holidays, we prepared in December 14<sup>th</sup>, 2021 about 40 liters of air-saturated water within the Aquarius pool vessel. The latter was then left in contact with the atmosphere of the experimental hall and at rest, around a temperature of  $17^\circ\text{C}$ , during 19 consecutive days. This time period corresponds approximately to the half of the 40 days that were shown associated with the hydrodynamic stabilization of nuclei of a size of the order of 1 nm (*cf.* Section 4.1.2). Right after the preparation of the water volume, no bubbles or nuclei were visible in the liquid phase. The smallest object being visible by naked eyes being of the order of 50  $\mu\text{m}$ , if some gas nuclei were present in water, they were hence of a size smaller than this limiting value. In January 3<sup>rd</sup>, 2022, *i.e.* 19 days later, the same water volume was then utilized for a pool-flashing test. The followed experimental procedure is the standard one, already discussed in Chapter 2. Briefly, the water was first heated at atmospheric pressure up to the required temperature of  $20^\circ\text{C}$ , by parametrizing the resistive heaters at a power of 250 W. In doing so, some convective movements developed in the pool vessel and one may wonder if this was enough for hydrodynamically destabilize the freely-floating nuclei, if they pre-existed. Actually in this very case, the bigger velocity scale reached within the liquid phase (provided the natural convection is more intensive than the Brownian motion) has an even more stabilizing effect [49], as one can figure out from Equation (4.4). Hence, in the interval and provided some freely-floating gas nuclei pre-existed, the latter were not expected to escape from the liquid free surface. Once at a temperature of  $20^\circ\text{C}$ , the liquid was then depressurized down to 22 mbar and the pool-flashing experiment started and lasted 7 hours. The next day, a comparative test was designed with an identical water volume regassed up to 8.8 mg of  $\text{O}_2$  /L, according to the standard bubbling procedure detailed in Chapter 2. Most important, the utilized water did not rest at all in the Aquarius pool vessel, prior to the test.

The obtained results are detailed next. First of all and as seen in Figure 4.24, when water was left at rest during 19 days prior to the test, fewer bubbles were seen nucleating within the liquid. The bubbling was however observed during a longer time period in this very case.

If the reduction in bubble nucleation within the liquid bulk is only slightly visible when comparing the above photographs, the effect is more discernible from the plot of the most significant thermodynamic quantities that characterize the present phenomenon: namely the liquid metastability degree  $\Delta T_{eq}$  and the dissolved  $\text{O}_2$  concentration  $C_{O_2}$ . Those quantities are exhibited in Figure 4.25. First, the  $\text{O}_2$  degassing kinetics appear significantly different between the two studied tests. This is phenomenologically consistent with the idea of an escape of freely-floating nuclei during the preliminary

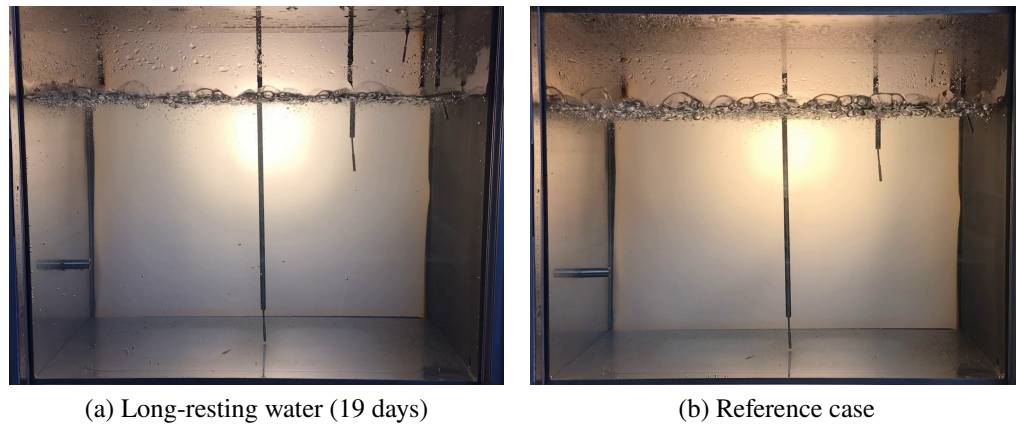


Figure 4.24: A photography of the Aquarius water pool taken 3 minutes after the test startup. One may note that fewer bubbles were seen nucleating within the liquid when the water was left at rest during 19 days prior to the test.

resting period. Indeed, with fewer available gas nuclei when the test was launched 19 days after its preparation, the degassing of water was necessarily slower, because of a reduced available interfacial area for transferring the dissolved species toward a gas phase. With this reduced transfer kinetics, it was then natural to observe a longer bubbling period. Then, the degassing and superheating kinetics being coupled, as already evidenced in Chapter 3, the time-trend of  $\Delta T_{eq}$  was necessarily slower in the case of a preliminary resting time. One may note that the liquid superheating kinetics appears however less sensitive to the above effect. At last, one can verify from Figure 4.26, showing the mass and vaporization rate time-variations of the two tests, that the observed differences in degassing and superheating kinetics cannot be explained by a subtle variation in their energy balance. Indeed, the liquid mass variation is clearly the same for both tests.

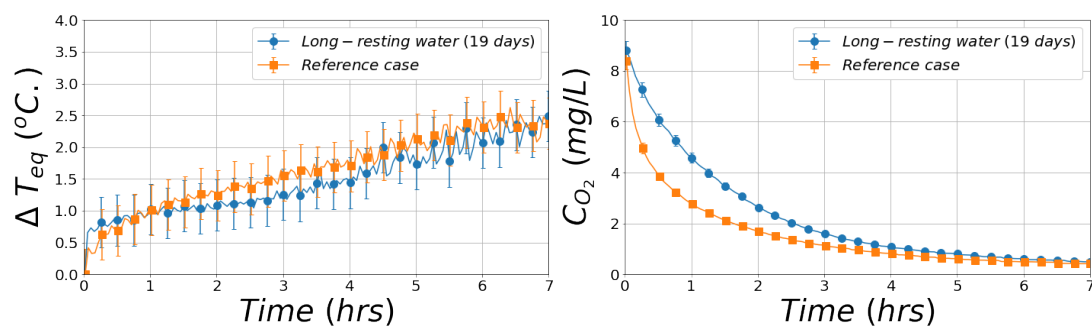


Figure 4.25: Time variations of the liquid thermal metastability degree  $\Delta T_{eq}$  (left graph) and of the dissolved  $O_2$  concentration  $C_{O_2}$  (right graph).

Finally, this comparative experimental study seems to indicate that the hypothesis of a main contribution of the freely-floating gas nuclei to the observed bubble nucleation is likely. We are however left with the same questions that animate the cavitation and

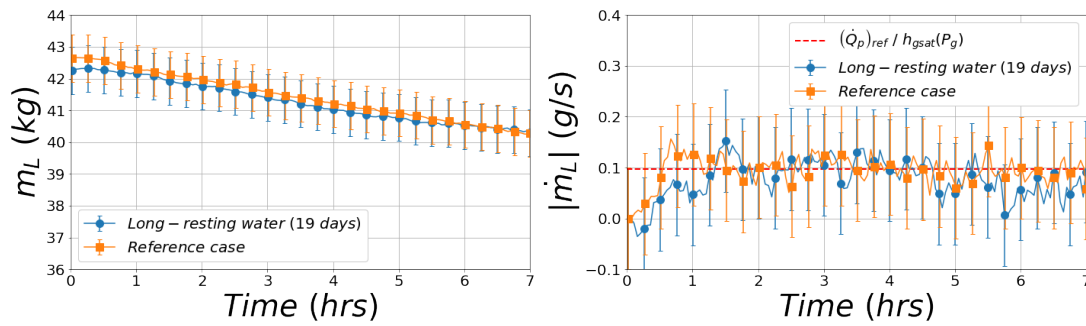


Figure 4.26: Time variations of the liquid pool mass  $m_L$  (left graph) and of the liquid vaporization rate  $\dot{m}_L$  (right graph).

thermal-hydraulic communities regarding the stabilizing mechanisms that may act on those freely-floating nuclei. As a perspective of this study, it might be interesting to further investigate the effect of a preliminary resting of water, by retaining much more resting durations. This would hence help consolidating those first promising results. Next, it would be wise to characterize those supposed pre-existing nuclei by means of modern experimental techniques.

### 4.3.3 An explanation for the late regime of sporadic and violent bubble nucleation

As discussed in Chapter 3, a peculiar type of nucleation is also classically observed during any pool flashing test. This mode occurs lately and sporadically and leads to a violent expansion of bubbles. The apparent high intensity of this bubble growth has been linked with the higher liquid superheats that are typically reached in the late stages of a test. Indeed, the bigger the liquid superheat, the faster and stronger the bubble growth [41]. In Chapter 3, we have shown that these sporadic and violent events are most often correlated with the fall of droplets onto the free surface of the superheated liquid. Hence, one may wonder by which mechanism a splashing droplet may lead to the introduction and/or formation of a gas nucleus right below the free surface, acting as a flashing initiator.

Let us start by having a close look at the interaction between a falling droplet and the liquid free surface during a typical pool flashing experiment. In Figure 4.27, we illustrate such an interaction by a series of photographs taken lately during the reference test introduced in Chapter 3. In this figure, the pictures are displayed every 40 ms. From the fifth and sixth pictures of the latter figure, it seems that immediately after the droplet impact, some gas volume appears, thereby materializing a gas nucleus for the following violent bubble growth. In order to get a better insight into this gas volume formation, another series of photographs was taken during the same late stage of the reference test. It is provided in Figure 4.28, where the pictures are displayed every 4 ms, with an emphasis on the event of a void formation right after the droplet impact. The

first picture of Figure 4.28 shows the void formed that way in the impacted liquid. This is the typical consequence of a droplet that splashes onto a liquid free surface, as early studied by *Worthington* in 1908 (*cf.* Figure 4.29 which shows a series of photographs of a droplet impact and its resulting void formation, published by *Worthington* in [127]). This interfacial configuration is however unstable and capillary forces are expected to close the formed void, which occasionally leaves some tiny remaining bubble [74], [114]. Apparently, for this studied impact, the closure of the formed void took approximately 4 ms, which is rather fast. The last picture of Figure 4.28 shows what clearly differs from the droplet impact studies evocated above. Indeed, as one can notice, the remaining nucleus suddenly grows and generates some void again. By no doubt, this growth is due to the relaxation of the metastable water in contact with the bubble. To conclude, in this section we have shown that the interaction between a falling droplet and the free surface of a superheated liquid is enough for yielding a significant liquid flashing, in consistency with what the literature reports about the hydrodynamic aspects of such an interaction.



Figure 4.27: A series of photographs taken during the late stage of the reference test, presented in Chapter 3. The pictures are displayed every 4 ms. The series shows the interaction of a falling droplet with the free surface of the superheated liquid. The interaction leads to the violent growth of a bubble.

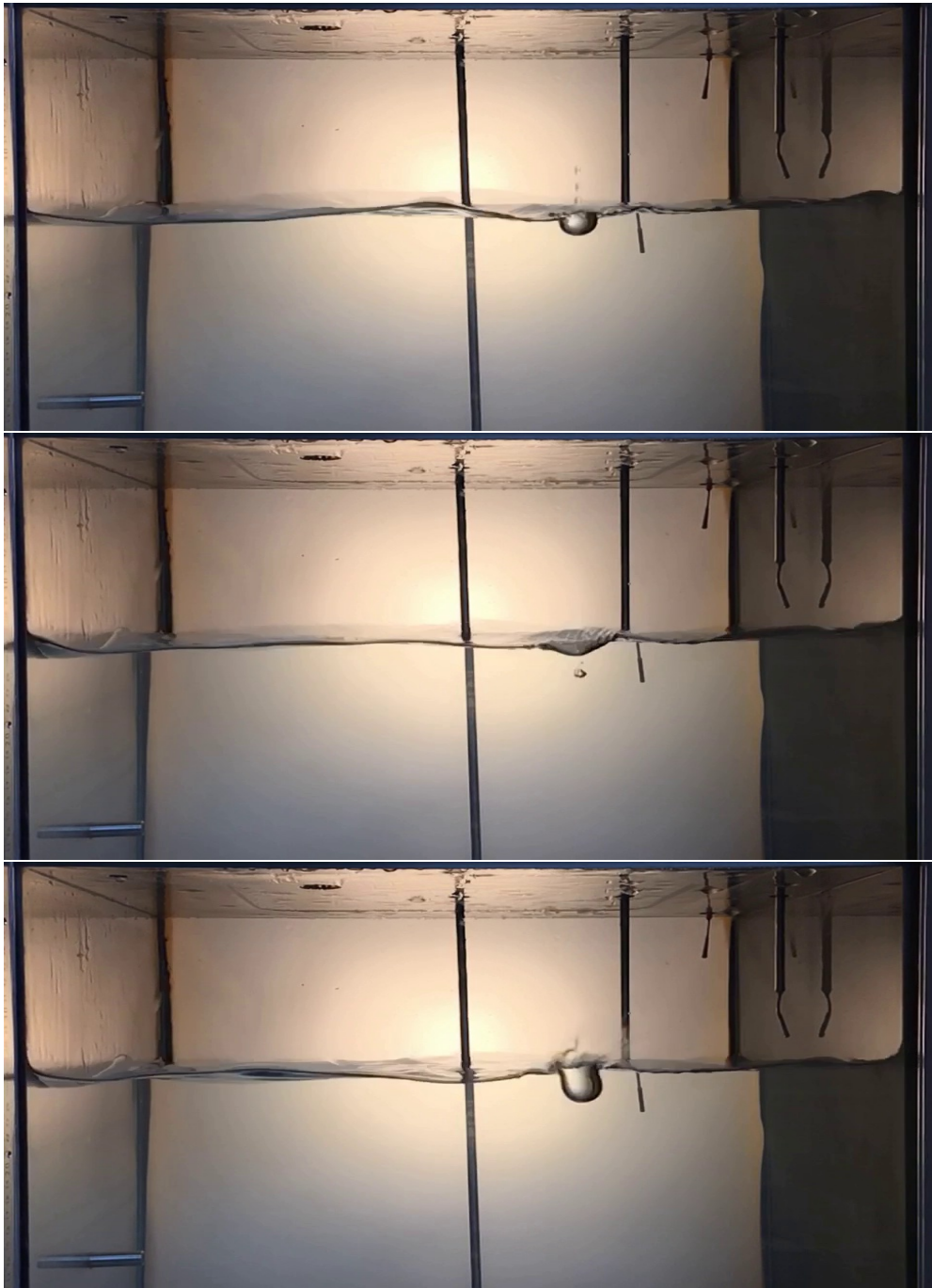


Figure 4.28: A series of photographs taken during the late stage of the reference test, presented in Chapter 3. The pictures are displayed every 4 ms. The series shows the interaction of a falling droplet with the free surface of the superheated liquid, with an emphasis on the event of a void formation right after the droplet impact.

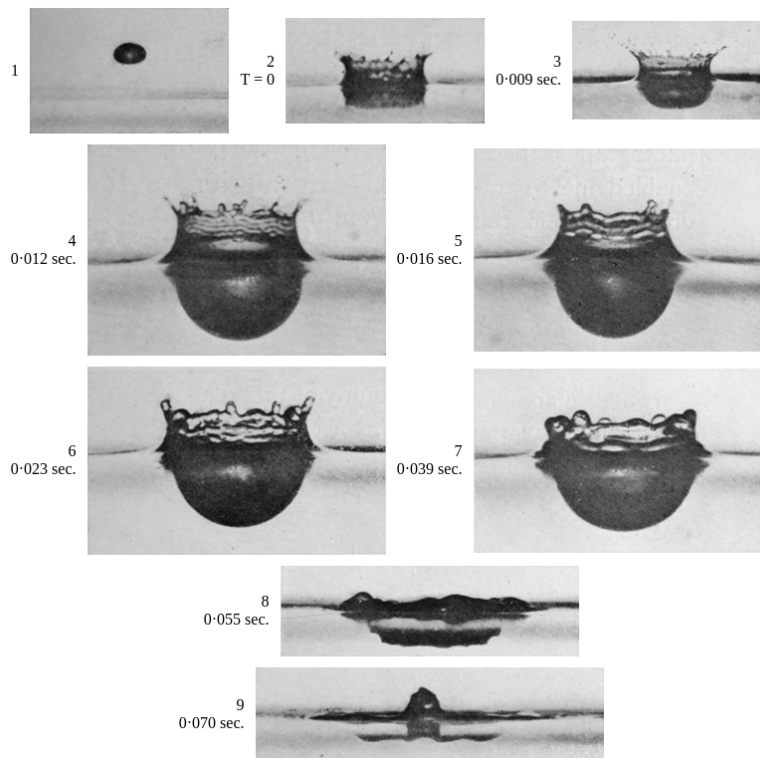


Figure 4.29: A series of photographs of a droplet impact and its resulting void formation, published by *Worthington* in 1908 and extracted from [127].

## Conclusions

In this chapter, the nucleation processes that are typically observed during a pool flashing experiment have been largely analyzed. First of all, a review of all envisioned nucleation modes has been provided. Those modes have been primarily classified on the basis of the order of magnitude of their energetic cost. Indeed, this cost appears as an interesting classification criterion since it is noticeably different whether a gas nucleus pre-exists or not within the metastable liquid. The modes obtained that way are:

- **The nucleation from a pre-existing gas nucleus:**

- Floating freely in the liquid;
- Entrapped in a solid wall cavity.

- **The so-called de novo nucleation:**

- Onto a solid surface;
- Within the liquid bulk.

Then, after having developed the theoretical frame behind these nucleation modes, quantitative evaluations have been made on the basis of the available Aquarius experimental data. Those studies have shown that the two so-called de novo nucleation modes can be confidently discarded, their occurrence conditions being really far from the ones of the presented experiments. Next, regarding the noticed bubble nucleation onto the heaters wall at the beginning of most of the performed experiments, the analysis has shown that the local thermodynamic conditions reached at that location made possible the emergence of bubbles in spite of negative wall superheats. This very fact is indeed the positive consequence of the achieved large dissolved gases supersaturations for most of the tests. The bubble nucleation onto the unheated rough wall of the pool vessel has been proven achievable as well, despite its typical non-observation. By going into details, it has been shown that the deactivation of the gas nuclei entrapped in the rough wall crevices in between two consecutive tests is a very likely process, contrarily to what is phenomenologically expected for the smoother walls. If the bubble nucleation observed onto the vessel's walls does rely on the existence of pre-existing gas nuclei, the one taking place within the liquid bulk is much more uncertain. With the intent to investigate that point, we have designed and conducted a specific test. The results of the latter seem to indicate that the hypothesis of a main contribution of the freely-floating gas nuclei to the observed bubble nucleation is likely. But we are still left with the same questions shared by the cavitation and thermal-hydraulic communities for decades regarding the possible stability mechanisms preserving those puzzling gas nuclei. At last, the interaction between a falling water droplet and the free surface of a superheated liquid has been studied. This interaction, occurring mainly in the late stage of a typical pool flashing experiment, has been proven sufficient for yielding a significant water flashing. The latter relaxation mechanism is indeed understood as being initiated by the gas entrained by the impacting droplet into the liquid pool.



# A characterization of the heat and mass transfers

*“Model building is the art of selecting those aspects of a process that are relevant to the question being asked.”*

— John H. Holland

## Introduction

This chapter presents a macroscopic characterization of the heat and mass transfers that have been discussed throughout this thesis. The characterization is first conducted in Section 5.1 by the definition and estimate, on the basis of the available empirical data, of heat and mass transfers coefficients. Then, with those coefficients introduced, we derive some dimensionless correlations in Section 5.2, thereby reducing the acquired experimental data to a limited and convenient set of mathematical expressions. At last, we provide the reader with a lumped-parameter model of the Aquarius pool in Section 5.3. The latter, taking advantage from the proposed heat and mass transfer correlations, is used to simulate a set of selected Aquarius experiments.

## 5.1 The estimate of the heat and mass transfer rates

### 5.1.1 The wall-to-liquid heat transfer coefficient

**An analytical expression for the heat transfer coefficient** The treated problem is idealized as illustrated in Figure 5.1. Let us denote as  $k_h$  the wall-to-liquid heat transfer coefficient, given in  $\text{W}/\text{m}^2/\text{K}$ , estimated at the heaters location. This quantity can be computed from the heat balance of the resistive heaters, which reads:

$$k_h S_h \Delta T_h = \dot{Q}_p - m_h C_h \frac{dT_h}{dt} \quad (5.1)$$

where  $S_h$ ,  $m_h$  and  $C_h$  are respectively the heating area, the heaters total mass and specific heat capacity. In this equation,  $T_h$  is the already presented heaters mean tempera-

ture, evaluated as:

$$T_h = \frac{1}{2} (\text{T131W} + \text{T134W}) \quad (5.2)$$

Moreover,  $\Delta T_h$  is the wall-to-fluid temperature difference, expressed as:

$$\Delta T_h = T_h - T_L \quad (5.3)$$

One can note that this equation does not include any other heat losses term than the convective heat transfer toward the liquid pool  $k_h S_h \Delta T_h$ . Indeed, as discussed in Chapter 2, the resistive heaters are both insulated at their bottom-end and the transverse heat conduction from the heaters to the pool's structure can be reasonably neglected, owing to the limited area of the involved transfer surfaces.

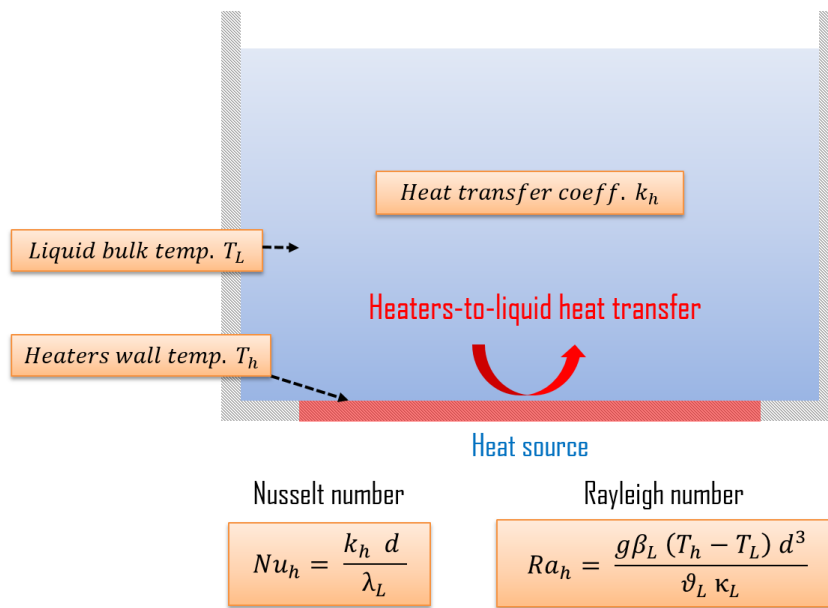


Figure 5.1: An idealization of the heat transfer taking place between the heated bottom wall and the liquid bulk.

**The variations of  $k_h$  during the reference test** Let us next estimate the time-trend of  $k_h$  throughout the reference test. For that purpose, we retain in what follows, on the basis of the heaters' technical specifications,  $m_h C_h = 2 \text{ kg} \times 500 \text{ J/kg/K} = 1000 \text{ J/K}$ . The heated surface, referred to as  $S_h$  represents 75% of the free surface area, as said in Chapter 2, which yields  $S_h = 0.101 \text{ m}^2$ . Applying Equation (5.1) to the empirical data of the reference test provided in Section 3.1.3 and the above parameters gives the results presented in the right-hand-side of Figure 5.2.

At first glance, the estimate of  $k_h$  appears almost constant throughout the reference test and of the order of  $800 \text{ W/m}^2/\text{K}$ . This value is consistent with the expected order of magnitude of a single-phase turbulent natural convection heat transfer coefficient in liquid water [73]. Further on,  $k_h$  is apparently higher during only a short initial period of the reference test, represented in Figure 5.2 as a vertical gray band. These higher

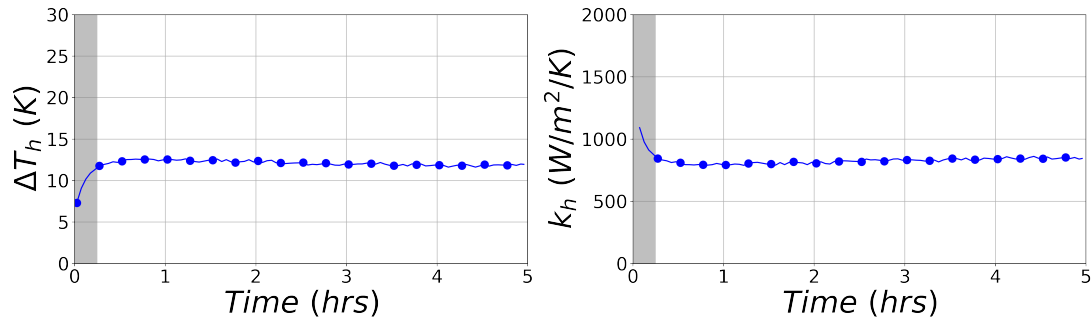


Figure 5.2: Reference test. Left: estimate of the heated wall temperature difference  $\Delta T_h$ . Right: estimate of the heated wall heat transfer coefficient  $k_h$ .

values of  $k_h$  are obviously the consequence of the reached lower values of  $\Delta T_h$  during that period, noticed in the left-hand-side of Figure 5.2. This period represents approximately 15 min and almost corresponds to the initial bubbling stage that was observed onto the heaters surface during the reference test (*cf.* Chapter 3 and for instance, Figure 3.3). Consensually, two-phase conditions are thought as promoting the heat and mass transfers in a liquid [73]. Up to that stage, the initial water boiling taking place onto the heaters wall is hence a significant candidate for explaining the observed trend in both  $\Delta T_h$  and  $k_h$ . Let us further investigate that point in what follows.

**The repeatability of  $k_h$**  The repeatability of the time-trend of  $k_h$  is later studied by means of the empirical data of the tests detailed in Section 3.1.4 - Table 3.1. The obtained results are visible in the next three figures.

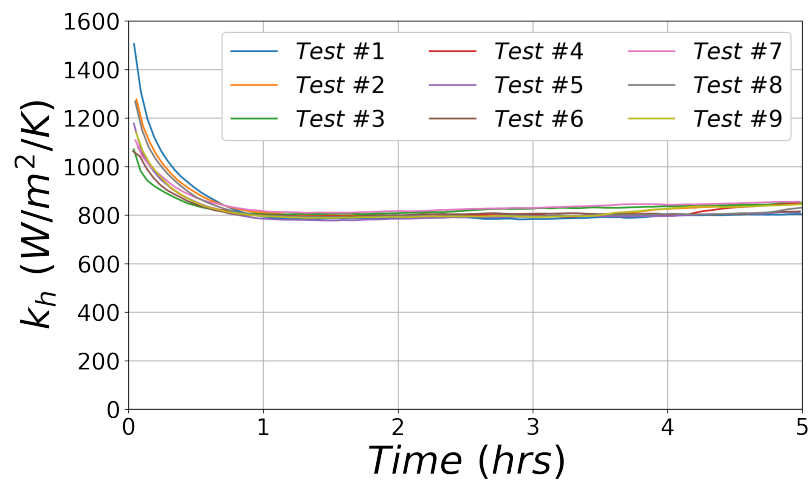


Figure 5.3: Repeated time-trends of  $k_h$ , the wall-to-liquid heat transfer coefficient.

One can notice from Figure 5.3, representing the  $k_h$  estimated from the repetition of nine identical tests that the latter heat transfer coefficient is not so much sensitive to the slight changes occurring from one test to another. This sensitivity is however at its highest magnitude during the initial hour of the repeated tests, as shown by the higher

scattering in the estimated  $k_h$  time-trends during that interval. This scattering can be quantified by computing an instant standard deviation from the repeated tests, denoted as  $\sigma_{k_h}$  and shown in Figure 5.4. It is important to note that this significant scattering does occur during a time period which is much larger than the previously evoked one, associated with the initial water boiling onto the heaters, which is typically of the order of a few minutes.

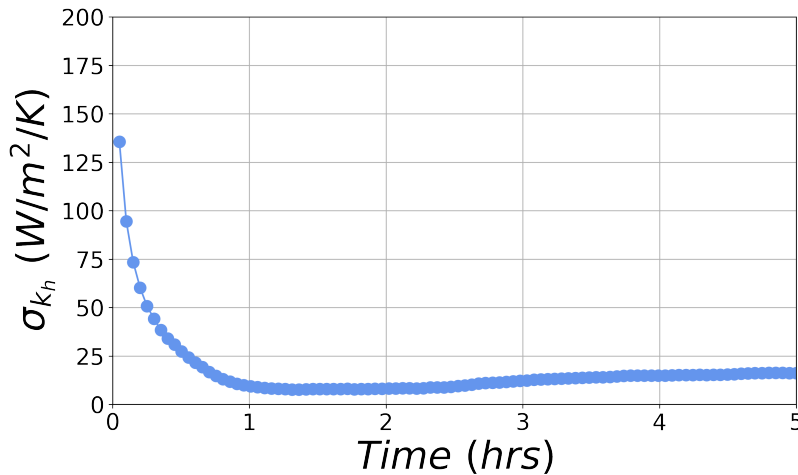


Figure 5.4: Standard deviation  $\sigma_{k_h}$  of the repeated time-trends of  $k_h$ .

Moreover, one can compute an average time-trend of  $k_h$  on the basis of the repeated tests. This average  $k_h$  is given in Figure 5.5, where the error bars are equal to the previous estimate of  $\sigma_{k_h}$  multiplied by 2.26, *i.e.* the value of the so-called Student's coefficient ensuring that those bars cover about 95% of all nine realizations of  $k_h$ . Importantly, the uncertainty range in this average  $k_h$  extends almost down to the time-average value of  $k_h$ , of the order of 800 W/m<sup>2</sup>/K as it has been said before. Therefore, one cannot conclude that the observed initial high values of  $k_h$  were due to the initial water boiling taking place onto the heaters wall, since owing to the above uncertainties, there exists a possibility that those large values were randomly caused.

**The sensitivity of  $k_h$  to the experimental control parameters** At last, it is interesting to further study how  $k_h$  is varying against changes in the heating power, initial pool level, operating pressure and initial content in dissolved gases. This is the purpose of the next discussion. The tests that are considered in what follows are the same than those studied in Section 3.3 and detailed in Tables 3.3-3.6. First is shown in Figure 5.6 the sensitivity of  $k_h$  to heating power variations. As expected,  $k_h$  appears as an increasing function of  $\dot{Q}_p$ , with the asymptotic values of  $k_h$  for a heating power of 1000 and 750 W being almost equal.

Second, Figure 5.7 exhibits the sensitivity of  $k_h$  to operating pressure variations. In the studied cases, the asymptotic value of  $k_h$  appears as a mildly increasing function of  $P_G$ . Most important, for the highest values of  $P_G$ ,  $k_h$  does not show any initial

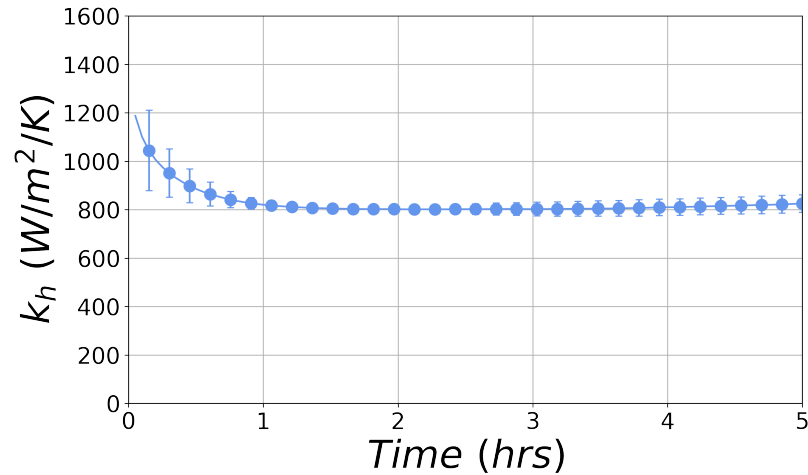


Figure 5.5: Average time-trend of the repeated  $k_h$  with its associated estimated uncertainty.

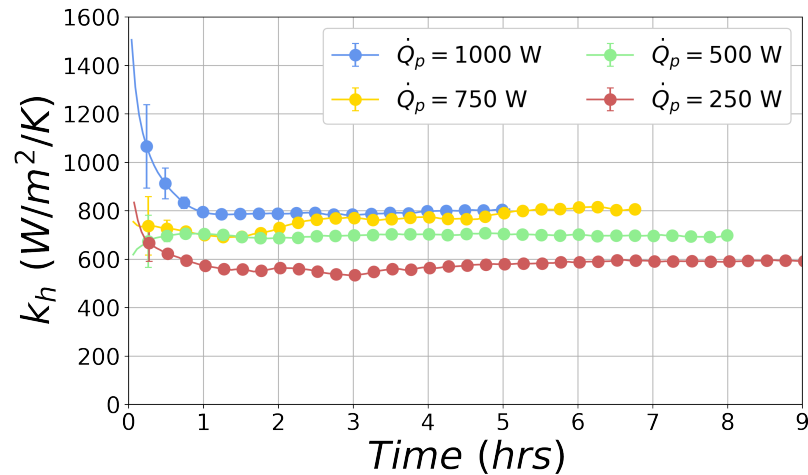


Figure 5.6: Sensitivity to heating power variations. Estimate of the heated wall heat transfer coefficient  $k_h$ .

large values, contrarily to the observation of an initially strong water boiling onto the heaters surface for those tests (*cf.* Section 3.3). Hence, this sustains the idea that the occasionally observed initial large variations of  $k_h$ , as the ones in Figure 5.5, are just random.

Third, we give in Figure 5.8 the variations of  $k_h$  for two different values of the initial pool level  $z_p(0)$ . As one can see, there is no significant difference in the time-trends of  $k_h$  whatever the retained initial pool level.

Fourth, in Figure 5.9 is provided the sensitivity of  $k_h$  to variations in the initial content in dissolved gases. As noticeable, the asymptotic value of  $k_h$  is not significantly affected by a variation in the initial dissolved gases content. Pointedly, the cases with the highest and lowest values for  $C_{O_2}(0)$  both lead to large variations of  $k_h$  during the first hour, whereas the intermediate case with  $C_{O_2}(0) = 1.25$  mg/L does not. This is

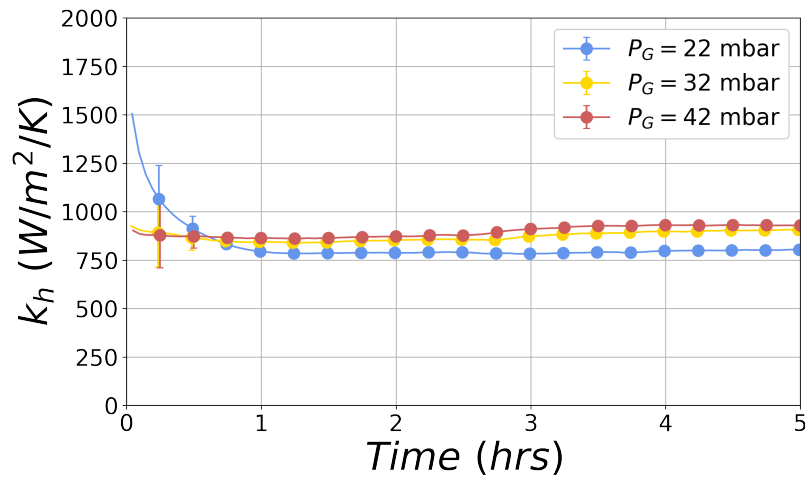


Figure 5.7: Sensitivity to operating pressure variations. Estimate of the heated wall heat transfer coefficient  $k_h$ .

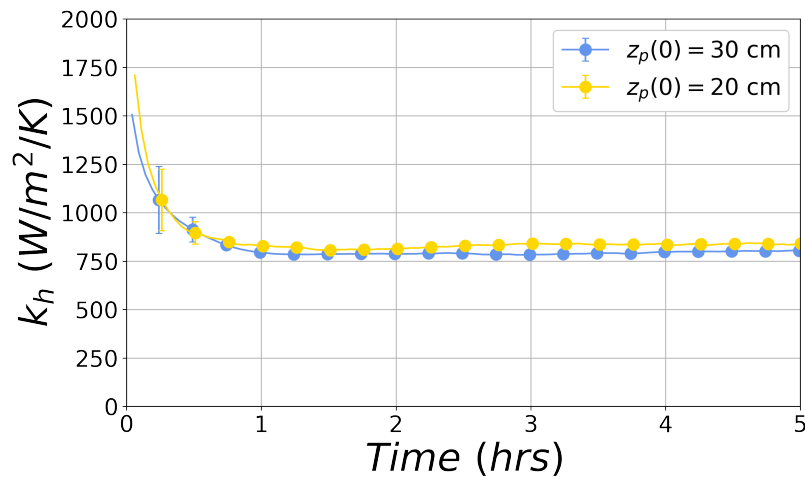


Figure 5.8: Sensitivity to initial pool level variations. Estimate of the heated wall heat transfer coefficient  $k_h$ .

clearly in a complete disagreement with the phenomenological observations given in Chapter 3. Indeed, we have emphasized that the case with a very low initial  $C_{O_2}(0) = 0.15$  mg/L did not lead to any bubble nucleation onto the heaters surface. Hence, large initial values of  $k_h$  cannot be phenomenologically expected in that case. This clearly confirms the idea that the occasionally observed initial large variations of  $k_h$  are just random and cannot be further considered as relevant. Finding their cause might be however beneficial for enhancing our understanding of the Aquarius test device specificities. This is left as a perspective of the present research.

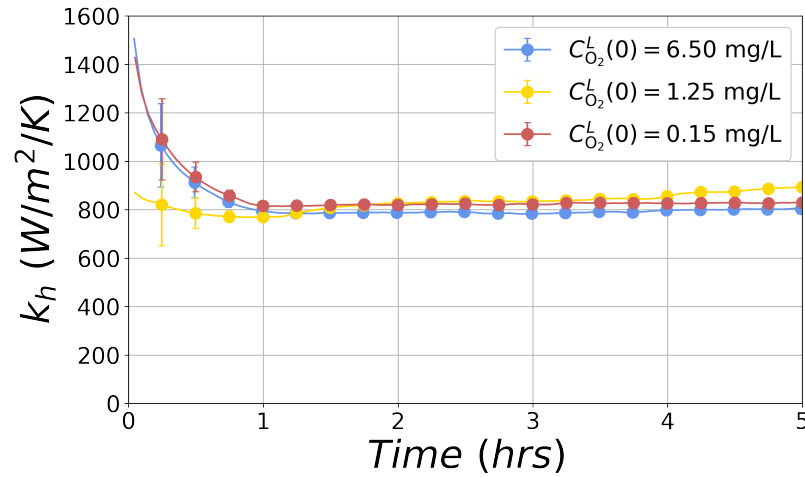


Figure 5.9: Sensitivity to initial content in dissolved gases variations. Estimate of the heated wall heat transfer coefficient  $k_h$ .

### 5.1.2 The gas/liquid heat transfer rate

**An analytical expression for the heat transfer rate** On the basis of the bubble growth observations discussed in Chapter 3, one can consider that the main part of the gas/liquid heat transfer behind the latter takes place in the vicinity of the liquid free surface (*i.e.* bubbles mostly grow underneath the free surface). The process is illustrated in Figure 5.10. In this case, one can model the liquid vaporization process by the following heat fluxes continuity equation:

$$k_T^L S_i \Delta T_{eq} = |\dot{m}_L| \mathcal{L}_w \quad (5.4)$$

with  $k_T^L$ , the gas/liquid heat transfer coefficient given in W/m<sup>2</sup>/K,  $S_i$  the gas/liquid interfacial area,  $\Delta T_{eq}$  the already introduced liquid metastability degree, equal to  $\langle T_L \rangle - T_{sat}(P_G)$ ,  $\dot{m}_L$  the liquid vaporization rate and  $\mathcal{L}_w$  the water latent heat. In Equation (5.4), both  $k_T^L$  and  $S_i$  are unknown in the general case and must be resolved jointly. Interestingly,  $S_i$  is doubtless equal to  $S_p$ , the liquid free surface area, in the single-phase regime of any experiment, thereby allowing a direct estimate of  $k_T^L$  only in this very case. In what follows, an emphasis will be put on the product  $k_T^L S_i$ , specifically referred to as the gas/liquid heat transfer rate.

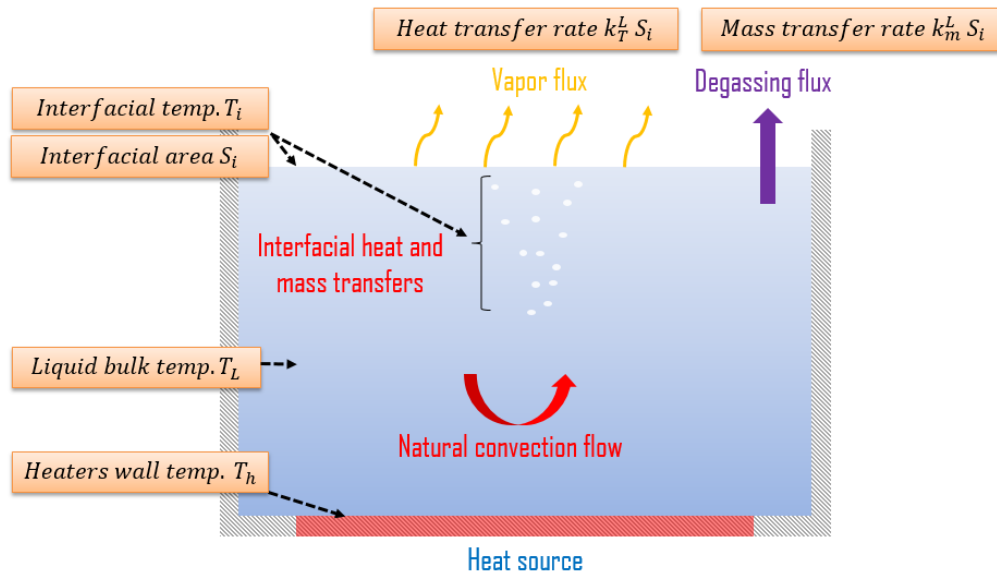


Figure 5.10: An idealization of the heat and mass transfers taking place between the liquid bulk and the overall gas/liquid interfacial area (all bubbles + pool free surface), during the two-phase regime.

**The variations of  $k_T^L S_i$  during the reference test** Let us estimate the time-trend of  $k_T^L S_i$  throughout the reference test. Applying Equation (5.4) to the empirical data of the reference test provided in Section 3.1.3, one gets the results presented in Figure 5.11. First of all, it is interesting to notice that  $k_T^L S_i$  peaks at a maximum value right during the strong bubbling stage highlighted in Chapter 3. Overall,  $k_T^L S_i$  decreases gradually toward an asymptotic value, denoted as  $(k_T^L S_i)_\infty$  and equal to 230 W/K. Being computed from the liquid thermal metastability degree  $\Delta T_{eq}$  (cf. Chapter 3, Figure 3.20),  $k_T^L S_i$  reaches  $(k_T^L S_i)_\infty$  from  $t \approx 3$  hrs accordingly. Up to that stage, one can postulate that the high values of  $k_T^L S_i$ , reached at the beginning of the reference test, are the signature of the observed initial strong bubbling. Let us further investigate that point in what follows.

**The repeatability of  $k_T^L S_i$**  The repeatability of  $k_T^L S_i$  is later studied by means of the empirical data of the tests detailed in Section 3.1.4 - Table 3.1. The obtained results are visible in the next three figures.

Firstly, one can see from Figure 5.12, representing the  $k_T^L S_i$  estimated from the repetition of nine identical tests that the latter heat transfer rate is moderately sensitive to the slight changes occurring from one test to another. Indeed, the overall trend given in Figure 5.11 is well repeated and all  $k_T^L S_i$  tend toward the asymptotic value  $(k_T^L S_i)_\infty = 230$  W/K of the reference test. This sensitivity is at its maximum during the initial stage of the repeated tests, as shown by the higher scattering in the estimated  $k_T^L S_i$  time-trends during that interval. The scattering can be approximated by means of an instantaneous standard deviation, computed from the repeated tests and denoted as  $\sigma_{k_T^L S_i}$ . The latter is shown in Figure 5.13.

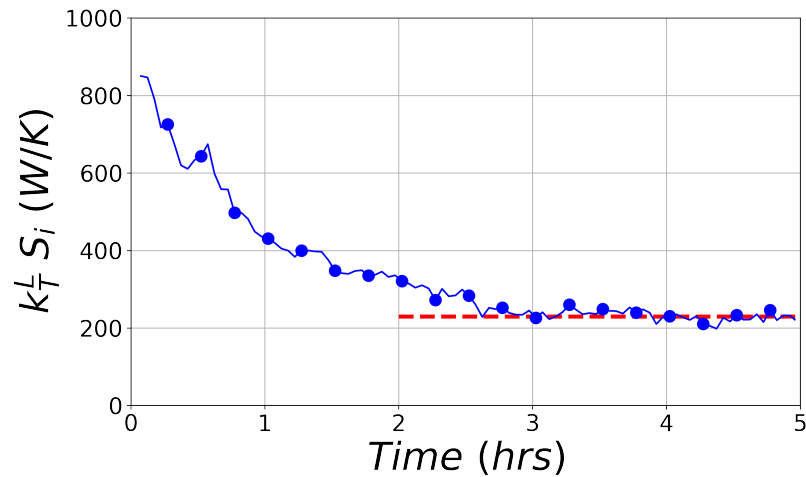


Figure 5.11: Reference test. Estimate of the gas/liquid heat transfer rate  $k_T^L S_i$ .

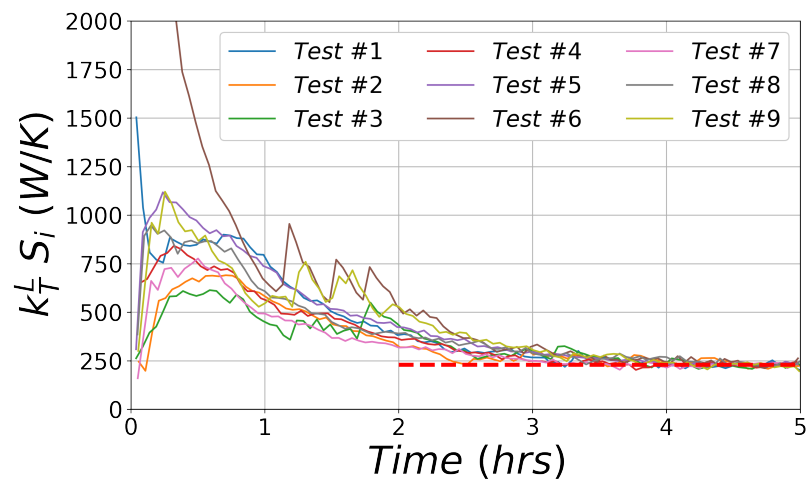


Figure 5.12: Repeated time-trends of  $k_T^L S_i$ , the gas/liquid heat transfer rate.

Moreover, one can compute an average time-trend of  $k_T^L S_i$  on the basis of the repeated tests. This average is given in Figure 5.14, where the error bars are equal to the previous estimate of  $\sigma_{k_T^L S_i}$  multiplied by 2.26, *i.e.* the value of the so-called Student's coefficient ensuring that those bars cover about 95% of all nine realizations of  $k_T^L S_i$ . Contrarily to what has been observed for the wall-to-liquid heat transfer coefficient  $k_h$ , the uncertainty range in the average  $k_T^L S_i$  does not extend down to the level of  $(k_T^L S_i)_\infty$ , of the order of 230 W/K. Therefore, the observed initial high values of  $k_T^L S_i$  are significant and most likely due to the initial strong bubbling taking place within the liquid pool.

**The sensitivity of  $k_T^L S_i$  to the experimental control parameters** At last, it is interesting to further study how  $k_T^L S_i$  is varying against changes in the heating power, initial pool level, operating pressure and initial content in dissolved gases. The tests that are

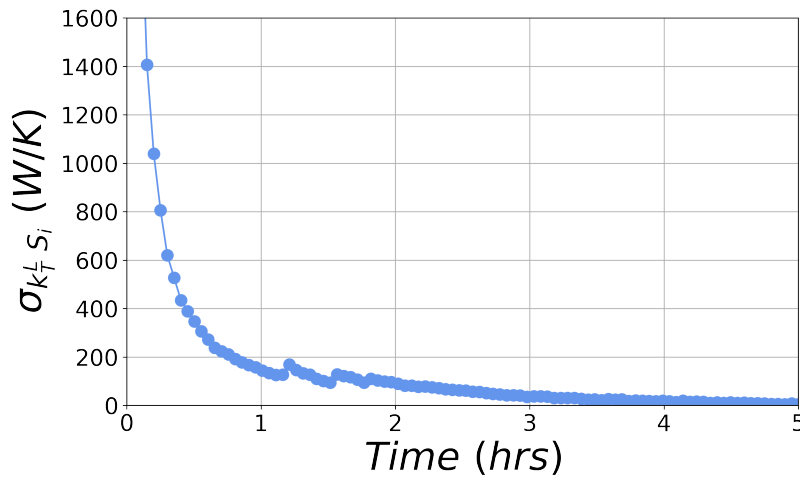


Figure 5.13: Standard deviation  $\sigma_{k_T^L S_i}$  of the repeated time-trends of  $k_T^L S_i$ .

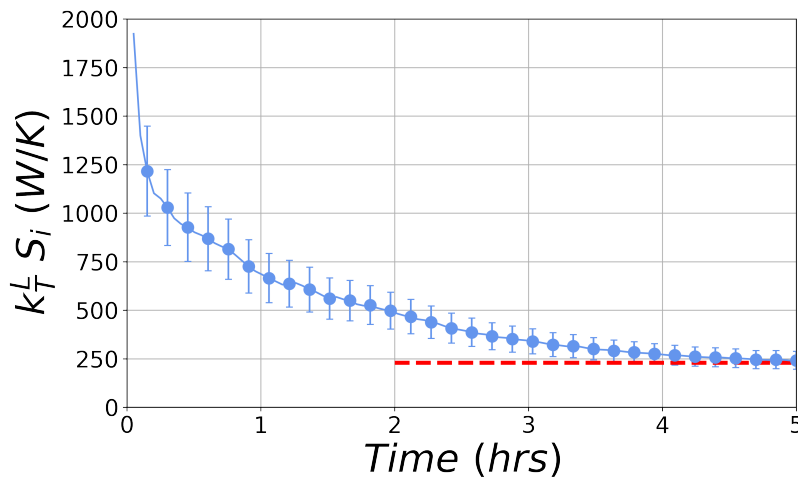


Figure 5.14: Average time-trend of the repeated  $k_T^L S_i$  with its associated estimated uncertainty.

considered for that purpose are the ones studied in Section 3.3 and detailed in Tables 3.3-3.6. First is shown in Figure 5.15 the sensitivity of  $k_T^L S_i$  to heating power variations. As expected,  $k_T^L S_i$  appears as an increasing function of  $\dot{Q}_p$ : both its maximum and asymptotic values are larger when  $\dot{Q}_p$  is increased.

Second, Figure 5.16 exhibits the sensitivity of  $k_T^L S_i$  to operating pressure variations. In the studied cases, the asymptotic value  $(k_T^L S_i)_\infty$  appears insensitive to  $P_G$ . But, the maximum value of  $k_T^L S_i$  strongly depends on  $P_G$ . The higher the pressure, the higher  $k_T^L S_i$ , which matches well with the noticed stronger bubbling for high values of  $P_G$  (cf. Section 3.3).

Third, we give in Figure 5.17 the variations of  $k_T^L S_i$  for two chosen initial pool levels  $z_p(0)$ . As one can see, there is no significant difference in the asymptotic value

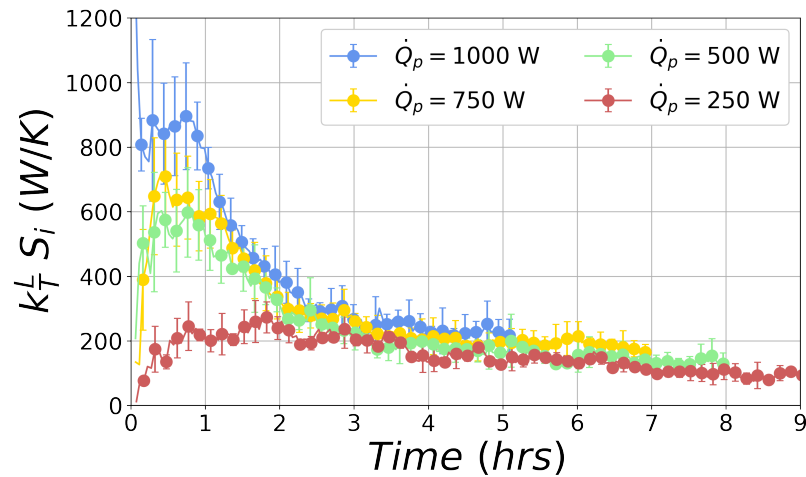


Figure 5.15: Sensitivity to heating power variations. Estimate of the gas/liquid heat transfer rate  $k_T^L S_i$ .

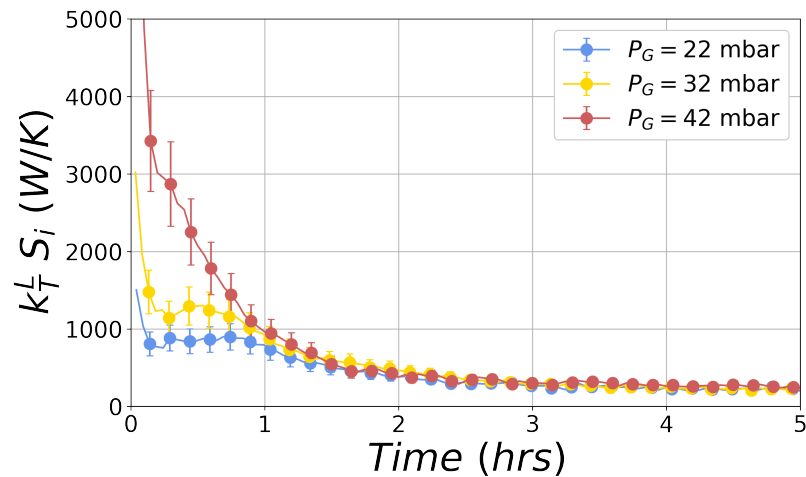


Figure 5.16: Sensitivity to operating pressure variations. Estimate of the gas/liquid heat transfer rate  $k_T^L S_i$ .

$(k_T^L S_i)_\infty$ , whatever the retained initial pool level. But, the maximum value of  $k_T^L S_i$  appears dependent to  $z_p(0)$ . The higher the initial pool level, the higher  $k_T^L S_i$ .

Fourth, in Figure 5.18 is provided the sensitivity of  $k_T^L S_i$  to variations in the initial content in dissolved gases. As visible, the asymptotic value of  $k_T^L S_i$  is not significantly affected by a variation in the initial dissolved gases content. Instead, the maximum value of  $k_T^L S_i$  does so during the bubbling stage of the studied experiments. The bigger the initial mass concentration  $C_{O_2}(0)$ , the higher the maximum  $k_T^L S_i$ . Pointedly, in the case with  $C_{O_2}(0) = 0.15$  mg/L, for which no bubbling was observed at all (*cf.* Section 3.3, Figure 3.52),  $k_T^L S_i$  never exceeds its asymptotic value  $(k_T^L S_i)_\infty = 230$  W/K. All in all, these results strongly sustain the hypothesis of a causality between the reached high values of  $k_T^L S_i$  and the bubbling taking place in the liquid pool.

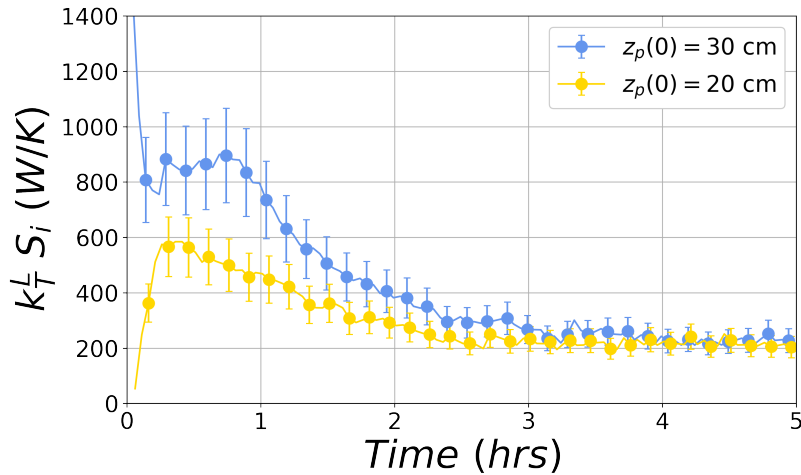


Figure 5.17: Sensitivity to initial pool level variations. Estimate of the gas/liquid heat transfer rate  $k_T^L S_i$ .

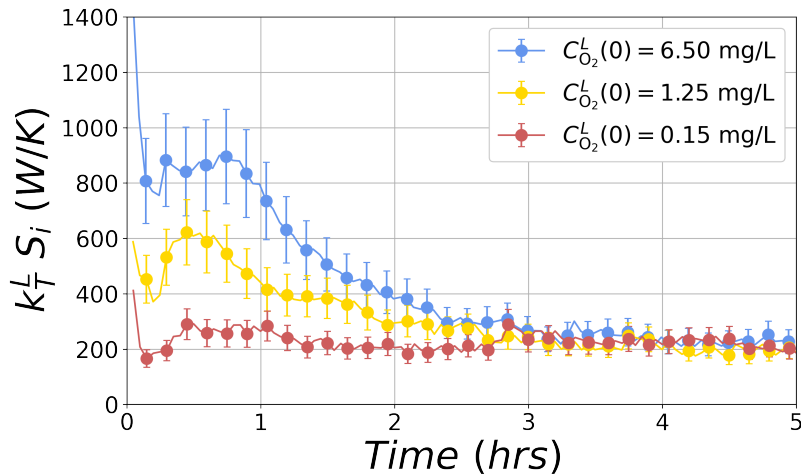


Figure 5.18: Sensitivity to initial content in dissolved gases variations. Estimate of the gas/liquid heat transfer rate  $k_T^L S_i$ .

### 5.1.3 The dissolved air mass transfer rate

**An analytical expression for the mass transfer rate** Let us denote as  $k_m^L$  the dissolved air mass transfer coefficient, given in  $\text{kg}/\text{m}^2/\text{s}$ , characterizing the overall degassing process of  $\text{O}_2$  and  $\text{N}_2$  species, depicted in the already presented Figure 5.10. With both  $\text{O}_2$  and  $\text{N}_2$  being largely diluted in water, this mass transfer coefficient can be related to the instant mass flux of dissolved air  $\dot{m}_a^L$ , given in  $\text{kg}/\text{s}$ , by means of the following simple linear relation [32]:

$$\dot{m}_a^L = - \underbrace{k_m^L S_p (\omega_a^L - \omega_a^{Li})}_{\text{transfer through free surface}} - \underbrace{k_m^L (S_i - S_p) (\omega_a^L - \omega_a^{Bi})}_{\text{transfer through bubbles}} \quad (5.5)$$

with  $S_i$  the total gas/liquid interfacial area,  $S_p$  the liquid free surface area,  $\omega_a^L$  the mass fraction of dissolved air, constant anywhere in water and equal to:

$$\omega_a^L = \frac{C_a}{\rho_L} \quad (5.6)$$

with  $C_a \approx C_{O_2}/0.34$  (cf. Appendix B for more details about the equivalence between the dissolved air and dissolved  $O_2$  variables) and  $\rho_L$ , the liquid density. Further,  $\omega_a^{Li}$  is the equilibrium value of  $\omega_a^L$ , supposedly reached at the liquid free surface and  $\omega_a^{Bi}$ , its counterpart at the bubbles interface. With an air partial pressure  $P_a^G$  in the vessel's atmosphere being approximately null throughout the studied experiments, then  $C_a^{Li}$  and consequently  $\omega_a^{Li} \approx 0$  according to the so-called Henry's law, as already discussed in Section 3.1.3. Moreover, we have shown in Section 3.2 that the liquid vaporization process completely dominates the bubble growth that is observed during any typical experiment. In this condition, one can reasonably assume that the gas content of the observed bubbles is mainly constituted by steam, yielding too  $P_a^B \approx 0$ , the partial pressure of air inside the bubbles and then at the liquid side  $\omega_a^{Bi} \approx 0$ , according to Henry's law. Hence:

$$\dot{m}_a^L \approx -k_m^L S_i \frac{C_a}{\rho_L} \quad (5.7)$$

In this equation,  $\dot{m}_a^L$  can be replaced by the time-derivative of  $C_a \approx C_{O_2}/0.34$ , which is a measured quantity. Noticing that:

$$m_a^L = C_a V_L \quad (5.8)$$

with  $V_L$  the liquid water volume, one gets:

$$\dot{m}_a^L = C_a \dot{V}_L + V_L \dot{C}_a \quad (5.9)$$

In addition, with:

$$V_L = \frac{m_L}{\rho_L} \quad (5.10)$$

then:

$$\dot{V}_L = \frac{1}{\rho_L} \dot{m}_L - \frac{m_L}{\rho_L^2} \dot{\rho}_L \quad (5.11)$$

Next, one can approximate  $\dot{\rho}_L$  as [96]:

$$\dot{\rho}_L = -\rho_L \beta_L \dot{T}_L \quad (5.12)$$

with  $\beta_L$ , the so-called liquid isobaric expansion coefficient, which yields:

$$\dot{m}_a^L = C_a \left( \frac{1}{\rho_L} \dot{m}_L + \frac{m_L}{\rho_L} \beta_L \dot{T}_L \right) + V_L \dot{C}_a \quad (5.13)$$

Inserting Equation (5.7) into (5.13) finally gives:

$$k_m^L S_i = - \left( \dot{m}_L + m_L \beta_L \dot{T}_L + \frac{m_L}{C_a} \dot{C}_a \right) \quad (5.14)$$

Equivalently, with  $\dot{C}_{O_2}/C_{O_2} \approx \dot{C}_a/C_a$  (cf. Appendix B), one gets:

$$k_m^L S_i = - \left( \dot{m}_L + m_L \beta_L \dot{T}_L + \frac{m_L}{C_{O_2}} \dot{C}_{O_2} \right) \quad (5.15)$$

In Equation (5.15), both  $k_m^L$  and  $S_i$  are unknown in the general case and must be resolved jointly, as identically noticed for the gas/liquid heat transfer. Interestingly,  $S_i$  is doubtless equal to  $S_p$ , the liquid free surface area, in the single-phase regime of any experiment, thereby allowing a direct estimate of  $k_m^L$  in this very case. In what follows, an emphasis will be put on the product  $k_m^L S_i$ , specifically referred to as the dissolved air mass transfer/degassing rate.

**The variations of  $k_m^L S_i$  during the reference test** Let us first evaluate the time-trend of  $k_m^L S_i$  throughout the reference test. Applying Equation (5.15) to the empirical data of the reference test provided in Section 3.1.3, one gets the results presented in Figure 5.19. First of all, it is interesting to notice that  $k_m^L S_i$  peaks at a maximum value right during the strong bubbling stage highlighted in Chapter 3 and at the same moment than  $k_T^L S_i$ . Then,  $k_m^L S_i$  decreases gradually toward a noisy asymptotic value, denoted as  $(k_m^L S_i)_\infty$  and approximately equal to 5 g/s. As for  $k_T^L S_i$ , it is likely that the high values of  $k_m^L S_i$ , reached at the beginning of the reference test, are the signature of the observed initial strong bubbling.

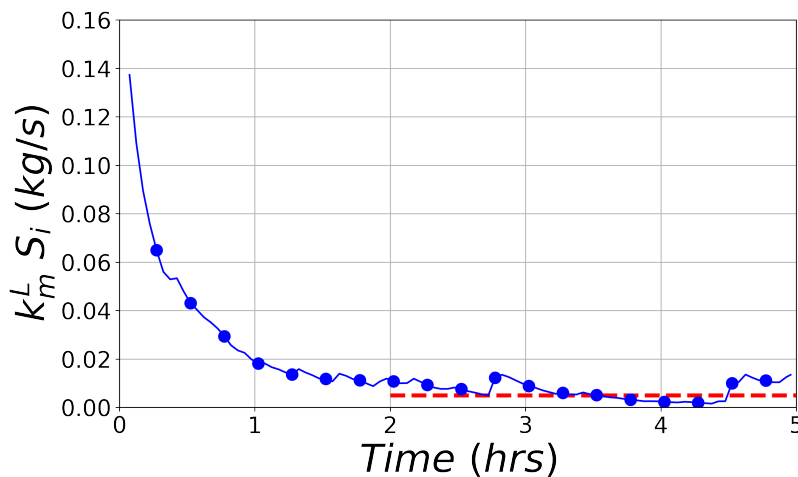


Figure 5.19: Reference test. Estimate of the dissolved air degassing rate  $k_m^L S_i$ .

**The repeatability of  $k_m^L S_i$**  The repeatability of  $k_m^L S_i$  is studied by means of the empirical data of the tests detailed in Section 3.1.4 - Table 3.1. The obtained results are visible in the next three figures.

Firstly, one can see from Figure 5.20, representing the  $k_m^L S_i$  estimated from the repetition of nine identical tests that the latter mass transfer rate is moderately sensitive

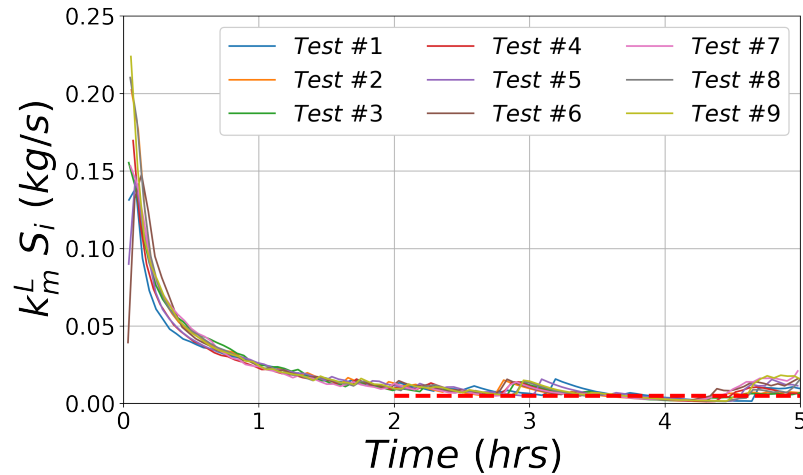


Figure 5.20: Repeated time-trends of  $k_m^L S_i$ , the dissolved air degassing rate.

to the slight changes occurring from one test to another. Indeed, the overall trend given in Figure 5.19 is well repeated and all  $k_m^L S_i$  tend toward the asymptotic value  $(k_m^L S_i)_\infty = 5 \text{ g/s}$  of the reference test. This sensitivity is at its maximum during the initial stage of the repeated tests, as shown by the higher scattering in the estimated  $k_m^L S_i$  time-trends during that interval. The scattering can be approximated by means of an instant standard deviation, computed from the repeated tests and denoted as  $\sigma_{k_m^L S_i}$ . The latter is shown in Figure 5.21.

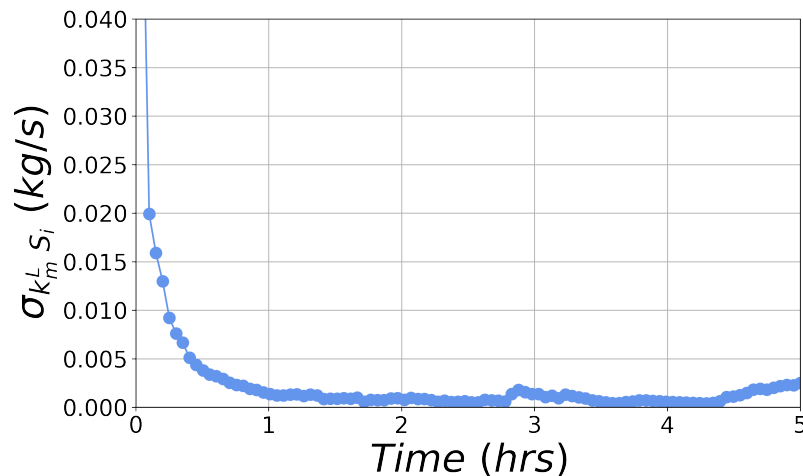


Figure 5.21: Standard deviation  $\sigma_{k_m^L S_i}$  of the repeated time-trends of  $k_m^L S_i$ .

Moreover, one can compute an average time-trend of  $k_m^L S_i$  on the basis of the repeated tests. This average is given in Figure 5.22, where the error bars are equal to the previous estimate of  $\sigma_{k_m^L S_i}$  multiplied by 2.26, *i.e.* the value of the so-called Student's coefficient ensuring that those bars cover about 95% of all nine realizations of  $k_m^L S_i$ . Contrarily to what has been observed for the wall-to-liquid heat transfer coefficient  $k_h$ , the uncertainty range in the average  $k_m^L S_i$  does not extend down to the level of  $(k_m^L S_i)_\infty$ ,

of the order of 5 g/s. Therefore, the observed initial high values of  $k_m^L S_i$  are judged significant and are most likely due to the initial strong bubbling taking place within the liquid pool.

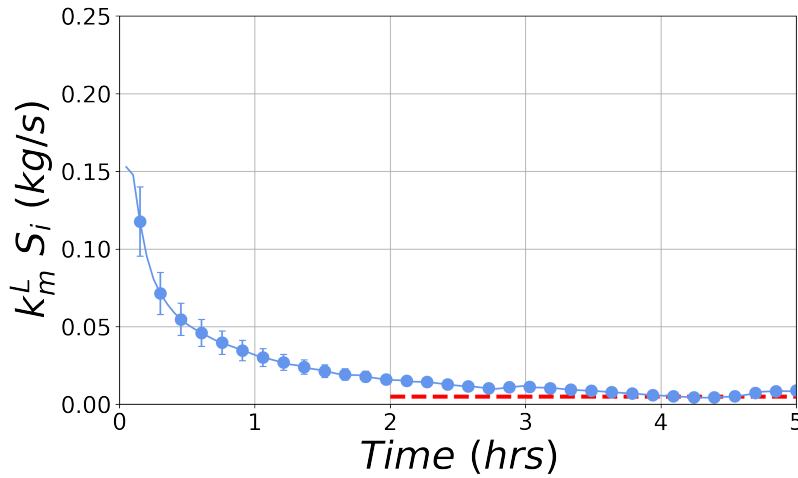


Figure 5.22: Average time-trend of the repeated  $k_m^L S_i$  with its associated estimated uncertainty.

**The sensitivity of  $k_m^L S_i$  to the experimental control parameters** At last, it is interesting to further study how  $k_m^L S_i$  is varying against changes in the heating power, initial pool level, operating pressure and initial content in dissolved gases. The tests that are considered for that purpose are the ones studied in Section 3.3 and detailed in Tables 3.3-3.6. First is shown in Figure 5.23 the sensitivity of  $k_m^L S_i$  to heating power variations. As expected,  $k_m^L S_i$  appears as an increasing function of  $\dot{Q}_p$ : both its maximum and asymptotic values are larger when  $\dot{Q}_p$  is increased. One may note, however, that the estimated  $k_m^L S_i$  being more noisy when compared with their heat transfer counterparts, the differences in the asymptotic value  $(k_m^L S_i)_\infty$  from one test to another are less straightforward.

Second, Figure 5.24 exhibits the sensitivity of  $k_m^L S_i$  to operating pressure variations. In the studied cases, the asymptotic value  $(k_m^L S_i)_\infty$  appears insensitive to  $P_G$ . This clearly differs from the observation done for  $k_T^L S_i$  in Figure 5.16. But owing to the small and more noisy values of  $k_m^L S_i$  reached at that very moment, one cannot draw a reliable conclusion from the above observation.

Third, we give in Figure 5.25 the variations of  $k_m^L S_i$  for two chosen initial pool levels  $z_p(0)$ . As one can see, there is no significant difference in the asymptotic value  $(k_m^L S_i)_\infty$ , whatever the retained initial pool level. But, the maximum value of  $k_m^L S_i$  appears slightly dependent to  $z_p(0)$ , as  $k_T^L S_i$  seems to be (*cf.* Figure 5.17). The higher the initial pool level, the higher  $k_m^L S_i$ .

Fourth, in Figure 5.26 is provided the sensitivity of  $k_m^L S_i$  to variations in the initial content in dissolved gases. As visible, the asymptotic value of  $k_m^L S_i$  is not significantly

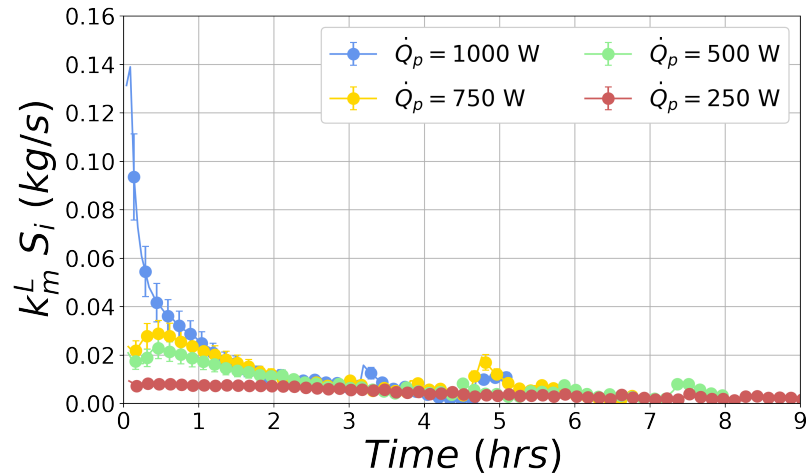


Figure 5.23: Sensitivity to heating power variations. Estimate of  $k_m^L S_i$ , the dissolved air degassing rate.

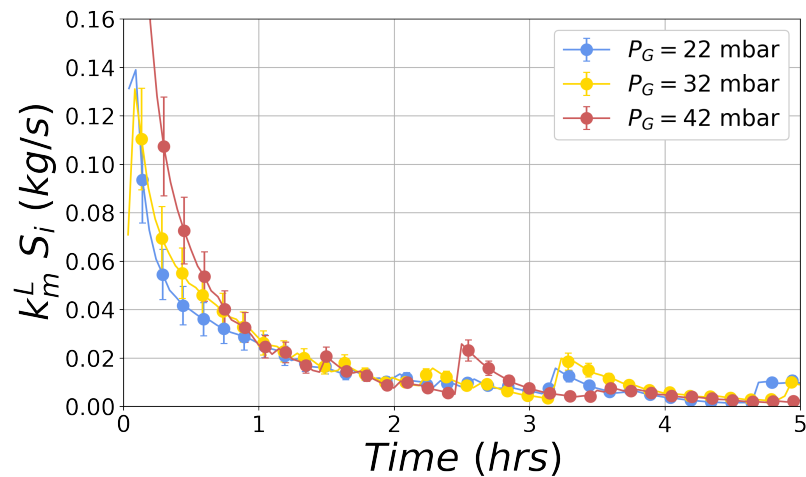


Figure 5.24: Sensitivity to operating pressure variations. Estimate of  $k_m^L S_i$ , the dissolved air degassing rate.

affected by a variation in the initial dissolved gases content. Instead, the maximum value of  $k_m^L S_i$  does so during the bubbling stage of the studied experiments. The bigger the initial mass concentration  $C_{O_2}^L(0)$ , the higher the maximum  $k_m^L S_i$ . Pointedly, in the case with  $C_{O_2}^L(0) = 0.15$  mg/L, for which no bubbling was observed at all (*cf.* Section 3.3, Figure 3.52),  $k_m^L S_i$  never exceeds its asymptotic value  $(k_m^L S_i)_\infty = 5$  g/s. All in all, these results strongly sustain the hypothesis of a causality between the reached high values of  $k_m^L S_i$  and the bubbling taking place in the liquid pool, as already emphasized for  $k_T^L S_i$ .

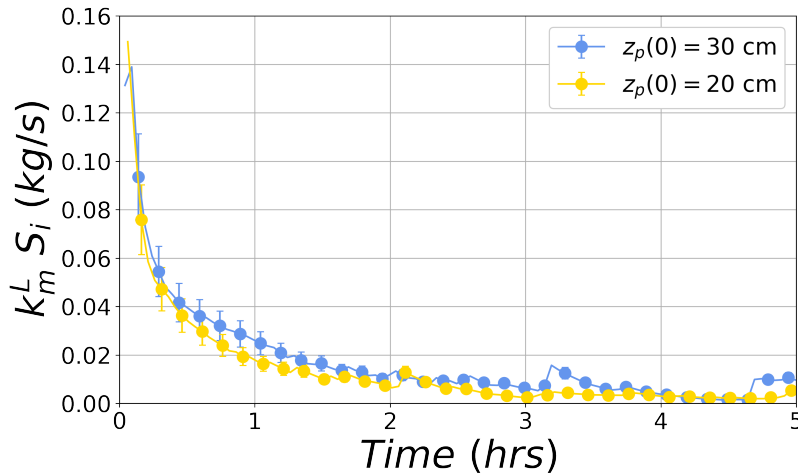


Figure 5.25: Sensitivity to initial pool level variations. Estimate of  $k_m^L S_i$ , the dissolved air degassing rate.

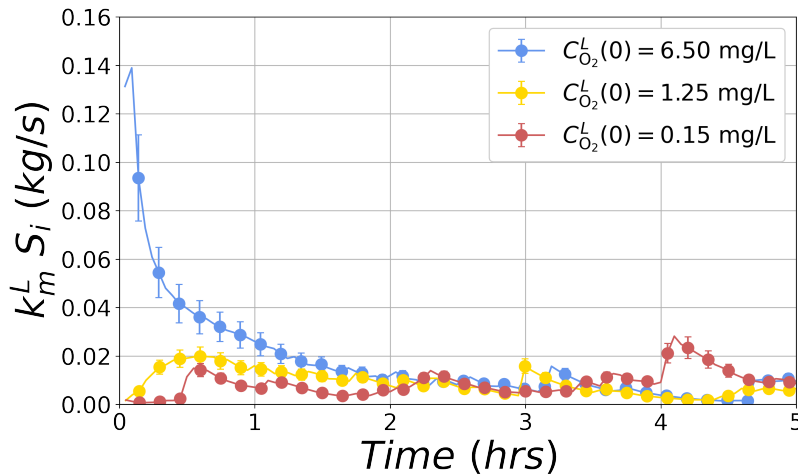


Figure 5.26: Sensitivity to initial content in dissolved gases variations. Estimate of  $k_m^L S_i$ , the dissolved air degassing rate.

## 5.2 Heat and mass transfers correlations

### 5.2.1 Methodology

In what follows, heat and mass transfers correlations are first derived from the data series of each test composing a so-called regular experimental matrix, detailed in Table 5.1. This regular matrix comprises 24 tests, each started with an identical dissolved  $O_2$  mass concentration of 6.5 mg/L. In details, the matrix consists in 24 combinations of values for the heating power  $\dot{Q}_p$ , the operating pressure  $P_G$  and the initial pool level  $z_p(0)$ . Then, the obtained correlations are systematically confronted with another set of experimental data based on the tests listed in Table 5.2, as a verification stage.

Table 5.1: The series of tests composing the so-called regular experimental matrix.

Date of achievement	$\dot{Q}_p$ (W)	$P_G$ (mbar)	$z_p(0)$ (cm)	$C_{O_2}(0)$ (mg/L)
November 25, 2021	1000	22	30	6.5
January 14, 2022	750	22	30	6.5
January 7, 2022	500	22	30	6.5
November 10, 2021	250	22	30	6.5
November 2, 2021	1000	22	20	6.5
February 7, 2022	750	22	20	6.5
January 31, 2022	500	22	20	6.5
November 16, 2021	250	22	20	6.5
February 14, 2022	1000	32	30	6.5
February 15, 2022	750	32	30	6.5
February 16, 2022	500	32	30	6.5
February 17, 2022	250	32	30	6.5
February 21, 2022	1000	32	20	6.5
February 22, 2022	750	32	20	6.5
February 23, 2022	500	32	20	6.5
February 24, 2022	250	32	20	6.5
October 29, 2021	1000	42	30	6.5
January 26, 2022	750	42	30	6.5
February 3, 2022	500	42	30	6.5
November 19, 2021	250	42	30	6.5
November 24, 2021	1000	42	20	6.5
January 27, 2022	750	42	20	6.5
February 2, 2022	500	42	20	6.5
November 18, 2021	250	42	20	6.5

Table 5.2: The series of tests used as a verification basis for the developed heat and mass transfers correlations.

Date of achievement	$\dot{Q}_p$ (W)	$P_G$ (mbar)	$z_p(0)$ (cm)	$C_{O_2}(0)$ (mg/L)
October 26, 2021	1000	22	30	0.15
January 18, 2022	750	22	30	0.15
January 11, 2022	500	22	30	0.15
November 9, 2021	250	22	30	0.15
October 22, 2021	1000	22	30	2.50
November 22, 2021	1000	22	30	1.40
November 15, 2021	250	22	30	1.25
December 12, 2021	250	22	30	9.50
January 4, 2022	250	22	30	8.80

## 5.2.2 The liquid-bulk-to-free-surface single-phase transfers

**Dimensionless numbers** Two correlations are given next. Both respectively quantify the intensity of the heat and dissolved gases transfers developing between the liquid bulk and its free surface during the single-phase regime, as depicted in Figure 5.27. Three dimensionless numbers are classically combined through the form of correlations for describing those transfers [35]. First is the liquid-side Rayleigh number, denoted as  $Ra_{Li}$  and equal to:

$$Ra_{Li} = \frac{g\beta_L(T_L - T_i) d^3}{\nu_L \kappa_L} \quad (5.16)$$

with  $g$  the gravitational acceleration,  $\beta_L$  the liquid thermal expansion coefficient,  $T_L$  the volume-averaged liquid bulk temperature (the  $\langle . \rangle$  space-averaging operator is here omitted),  $T_i$  the area-averaged free surface temperature (*idem*),  $d$  a length variable characterizing the treated problem and  $\nu_L$ ,  $\kappa_L$ , respectively the liquid kinematic viscosity and thermal diffusivity. This number characterizes the natural convection flow behind the studied heat and mass transfers. Another relevant quantity is the so-called Nusselt number  $Nu_{Li}$ , which is a dimensionless form of the already introduced heat transfer coefficient  $k_T^L$ . This number reads:

$$Nu_{Li} = \frac{k_T^L d}{\lambda_L} \quad (5.17)$$

with  $\lambda_L$ , the liquid thermal conductivity. Similarly for the mass transfer coefficient, denoted as  $k_m^L$  for the dissolved gases, one can introduce a so-called Sherwood number  $Sh_{Li}$ , expressed as:

$$Sh_{Li} = \frac{k_m^L d}{\mathcal{D}_{a,w}^L} \quad (5.18)$$

with  $\mathcal{D}_{a,w}^L$ , the diffusion coefficient of dissolved air in water.

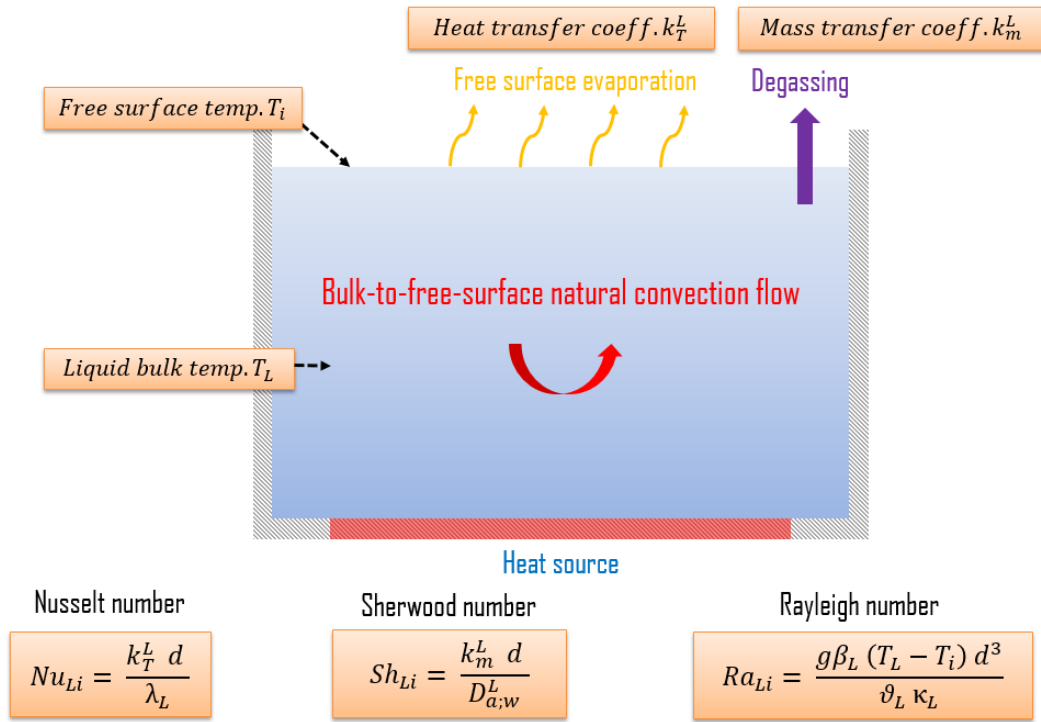


Figure 5.27: An idealization of the heat and mass transfers taking place between the liquid bulk and its free surface during the single-phase regime.

**The computation of time-averaged values** In what follows is detailed the way a time-averaged value of the retained dimensionless numbers is computed for each experiment of the regular test matrix. Those quantities are later referred to as  $(Ra_{Li})_\infty$ ,  $(Nu_{Li})_\infty$  and  $(Sh_{Li})_\infty$ . Focusing only on the data of those tests in link with the single phase regime, they read:

$$(Ra_{Li})_\infty = \frac{1}{\tau_{1\phi}} \int_{\tau_{1\phi}} \frac{g \beta_L (T_L - T_i) d^3}{\nu_L \kappa_L} dt \quad (5.19)$$

$$(Nu_{Li})_\infty = \frac{1}{\tau_{1\phi}} \int_{\tau_{1\phi}} \frac{k_T^L d}{\lambda_L} dt \quad (5.20)$$

$$(Sh_{Li})_\infty = \frac{1}{\tau_{1\phi}} \int_{\tau_{1\phi}} \frac{k_m^L d}{\mathcal{D}_{a:w}^L} dt \quad (5.21)$$

with  $t$ , the time variable and  $\tau_{1\phi}$ , the time interval along which the single-phase data averaging is conducted. This latter quantity is fixed to 30 min, which yields with a data sampling interval set to 3 min (*cf.* Chapter 2) 10 data points. In the above equations,  $k_T^L$  and  $k_m^L$  are respectively equal to:

$$k_T^L = \frac{|\dot{m}_L| \mathcal{L}_w}{S_i \Delta T_{eq}} \quad (5.22)$$

$$k_m^L = -\frac{1}{S_i} \left( \dot{m}_L + m_L \beta_L \dot{T}_L + \frac{m_L}{C_{O_2}^L} \dot{C}_{O_2}^L \right) \quad (5.23)$$

with  $S_i = S_p$  in the single-phase regime.

**The choice of a transfer length-scale** In the above estimates of the considered dimensionless numbers, a choice for the length-scale  $d$  is to be made. In the case of a natural convection heat transfer in a horizontal layer of fluid, a theoretical analysis of the problem, such as the one achieved by *Turner* in [116], highlights the layer thickness as a relevant length-scale. In the present configuration, this layer thickness is naturally the liquid collapsed level  $z_p$  and hence, in the further developments:

$$d = z_p \quad (5.24)$$

**The liquid-bulk-to-free-surface heat transfer** A specific type of power law involving the so-called Nusselt  $Nu_{Li}$  and Rayleigh  $Ra_{Li}$  dimensionless numbers is commonly used for reducing the data of single-phase natural convection heat transfer experiments [116]. This power law generically reads:

$$Nu_{Li} = C \times Ra_{Li}^n \quad (5.25)$$

with  $C$  and  $n$ , the so-called pre-factor and exponent of the law, that are classically adjusted against the experimental data. Such an adjustment was done on the basis of the 24 tests of the regular matrix. The obtained results are given in Figure 5.28. In the latter, one may note that the 24 data points are colored according to their associated operating pressure. The symbols of those points differ depending on the value of the initial pool level. As one can observe, the Nusselt and Rayleigh numbers associated with the single-phase regime of all the achieved tests appear significantly correlated through the form of the power law suggested above, with an average regression coefficient  $R^2$  of 0.66. The law obtained for the single phase regime of those tests is thus equal to:

$$(Nu_{Li})_{\infty} = 0.6 \times (Ra_{Li})_{\infty}^{0.33} \quad (5.26)$$

where one can recognize the typical value of 0.33 of the law exponent, relating to natural convection turbulent flows [116] and an estimated pre-factor of 0.6.

Next, one can verify from Figure 5.29 that the tests initiated with a different amount of dissolved oxygen comply with the obtained correlation as well. For the single-phase regime, this highlights the lack of relationship between the instant amount of dissolved gases in the liquid and the developed natural convection heat transfer. The latter being triggered by a heating-induced liquid density difference, this result shows that the instant amount of dissolved gases does not impact significantly the driving liquid density difference. This is fully consistent with the estimated dissolved gases molar fractions  $x_a^L$  throughout any test: those gases are highly diluted in water, *i.e.*  $x_a^L \ll x_w^L$  (*cf.* Chapter 3).

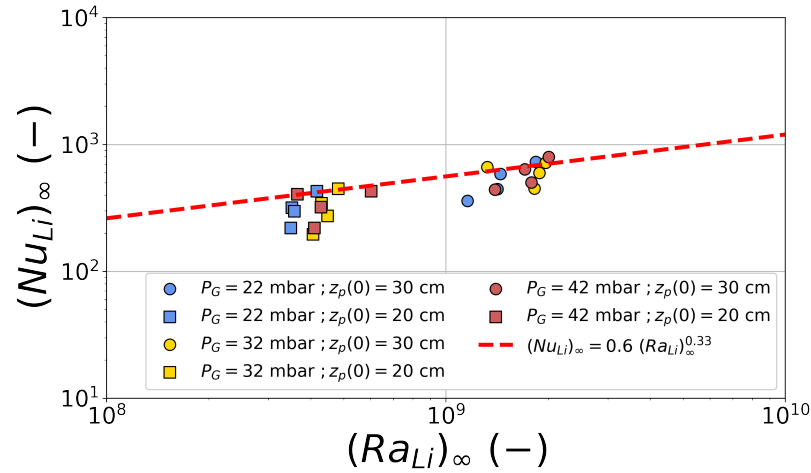


Figure 5.28: The Nusselt versus Rayleigh numbers natural convection heat transfer correlation obtained in the single-phase regime from the 24 tests of the regular matrix. This correlation reflects the liquid-bulk-to-free-surface heat transfer behind the free surface evaporation process.

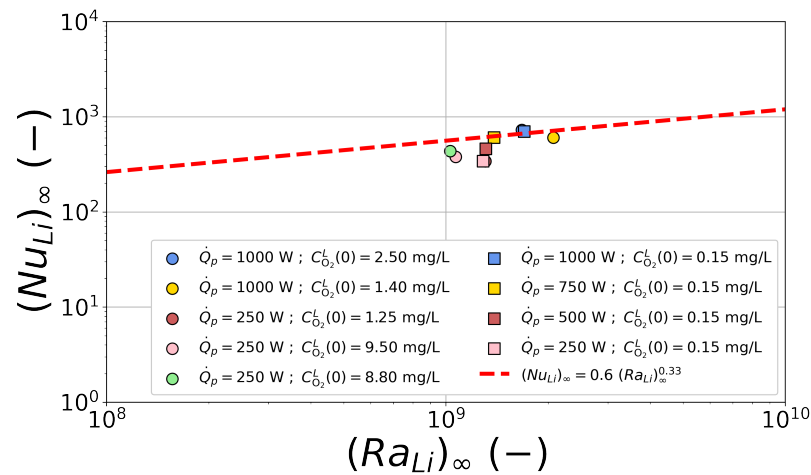


Figure 5.29: The tests initiated with a different amount of dissolved oxygen comply as well with the Nusselt versus Rayleigh natural convection heat transfer correlation, obtained in the single-phase regime, from the 24 tests of the regular matrix. This correlation reflects the liquid-bulk-to-free-surface heat transfer behind the free surface evaporation process.

**The liquid-bulk-to-free-surface dissolved gases transfer** In the single-phase regime of any test, as it has been discussed in Chapter 3, the degassing process of the  $O_2$  and  $N_2$  species dissolved in water is dominated by the single-phase natural convection flows developing at pool scale. The latter flows being well described by means of the Rayleigh number  $Ra_{Li}$ , as shown beforehand, one may thus expect that the single-phase degassing process is described by a Rayleigh  $Ra_{Li}$  versus Sherwood  $Sh_{Li}$  correlation, analogous to the one identified above for the heat transfer. Such a generic correlation

reads:

$$Sh_{Li} = C \times Ra_{Li}^n \quad (5.27)$$

with  $C$  and  $n$ , still the so-called pre-factor and exponent of the law, classically adjusted against the experimental data. As for the heat transfer, such an adjustment was done on the basis of the 24 tests of the regular matrix. The obtained results are given in Figure 5.30. As one can note, the Sherwood and Rayleigh numbers associated with the single-phase regime of all the achieved tests appear correlated through the form of the power law suggested above. However, the obtained fit appears less accurate than the one of the single-phase heat transfer, as reflected by an average regression coefficient  $R^2$  here equal to 0.30. Most likely, this is the consequence of the scattered and very small measured values of the dissolved  $O_2$  mass concentration during the single-phase regime when the gas depletion is almost complete (*cf.* Chapter 3). Keeping this limitation in mind, the law obtained for the single-phase regime of those tests reads:

$$(Sh_{Li})_{\infty} = 1.6 \times (Ra_{Li})_{\infty}^{0.33} \quad (5.28)$$

where one can recognize the typical value of 0.33 of the law exponent, relating to natural convection turbulent flows [116] and an estimated pre-factor of 1.6.

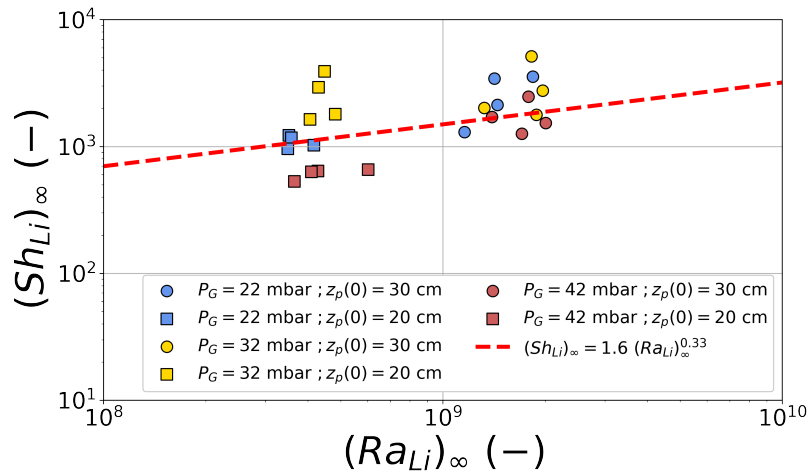


Figure 5.30: The Sherwood versus Rayleigh numbers natural convection mass transfer correlation obtained in the single-phase regime from the 24 tests of the regular matrix. This correlation reflects the liquid-bulk-to-free-surface dissolved gases transfer behind the degassing process.

At last, as for the heat transfer, one can verify from Figure 5.31 that the tests initiated with a different amount of dissolved oxygen comply with the obtained correlation as well, with however much more scattering, in agreement with what has been discussed beforehand.

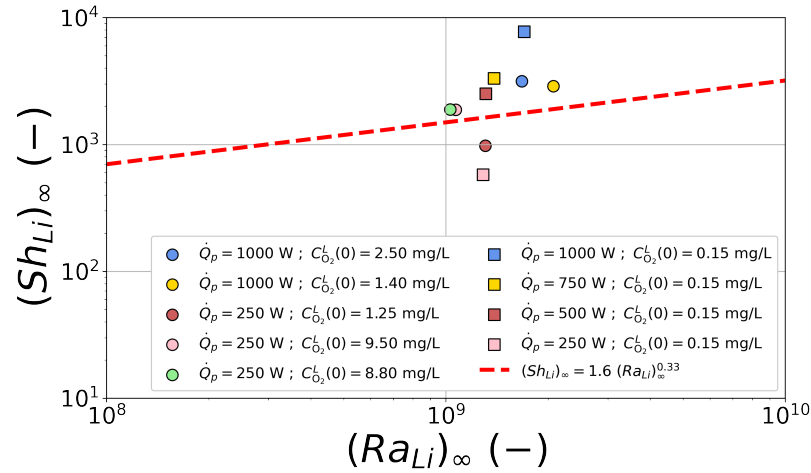


Figure 5.31: The tests initiated with a different amount of dissolved oxygen comply as well with the Sherwood versus Rayleigh natural convection mass transfer correlation, obtained in the single-phase regime, from the 24 tests of the regular matrix. This correlation reflects the liquid-bulk-to-free-surface dissolved gases transfer behind the degassing process.

### 5.2.3 The heated-wall-to-liquid heat transfer

**Dimensionless numbers** A correlation describing the heat transfer developing between the heated bottom wall and the liquid bulk is given below. This process is illustrated in Figure 5.1. As for the liquid-bulk-to-free-surface single-phase natural convection heat and mass transfers discussed in Section 5.2.2, two dimensionless numbers are classically combined through the form of a correlation for describing the bottom-wall-to-liquid heat transfer [35]. First is the liquid-side Rayleigh number, later denoted as  $Ra_h$  and equal to:

$$Ra_h = \frac{g\beta_L(T_h - T_L)d^3}{\nu_L\kappa_L} \quad (5.29)$$

with  $g$  the gravitational acceleration,  $\beta_L$  the liquid thermal expansion coefficient,  $T_L$  the volume-averaged liquid bulk temperature (the  $\langle \cdot \rangle$  space-averaging operator is here omitted),  $T_h$  the area-averaged heated wall temperature (*idem*),  $d$  a length variable characterizing the treated problem and  $\nu_L$ ,  $\kappa_L$ , respectively the liquid kinematic viscosity and thermal diffusivity. This number characterizes the natural convection flow behind the studied heat transfer. Another relevant quantity is the so-called Nusselt number  $Nu_h$ , which is a dimensionless form of the already introduced heat transfer coefficient  $k_h$ . This number reads:

$$Nu_h = \frac{k_h d}{\lambda_L} \quad (5.30)$$

with  $\lambda_L$ , the liquid thermal conductivity.

**The computation of time-averaged values** In what follows is detailed the way a time-averaged value of the retained dimensionless numbers is computed for each ex-

periment of the regular test matrix. Those quantities are later referred to as  $(Ra_h)_\infty$  and  $(Nu_h)_\infty$ . Discarding the first data points of each time series, the latter being typically scattered and irrelevant when related to the bottom wall heat transfer coefficient, as seen in Section 5.1:

$$(Ra_h)_\infty = \frac{1}{\tau} \int_{\tau} \frac{g\beta_L(T_h - T_L) d^3}{\nu_L \kappa_L} dt \quad (5.31)$$

$$(Nu_h)_\infty = \frac{1}{\tau} \int_{\tau} \frac{k_h d}{\lambda_L} dt \quad (5.32)$$

with  $t$ , the time variable and  $\tau$ , the time interval along which the data averaging is conducted. This latter quantity is fixed as the last 30 min of each test, which yields with a data sampling interval set to 3 min (*cf.* Chapter 2) 10 data points. In the above equation,  $k_h$  is equal to:

$$k_h = \frac{1}{S_h \Delta T_h} \left( \dot{Q}_p - m_h C_h \frac{dT_h}{dt} \right) \quad (5.33)$$

**The choice of a transfer length-scale** In the above estimates of the considered dimensionless numbers, a choice for the length-scale  $d$  is to be made. In the case of a natural convection heat transfer in a horizontal layer of fluid, a theoretical analysis of the problem, such as the one achieved by *Turner* in [116], highlights the layer thickness as a relevant length-scale. In the present configuration, this layer thickness is naturally the liquid collapsed level  $z_p$  and hence, in the further developments:

$$d = z_p \quad (5.34)$$

**The heated-wall-to-liquid heat transfer** A specific type of power law involving the so-called Nusselt  $Nu_h$  and Rayleigh  $Ra_h$  dimensionless numbers is commonly used for reducing the data of single-phase natural convection heat transfer experiments [116]. This power law generically reads:

$$Nu_h = C \times Ra_h^n \quad (5.35)$$

with  $C$  and  $n$ , the already introduced pre-factor and exponent of the law, that are classically adjusted against the experimental data. Such an adjustment was done on the basis of the 24 tests of the regular matrix. The obtained results are given in Figure 5.32. In the latter, one may note that the 24 data points are colored according to their associated operating pressure. The symbols of those points differ depending on the value of the initial pool level. As one can observe, the Nusselt and Rayleigh numbers associated with the single-phase regime of all the achieved tests appear significantly correlated through the form of the power law suggested above, with a fairly good average regression coefficient  $R^2$  of 0.91. The law obtained for the heated-wall-to-liquid heat transfer of those tests is thus equal to:

$$(Nu_h)_\infty = 0.23 \times (Ra_h)_\infty^{0.33} \quad (5.36)$$

where one can recognize the typical value of 0.33 of the law exponent, relating to natural convection turbulent flows [116] and an estimated pre-factor of 0.23.

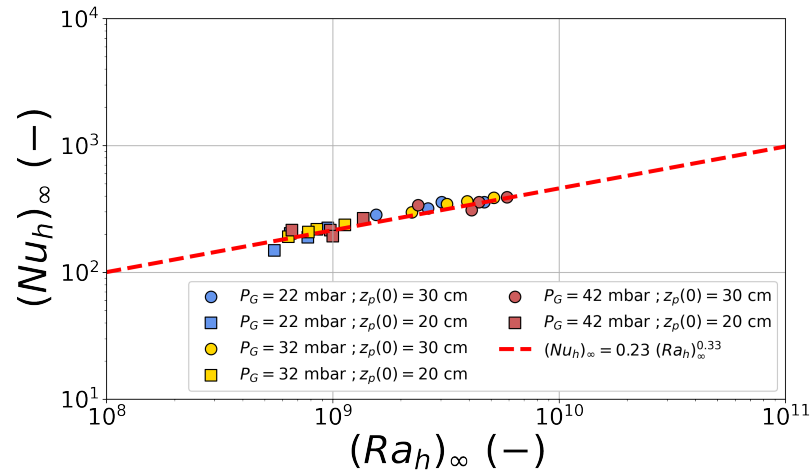


Figure 5.32: The Nusselt versus Rayleigh numbers natural convection heat transfer correlation obtained from the 24 tests of the regular matrix. This correlation reflects the heated-wall-to-liquid heat transfer.

Next, one can verify from Figure 5.33 that the tests initiated with a different amount of dissolved oxygen comply with the obtained correlation as well. As already seen before in this chapter, this highlights the lack of relationship between the instant amount of dissolved gases in the liquid and the developed natural convection heat transfer. The latter being triggered by a heating-induced liquid density difference, this result shows that the instant amount of dissolved gases does not impact significantly the driving liquid density difference. This is fully consistent with the estimated dissolved gases molar fractions  $x_a^L$  throughout any test: those gases are highly diluted in water, *i.e.*  $x_a^L \ll x_w^L$  (*cf.* Chapter 3).

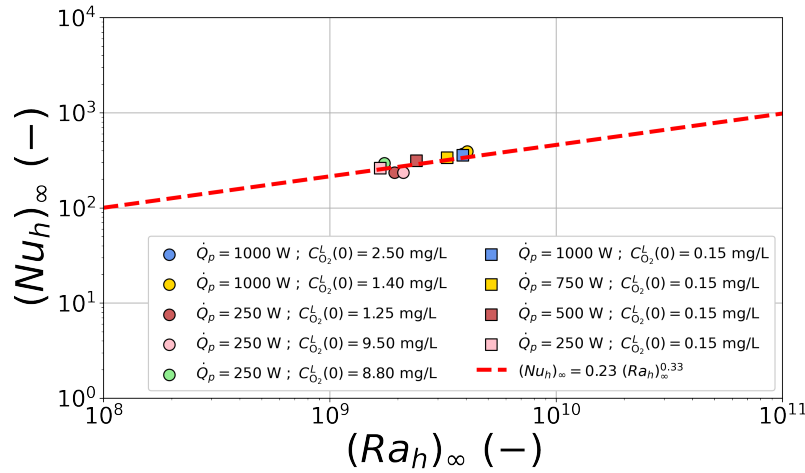


Figure 5.33: The tests initiated with a different amount of dissolved oxygen comply as well with the Nusselt versus Rayleigh natural convection heat transfer correlation, obtained from the 24 tests of the regular matrix. This correlation reflects the heated-wall-to-liquid heat transfer.

## 5.2.4 The two-phase heat and mass transfers

**Dimensionless numbers** In what follows, two correlations are proposed for describing respectively the heat and mass transfers taking place between the liquid bulk and the overall gas/liquid interfacial area (all bubbles and pool free surface) in the two-phase regime, as illustrated in Figure 5.10. Resulting from an initial search by trial-and-error, a set of four dimensionless numbers has been proven relevant for representing those two-phase heat and mass transfers. These numbers are successively presented next.

First of all is a dimensionless form of the heat transfer rate  $k_T^L S_i$ , denoted as  $\Phi_T$ , which reads:

$$\Phi_T = \frac{k_T^L S_i}{(k_T^L S_i)_o} \quad (5.37)$$

where  $(k_T^L S_i)_o$  is an estimated single-phase heat transfer rate, corresponding to the system's temperatures and pressure reached during the two-phase regime and with  $S_i = S_p$ . The quantity  $(k_T^L S_i)_o$  is computed by means of Equation (5.26) as:

$$(k_T^L S_i)_o = 0.6 \times Ra_{Li}^{0.33} \times \frac{\lambda_L S_p}{z_p} \quad (5.38)$$

Let us highlight the physical meaning of the introduced variable  $\Phi_T$ . Provided the system's temperatures and pressure,  $\Phi_T$  quantifies the deviation of the actual two-phase heat transfer rate from its single-phase counterpart, estimated as above. The latter is hence expected to be always bigger than unity during the bubbling stage and equal to unity, with  $(k_T^L S_i)_o = (k_T^L S_i)_\infty$ , once the system's asymptotic state is reached. In a similar fashion, one can introduce  $\Phi_m$ , a dimensionless form of the mass transfer rate

$k_m^L S_i$ , defined as:

$$\Phi_m = \frac{k_m^L S_i}{(k_m^L S_i)_o} \quad (5.39)$$

where  $(k_m^L S_i)_o$  is an estimated single-phase mass transfer rate, corresponding to the system's temperatures, dissolved gases concentration and pressure reached during the two-phase regime and with  $S_i = S_p$ . The quantity  $(k_m^L S_i)_o$  is computed by means of Equation (5.28) as:

$$(k_m^L S_i)_o = 1.6 \times Ra_{Li}^{0.33} \times \frac{\mathcal{D}_{a;w}^L S_p}{z_p} \quad (5.40)$$

Next is the so-called Gibbs number, denoted as  $Gb$  and representing a dimensionless form of the energetic cost  $\Delta F_{max}$  associated with any bubble nucleation process (*cf.* Chapter 4). This number reads [18]:

$$Gb = \frac{\Delta F_{max}}{k_B T_L} \quad (5.41)$$

with  $k_B$  the so-called Boltzmann's constant and:

$$\Delta F_{max} = \frac{16}{3} \frac{\pi \sigma^3}{(P_a^L + P_{sat}(T_L) - P_G)^2} \quad (5.42)$$

(*cf.* Chapter 4). At last is the already introduced Rayleigh number  $Ra_L$ , defined as:

$$Ra_L = \frac{g \beta_L \Delta T_L d^3}{\nu_L \kappa_L} \quad (5.43)$$

with:

$$\Delta T_L = T_h - T_{sat}(P_G) \quad (5.44)$$

**The choice of a transfer length-scale** In the below estimates of the considered Rayleigh number  $Ra_L$ , a choice for the length-scale  $d$  is to be made. In the case of a natural convection heat transfer in a horizontal layer of fluid, a theoretical analysis of the problem, such as the one achieved by *Turner* in [116], highlights the layer thickness as a relevant length-scale. In the present configuration, this layer thickness is naturally the liquid collapsed level  $z_p$  and hence, in the further developments:

$$d = z_p \quad (5.45)$$

**Data processing** Contrarily to what has been done earlier in this section regarding the developed single-phase heat and mass transfer correlations, the time-series of each test composing the regular matrix was not time-averaged. Instead, at any time of the bubbling regime of those tests, the above four dimensionless numbers were all estimated, yielding time-series of  $\Phi_T$ ,  $\Phi_m$ ,  $Gb$  and  $Ra_L$ . Indeed, as it has been discussed in Chapter 3, the two-phase regime is unsteady, making here irrelevant the time-averaging process achieved earlier for the single-phase data.

**The dimensionless two-phase heat transfer rate** With the aim to correlate dimensionless numbers in the field of fluid mechanics, a specific type of mathematical function is often considered: the so-called power law [9]. The latter is hence an interesting candidate for correlating the two-phase data acquired from Aquarius experiments. In the present case, restricting only to those numbers in link with the two-phase heat transfer, such a law can be generically expressed as:

$$\Phi_T = C_T \times Gb^{n_1} \times Ra_L^{n_2} \quad (5.46)$$

with  $C_T$ , a pre-factor and  $n_1$  and  $n_2$ , two exponents. By means of this law, let us investigate the potential correlation existing between  $\Phi_T$ ,  $Gb$  and  $Ra_L$  in a step-by-step fashion. First of all, considering the time-series of all the tests composing the regular matrix, a graph representing the obtained  $\Phi_T$  versus  $Gb$  is plotted. It is given in Figure 5.34. As one can notice,  $\Phi_T$  appears negatively correlated to  $Gb$ , with an exponent  $n_1 = -0.33$ . According to the correlation, the bigger the energetic cost for bubble nucleation (*i.e.* the bigger  $Gb$ ), the lesser the intensity of the two-phase heat transfer rate (*i.e.* the closer  $\Phi_T$  from unity). This interesting finding does appear in complete agreement with the phenomenological observations discussed earlier in Chapter 3.

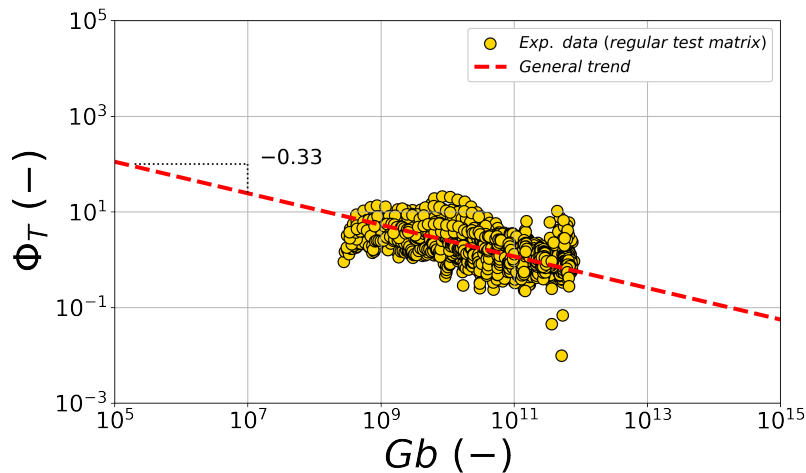


Figure 5.34: Plotting of  $\Phi_T$  versus  $Gb$ , achieved on the basis of the time-series of the tests composing the regular matrix.

Having found out the value taken by  $n_1$ , another plotting exhibiting  $\Phi_T/Gb^{-0.33}$  versus  $Ra_L$  allows estimating the pre-factor  $C_T$  and the remaining exponent  $n_2$ . This plot is shown in Figure 5.35. At first glance, the data seems correlated according to the proposed power law, with an exponent  $n_2 = 1.5$ . This indicates that the intensification of the two-phase heat transfer rate is an increasing function of the intensity of the natural convection flow of the liquid phase, here represented by  $Ra_L$ , as one might expect. However, the data appears clearly separated into two bunches of points, each having its own value for the pre-factor  $C_T$ .

Going deeper in the analysis by plotting each data point according to the retained initial pool level, as performed in Figure 5.36, unveils this peculiarity: the value taken

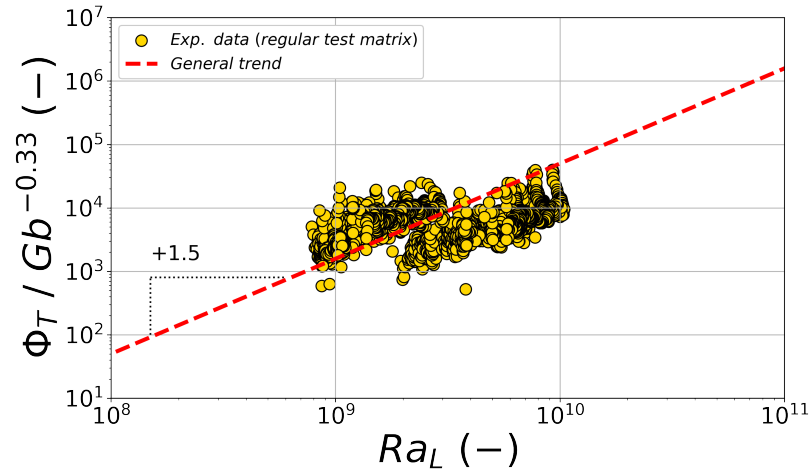


Figure 5.35: Plotting of  $\Phi_T / Gb^{-0.33}$  versus  $Gb$ , achieved on the basis of the time-series of the tests composing the regular matrix.

by  $C_T$  seems dependent to the initial pool level. The expected two values for  $C_T$  are estimated through the graph given in Figure 5.37. One gets:

- $C_T = 1.86 \times 10^{-11}$  for  $z_p(0) = 30$  cm;
- $C_T = 1.15 \times 10^{-10}$  for  $z_p(0) = 20$  cm;

from which one can note that the value for  $C_T$  is reversely correlated to the initial pool level. Owing to the limited set of available data (*i.e.* only two values for the initial pool level were retained in the regular test matrix), this mathematical relationship can be approximated by the following linear law:

$$C_T \approx -9.64 \times 10^{-12} z_p(0) + 3.08 \times 10^{-10} \quad (5.47)$$

with  $z_p(0)$  given in cm. Of course, a later use of this correlation giving  $C_T$  is to be strictly limited to the retained range of explored initial pool levels, *i.e.* 20-30 cm. Indeed, this simple linear correlation is most likely far from the actual mathematical expression for  $C_T$ , as suggested by the existence of negative values of  $C_T$  for  $z_p(0) > 32$  cm, which is physically inconsistent. Let us next verify if the tests initiated with a different amount of dissolved oxygen comply with the obtained two-phase correlation. It is to be recalled that those tests were all initiated at a pool level  $z_p(0) = 30$  cm. The data obtained from those tests does comply with the correlation with the right expected value for  $C_T$ , as one can remark from Figure 5.38. This highlights that it is not directly the instant amount of dissolved gases in the liquid that matters for the intensity of the two-phase heat transfer. It does so however indirectly through the correlation between  $\Phi_T$  and  $Gb$ , the latter number being the dimensionless cost for bubble nucleation and obviously, a function of the amount of dissolved gases.

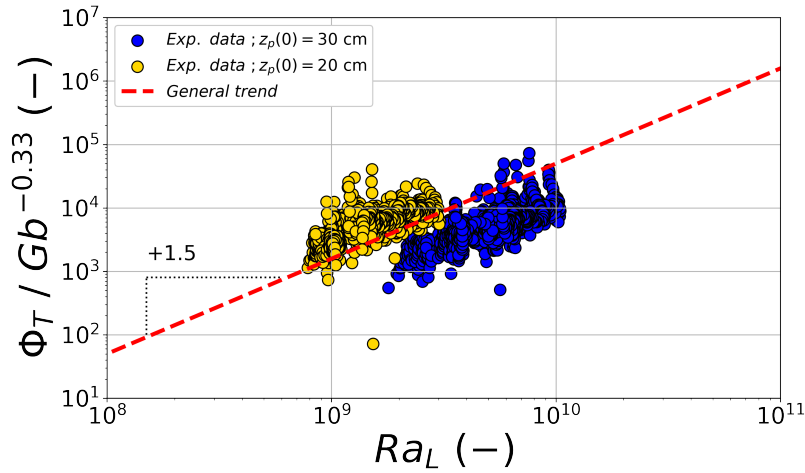


Figure 5.36: Plotting of  $\Phi_T / Gb^{-0.33}$  versus  $Gb$ , with a color scale taking into account the retained initial pool level, achieved on the basis of the time-series of the tests composing the regular matrix.

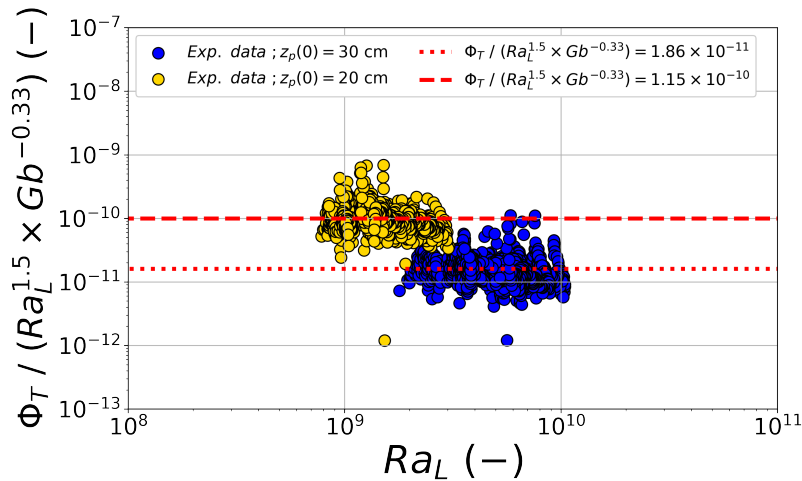


Figure 5.37: Plotting of  $\Phi_T / Gb^{-0.33} / Ra_L^{1.5}$  versus  $Gb$ , with a color scale taking into account the retained initial pool level, achieved on the basis of the tests composing the regular matrix.

Eventually, one can summarize the above investigations through the form of the below power law:

$$\Phi_T = C_T \times Gb^{-0.33} \times Ra_L^{1.5} \quad (5.48)$$

where the pre-factor  $C_T$  is given by Equation (5.47).

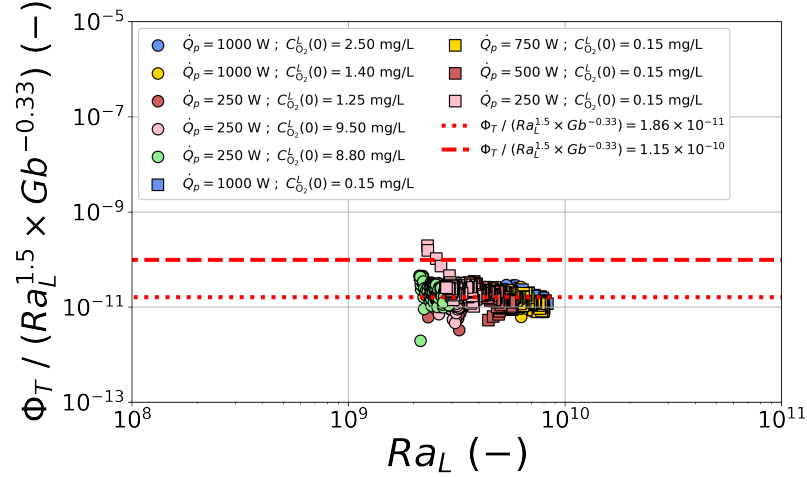


Figure 5.38: Plotting of  $\Phi_T/Gb^{-0.33}/Ra_L^{1.5}$  versus  $Gb$ , achieved on the basis of the time-series of the tests initiated with a different amount of dissolved oxygen.

**The dimensionless two-phase mass transfer rate** In a way similar than the one developed above for the heat transfer, one can retain as a first guess the following power law as an interesting candidate for reducing the two-phase mass transfer data:

$$\Phi_m = C_m \times Gb^{n_1} \times Ra_L^{n_2} \quad (5.49)$$

with  $C_m$ , a pre-factor and  $n_1$  and  $n_2$ , two exponents. Let us investigate next the potential correlation existing between  $\Phi_m$ ,  $Gb$  and  $Ra_L$  in an analogous step-by-step fashion. First of all, considering the time-series of all the tests composing the regular matrix, a graph representing the obtained  $\Phi_m$  versus  $Gb$  is plotted. It is given in Figure 5.39. As one can notice,  $\Phi_m$  appears negatively correlated to  $Gb$ , with an exponent  $n_1 = -0.33$ , as for the heat transfer. According to the correlation, the bigger the energetic cost for bubble nucleation (*i.e.* the bigger  $Gb$ ), the lesser the intensity of the two-phase mass transfer rate too (*i.e.* the closer  $\Phi_m$  from unity). This interesting finding does still appear in complete agreement with the phenomenological observations discussed earlier in Chapter 3.

Having found out the value taken by  $n_1$ , another plotting exhibiting  $\Phi_m/Gb^{-0.33}$  versus  $Ra_L$  allows estimating the pre-factor  $C_m$  and the remaining exponent  $n_2$ . This plot is shown in Figure 5.40. At first glance, the data seems identically correlated according to the proposed power law, with an exponent  $n_2 = 1.5$ . This indicates that the intensification of the two-phase mass transfer rate is an increasing function of the intensity of the natural convection flow of the liquid phase, here represented by  $Ra_L$ , as one might expect. However, as already emphasized for the heat transfer, the data appears clearly separated into two bunches of points, each having its own value for the pre-factor  $C_m$ .

Going deeper in the analysis by plotting each data point according to the retained initial pool level, as performed in Figure 5.41, unveils this peculiarity: the value taken

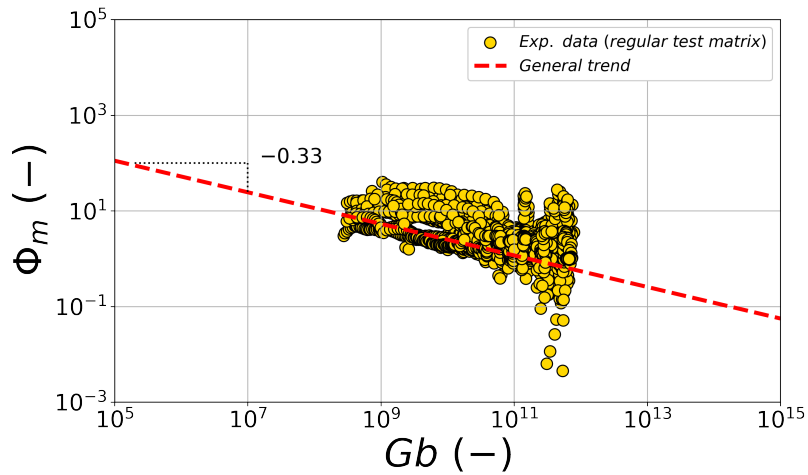


Figure 5.39: Plotting of  $\Phi_m$  versus  $Gb$ , achieved on the basis of the time-series of the tests composing the regular matrix.

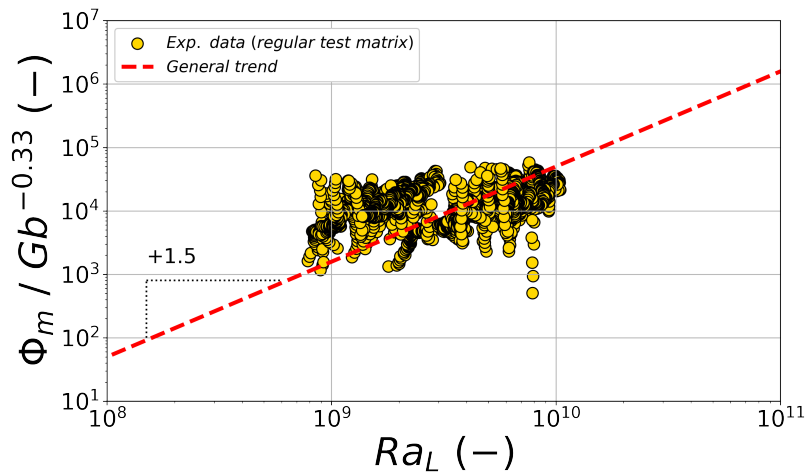


Figure 5.40: Plotting of  $\Phi_m / Gb^{-0.33}$  versus  $Gb$ , achieved on the basis of the time-series of the tests composing the regular matrix.

by  $C_m$  still seems dependent to the initial pool level. The expected two values for  $C_m$  are estimated through the graph given in Figure 5.42. One gets:

- $C_m = 4.18 \times 10^{-11}$  for  $z_p(0) = 30$  cm;
- $C_m = 2.47 \times 10^{-10}$  for  $z_p(0) = 20$  cm;

from which one can note that the value for  $C_m$  is reversely correlated to the initial pool level. As one can note, those values are approximately two times bigger than the ones obtained earlier for  $C_T$ . Owing to the limited set of available data (*i.e.* only two values for the initial pool level were retained in the regular test matrix), this mathematical

relationship can be approximated by the following linear law:

$$C_m \approx -2.05 \times 10^{-12} z_p(0) + 6.57 \times 10^{-10} \quad (5.50)$$

with  $z_p(0)$  given in cm. Let us next verify if the tests initiated with a different amount of dissolved oxygen comply with this apparent correlation. It is to be recalled that those tests were all initiated at a pool level  $z_p(0) = 30$  cm. The data obtained from those tests does comply with the correlation with the right expected value for  $C_m$ , as one can remark from Figure 5.43. This highlights that it is not directly the instant amount of dissolved gases in the liquid that matters for the intensity of the two-phase mass transfer. It does so however indirectly through the correlation between  $\Phi_m$  and  $Gb$ , the latter number being the dimensionless cost for bubble nucleation and obviously, a function of the amount of dissolved gases.

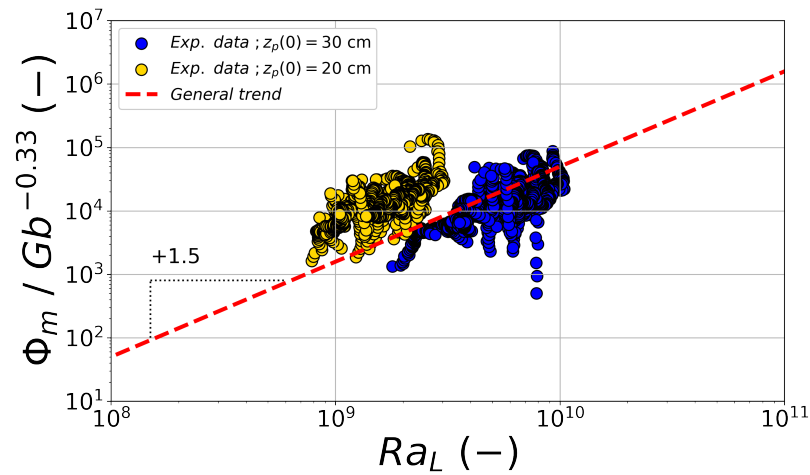


Figure 5.41: Plotting of  $\Phi_m / Gb^{-0.33}$  versus  $Gb$ , with a color scale taking into account the retained initial pool level, achieved on the basis of the time-series of the tests composing the regular matrix.

Eventually, one can summarize the above investigations through the form of the below power law:

$$\Phi_m = C_m \times Gb^{-0.33} \times Ra_L^{1.5} \quad (5.51)$$

where the pre-factor  $C_m$  is given by Equation (5.50).

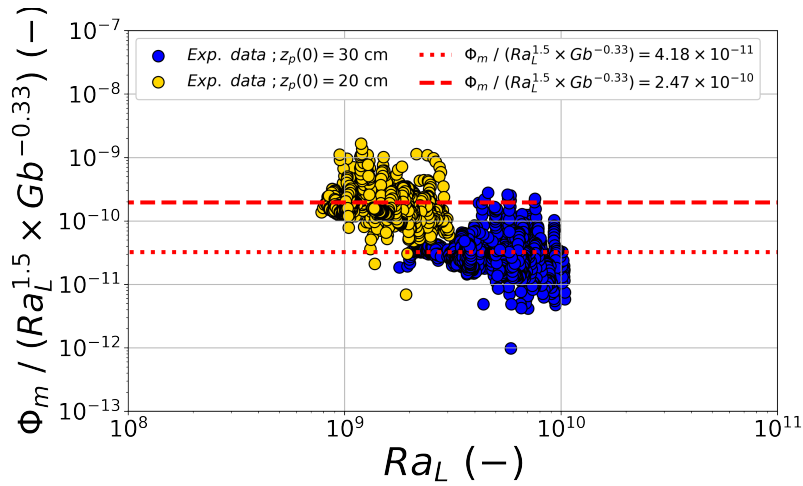


Figure 5.42: Plotting of  $\Phi_m/Gb^{-0.33}/Ra_L^{1.5}$  versus  $Gb$ , with a color scale taking into account the retained initial pool level, achieved on the basis of the time-series of the tests composing the regular matrix.

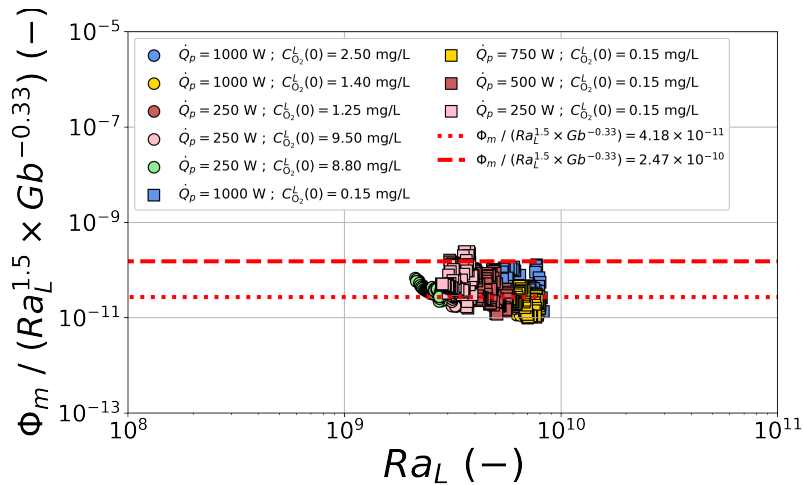


Figure 5.43: Plotting of  $\Phi_m/Gb^{-0.33}/Ra_L^{1.5}$  versus  $Gb$ , achieved on the basis of the time-series of the tests initiated with a different amount of dissolved oxygen.

### 5.3 A lumped-parameter model of the Aquarius pool

In this last section, we provide the reader with a so-called lumped parameter model of the Aquarius pool, which integrates the previously defined heat and mass transfer correlations. The model is then used to simulate some of the achieved tests as a way to verify its implemented constitutive equations and correlations.

#### 5.3.1 Model description

**The resolved problem** The proposed lumped-parameter model describes the mass and energy balance equations governing the liquid pool volume  $V_L$ , depicted in Figure

5.44. Three so-called conservative variables, whose time-evolution is dictated by these balance equations, are attributed to the control volume:

- $m_L$ : the liquid mass;
- $m_a^L$ : the total mass of all gases dissolved in the liquid;
- $U_L$ : the total internal energy of the liquid.

As a modeling assumption, two bounding surfaces allow heat and mass exchanges between the control volume  $V_L$  and its surrounding environment. First is the total heaters area, denoted as  $S_h$ , which is restricted to heat exchanges. Second is the gas/liquid interfacial area  $S_i$  introduced earlier in this chapter. Across this interface, both heat and mass transfers may develop. Specifically regarding the mass exchanges, both water and dissolved gases may transfer toward the outer environment through the latter. By limiting the exchanges to these two very areas, the heat losses that may develop between the liquid volume  $V_L$  and the outer environment are precisely neglected. As seen in Chapter 3, those losses are practically negligible for most of the studied configurations, thereby justifying their disregard. Further on, the thermal inertia of the heated wall is not modeled and the heated-wall-to-liquid heat transfer is assumed steady at any considered time along the simulations. Then, the gas bulk in contact with the liquid volume through the interfacial area  $S_i$  is supposed exclusively composed of steam at the temperature  $T_{sat}(P_G)$  and pressure  $P_G$ . In turn, this implies that  $\omega_a^{Li} = 0$ , as already discussed in Chapter 3. At last, with  $k_m^L S_i$  and  $k_T^L S_i$ , respectively the dissolved gases and heat transfer rates at the gas/liquid interface, the mass and energy balance equations governing the control volume read:

$$\frac{dm_a^L}{dt} = -k_m^L S_i \omega_a^L \quad (5.52)$$

$$\frac{dm_L}{dt} = \frac{-k_T^L S_i}{\mathcal{L}_w} (T_L - T_{sat}(P_G)) \quad (5.53)$$

$$\frac{dU_L}{dt} = \dot{Q}_p - \left| \frac{dm_L}{dt} \right| h_{gsat}(P_G) - P_G \frac{dV_L}{dt} \quad (5.54)$$

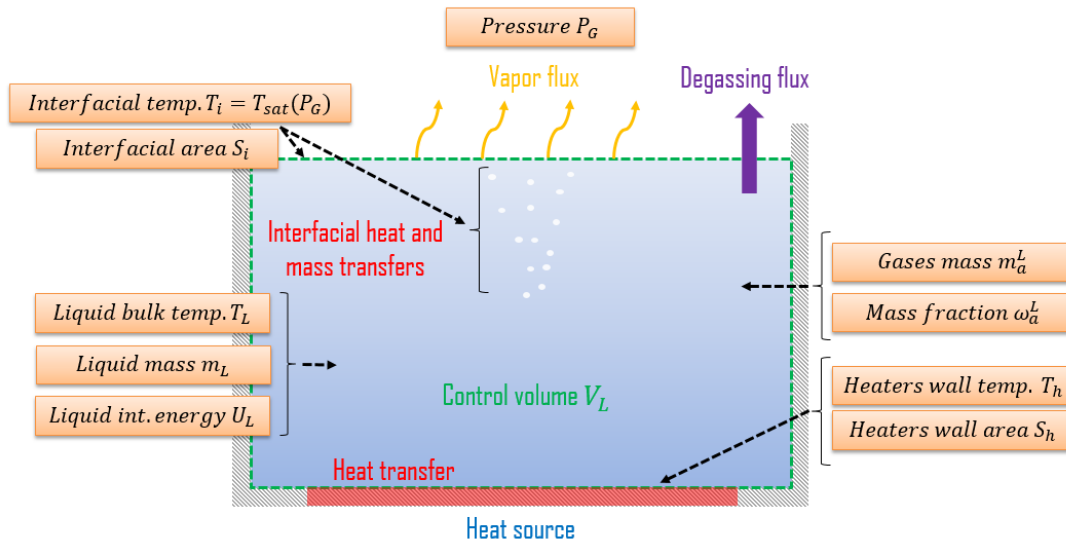


Figure 5.44: Illustration of the modeled control volume  $V_L$  and its associated conservative and state variables.

**Closure relations** In order to be resolved, the above system of equations requires the closure of some of its constitutive variables. First of all are the so-called state variables  $T_L$  and  $\omega_a^L$ , respectively the volume-averaged liquid bulk temperature and dissolved gases mass fraction (the  $\langle \cdot \rangle$  space-averaging operator is here omitted). Provided  $m_L$  and  $U_L$ , one can deduce  $T_L$  by first computing the specific liquid internal energy  $u_L(T_L, P_G)$  as:

$$u_L(T_L, P_G) = \frac{U_L}{m_L} \quad (5.55)$$

Then, making use of a thermophysical properties database:

$$u_L(T_L, P_G) \rightarrow T_L \quad (5.56)$$

Next,  $\omega_a^L$  is simply approximated by:

$$\omega_a^L \approx \frac{m_a^L}{m_L} \quad (5.57)$$

provided the dissolved gases are highly diluted in water. Importantly, the control volume  $V_L$  is to be calculated. This is done as:

$$V_L = \frac{m_L}{\rho_L(T_L, P_G)} \quad (5.58)$$

with  $\rho_L(T_L, P_G)$  the liquid density, estimated once  $T_L$  is known. Further on are the variables involved in the exchanged heat and mass fluxes:  $k_m^L S_i$  and  $k_T^L S_i$ , respectively the already introduced dissolved gases and heat interfacial transfer rates. Those variables are estimated by means of Equations (5.48) and (5.51) derived in Section 5.2. In the latter, through the computation of the Rayleigh number  $Ra_L$ , one has to provide a value for

the unresolved heated wall temperature  $T_h$ . Reminding that the heated-wall-to-liquid heat transfer is assumed steady:

$$T_h = T_L + \frac{\dot{Q}_p}{k_h S_h} \quad (5.59)$$

Then, combining Equations (5.59) and (5.36), this yields:

$$T_h = T_L + \left( \frac{1}{0.23} \frac{\dot{Q}_p}{S_h \lambda_L} \left( \frac{\kappa_L \nu_L}{g \beta_L} \right)^{1/3} \right)^{3/4} \quad (5.60)$$

with the already introduced liquid bulk parameters  $\kappa_L$ ,  $\nu_L$ ,  $\lambda_L$  and  $\beta_L$  estimated by means of a thermophysical properties database, at temperature  $T_L$  and pressure  $P_G$ . In the Gibbs number  $Gb$ , two more variables are to be fixed:  $P_a^L$  and  $P_{sat}(T_L)$ , respectively the partial pressure of the dissolved gases in solution within the liquid and the water saturation pressure at temperature  $T_L$ . If the last of the latter variables is directly given by any thermophysical properties database once  $T_L$  is known,  $P_a^L$  requires more attention. Provided  $\omega_a^L$  and  $T_L$ ,  $P_a^L$  can be estimated by means of the already discussed Henry's law:

$$P_a^L = \omega_a^L \frac{\mathcal{H}_a(T_L)}{\mathcal{M}_a} \quad (5.61)$$

with  $\mathcal{H}_a(T_L)$ , the so-called Henry's constant of dissolved air, evaluated at temperature  $T_L$  and  $\mathcal{M}_a$  the air molar mass. At last,  $P_G$  and  $\dot{Q}_p$  are fixed and imposed prior to the solving of the above system of differential equations. Identically,  $\mathcal{L}_w$ ,  $T_{sat}(P_G)$  and  $h_{g,sat}(P_G)$  are also constant and given by any thermophysical properties database, once  $P_G$  is known. All those steps are numerically implemented in the code given in Appendix E.

**Evaluation of fluid thermophysical properties** When needed, all fluid properties are evaluated using the open-source database called *CoolProp* [10]. It allows accessing pure and pseudo-pure fluid properties, including water and air/vapor mixtures. *CoolProp* development, verification and validation is mainly supported by University of Liege and Denmark Technical University.

**Numerical scheme and discretized equations** In the computational program written for simulating the Aquarius experiments, a so-called Euler implicit numerical scheme has been retained and coded (*cf.* Appendix F). Indeed, the latter typically offers a good numerical stability. At a fixed time step  $\Delta t$ , it is however numerically more costly than its explicit counterpart [101]. But, owing to the somewhat limited physical duration of the simulated tests, its choice is fully relevant. The resolved system of equations is first expressed through a matrix form as follows:

$$\frac{dY}{dt} = F(X, t) \quad (5.62)$$

with  $t$  the time variable,  $Y$  the so-called vector of the conservative variables:

$$Y = \begin{bmatrix} m_a^L \\ m_L \\ U_L \end{bmatrix} \quad (5.63)$$

with  $X$  the so-called vector of state variables:

$$X = \begin{bmatrix} \omega_a^L \\ m_L \\ T_L \end{bmatrix} \quad (5.64)$$

then with  $F$  the so-called flux function, returning as a vector form the right-hand-side of the resolved system of equations, provided  $X$  and  $t$ . The discretization of the above system of equations according to an Euler implicit scheme reads:

$$\frac{Y_{n+1} - Y_n}{\delta t} = F(X_{n+1}, t_{n+1}) \quad (5.65)$$

with index:

- $n$  attributed to the variables estimated at time  $t_n$ ;
- $n+1$  attributed to the variables estimated at time  $t_{n+1} = t_n + \delta t$ .

At each time step, knowing  $X_n$  and  $Y_n$ ,  $X_{n+1}$  and  $Y_{n+1}$  are solved iteratively by a coded Newton algorithm (*cf.* Appendix F). The algorithm convergence is considered if the following condition on  $Y$  is fulfilled:

$$\left| \frac{Y^{i+1} - Y^i}{Y^{i+1}} \right| \leq \epsilon \quad (5.66)$$

with  $i$ , the iteration index and  $\epsilon$ , some arbitrary convergence criterion  $\ll 1$ .

### 5.3.2 The simulation of the reference case

In this section, we provide the results of the simulation of the reference case, done with the lumped-parameter model previously described. Let us first recall the characteristics of the reference test, achieved on April 12, 2022:

- **Thermal power**  $\dot{Q}_p = 1000$  W;
- **Operating pressure**  $P_G = 22$  mbar;
- **Initial liquid temperature**  $T_L(0) = 20^\circ\text{C}$ ;
- **Initial pool level**  $z_p(0) = 30$  cm;
- **Initial content in dissolved oxygen**  $C_{O_2}(0) = 5.8$  mg/L (value in excess at a pressure of 22 mbar).

Next, the presented simulation was conducted with those characteristics and the following numerical settings:

- **Time step**  $\Delta t = 180$  s;
- **Precision**  $\epsilon = 10^{-6}$ ;
- **Maximum iteration number**  $\text{Max}(N_{iter}) = 10$ .

The obtained results are successively presented in the figures below. First of all are depicted, respectively in the left and right-hand sides of Figure 5.45, the time-trend of the liquid mass  $m_L$  and of the liquid vaporization rate  $\dot{m}_L$ . As one can observe, the simulation reproduces well those two quantities, thereby verifying two important points. On one hand, this good fitting confirms that the heat losses at pool's boundaries, omitted in the lumped-parameter model, are reasonably negligible. On the other hand, the mass and energy balances of the modeled liquid pool are certainly well resolved.

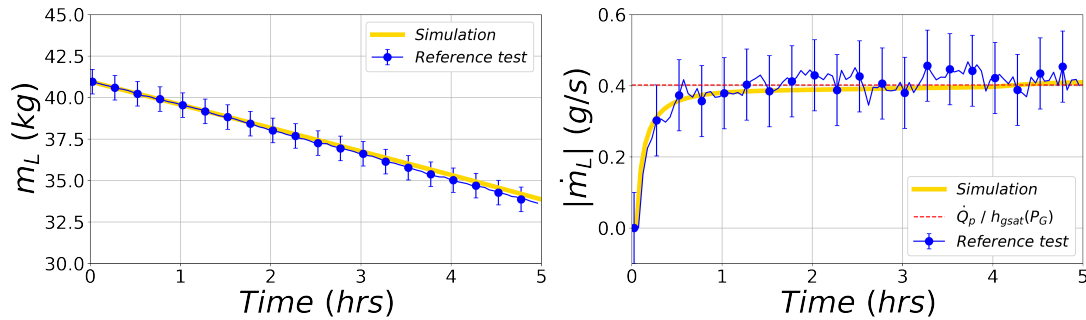


Figure 5.45: Simulation of the reference test. Left: liquid mass  $m_L$ . Right: liquid vaporization rate  $\dot{m}_L$ .

Next, we compare in Figure 5.46 the simulated liquid thermal metastability degree  $\Delta T_{eq}$  with the one estimated from the reference test data. It is to be noted that the overall trend of this very variable is well reproduced, with however some apparent slight delay, of the order of 30 min. The actual asymptotic value of  $\Delta T_{eq}$ , denoted as  $\Delta T_{eq,\infty}$ , is almost reached by the simulation, with a discrepancy of the order of  $0.5^\circ\text{C}$ .

As it has been widely discussed in Chapter 3, the instant amount of dissolved gases contained in the liquid pool is another important variable for describing the phenomenon. Its related counterparts, *i.e.* the dissolved  $\text{O}_2$  mass concentration  $C_{\text{O}_2}$  and degassing rate  $\dot{C}_{\text{O}_2}$ , are both plotted in Figure 5.47. Overall, one can notice that the trend of the latter two variables is well reproduced by the lumped-parameter model. But, as for the thermal metastability degree depicted in Figure 5.46, there exists some time lag between the simulated and actual  $\dot{C}_{\text{O}_2}$  which is of the order of 30 min too. Obviously, this lag leads to some appreciable discrepancy in the simulated and actual maximum values of  $\dot{C}_{\text{O}_2}$ , as seen in the right-hand-side graph of Figure 5.47.

Further on, let us compare the simulated heated wall temperature difference  $\Delta T_h$  and heat transfer coefficient  $k_h$  with the actual ones. This is done in Figure 5.48. As

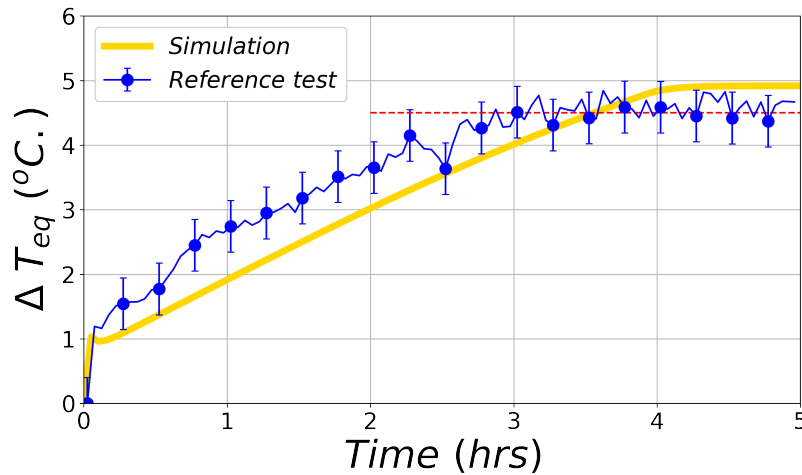


Figure 5.46: Simulation of the reference test. Time-trend of the thermal metastability degree of the heated liquid  $\Delta T_{eq}$ .

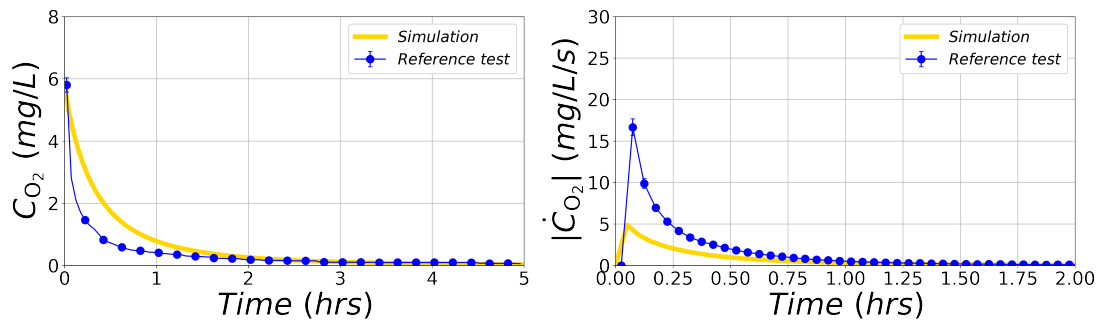


Figure 5.47: Simulation of the reference test. Left: dissolved oxygen mass concentration  $C_{O_2}$ . Right: oxygen degassing rate  $\dot{C}_{O_2}$ .

one can see, those variables are both well simulated, with however, some significant mismatch during the first minutes of the test. As discussed earlier in this chapter, the initial excess values of  $k_h$ , in link with some smaller temperature difference  $\Delta T_h$ , are most likely random, which makes uncertain the utilized heat transfer correlation during that very moment of the simulation, thereby explaining the initial discrepancy between the simulated and actual heaters variables. The simulated interfacial heat and mass transfer rates, denoted as  $k_T^L S_i$  and  $k_m^L S_i$ , exhibit a similar trend with an appreciable discrepancy at the beginning of the reference test (Figure 5.49), which is most likely due to the same reasons. This is also reflected in Figure 5.50, showing the two dimensionless quantities  $\Phi_T$  and  $\Phi_m$ .

At last, when combining both  $\Delta T_{eq}$  and  $C_{O_2}$  in Figure 5.51, as firstly done in Section 3.1.3, it can be observed that the correlation between the instant liquid thermal metastability degree and dissolved  $O_2$  mass concentration is fairly well reproduced, with the same doubly-linear trend. This result may seem surprising at first glance, on the basis of the time lags that have been highlighted above. But, these time lags being of the

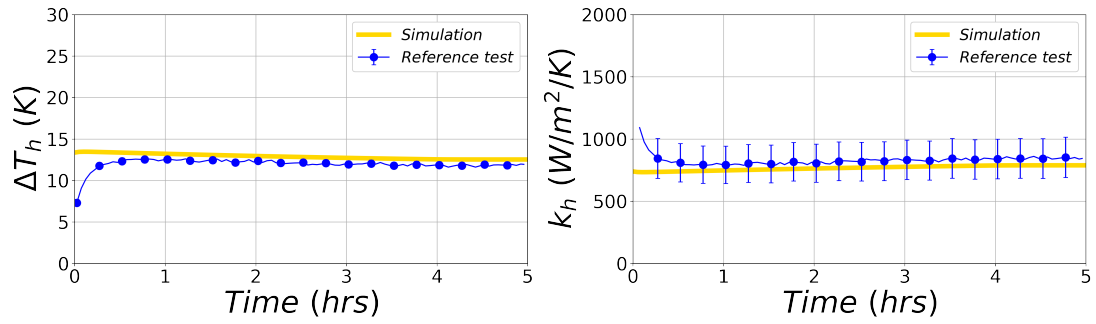


Figure 5.48: Simulation of the reference test. Left: heated wall temperature difference  $\Delta T_h$ . Right: heated wall heat transfer coefficient  $k_h$ .

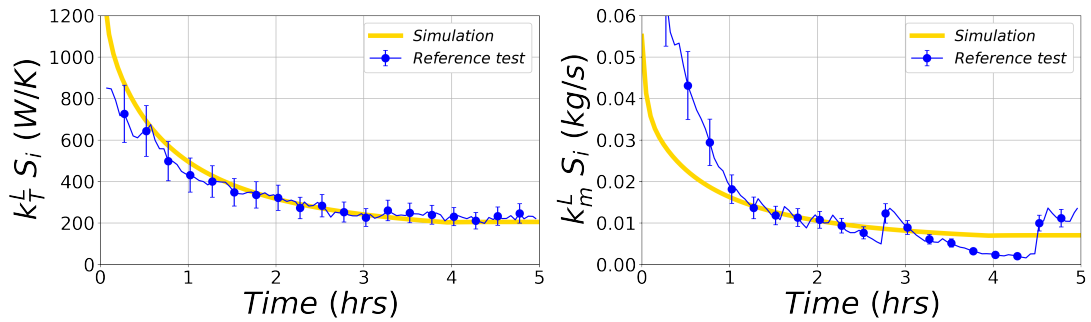


Figure 5.49: Simulation of the reference test. Left: interfacial heat transfer rate  $k_T^L S_i$ . Right: interfacial mass transfer rate  $k_m^L S_i$ .

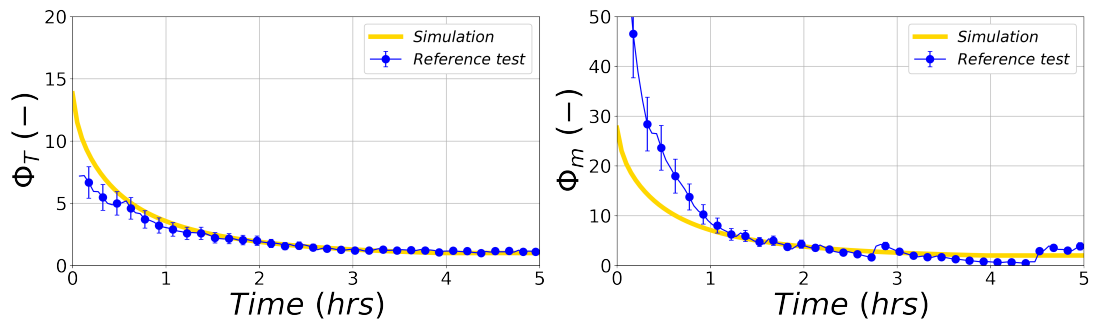


Figure 5.50: Simulation of the reference test. Dimensionless quantities  $\Phi_T$  and  $\Phi_m$  associated with the interfacial heat and mass transfer rates  $k_T^L S_i$  and  $k_m^L S_i$ .

same order of magnitude for both  $\Delta T_{eq}$  and  $C_{O_2}$ , it is not counter-intuitive to observe nevertheless the same correlation between these variables.

Overall, having those first results in mind, one can argue that the proposed lumped-parameter model of the Aquarius pool is able to simulate the reference test with little and understood discrepancies. Let us see in the next subsections if the model still does so for other experimental configurations. For more clearness, we will focus in what follows on a limited but sufficient set of liquid pool variables: the liquid thermal metastability degree  $\Delta T_{eq}$ , mass  $m_L$  and vaporization rate  $\dot{m}_L$ , the dissolved  $O_2$  mass concentration

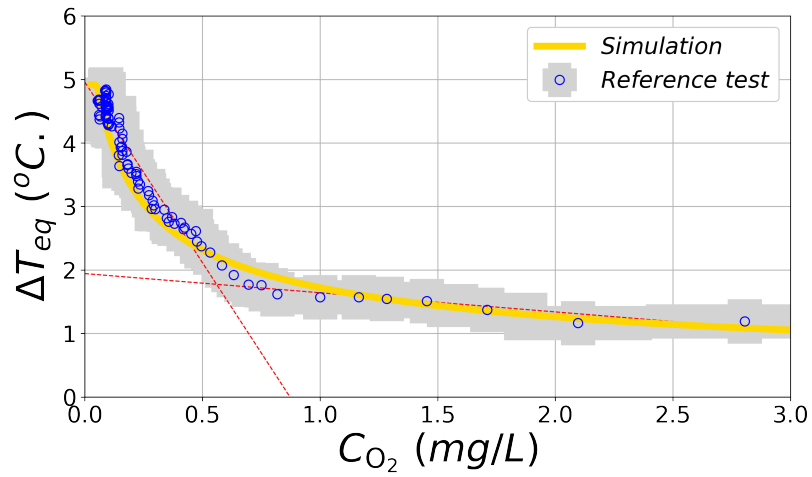


Figure 5.51: Simulation of the reference test. Correlation between the variables reflecting the liquid degassing and heat-up kinetics,  $C_{O_2}$  and  $\Delta T_{eq}$ .

$C_{O_2}$  and degassing rate  $\dot{C}_{O_2}$  and the interfacial heat and mass transfer rates  $k_T^L S_i$  and  $k_m^L S_i$ .

### 5.3.3 The simulation of sensitivity cases

The simulations that are presented next were all performed using the below numerical settings, as for the simulated reference case:

- **Time step**  $\Delta t = 180$  s;
- **Precision**  $\epsilon = 10^{-6}$ ;
- **Maximum iteration number**  $\text{Max}(N_{iter}) = 10$ .

Obviously, each simulation was initialized with the parameters of its corresponding sensitivity test. This is detailed in what follows.

**Variations of the heating power** The later study focuses on the ability of the lumped-parameter model to reproduce the phenomenon sensitivity to the heating power. The four tests, simulated for that purpose, are the ones given in Table 5.3. The latter were all initiated at identical values of  $P_G$ ,  $z_p(0)$  and  $C_{O_2}(0)$ , with the intent to separate the potential effects of those parameters from the one, expected, of the heating power. Four different values of the heating power  $\dot{Q}_p$  were retained: 1000, 750, 500 and 250 W.

Table 5.3: The series of tests, retained and simulated, for investigating the effect of the heating power on the phenomenon.

Date of achievement	$\dot{Q}_p$ (W)	$P_G$ (mbar)	$z_p(0)$ (cm)	$C_{O_2}(0)$ (mg/L)
November 25, 2021	1000	22	30	6.5
January 14, 2022	750	22	30	6.5
January 7, 2022	500	22	30	6.5
November 10, 2021	250	22	30	6.5

At first, Figure 5.52 gives the time-trends of the simulated liquid thermal metastability degrees  $\Delta T_{eq}$  and dissolved  $O_2$  mass concentrations  $C_{O_2}$ . As one can remark, the overall trend of those parameters is well captured by the proposed lumped-parameter model, with  $\Delta T_{eq}$  systematically tending toward its asymptotic value  $\Delta T_{eq;\infty}$  after some initial transient and with  $C_{O_2}$  tending toward zero. Importantly, as experimentally evidenced, the higher the heating power, the higher  $\Delta T_{eq;\infty}$ . Indeed as discussed in Chapter 3, with an increased heat supply and at fixed atmospheric conditions on top of the free surface, the system is expected to reach a higher liquid bulk temperature for equilibrating this supply with the free surface evaporation heat removal. Apparently, this effect is well caught by the model. However, one may note that the simulated  $\Delta T_{eq;\infty}$  deviate from their compared empirical value for a heating power of 500 and 250 W, with discrepancies of the order of  $\pm 1^\circ\text{C}$ . As detailed in Section 5.3.3, in the presented model  $\Delta T_{eq;\infty}$  is fixed according to  $\dot{Q}_p$  and the value taken by  $k_T^L S_i$  during the single-phase regime. Therefore, this point clearly reflects an imperfection, though moderate, in the estimate of the single-phase value for the heat transfer rate  $k_T^L S_i$ . This is clearly visible in the left-hand-side of Figure 5.54, giving the simulated time-trends of  $k_T^L S_i$ . But this

has no consequence at all on the simulation of the pool energy balance, as reflected by the left-hand-side of Figure 5.53, giving the time-trends of  $\dot{m}_L$ . Further on, with a higher  $\dot{Q}_p$ , the natural convection flow developing at pool scale is expected to be more intensive, thereby impacting the measured  $O_2$  degassing kinetics. This effect is reproduced as well by the model, as seen in the right-hand-side of Figures 5.52-5.54, showing respectively the variations of  $C_{O_2}$ ,  $\dot{C}_{O_2}$  and  $k_m^L S_i$ .

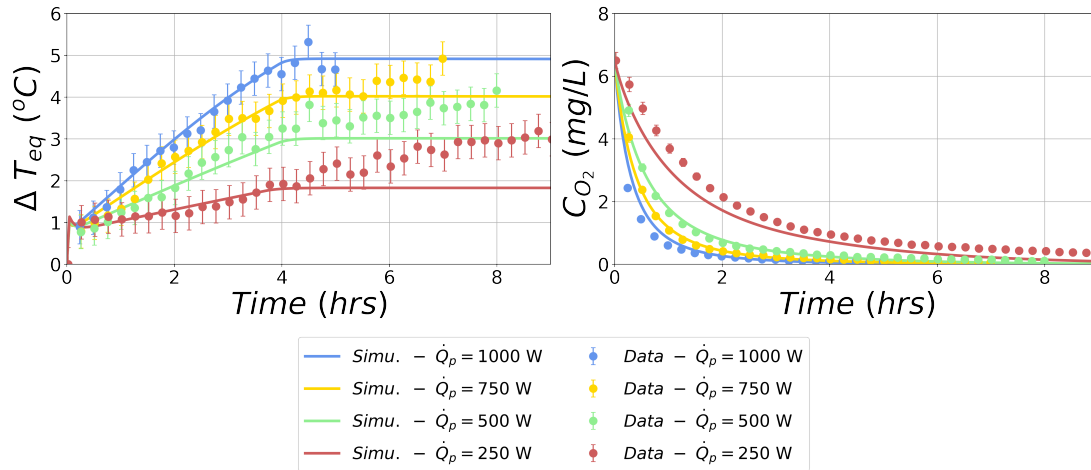


Figure 5.52: Simulated sensitivity to heating power variations. Left: estimated liquid thermal metastability degree  $\Delta T_{eq}$ . Right: measured dissolved  $O_2$  mass concentration  $C_{O_2}$ .

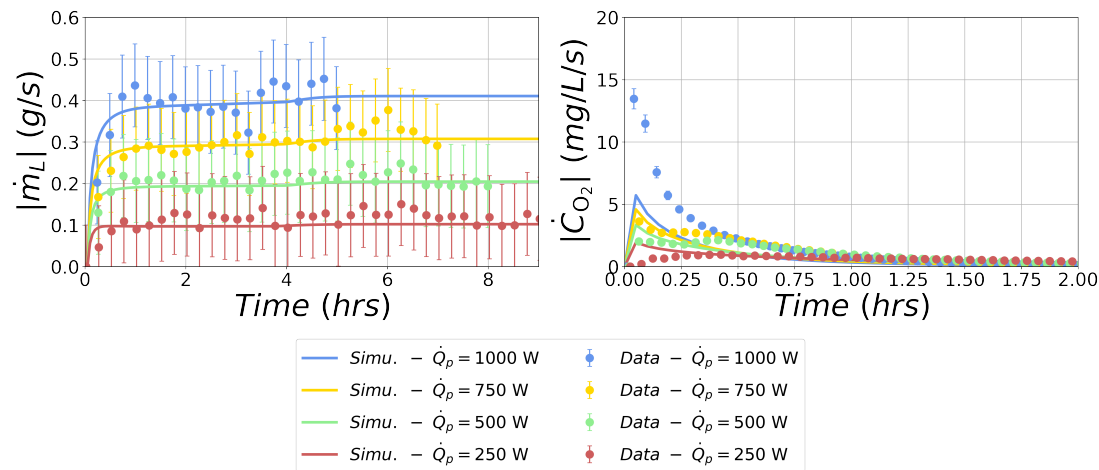


Figure 5.53: Simulated sensitivity to heating power variations. Left: estimated liquid vaporization rate  $\dot{m}_L$ . Right: estimated oxygen degassing rate  $\dot{C}_{O_2}$ .

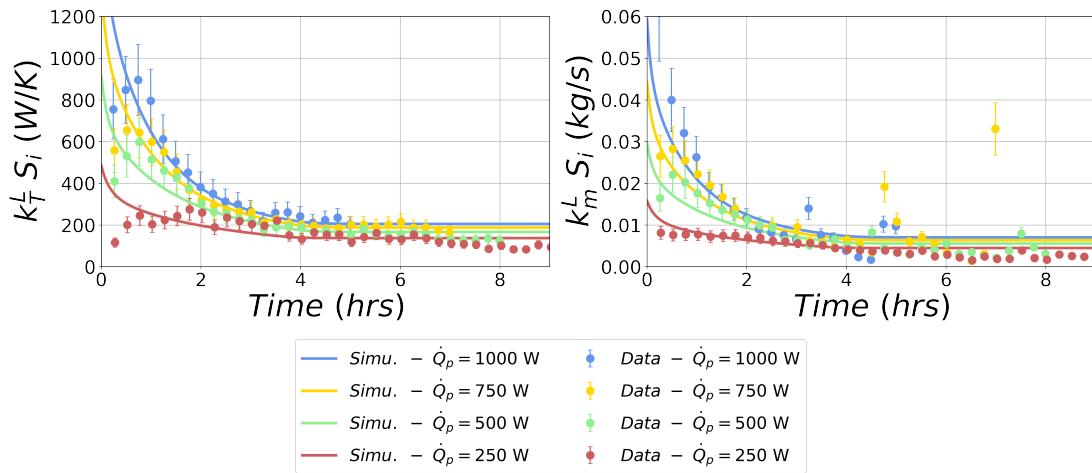


Figure 5.54: Simulated sensitivity to heating power variations. Left: interfacial heat transfer rate  $k_T^L S_i$ . Right: interfacial mass transfer rate  $k_m^L S_i$ .

**Variations of the operating pressure** Another study centered around the phenomenon sensitivity to the operating pressure was achieved. For that aim, three tests were simulated.  $\dot{Q}_p$ ,  $z_p(0)$  and  $C_{O_2}(0)$  were respectively fixed to 1000 W, 30 cm and 6.5 mg/L. Three values for  $P_G$  complying with the experimental limitations of the Aquarius device were further considered: 22, 32 and 42 mbar (*cf.* Table 5.4). The obtained results are given in the following three figures.

Table 5.4: The series of tests, retained and simulated, for investigating the effect of the operating pressure on the phenomenon.

Date of achievement	$\dot{Q}_p$ (W)	$P_G$ (mbar)	$z_p(0)$ (cm)	$C_{O_2}(0)$ (mg/L)
November 25, 2021	1000	22	30	6.5
February 14, 2022	1000	32	30	6.5
October 29, 2021	1000	42	30	6.5

Overall, the operating pressure effect discussed in Section 3.3 is well reproduced by the lumped-parameter model. Indeed, it appears that the higher  $P_G$ , the faster the liquid superheating and degassing kinetics, as seen from Figure 5.55 and the right-hand-side of Figure 5.56. This is the consequence of increased heat and mass transfer rates as the operating pressure is fixed to higher values, as noticeable in Figure 5.57. At last, one can remark that the dependence of  $\Delta T_{eq;\infty}$  to  $P_G$ , first introduced in Section 3.3, is well captured too (*cf.* Figure 5.55, left-hand-side).

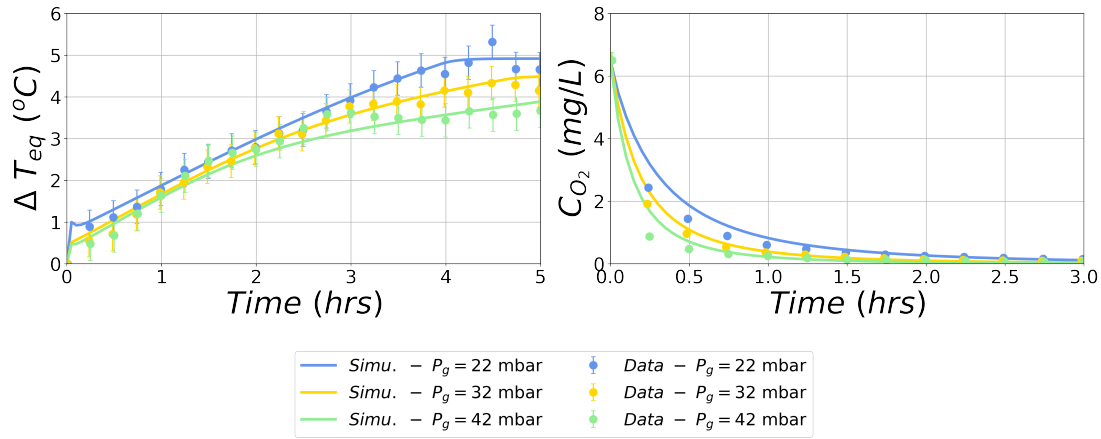


Figure 5.55: Simulated sensitivity to operating pressure variations. Left: estimated liquid thermal metastability degree  $\Delta T_{eq}$ . Right: measured dissolved  $O_2$  mass concentration  $C_{O_2}$ .

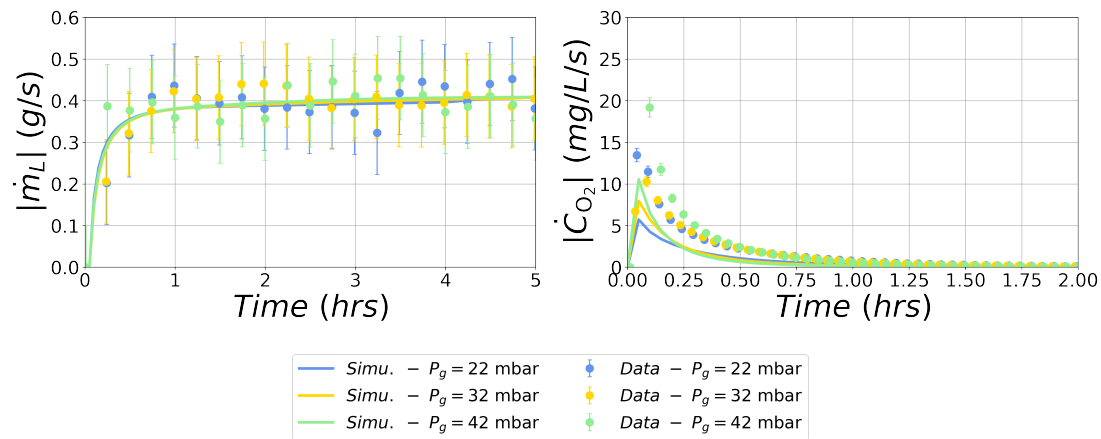


Figure 5.56: Simulated sensitivity to operating pressure variations. Left: estimated liquid vaporization rate  $\dot{m}_L$ . Right: estimated oxygen degassing rate  $\dot{C}_{O_2}$ .

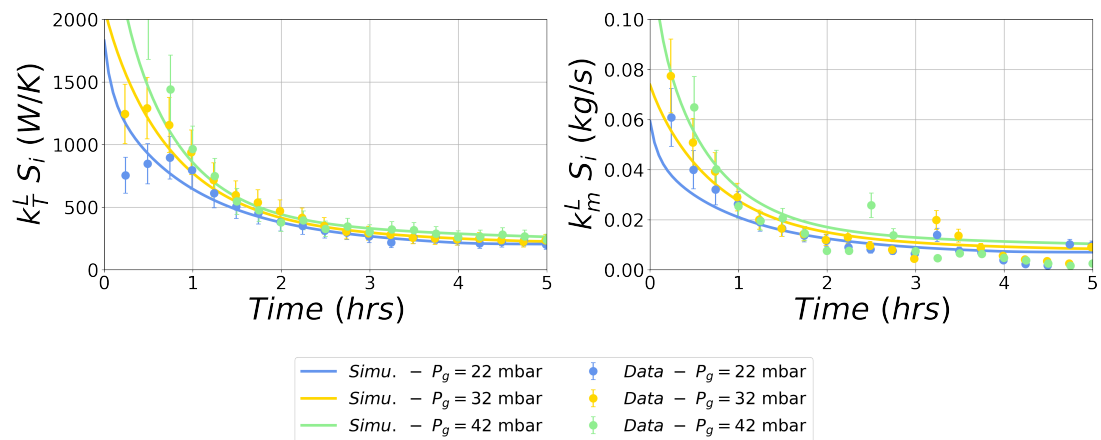


Figure 5.57: Simulated sensitivity to operating pressure variations. Left: interfacial heat transfer rate  $k_T^L S_i$ . Right: interfacial mass transfer rate  $k_m^L S_i$ .

**Variations of the initial pool level** The study of the initial pool level effect is presented next. The latter is based on the simulation of two tests, performed at an operating pressure of 22 mbar, an initial mass concentration in dissolved  $O_2$  of 6.5 mg/L and two distinct values for the initial pool level: 20 and 30 cm. A heating power of 1000 W was chosen for conducting those tests (*cf.* Table 5.5).

Table 5.5: The series of tests, retained and simulated, for investigating the effect of the initial pool level on the phenomenon.

Date of achievement	$\dot{Q}_p$ (W)	$P_G$ (mbar)	$z_p(0)$ (cm)	$C_{O_2}(0)$ (mg/L)
November 25, 2021	1000	22	30	6.5
November 2, 2021	1000	22	20	6.5

The obtained results are given below. As one can successively observe from Figures 5.58-5.60, the effect of the initial pool level discussed in Section 3.3 is well caught by the proposed lumped-parameter model. Indeed, we have previously shown that the value taken by the initial pool level impacts both the liquid superheating and degassing kinetics, with those kinetics being faster at low values of  $z_p(0)$ . The achieved simulations do appear in good agreement with this empirical fact.

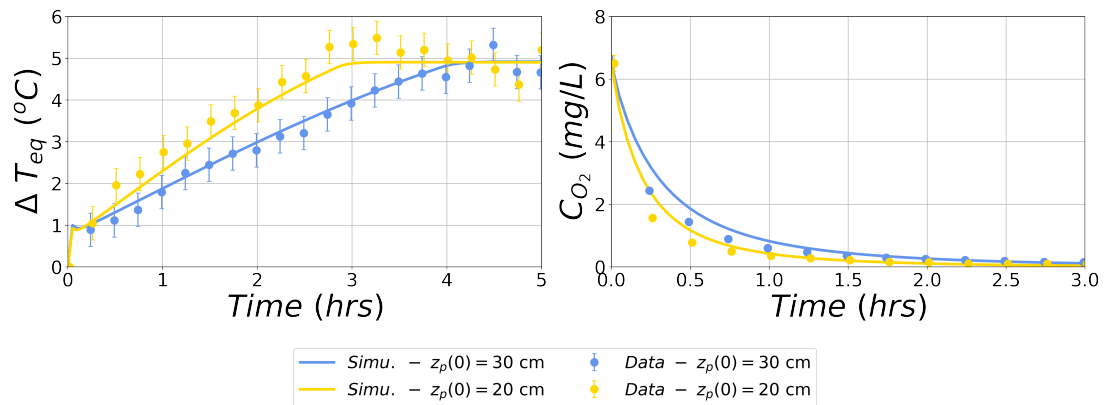


Figure 5.58: Simulated sensitivity to initial pool level variations. Left: estimated liquid thermal metastability degree  $\Delta T_{eq}$ . Right: measured dissolved  $O_2$  mass concentration  $C_{O_2}$ .

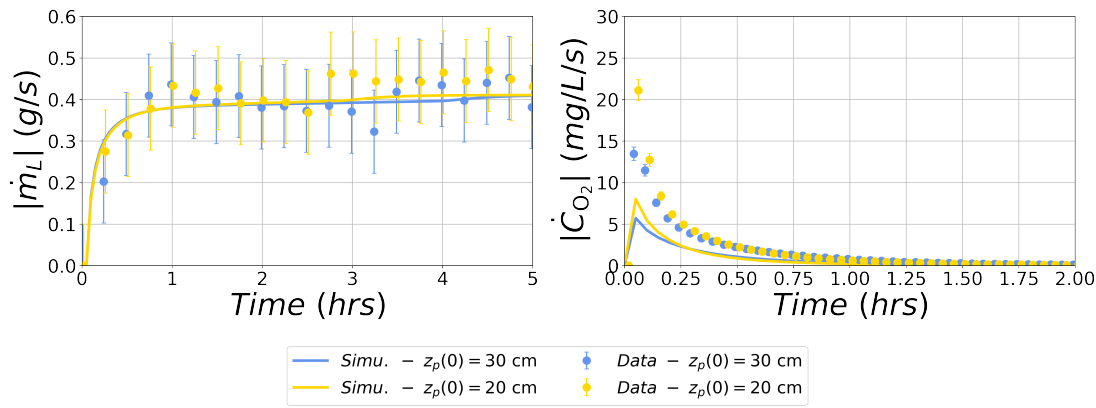


Figure 5.59: Simulated sensitivity to initial pool level variations. Left: estimated liquid vaporization rate  $\dot{m}_L$ . Right: estimated oxygen degassing rate  $\dot{C}_{O_2}$ .

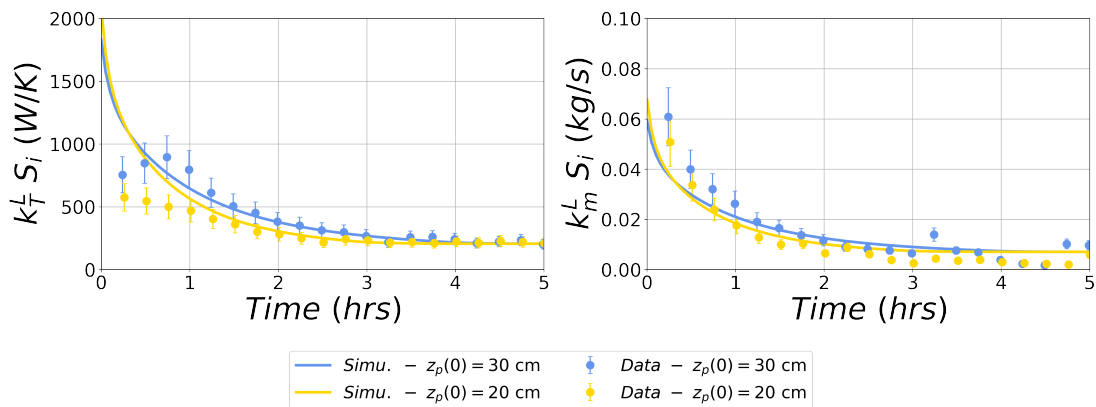


Figure 5.60: Simulated sensitivity to initial pool level variations. Left: interfacial heat transfer rate  $k_T^L S_i$ . Right: interfacial mass transfer rate  $k_m^L S_i$ .

**Variations of the initial content in dissolved gases** At last, a focus was made on the effect of the initial content in dissolved gases. In this perspective, three more tests were retained and later simulated. Their relevant parameters are detailed in Table 5.6 and the obtained results are provided in the following three figures.

Table 5.6: The series of tests, retained and simulated, for investigating the effect of the initial content in dissolved gases on the phenomenon.

Date of achievement	$\dot{Q}_p$ (W)	$P_G$ (mbar)	$z_p(0)$ (cm)	$C_{O_2}(0)$ (mg/L)
November 25, 2021	1000	22	30	6.5
November 22, 2021	1000	22	30	1.25
October 26, 2021	1000	22	30	0.15

Overall, the conducted simulations do appear in good agreement with the empirical data, as seen in Figures 5.61-5.63. Indeed, complying with the observations, the simulations yielded differences in the liquid superheating and degassing kinetics of the order of a few hours, depending on the retained initial amount in dissolved  $O_2$ .

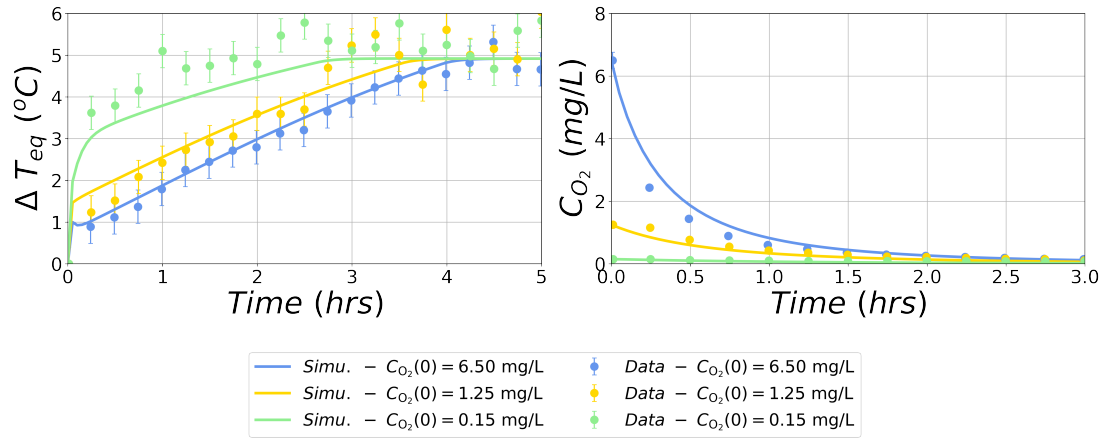


Figure 5.61: Simulated sensitivity to initial content in dissolved gases variations. Left: estimated liquid thermal metastability degree  $\Delta T_{eq}$ . Right: measured dissolved  $O_2$  mass concentration  $C_{O_2}$ .

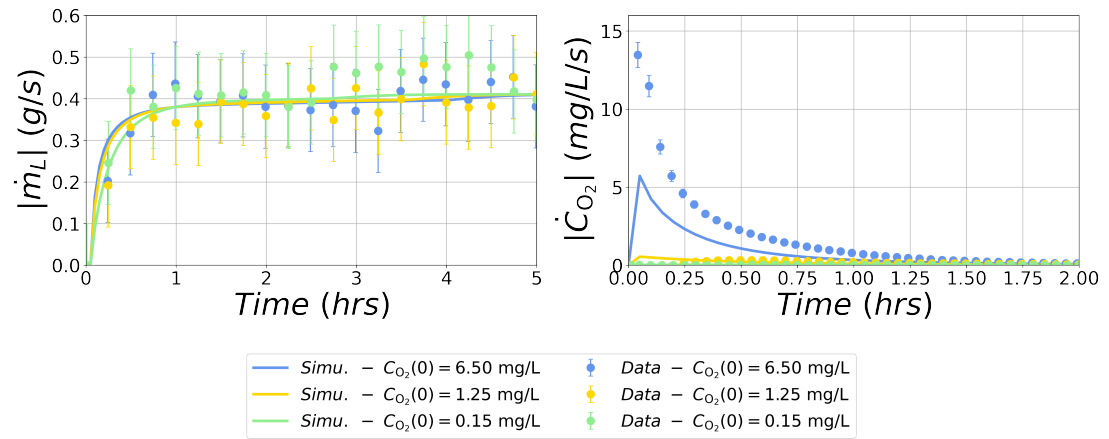


Figure 5.62: Simulated sensitivity to initial content in dissolved gases variations. Left: estimated liquid vaporization rate  $\dot{m}_L$ . Right: estimated oxygen degassing rate  $\dot{C}_{O_2}$ .

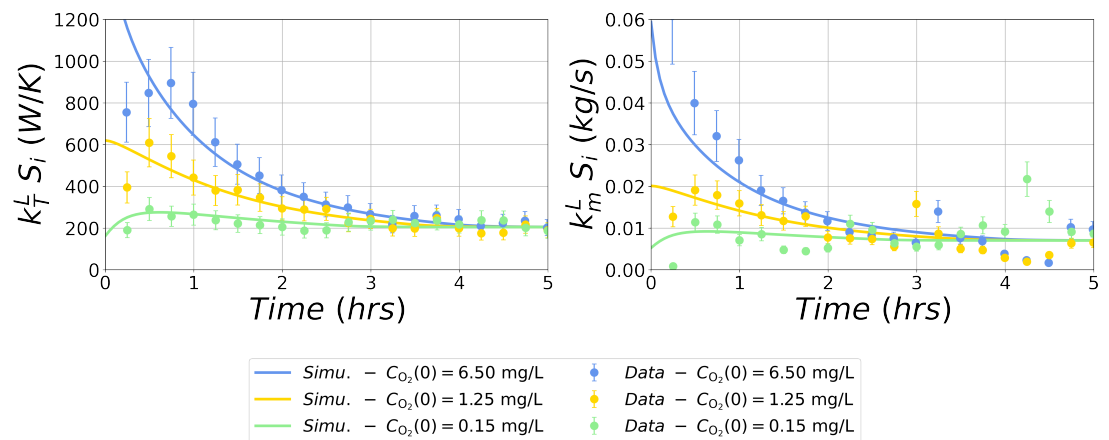


Figure 5.63: Simulated sensitivity to initial content in dissolved gases variations. Left: interfacial heat transfer rate  $k_T^L S_i$ . Right: interfacial mass transfer rate  $k_m^L S_i$ .

## Conclusions

In this chapter, we have characterized the heat and mass transfers that have been widely evocated throughout the thesis. The studied processes are the heated-wall-to-liquid heat transfer and the liquid-bulk-to-gas/liquid-interface heat and mass transfers. The latter have been first quantified by means of three introduced coefficients:  $k_h$ ,  $k_T^L$  and  $k_m^L$ . First, all the performed estimates of  $k_h$  have been found consistent with the expected order of magnitude of single-phase natural convection heat transfer coefficients in liquid water. However, the estimated  $k_h$  have been occasionally shown higher during only a short initial period of some tests. This point has been further investigated and we have come up with the conclusion that those sometimes observed initial large variations of  $k_h$  are most likely random and cannot be considered as relevant or due to any bubbling process. However regarding  $k_T^L$  and  $k_m^L$ , the presented study has highlighted some initial high values of the latter transfer rates that are significant and most likely due to the strong bubbling taking place within the liquid pool when water flashes. Further on, a set of heat and mass transfer correlations has been derived from the data series of each test composing a so-called regular experimental matrix and verified against some additional tests. The single-phase correlations that have been obtained are rather classical and link on one hand the emblematic dimensionless number of natural convection flows, *i.e.* the Rayleigh number, with on the other hand, the well-known Nusselt and Sherwood numbers of convective heat and mass transfers. The correlations that have been found for the two-phase regime are in turn rather original in their mathematical formulation. Interestingly, those correlations link the transfers intensification that is classically observed under bubbling conditions to the Gibbs number, associated with bubble nucleation processes. Another interesting point is the dependency between the pre-factor of those correlations and the initial water level, imposed prior to any test. Although this effect has been modeled too by means of a simple dimensional linear relation, its root mechanism is worth being unveiled by future studies and its expression is to be better characterized by means of more tests. Finally, we have proposed a lumped-parameter model of the Aquarius pool. The model has been successfully compared with the available empirical data, with moderate discrepancies that would motivate as a perspective of the present thesis, some improvement of the utilized heat and mass transfer correlations.

---

# Conclusions

*“There is no real ending. It’s just the place where you stop the story.”*

— Frank Herbert

## Main outcomes of the doctoral research

The present doctoral research has focused on the gravity-driven flashing of metastable water, a phenomenon which is for instance encountered in natural geysers. Specifically, the emphasis has been put on the case of a pool heated from below. One can find two evocations of this case in the scientific literature: the so-called phreatic volcanic eruptions and the loss-of-cooling accidents in the storage pools of spent nuclear fuels. The present doctoral research, performed in the frame of IRSN’s missions in nuclear safety, has concentrated on the latter configuration. However and to our best knowledge, the available scientific literature does not provide any empirical data regarding the phenomenon in this very case. A wealth of data, close to the case of interest and related to genuine geysers or unheated depressurized pools has been identified. But as discussed during the introduction of the present thesis, the extrapolation of those available results to the studied case is not straightforward and some questions were still open prior to the launch of this research:

- *Does the phenomenon exist in a pool-type geometry, heated from below?*
- *If the phenomenon exists, what are its main characteristics, including the metastable water relaxation processes?*
- *Are we able to model as simple as possible the studied physics for further macroscopic transient simulations?*

Clearly, with the identified lack of empirical information about the studied case in the scientific literature, providing an answer to the above questions implies performing some new experiments. This motivated the design of the test device called Aquarius, central to this doctoral research. For that purpose, a novel downscaling methodology has been developed by the present author. The method mainly consists in:

- An homothetical pool size reduction;

- The conservation of the working fluid, *i.e.* water in the present case;
- The conservation of the 1:1 scale pool heat power density, given in  $\text{W}/\text{m}^3$ , which avoids distorting the heat and mass transfers kinetics;
- An operating pressure distortion.

Let us briefly recall what is the intent of this last distortion. As shown, an operating pressure distortion allows conserving a large saturation temperature vertical difference even at a reduced scale, with an appropriate choice of system's pressure. Indeed, in the low-pressure case, because of existing steep variations in saturation temperature against pressure, a little variation in hydrostatic pressure, provided by a reduced pool level, might be enough for achieving some large vertical difference required for the emergence of any flashing of metastable water. By taking some height, this similarity approach, unmentioned yet in the scientific literature to our knowledge, might be beneficial to other types of applications where the gravity-driven flashing is expected to occur, providing a way to reduce the size and hence the cost of the envisioned experiments and keeping water as the working fluid (*e.g.* for 1D-geysers or the pools constituting a passive cooling capacity for some light water nuclear reactors). Next, the characteristics of a reference spent-fuel-pool have been introduced and have allowed defining an appropriate scale for the Aquarius test device. With a spent fuel pool nominal water level of 10 m, we have retained a scaling ratio of 1:25, yielding an Aquarius pool maximum height of 40 cm, which is fairly reasonable with the intent to perform a laboratory-scale experiment. Further on, the application of the above method imposes to reduce the operating pressure from 1 bar to 22 mbar, for reproducing the 20°C saturation temperature vertical difference of the reference pool at the scale of Aquarius. The maximum heating power has also been distorted from a 1-MW reference value to 1 kW. However, one may wonder if the choice of this scaling ratio allows reproducing properly the studied physics. This question has been addressed at the very beginning of the present thesis. Indeed, it has been shown that with regards to the reference pool, a scaling ratio of 1:25 keeps unchanged the turbulent nature of the free convection flows developing at pool scale and does not modify too much the dynamics of the produced bubbles. Next, thanks to some of the Aquarius technical features and to a pre-consolidated test procedure, we have shown that one can control during any envisioned experiment:

- The initial liquid pool level;
- The heating power;
- The spatial distribution of the heat supply onto the vessel's bottom wall;
- The operating pressure;
- The initial amount of gases in dissolution within the liquid;

while measuring temperatures and pressures at various locations and the amount of dissolved oxygen.

Having developed this experimental tool, we have provided a first insight into the physics of the gravity-driven flashing of water in a pool heated from below. This insight has been given through the analysis of a typical experiment, whose results were fairly well repeatable. The former has highlighted some features that appear specific to the phenomenon. First of all, we have shown that the liquid pool usually evolves according to a two-stage process. During the first stage, the pool has been proven subjected to a strong and continuous bubbling. In this interval, numerous bubbles have been identified nucleating from three distinct locations:

- Within the liquid bulk, underneath the free surface;
- At the heated bottom wall;
- At the unheated and rough vertical wall.

For those experiments conducted with an initially large chemical disequilibrium in dissolved gases, the so-called bulk nucleation is always present, whatever the retained heating power, initial pool level or operating pressure, over the studied parameters range. Later, the bubbles nucleating that way typically grow in a fast and often explosive fashion. A theoretical analysis, further confirmed by means of a dedicated experiment, has allowed one to associate this exaggerated growth with the so-called flashing process. Indeed, our developments have evidenced that the other two potential mechanisms that may lead to a bubble growth, *i.e.* the decompression felt by an uprising bubble and the capture of dissolved gases, are practically negligible when compared to the flashing. Next, the nucleation onto the vessel's heated wall has been observed only for those tests conducted with a heating power bigger than 250 W. At last, we have shown that when the vessel's rough and unheated wall is not pre-dried out prior to a test, the occurrence of bubble nucleation onto this very surface is never reached. This has questioned the potential deactivation mechanisms that may act on the gas nuclei pre-entrapped in this wall's crevices. The second phenomenological stage that has been discussed is referred to as single-phase stage. The latter is characterized by a quasi-absence of bubble nucleation. During this same stage, the observation of nucleation has been indeed shown as a rare and violent event, randomly initiated by some external perturbation (*e.g.* a falling droplet, a detaching bubble). Then, we have conducted a sensitivity analysis regarding four control parameters of the Aquarius tests. The analysis has allowed emphasizing some more features of the phenomenon. It has indeed appeared that in a pool heated from below, having a large vertical variation of the saturation temperature, the excess of the proposed liquid thermal metastability degree  $\Delta T_{eq}$  is influenced by a great variety of circumstances. Those circumstances being in the present study and by order of importance, the initial amount of dissolved gases and the heating power, the operating pressure, the initial pool level. Importantly, those observations clearly validate the experimental similarity approach, proposed at the beginning

of this research, the studied phase-change phenomenon, envisioned in large pools, being observed at the small scale of the Aquarius device. It is also worth pointing out that instead of observing a cyclic flashing as for geysers, the emergence of bubbles has appeared steady in the present experiments. This is in complete agreement with what is reported in the scientific literature about the relationship between the so-called system's aspect ratio and the steadiness of the phenomenon: for aspect ratios smaller than unity, the superheated water vaporization process is no longer cyclic. Eventually, we have provided an overview of some additional tests that were conducted with the intent to force the bubble nucleation processes in a specific location within the liquid pool. Localizing the heat source onto the heated bottom wall and later, inclining the pool from the horizontal plane, has led to a localized bulk nucleation, thereby highlighting a significant link between the latter process and the natural convection flow taking place within the continuous liquid phase.

Then, the nucleation processes that are typically observed during a pool flashing experiment have been largely analyzed. First of all, a review of all envisioned nucleation modes has been provided. As proposed, those modes have been primarily classified on the basis of the order of magnitude of their energetic cost. Indeed, this cost appears as an interesting classification criterion since it is noticeably different whether a gas nucleus pre-exists or not within the metastable liquid. The modes obtained that way are:

- The nucleation from a pre-existing gas nucleus:
  - Floating freely in the liquid;
  - Entrapped in a solid wall cavity.
- The so-called de novo nucleation:
  - Onto a solid surface;
  - Within the liquid bulk.

Later, after having developed the theoretical frame behind these nucleation modes, quantitative evaluations have been made on the basis of the available Aquarius experimental data. Those studies have shown that the two so-called de novo nucleation modes can be confidently discarded, their occurrence conditions being really far from the ones of the presented experiments. Regarding the noticed bubble nucleation onto the heaters wall at the beginning of most of the performed experiments, the analysis has shown that the local thermodynamic conditions reached at that location made possible the emergence of bubbles in spite of negative wall superheats. This very fact is indeed the positive consequence of the achieved large dissolved gases supersaturations for most of the tests. The bubble nucleation onto the unheated rough wall of the pool vessel has been proven achievable as well, despite its typical non-observation. By going into details, it has been shown that the deactivation of the gas nuclei entrapped in the rough wall crevices in between two consecutive tests is a very likely process. If the bubble

nucleation observed onto the vessel's walls does rely on the existence of pre-existing gas nuclei, the one taking place within the liquid bulk is much more uncertain. With the intent to investigate that point, we have designed and conducted a specific test. The results of the latter seem to indicate that the hypothesis of a main contribution of the freely-floating gas nuclei to the observed bubble nucleation is likely. But we are still left with the same questions shared by the cavitation and thermal-hydraulic communities for decades regarding the possible stability mechanisms preserving those puzzling gas nuclei. At last, the interaction between a falling water droplet and the free surface of a superheated liquid has been studied. This interaction, occurring mainly in the late stage of a typical pool flashing experiment, has been proven sufficient for yielding a significant water flashing. The latter relaxation mechanism is indeed understood as being initiated by the gas entrained by the impacting droplet into the liquid pool.

At last, we have characterized the heat and mass transfers that have been widely evocated throughout the thesis. The studied processes are the heated-wall-to-liquid heat transfer and the liquid-bulk-to-gas/liquid-interface heat and mass transfers. Those transfers have been first quantified by means of three introduced coefficients:  $k_h$ ,  $k_T^L$  and  $k_m^L$ . First, all the performed estimates of  $k_h$  have been found consistent with the expected order of magnitude of single-phase natural convection heat transfer coefficients in liquid water. However, the estimated  $k_h$  have been occasionally shown higher during only a short initial period of some tests. This point has been further investigated and we have come up with the conclusion that those sometimes observed initial large variations of  $k_h$  are most likely random and cannot be considered as relevant or due to any bubbling process. However regarding  $k_T^L$  and  $k_m^L$ , the presented study has highlighted some initial high values of the latter transfer rates that are significant and most likely due to the strong bubbling taking place within the liquid pool when water flashes. Further on, a set of heat and mass transfer correlations has been derived from the data series of each test composing a so-called regular experimental matrix and verified against some additional tests. The single-phase correlations that have been obtained are rather classical and link on one hand the emblematic dimensionless number of natural convection flows, *i.e.* the Rayleigh number, with on the other hand, the well-known Nusselt and Sherwood numbers of convective heat and mass transfers. The correlations that have been found for the two-phase regime are in turn rather original in their mathematical formulation. Interestingly, those correlations link the transfers intensification that is classically observed under bubbling conditions to the Gibbs number, associated with bubble nucleation processes. Another interesting point is the dependency between the pre-factor of those correlations and the initial water level, imposed prior to any test. Although this effect has been modeled too by means of a simple linear relation, its root mechanism is worth being unveiled by future studies and its expression is to be better characterized by means of more tests. Finally, we have proposed a lumped-parameter model of the Aquarius pool. The model has been successfully compared with the available empirical data, with moderate discrepancies.

## Identified perspectives

In 2017, the American author *John M. Green* wrote in his book *Turtles All the Way Down* a few words that are worth being shared here:

“What I love about Science is that as you learn, you don’t really get answers. You just get better questions”.

While concluding the present doctoral research, we do have precisely the same feeling. Indeed, if the scientific questions that have been raised at the beginning of this thesis are now answered, some more issues have resulted, as it has been discussed. Naturally, proposing an answer to any of these new and interesting questions and again raising some more issues is a perspective of the conducted research. Let us detail what could be done in this direction.

First of all, the gravity-driven flashing of metastable water which has been proven observable in pools heated from below is to be further characterized. In particular, it could be beneficial to refine our understanding of the heat and mass transfers occurring in the studied configuration, for instance by getting some more empirical data at a local scale, be it related to the liquid velocities or the spatial distribution of the bubbles. For doing so, one could make use of advanced non-intrusive flow visualization techniques, such as the so-called shadowgraphy, which could provide information about the bubbles spatial distribution and/or flow topology, or the Particle Image Velocimetry (PIV), which could allow characterizing the liquid phase velocity field [115]. In turn, having this finer data available would help challenging and/or improving the most advanced two-phase Computational Fluid Dynamics (CFD) modeling to date, which is recognized by the thermal-hydraulics community as being not fully validated in the field of flashing flows [72]. As mentioned by *Liao and Lucas* in their recent review on that topic, an accurate treatment of flashing flows requires the use of a so-called poly-disperse CFD modeling because of the usually met broad bubble size spectra [72]. For doing so, the so-called 3D, two-fluid 6-equation model, first developed by *Ishii and Hibiki* [57] is the most relevant choice according to *Liao and Lucas*. In the CFD version of this model, the turbulence is classically represented by a so-called *Reynolds Averaged Navier-Stokes* approach, whose validation requires fine data related to the velocity field of the continuous phase (here the water), hence the need for a PIV characterization of the latter in the Aquarius pool. Regarding the bubble nucleation and dynamics, it is usually recommended to introduce within the above model an additional interfacial area concentration or total bubble number density transport equation, taking into account the potential poly-dispersion of the bubble sizes [72]. In order to validate this type of additional model, well-resolved observations performed at the bubble scale are particularly required, hence the mentioned need for more information about the bubbles spatial distribution during the Aquarius experiments. All in all, those combined experimental and modeling activities could provide a validated simulation tool for fur-

ther full-scale spent-fuel-pool loss-of-cooling accident simulations, which constitutes the final motivation of those researches performed at IRSN.

Next is the interesting question of the nature of the freely-floating nuclei that seem to stand behind the observed spontaneous emergence of bubbles within the liquid bulk. With the intent to better characterize the population of those postulated nuclei, one could make use of so-called time-resolved ultrasonic spectroscopy techniques that allow accessing gas nuclei size distributions in a non-intrusive and rather precise way [71]. In addition to some potential phenomenological outcomes, this technique would yield some crucial data for validating a poly-dispersed bubble modeling such as the one mentioned above.

The mechanisms according to which the gas nuclei postulated entrapped within the crevices of the unheated rough wall deactivate from one test to another could be further analyzed as well. For that purpose, conducting interface-resolved simulations such as the ones of *Lohse et al.* discussed in this thesis might be beneficial [16].

Taking advantage from the same type of simulation tools might also be interesting for further studying the violent interaction of a falling droplet with the liquid free surface, observed lately during every conducted test. With an additional resolution of the heat and mass transfers between the gas nucleus formed by the impacting droplet and the metastable water, one could hence estimate this peculiar flashing process.

At last, a better characterization of the heat and mass transfer correlations that have been defined during the present research appears unavoidable. First of all, the single-phase mass transfer correlation describing the O<sub>2</sub> degassing process needs to be improved, taking benefit from more precise measurements when the gas depletion is almost complete (*i.e.* by using a dissolved O<sub>2</sub> optical sensor of better accuracy). Next, the pre-factor of the obtained two-phase heat and mass transfer correlations is to be further investigated and its mathematical expression refined by means of more tests started with a wide range of initial pool levels. Eventually, the dependency between this pre-factor and the initial pool level is a topic by itself that deserves some more attention.

By no doubt, each discussed research path has the potential to bring some more interesting data about the studied phenomenon and for sure, some more questions to be addressed, in an endless way. And this is of course what makes Science so beautiful...



---

## Bibliography

- [1] AirLiquide, Gas Encyclopaedia, Elsevier, 1976.
- [2] E. T. Allen, A. L. Day, Hot Springs of the Yellowstone National Park, Carnegie Institution of Washington 466 (1935) 525.
- [3] R. E. Apfel, The role of impurities in cavitation threshold determination, Journal of Acoustical Society of America 48 (1970) 1179–1189.
- [4] M. Arora, C.-D. Ohl, K. Mørch, Cavitation inception on micro-particles: A self-propelled particle accelerator, Physical Review Letters 92 (2004) 174501.
- [5] A. A. Atchley, A. Prosperetti, The crevice model of bubble nucleation, Journal of Acoustical Society of America 86 (1989) 1065–1084.
- [6] S. G. Bankoff, Ebullition from solid surfaces in the absence of a pre-existing gaseous phase, Transactions of the ASME 79 (1957) 735–740.
- [7] S. G. Bankoff, Entrapment of gas in the spreading of a liquid over a rough surface, American Institute of Chemical Engineers Journal 4 (1958) 24–26.
- [8] S. G. Bankoff, The prediction of surface temperature at incipient boiling, Chemical engineering progress symposium series 55 (1959) 87.
- [9] G. I. Barenblatt, Scaling, self-similarity, and intermediate asymptotics, Cambridge University Press, 1996.
- [10] I. H. Bell, J. Wronski, S. Quoilin, V. Lemort, Pure and pseudo pure fluid thermophysical property evaluation and the open-source thermophysical property library CoolProp, Industrial and Engineering Chemistry Research 53 (2014) 2498–2508.
- [11] R. Bergmann, D. van der Meer, S. Gekle, A. van der Bos, D. Lohse, Controlled impact of a disc on a water surface: Cavity dynamics, Journal of Fluid Mechanics 633 (2009) 381.

- [12] L. Bernath, Theory of bubble formation in liquids, *Ind. Engng. Chem. Journal* 44 (1952) 1310–1313.
- [13] R. Bird, W. Stewart, E. Lightfoot, *Transport Phenomena - Revised Second Edition*, John Wiley & Sons, 2007.
- [14] M. Blander, J. L. Katz, Bubble nucleation in liquids, *American Institute of Chemical Engineers Journal* 21 (1975) 833–848.
- [15] B. M. Borkent, M. Arora, C.-D. Ohl, Reproducible cavitation activity in water-particle suspensions, *Journal of Acoustical Society of America* 121 (2007) 1406–1412.
- [16] B. M. Borkent, S. Gekle, A. Prosperetti, D. Lohse, Nucleation threshold and deactivation mechanisms of nanoscopic cavitation nuclei, *Physics of Fluids* 21 (2009) 102003.
- [17] H. Bouasse, *Capillarité : phénomènes superficiels*, Delagrave, 1924.
- [18] C. Brennen, *Cavitation and bubble dynamics*, Cambridge University Press, 2014.
- [19] N. V. Brilliantov, J. Schmidt, F. Spahn, Geysers of Enceladus: Quantitative analysis of qualitative models, *Planetary and Space Science* 56 (2008) 1596–1606.
- [20] J. E. Burman, *Bubble growth in supersaturated solution*, Ph.D. thesis, Imperial College, London, 1974.
- [21] C. Caudron, B. Taisne, J. Neuberg, A. D. Jolly, B. Christenson, T. Lecocq, Suparjan, D. Syahbana, G. Suantika, Anatomy of phreatic eruptions, *Earth, Planets and Space* 70 (2018) 168.
- [22] F. Caupin, E. Herbert, Cavitation in water: a review, *Comptes Rendus de Physique* 7 (2006) 1000–1017.
- [23] H. Cavendish, *Theory of Boiling*, Unpublished manuscript, 1780.
- [24] H. Chang, *Inventing Temperature - Measurement and Scientific Progress*, Oxford University Press, 2004.
- [25] H. Chang, The Myth of the Boiling Point, *Science Progress* 91 (2008) 219–240.
- [26] R. Clift, J. R. Grace, M. E. Weber, *Bubbles, drops and particles*, Dover publications, 1978.
- [27] R. Cole, 'Boiling nucleation' in *Advances in Heat Transfer*, Vol. 10, Harnett, J.P. and Irvine Jr., Th.F. (editors), Academic Press, 1974.

- [28] R. Cole, H. L. Shulman, Bubble growth rates at high Jakob numbers, *International Journal of Heat and Mass Transfer* 9 (1966) 1377–1390.
- [29] J. G. Collier, J. R. Thome, *Convective boiling and condensation - third edition*, Oxford Science Publications, 1996.
- [30] L. A. Crum, Tensile strength of water, *Nature* 278 (1979) 148–149.
- [31] L. A. Crum, Nucleation and stabilization of microbubbles in water, *Applied Scientific Research* 38 (1982) 101–115.
- [32] E. Cussler, *Diffusion - Third Edition*, Cambridge University Press, 2009.
- [33] P.-G. De Gennes, F. Brochard-Wyart, D. Quéré, *Gouttes, bulles, perles et ondes*, Belin, 2005.
- [34] P. Debenedetti, *Metastable Liquids: Concepts and Principles*, Princeton University Press, 1996.
- [35] G. Delaplace, K. Loubière, F. Ducept, R. Jeantet, *Modélisation en génie des procédés par analyse dimensionnelle - Méthode et exemples résolus*, Lavoisier - collection Tec & Doc, 2014.
- [36] J. M. Delhaye, M. Giot, M. L. Riethmuller, *Thermohydraulics of two-phase systems for industrial design and nuclear engineering*, McGraw-Hill Book Company, 1981.
- [37] N. Draper, H. Smith, *Applied regression analysis*, third edition, John Wiley and Sons, 1998.
- [38] P. S. Epstein, M. S. Plesset, On the stability of gas bubbles in liquid-gas solutions, *Journal of Chemical Physics* 18 (1950) 1505–1509.
- [39] J.-L. Fanchon, *Guide des sciences et technologies industrielles*, Nathan, 2008.
- [40] R. E. Faw, R. J. Vanvleet, D. L. Schmidt, Pre-pressurization effects on initiation of subcooled pool boiling during pressure and power transients, *International Journal of Heat and Mass Transfer* 29 (1986) 1427–1437.
- [41] H. K. Forster, N. Zuber, Growth of a vapor bubble in a superheated liquid, *Journal of Applied Physics* 25 (1954) 474–478.
- [42] F. E. Fox, K. F. Herzfeld, Gas bubbles with organic skin as cavitation nuclei, *Journal of the Acoustical Society of America* 26 (1954) 984–989.
- [43] J.-P. Franc, J.-M. Michel, *Fundamentals of cavitation*, Kluwer Academic Publishers, 2004.

- [44] W. Fritz, W. Ende, *Über den Verdampfungsvorgang nach Kinematographischen Aufnahmen an Dampfblasen*, *Physikalische Zeitschrift* 37 (1936) 391–401.
- [45] M. Furuya, et al., *Flashing-induced density wave oscillations in a natural circulation BWR - mechanisms of instability and stability map*, *Nuclear Engineering and Design* 235 (2005) 1557–1569.
- [46] S. Gopalakrishna, V. M. Purushothaman, N. Lior, *An experimental study of flash evaporation from liquid pools*, *Desalination* 65 (1987) 139–151.
- [47] D. Green, M. Southard, *Perry's Chemical Engineers' Handbook - 9<sup>th</sup> Edition*, MacGraw-Hill, 2018.
- [48] A. Guillemin, *La vapeur*, Hachette, 1875.
- [49] E. Guyon, J.-P. Hulin, L. Petit, *Hydrodynamique physique*, 3<sup>e</sup> édition, EDP Sciences / CNRS Editions, 2012.
- [50] E. N. Harvey, A. H. Whiteley, W. D. McElroy, D. C. Peace, D. K. Barnes, *Bubble formation in animals - I*, *Journal of Cell Comparative Physiology* 24 (1944) 1–22.
- [51] E. N. Harvey, A. H. Whiteley, W. D. McElroy, D. C. Peace, D. K. Barnes, *Bubble formation in animals - II*, *Journal of Cell Comparative Physiology* 24 (1944) 23–34.
- [52] R. Higbie, *The rate of absorption of a pure gas into a still liquid during short periods of exposure*, *Transactions of the American Institute of Chemical Engineers* 31 (1935) 365–389.
- [53] R. E. Holtz, *The effect of pressure-temperature history upon incipient boiling superheats in liquid metals*, Tech. Rep. ANL-7184, Argonne National Laboratory, 1966.
- [54] Y. Y. Hsu, *On the size range of active nucleation cavities on a heating surface*, *Transactions of the ASME* 94 (1962) 207–212.
- [55] Y. Y. Hsu, R. W. Graham, *An analytical and experimental study of the thermal boundary layer and the ebullition cycle in nucleate boiling*, Tech. Rep. TN-D-594, NASA, 1961.
- [56] J. Huyghe, G. Barois, A. Michel, H. Mondin, *Étude expérimentale de l'autovaporisation en eau stagnante faiblement surchauffée et analyse de l'écoulement en canal d'un liquide en cours de détente*, *Desalination* 4 (1968) 209–219.
- [57] M. Ishii, T. Hibiki, *Thermo-Fluid Dynamics of Two-Phase Flow*, Second Edition, Springer, 2011.

- [58] M. Ishii, I. Kataoka, Scaling laws for thermal-hydraulic system under single-phase and two-phase natural circulation, *Nuclear Engineering and Design* 81 (1984) 411–425.
- [59] JCGM, Guide to the expression of uncertainty in measurement, Tech. Rep. JCGM 100:2008, JCGM, 2008.
- [60] S. Y. Jiang, M. S. Yao, J. H. Bo, S. R. Wu, Experimental Simulation Study on Startup of the 5 MW Nuclear Heating Reactor, *Nuclear Engineering and Design* 158 (1995) 111–123.
- [61] B. D. Johnson, R. C. Cooke, Generation of stabilized microbubbles in seawater, *Science* 213 (1981) 209–211.
- [62] S. F. Jones, G. M. Evans, K. P. Galvin, Bubble nucleation from gas cavities - a review, *Advances in Colloid and Interface Science* 80 (1999) 27–50.
- [63] S. F. Jones, G. M. Evans, K. P. Galvin, The cycle of bubble production from a gas cavity in a supersaturated solution, *Advances in Colloid and Interface Science* 80 (1999) 51–84.
- [64] J. I. Kim, N. Lior, Some critical transitions in pool flash evaporation, *International Journal of Heat and Mass Transfer* 40 (1997) 2363–2372.
- [65] R. T. Knapp, Cavitation and nuclei, *Transactions of the ASME* 80 (1958) 1315–1324.
- [66] N. I. Kolev, Uniqueness of the elementary physics driving heterogeneous nucleate boiling and flashing, *Nuclear Engineering and Technology* 38 (2006) 175–184.
- [67] H. M. Kottowski-Dümenil, *Liquid metal thermal-hydraulics*, Inforum Verlag, 1994.
- [68] R. Krishnamurti, On the transition to turbulent convection, *Journal of Fluid Mechanics* 42 (1970) 295.
- [69] R. T. Lahey Jr., *Boiling heat transfer*, Elsevier Science Publishers B.V., 1992.
- [70] R. Lakkaraju, R. J. A. M. Stevens, P. Oresta, R. Verzicco, D. Lohse, A. Prosperetti, Heat transport in bubbling turbulent convection, *Proceedings of the National Academy of Sciences* 110 (2013) 9237–9242.
- [71] V. Leroy, A. Strybulevych, T. Norisuye, Time-resolved ultrasonic spectroscopy for bubbles, *AIChE J.* 63 (2017) 4666–4672.
- [72] Y. Liao, D. Lucas, Computational modeling of flash boiling flows: A literature survey, *International Journal of Heat and Mass Transfer* 111 (2017) 246–265.

- [73] J. Lienhard IV, J. Lienhard V, *A Heat Transfer Textbook*, fifth edition, Phlogiston Press, 2020.
- [74] G. Liger-Belair, *La physique des bulles de champagne*, EDP Sciences - Annales de Physique, 2002.
- [75] E. Lightfoot, E. Cussler, R. Rettig, Applicability of the Stefan-Maxwell Equations to Multicomponent Diffusion in Liquids, *A.I.Ch.E. Journal* 8 (1962) 708–710.
- [76] J. J. Lorenz, B. B. Mikic, W. M. Rohsenow, The effect of surface conditions on boiling characteristics, in: *Proc. 5<sup>th</sup> International Heat Transfer Conference*, Tokyo, Japan, 1974.
- [77] X. Lu, A. Watson, A review of geysering flows, in: *Proc. 24<sup>th</sup> NZ Geothermal Workshop*, 2002.
- [78] D. Ma, *Experimental Studies of Water Quality Effects on Tip Vortex Cavitation*, Master's thesis, University of Minnesota, 1994.
- [79] A. L. Manera, et al., Stability of natural-circulation-cooled boiling water reactors during startup: experimental results, *Nuclear Technology* 143 (2003) 77–88.
- [80] H. J. Maris, Introduction to the physics of nucleation, *Comptes Rendus de Physique* 7 (2006) 946–958.
- [81] J. Martin, Definition of the experimental MIDI facility – DENOPI project axis 1, Tech. Rep. RT PSN-RES/SEMIA/2018-00002 – BDD-ST SEMIA 2018-007, IRSN, 2018.
- [82] J. Martin, Interpretation report of MIDI facility experimental results – DENOPI project axis 1, Tech. Rep. RT PSN-RES/SEMIA/2022-00587 - BDD-ST SEMIA 2022-128, IRSN, 2022.
- [83] J. Martin, G. Brillant, C. Duriez, N. Trégourès, C. Marquié, The IRSN DENOPI project: a research program on spent-fuel-pool loss-of-cooling and loss-of-coolant accidents, in: *Proc. 17<sup>th</sup> NURETH conference*, ANS, Xi'an, Shaanxi, China, Sept. 3-8, 2017.
- [84] S. Michaïe, *Experimental study of the fundamental phenomena involved in pool boiling at low pressure*, Ph.D. thesis, Université de Lyon, 2018.
- [85] B. Migot, G. Brillant, J. Martin, S. Morin, DENOPI project devoted to spent fuel pool accidents: overview on the thermal hydraulics experimental facilities, in: *Proc. 19<sup>th</sup> NURETH conference*, ANS, Brussels, Belgium, March 6-11, 2021.
- [86] B. B. Mikic, W. M. Rohsenow, W. M. Griffith, On bubble growth rates, *International Journal of Heat and Mass Transfer* 13 (1970) 657–666.

- [87] K. Mørch, Reflections on cavitation nuclei in water, *Physics of Fluids* 19 (2007) 072104.
- [88] K. Mørch, Cavitation nuclei, experiments and theory, *Journal of Hydrodynamics* 21 (2009) 176–189.
- [89] Y. Mori, K. Hijikata, T. Nagatani, Effect of dissolved gas on bubble nucleation, *International Journal of Heat and Mass Transfer* 19 (1976) 1153–1159.
- [90] D. W. Murphy, An experimental investigation of geysering in vertical tubes, *Advances in Cryogenic Technology* I-7 (1965) 353–359.
- [91] D. Narezo Guzman, Y. Xie, S. Chen, D. Fernandez Rivas, C. Sun, D. Lohse, G. Ahlers, Heat-flux enhancement by vapour-bubble nucleation in Rayleigh-Bénard turbulence, *Journal of Fluid Mechanics* 787 (2016) 331–366.
- [92] W. Nernst, Theorie der reaktionsgeschwindigkeit in heterogenen systemen, *Zeitschrift für Physikalische Chemie* 47 (1904) 52–55.
- [93] OECD/NEA, Status report on spent Fuel Pools under Loss-of-Cooling and Loss-of-Coolant Accident Conditions, Tech. Rep., 2014.
- [94] OECD/NEA, Phenomena Identification and Ranking Table : R&D Priorities for Loss-of-Cooling and Loss-of-Coolant Accidents in Spent Nuclear Fuel Pools, Tech. Rep., 2018.
- [95] J. Paniagua, U. S. Rohatgi, V. Prasad, Modeling of Thermal Hydraulic Instabilities in Single Heated Channel Loop During Startup Transients, *Nuclear Engineering and Design* 193 (1999) 207–226.
- [96] P. Papon, J. Leblond, *Thermodynamique des états de la matière*, Hermann, 1990.
- [97] M.-H. Park, J.-H. Lee, Turbulent natural convection flow and heat transfer in an inclined square enclosure, *Korean Society of Mechanical Engineers Journal* 6 (1992) 16–23.
- [98] G. A. Pinhasi, A. Ullmann, A. Dayan, Modeling of flashing two-phase flow, *Reviews in Chemical Engineering* 21 (2005) 133–244.
- [99] B. Poling, J. Prausnitz, J. O’Connell, *The Properties of Gases and Liquids - Fifth Edition*, MacGraw-Hill, 2001.
- [100] J. S. Rinehart, *Geysers and Geothermal Energy*, Springer-Verlag, New-York, 1980.
- [101] J.-H. Saiac, *L’informatique appliquée au calcul scientifique*, Dunod, 1989.
- [102] R. Sander, Compilation of Henry’s law constants (version 4.0) for water as solvent, *Atmospheric Chemistry and Physics* 15 (2015) 4399–4981.

- [103] D. Saury, S. Harmand, M. Siroux, Flash evaporation from a water pool: Influence of the liquid height and of the depressurization rate, *International Journal of Thermal Sciences* 44 (2005) 953–965.
- [104] J. D. Seader, E. J. Henley, D. Keith Roper, *Separation process principles: chemical and biochemical operations - 3<sup>rd</sup> edition*, John Wiley & Sons, Inc., 2011.
- [105] T. Shin, O. Jones, Nucleation and flashing in nozzles - 1, *International Journal of Multiphase flow* 19 (1993) 943–964.
- [106] R. M. Singer, R. E. Holtz, On the role of inert gas in incipient boiling liquid metal experiments, *International Journal of Heat and Mass Transfer* 12 (1969) 1045–1060.
- [107] A. Singh, B. B. Mikic, W. M. Rohsenow, Active sites in boiling, *Journal of Heat Transfer* 98 (1976) 401–406.
- [108] M. G. Sirotyuk, Stabilization of gas bubbles in water, *Soviet Physics - Acoustics* 16 (1970) 237–240.
- [109] J.-W. Song, D.-L. Zeng, L.-W. Fan, Temperature dependence of contact angles of water on a stainless steel surface at elevated temperatures and pressures: In situ characterization and thermodynamic analysis, *Journal of Colloid and Interface Science* 561 (2020) 870–880.
- [110] M. Strasberg, Onset of ultrasonic cavitation in tap water, *Journal of Acoustical Society of America* 31 (1959) 163–176.
- [111] L. A. Swanger, W. C. Rhines, On the necessary conditions for homogeneous nucleation of gas bubbles in liquids, *Journal of Crystal Growth* 12 (1972) 323–326.
- [112] J. Taylor, *An introduction to error analysis, second edition*, University Science Books, 1997.
- [113] TEPCO, *Impact at the Fukushima Daiichi nuclear power station due to the Great East Japan Earthquake*, Tech. Rep., 2012.
- [114] T. Tran, H. de Maleprade, C. Sun, D. Lohse, Air entrainment during impact of droplets on liquid surfaces, *Journal of Fluid Mechanics* 726 (2013) R3.
- [115] C. Tropea, A. L. Yarin, J. F. Foss, *Springer Handbook of Experimental Fluid Mechanics*, Springer Verlag, 2007.
- [116] J. S. Turner, *Buoyancy effects in fluids*, Cambridge University Press, 1973.
- [117] M. R. Urban, *Aspects of bubble formation in dissolved air flotation*, Ph.D. thesis, Imperial College, London, 1978.

- [118] J. Valence, B. Poussery, *Le carnet du régleur*, 18<sup>ème</sup> édition, Dunod, 2017.
- [119] S. J. D. van Stralen, R. Cole, W. M. Sluyter, M. S. Sohal, Bubble growth rates in nucleate boiling of water at subatmospheric pressures, *International Journal of Heat and Mass Transfer* 18 (1975) 655–669.
- [120] F. Vella, Guide type EPR N°37 "calcul des incertitudes de mesure", Tech. Rep. E.T.DOFC/08-0251-B BPA, EDF, 2011.
- [121] N. Vernier, C. Even-Beaudoin, *Thermodynamique*, Dunod, 2020.
- [122] A. Wassel, A. Mills, D. Bugby, R. Oehlberg, Analysis of radionuclide retention in water pools, *Nuclear Engineering and Design* 90 (1985) 87–104.
- [123] R. N. Wenzel, Resistance of solid surfaces to wetting by water, *Industrial and Engineering Chemistry* 28 (1936) 988–994.
- [124] J. W. Westwater, 'Boiling of liquids' in *Advances in Chemical Engineering*, Vol. 2, Drew, T.B. and Hooper, J.P. (editors), Academic Press, 1958.
- [125] R. H. S. Winterton, Nucleation of boiling and cavitation, *Journal of Physics D: Applied Physics* 10 (1977) 2041–2056.
- [126] D. Wise, G. Houghton, The diffusion coefficients of ten slightly soluble gases in water at 10-60°C, *Chemical Engineering Science* 21 (1966) 999–1010.
- [127] A. M. Worthington, *A study of splashes*, Longmann and Green London, 1908.
- [128] G. Yadigaroglu, M. Zeller, Fluid-to-fluid scaling for a gravity and flashing-driven natural circulation loop, *Nuclear Engineering and Design* 151 (1994) 49–64.
- [129] F. Yan, *Modélisation de l'autovaporisation en écoulements subcritiques et critiques*, Ph.D. thesis, Université Catholique de Louvain (Louvain-la-Neuve - Belgique), 1991.
- [130] F. Yan, M. Giot, Mechanisms of nucleation in flashing flows, in: *Proc. 7<sup>th</sup> EURO THERM seminar, Thermal Non-Equilibrium in Two-Phase Flow*, Roma, Italy, 1989.
- [131] D. E. Yount, Skins of varying permeability: a stabilization mechanism for gas cavitation nuclei, *Journal of Acoustical Society of America* 65 (1978) 1429–1439.
- [132] J. Zheng, S. Mao, A thermodynamic model for the solubility of N<sub>2</sub>, O<sub>2</sub> and Ar in pure water and aqueous electrolyte solutions and its applications, *Applied Geochemistry* 107 (2019) 58–79.



## The liquid pool mass determination method

In order to best-estimate the liquid pool mass throughout a test, an in-line measurement of the vertical hydrostatic pressure difference within the Aquarius vessel is performed. Indeed according to the hydrostatic law, in a vertically uniform geometry as the pool vessel, the liquid mass  $m_L$  standing in between two successive pressure measurements  $P(z_1)$  and  $P(z_2)$  is linearly related to the pressure difference  $\Delta P = P(z_2) - P(z_1)$ . Therefore, a prior determination of this relationship further allows determining a liquid mass according to the in-line measurement of  $\Delta P$ . This pressure difference, denoted as  $\Delta P_{pool}$ , is respectively computed as follows:

$$\Delta P_{pool} = P150Ap - P140Ap \quad (\text{A.1})$$

A series of qualification tests was performed at the launch of the present research. The tests consisted in the gradual filling of the vessel with known water volumes. Once filled up, the vessel was then depressurized down to 50 mbar in order to reach the measuring range of the pressure sensors and the pressure difference  $\Delta P_{pool}$  was recorded. The pool was repeatedly filled up with a 5 L beaker. The correspondence between the beaker volume and the added water mass was checked by means of a calibrated balance and yielded:

$$V_{5.0\text{ L}} \Leftrightarrow 5.076 \pm 0.001 \text{ kg} \quad (\text{A.2})$$

Importantly, the error resulting from the vessel filling stage is postulated to be at least equal to one volume graduation of the used beaker:

$$\delta_{5.0\text{ L}} = 0.1 \text{ L} \Leftrightarrow 0.102 \pm 0.001 \text{ kg} \quad (\text{A.3})$$

The pressure measurement uncertainties are detailed in Appendix D. The tests series was repeated three times in order to assess the accuracy of this very process. The obtained results are given in Figure A.1. The mass and pressure difference error bars, of relatively negligible size, are omitted in these graphs. As one can notice, those measurements were highly repeatable. The average standard deviation of the pressure

difference measurement, computed from one test series to another, is of 0.05 mbar for the Aquarius vessel, which is of the order of the pressure sensors uncertainty. A linear regression was then performed based on those measurements and yielded the following  $\Delta P = f(m_L)$  relationship:

$$\Delta P_{pool} = 0.72 m_L - 0.43 \quad (\text{A.4})$$

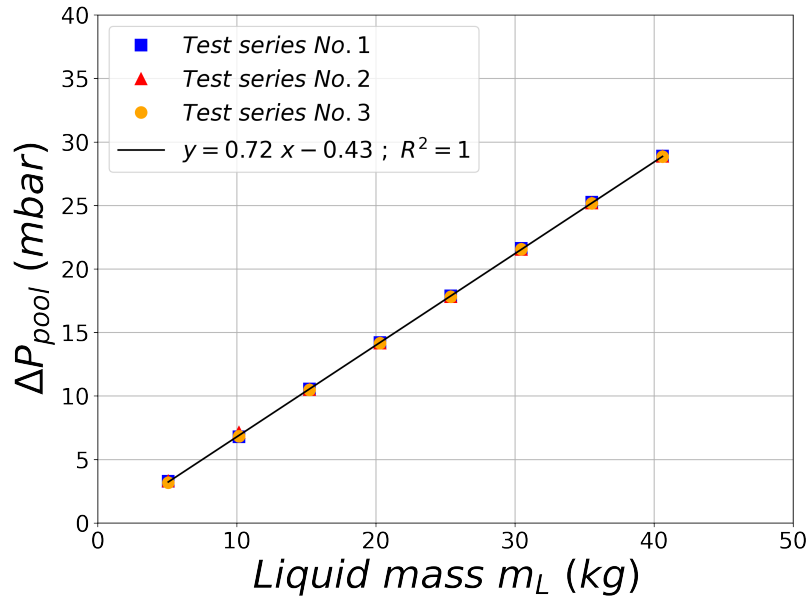


Figure A.1: Aquarius vessel  $\Delta P = f(m_L)$  relationship.

# A modeling of the O<sub>2</sub> and N<sub>2</sub> degassing from a water pool

## B.1 Problem description

The studied thermodynamic system consists in a ternary mixture of two dissolved gaseous species, *i.e.* the O<sub>2</sub> and N<sub>2</sub> referred to as the solutes, and liquid water, the solvent. The system's composition is defined by means of the molar fractions  $x_{O_2}^L$ ,  $x_{N_2}^L$  and  $x_w^L$ , respectively referring to the oxygen, nitrogen and water species. Obviously:

$$x_{O_2}^L + x_{N_2}^L + x_w^L = 1 \quad (\text{B.1})$$

The mixture is also defined by a single temperature  $T_L$  and pressure  $P_L$ . It is assumed separated from a bounding gas phase by an interface, as depicted in Figure B.1, whose liquid-side composition is described by  $x_{O_2}^{Li}$ ,  $x_{N_2}^{Li}$  and  $x_w^{Li}$ , the species molar fractions at that location, and:

$$x_{O_2}^{Li} + x_{N_2}^{Li} + x_w^{Li} = 1 \quad (\text{B.2})$$

The liquid-side O<sub>2</sub> and N<sub>2</sub> fractions are related to their gaseous counterpart by the so-called *Henry's law of solubility*, which reads, for each species:

$$x_{O_2}^{Gi} = \frac{x_{O_2}^{Li} \mathcal{H}_{O_2}(T_I)}{P_G} \quad (\text{B.3})$$

$$x_{N_2}^{Gi} = \frac{x_{N_2}^{Li} \mathcal{H}_{N_2}(T_I)}{P_G} \quad (\text{B.4})$$

where  $P_G$  is the gas phase total pressure,  $\mathcal{H}_{O_2}(T_I)$  and  $\mathcal{H}_{N_2}(T_I)$  are respectively the O<sub>2</sub> and N<sub>2</sub> Henry's volatility constant (in Pa/mol/mol), at temperature  $T_I$  (which is *a priori* different from  $T_L$ ). The gas-side water molar fraction is related to the interfacial pressure  $P_G$  and temperature  $T_I$  by the so-called *Raoult's law*:

$$x_w^{Gi} = \frac{P_{sat}(T_I)}{P_G} \quad (\text{B.5})$$

with  $P_{sat}(T_I)$ , the water saturation pressure at temperature  $T_I$ . If the gas/liquid interface is curved, there exists a pressure jump across that interface. This interfacial jump can be described by the so-called *Laplace-Young equation*:

$$P_G - P_L = \sigma(T_I) \mathcal{C}_I \quad (\text{B.6})$$

with  $\sigma$  being the gas/liquid couple surface tension (given in  $\text{J}/\text{m}^2$ ) and  $\mathcal{C}_I$  the interfacial curvature (given in  $\text{m}^{-1}$ ). Singularly:

- $\mathcal{C}_I = 2/R_I$  for a spherical interface of radius  $R_I$ ;
- $\mathcal{C}_I = 0$  for a planar interface.

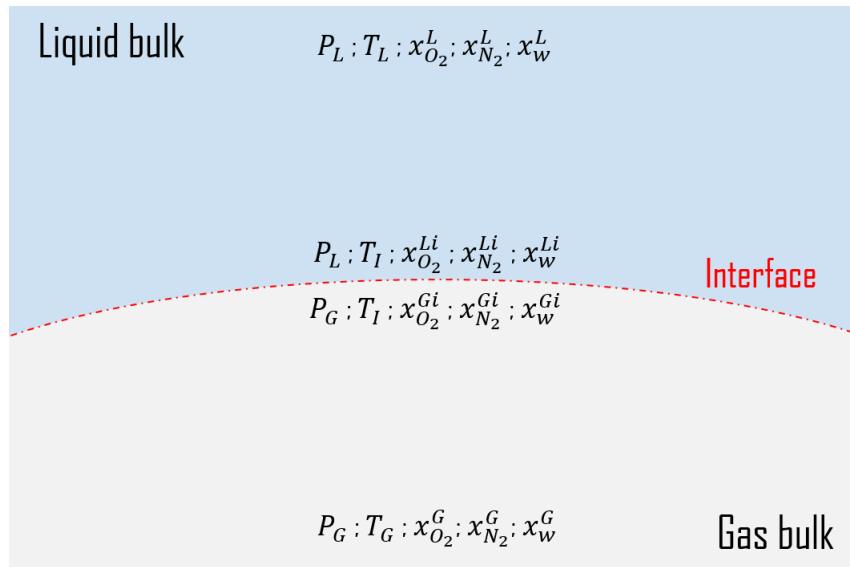


Figure B.1: Illustration of the gas/liquid interface separating the studied ternary mixture of water and dissolved  $O_2$  and  $N_2$  from a gas bulk.

Provided a composition gradient of  $O_2$  and  $N_2$  in the vicinity of the interface, species molar fluxes that tend to rebalance the compositions should develop within the solvent. We later denote those fluxes (given in  $\text{mol}/\text{m}^2/\text{s}$ ):

- $j_{O_2}^L$ : the liquid-side  $O_2$  molar flux;
- $j_{N_2}^L$ : the liquid-side  $N_2$  molar flux.

The present problem consists in predicting the molar fluxes of each solute corresponding to a given driving composition gradient. We first provide the solubility and diffusivity empirical data needed for treating the problem in Section B.2. Then, we derive an analytical expression for the species molar fluxes, on the basis of the *generalized Maxwell-Stefan transport equation*, in Section B.3. At last, we show in Section B.4 that the present ternary thermodynamic system can be equivalently described as a binary one and we provide a set of equivalence mathematical relationships for doing so.

## B.2 The solubility and diffusivity of air, O<sub>2</sub> and N<sub>2</sub> in water

### B.2.1 The Henry's volatility constants

First of all, the Henry's volatility constants of O<sub>2</sub> and N<sub>2</sub> that read  $\mathcal{H}_{O_2}(T_I)$  and  $\mathcal{H}_{N_2}(T_I)$ , can be reliably predicted by means of the empirical data published in [1]. The data is primarily given in this handbook through the form of a so-called Bunsen coefficient, an old-fashioned dimensionless equivalent of the Henry's constant [102]. The Bunsen coefficients, denoted as  $\alpha_{O_2}$  and  $\alpha_{N_2}$  are then converted into the targeted Henry's volatility constants as follows:

$$\mathcal{H}_{O_2}(T_I) = \frac{\rho_w(T_I)\mathcal{R}T^{STP}}{\alpha_{O_2}(T_I)\mathcal{M}_w} \quad (\text{B.7})$$

$$\mathcal{H}_{N_2}(T_I) = \frac{\rho_w(T_I)\mathcal{R}T^{STP}}{\alpha_{N_2}(T_I)\mathcal{M}_w} \quad (\text{B.8})$$

with:

- $\rho_w(T_I)$ , the solvent density (in kg/m<sup>3</sup>), computed at temperature  $T_I$ ;
- $\mathcal{M}_w = 18 \times 10^{-3}$  kg/mol, the solvent molar mass;
- $\mathcal{R} = 8.314$  J/mol/K, the perfect gas constant;
- $T^{STP} = 273.15$  K, the so-called standard temperature.

The corresponding temperature-dependent constants for O<sub>2</sub> and N<sub>2</sub> are summarized in Table B.1. In this very table are also provided the Henry's volatility constants of the dissolved air, that were extracted *as is* from [47]. At last, we give a graphical representation of the collected data in Figure B.2.

Table B.1: The Henry's volatility constants of air, O<sub>2</sub> and N<sub>2</sub> in dissolution within water (in Pa/mol/mol) according to the data published in [1] and [47].

$T_I$ (°C)	0	5	10	15	20	25	30	40	50	60	70	80	90	100
$\mathcal{H}_a \times 10^{-9}$	4.32	4.88	5.49	6.07	6.64	7.20	7.71	8.70	9.46	10.1	10.5	10.7	10.8	10.8
$\mathcal{H}_{O_2} \times 10^{-9}$	2.55	2.90	3.28	3.64	4.01	4.39	4.75	5.35	5.89	6.28	6.65	6.88	6.99	7.02
$\mathcal{H}_{N_2} \times 10^{-9}$	5.30	5.96	6.64	7.30	7.99	8.62	9.22	10.4	11.3	12.0	12.5	12.6	12.6	12.6

### B.2.2 The water-solute binary diffusivities

In what follows, the binary diffusivities of air, O<sub>2</sub> and N<sub>2</sub> in liquid water are estimated from the data published by *Wise and Houghton* in [126]. Those quantities, given in m<sup>2</sup>/s, are respectively denoted:

- $\mathcal{D}_{a:w}^L$ , for the dissolved air;

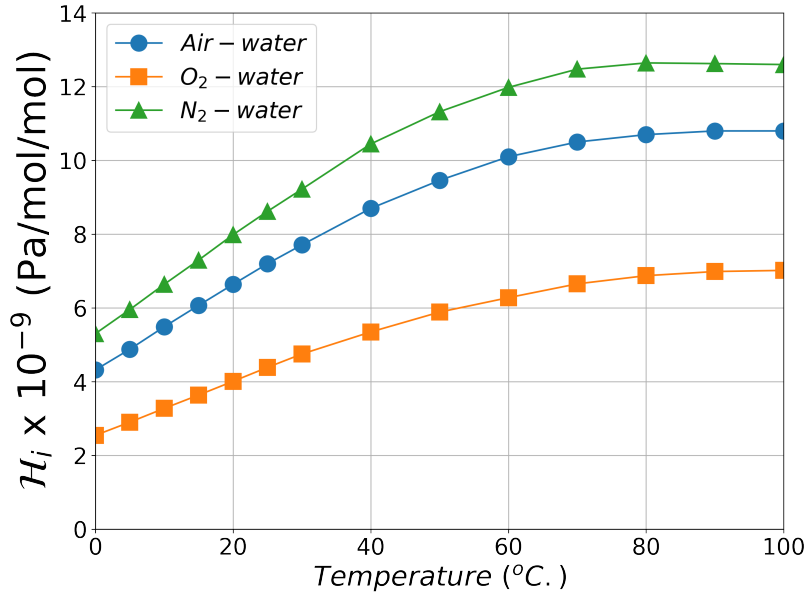


Figure B.2: The temperature-dependent Henry's volatility constants of air,  $O_2$  and  $N_2$  in dissolution within water (in Pa/mol/mol) according to the data published in [1] and [47].

- $\mathcal{D}_{O_2;w}^L$ , for the dissolved  $O_2$  ;
- $\mathcal{D}_{N_2;w}^L$ , for the dissolved  $N_2$  .

In this publication, the diffusivities were determined empirically by studying the dissolution process of controlled non-condensable bubbles in gas-free water, over the temperature range 10-60°C. The data is summarized in Table B.2 and graphically represented in Figure B.3. The authors estimated a  $\pm 10\%$  overall uncertainty associated with each diffusion coefficient, corresponding to the magnitude of the error bars visible in this very figure.

Table B.2: The diffusivities of air,  $O_2$  and  $N_2$  in liquid water, empirically determined and reported by *Wise and Houghton* in [126].

$T$ (°C)	10	20	30	40	50	60
$\mathcal{D}_{a;w}^L \times 10^9$	2.0	2.5	3.2	4.0	4.9	6.3
$\mathcal{D}_{O_2;w}^L \times 10^9$	1.7	2.3	2.8	3.8	4.2	5.7
$\mathcal{D}_{N_2;w}^L \times 10^9$	1.8	2.6	3.5	4.3	5.1	6.5

### B.3 The molar flux of the dissolved species

For treating the multicomponent diffusion of  $O_2$  and  $N_2$  in water, let us first idealize the problem. The diffusion of each species is assumed to take place along a stagnant film of the studied mixture. *A priori*, the film thickness is species-dependent and we denote

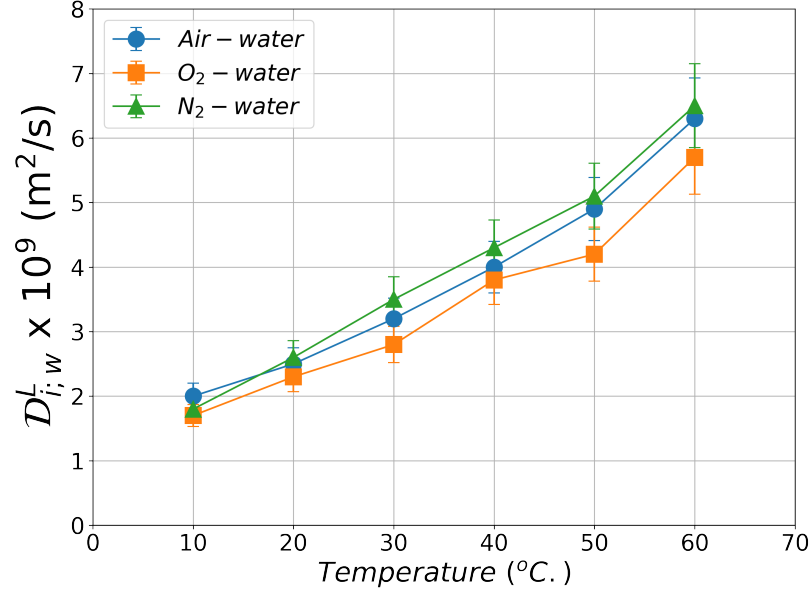


Figure B.3: The temperature-dependent diffusivities of air, O<sub>2</sub> and N<sub>2</sub> in liquid water, empirically determined and reported by *Wise and Houghton* in [126].

$\delta_{O_2}^L$  and  $\delta_{N_2}^L$  its value, respectively for the O<sub>2</sub> and N<sub>2</sub> components. The spatial extension of the film is bounded, on one hand, by the gas/liquid interface and on the other hand, by the liquid bulk, as depicted in Figure B.4. The gradients of the transported variables defining the mixture (*e.g.* a temperature and/or a species molar fraction) are assumed non-null within the film and null within the gas and liquid bulks surrounding it. The diffusion is further assumed one-dimensional (oriented along *z*-axis) and stationary. In doing so, we are adopting the so-called *film theory*, first introduced by *Nernst* in 1904 [92]. This is the simplest available idealization of the mass transfers across a gas/liquid interface [32]. However, even when combined with appropriate species diffusion equations, it remains poorly accurate unless the film thickness is known. The most common way in computing this thickness and having reliable transfer estimates is to relate the film to the viscous part of the boundary layer that forms at the limits of a turbulent flow (*e.g.* a wall or a gas/liquid interface) [13].

In what follows, we first introduce the so-called generalized Maxwell-Stefan multicomponent equations that are relevant for treating the present problem (Subsection B.3.1). We also show that those equations reduce to the simpler multi-Fickian case, by considering that the studied system is a highly dilute ideal mixture. Next, we provide a space-integrated solution to these equations (Subsection B.3.2) and we propose an estimate for the species-dependent film thickness (Subsection B.3.3).

### B.3.1 The local multicomponent diffusion equations

The generalized Maxwell-Stefan equation linking the composition gradient of species  $\alpha$  with the composition and vectorial molar fluxes of the other  $\beta$  species, with  $\beta \in \{1, N\}$

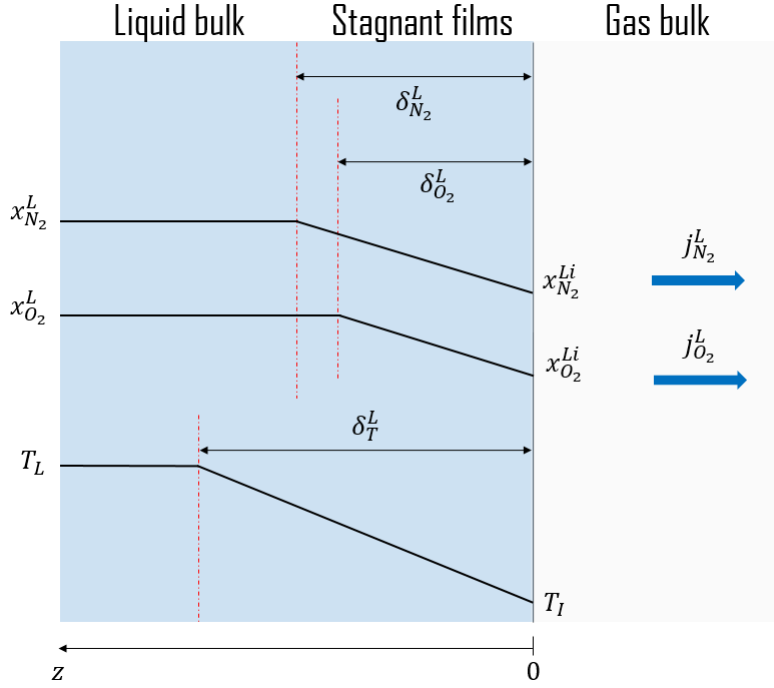


Figure B.4: Illustration of the postulated heat and mass transfer films where the temperature and composition gradients are non-null, in the vicinity of the gas/liquid interface.

and  $\beta \neq \alpha$ , reads [75]:

$$\frac{\partial(\text{Ln } a_{\alpha}^L)}{\partial(\text{Ln } x_{\alpha}^L)} \nabla x_{\alpha}^L = - \sum_{\beta=1}^N \frac{1}{C_L \mathcal{D}_{\alpha;\beta}^L} (x_{\beta}^L \vec{j}_{\alpha} - x_{\alpha}^L \vec{j}_{\beta}) \quad (\text{B.9})$$

with  $a_{\alpha}^L$ , the chemical activity of species  $\alpha$  in the solvent,  $C_L$ , the mixture molar concentration and  $\mathcal{D}_{\alpha;\beta}^L$ , the binary diffusion coefficient of the  $(\alpha; \beta)$  couple. Once applied to the  $O_2$  and  $N_2$  solutes and water solvent, Equation (B.9) yields:

$$\frac{\partial(\text{Ln } a_{O_2}^L)}{\partial(\text{Ln } x_{O_2}^L)} C_L \nabla x_{O_2}^L = -\vec{j}_{O_2} \left( \frac{x_w^L}{\mathcal{D}_{O_2;w}^L} + \frac{x_{N_2}^L}{\mathcal{D}_{O_2;N_2}^L} \right) + \vec{j}_w \frac{x_{O_2}^L}{\mathcal{D}_{O_2;w}^L} + \vec{j}_{N_2} \frac{x_{O_2}^L}{\mathcal{D}_{O_2;N_2}^L} \quad (\text{B.10})$$

$$\frac{\partial(\text{Ln } a_{N_2}^L)}{\partial(\text{Ln } x_{N_2}^L)} C_L \nabla x_{N_2}^L = -\vec{j}_{N_2} \left( \frac{x_w^L}{\mathcal{D}_{N_2;w}^L} + \frac{x_{O_2}^L}{\mathcal{D}_{N_2;O_2}^L} \right) + \vec{j}_w \frac{x_{N_2}^L}{\mathcal{D}_{N_2;w}^L} + \vec{j}_{O_2} \frac{x_{N_2}^L}{\mathcal{D}_{N_2;O_2}^L} \quad (\text{B.11})$$

First of all, as already discussed, the studied ternary system can be reasonably seen as an ideal mixture. In such a case, the chemical activity of the two solutes is equal to their molar fraction [99]:

$$a_{O_2}^L = x_{O_2}^L \text{ and } a_{N_2}^L = x_{N_2}^L \quad (\text{B.12})$$

which yields:

$$\frac{\partial(\text{Ln } a_{O_2}^L)}{\partial(\text{Ln } x_{O_2}^L)} = \frac{\partial(\text{Ln } a_{N_2}^L)}{\partial(\text{Ln } x_{N_2}^L)} = 1 \quad (\text{B.13})$$

Next, under the assumption that the two solutes diffuse through a film of stagnant solvent, then:

$$\vec{j}_w = \vec{0} \quad (\text{B.14})$$

This gives:

$$C_L \nabla x_{O_2}^L = -\vec{j}_{O_2} \left( \frac{x_w^L}{\mathcal{D}_{O_2;w}^L} + \frac{x_{N_2}^L}{\mathcal{D}_{O_2;N_2}^L} \right) + \vec{j}_{N_2} \frac{x_{O_2}^L}{\mathcal{D}_{O_2;N_2}^L} \quad (\text{B.15})$$

$$C_L \nabla x_{N_2}^L = -\vec{j}_{N_2} \left( \frac{x_w^L}{\mathcal{D}_{N_2;w}^L} + \frac{x_{O_2}^L}{\mathcal{D}_{N_2;O_2}^L} \right) + \vec{j}_{O_2} \frac{x_{N_2}^L}{\mathcal{D}_{N_2;O_2}^L} \quad (\text{B.16})$$

Further, with the high dilution of  $O_2$  and  $N_2$  within the solvent, the cross-diffusion between those two solutes can be reasonably neglected, which reads:

$$\mathcal{D}_{O_2;N_2}^L = \mathcal{D}_{N_2;O_2}^L \approx 0 \quad (\text{B.17})$$

Then:

$$\underbrace{\mathcal{D}_{O_2;N_2}^L \left( C_L \nabla x_{O_2}^L + \vec{j}_{O_2} \frac{x_w^L}{\mathcal{D}_{O_2;w}^L} \right)}_{\approx 0} = \vec{j}_{N_2} x_{O_2}^L - \vec{j}_{O_2} x_{N_2}^L \quad (\text{B.18})$$

$$\underbrace{\mathcal{D}_{N_2;O_2}^L \left( C_L \nabla x_{N_2}^L + \vec{j}_{N_2} \frac{x_w^L}{\mathcal{D}_{N_2;w}^L} \right)}_{\approx 0} = \vec{j}_{O_2} x_{N_2}^L - \vec{j}_{N_2} x_{O_2}^L \quad (\text{B.19})$$

which gives identically:

$$\vec{j}_{N_2} x_{O_2}^L = \vec{j}_{O_2} x_{N_2}^L \quad (\text{B.20})$$

Thus, obviously the two  $O_2$ - $N_2$  cross-diffusion terms cancel out within Equations (B.15) and (B.16). At last, still under the assumption of a high dilution of  $O_2$  and  $N_2$ :

$$x_w^L \approx 1 \quad (\text{B.21})$$

This yields the following simplifications of the generalized Maxwell-Stefan Equations (B.10) and (B.11):

$$\vec{j}_{O_2} = -C_L \mathcal{D}_{O_2;w}^L \nabla x_{O_2}^L \quad (\text{B.22})$$

$$\vec{j}_{N_2} = -C_L \mathcal{D}_{N_2;w}^L \nabla x_{N_2}^L \quad (\text{B.23})$$

All in all, we can notice that in the present problem, a good approximation of the multicomponent diffusion of  $O_2$  and  $N_2$  in water is the so-called multi-Fickian approach for which each individual molar flux is described by the first Fick's law. The approximation holds true while the water,  $O_2$  and  $N_2$  mixture behaves thermodynamically as an ideal mixture. As already discussed, a deviation from the Henry's law is the analogous of a deviation from ideality for such a mixture. The Henry's law of  $O_2$  and  $N_2$  solubility in water holding true for pressures up to 100 bar [132], this hence gives a validity boundary to the present multi-Fickian approximation.

### B.3.2 The space-integrated equations

The spatial integration of Equations (B.22) and (B.23) over their species-dependent film thickness trivially yields:

$$j_{O_2} = -C_L \mathcal{D}_{O_2;w}^L \frac{x_{O_2}^L - x_{O_2}^{Li}}{\delta_{O_2}^L} \quad (\text{B.24})$$

$$j_{N_2} = -C_L \mathcal{D}_{N_2;w}^L \frac{x_{N_2}^L - x_{N_2}^{Li}}{\delta_{N_2}^L} \quad (\text{B.25})$$

with:

$$j_{O_2} = \vec{j}_{O_2} \cdot \vec{z} \quad (\text{B.26})$$

$$j_{N_2} = \vec{j}_{N_2} \cdot \vec{z} \quad (\text{B.27})$$

### B.3.3 The estimate of the species-dependent film thicknesses

When the liquid mixing is only provided by natural thermal convection, as in the presented problem, one can estimate the species-dependent film thicknesses  $\delta_{O_2}^L$  and  $\delta_{N_2}^L$  by means of the well-known *Chilton-Colburn analogy* [32]. This empirical analogy reads, for each solute:

$$k_{O_2}^L = \frac{k_T^L}{\mathcal{C}_p^L} \left( \frac{\mathcal{D}_{O_2;w}^L}{\kappa_L} \right)^{2/3} \quad (\text{B.28})$$

$$k_{N_2}^L = \frac{k_T^L}{\mathcal{C}_p^L} \left( \frac{\mathcal{D}_{N_2;w}^L}{\kappa_L} \right)^{2/3} \quad (\text{B.29})$$

with  $k_{O_2}^L$  and  $k_{N_2}^L$ , the  $O_2$  and  $N_2$  mass transfer coefficients (in mol/m<sup>2</sup>/s),  $k_T^L$ , the liquid-side heat transfer coefficient (in W/m<sup>2</sup>/K),  $\mathcal{C}_p^L$  the liquid mixture molar heat capacity (in J/mol/K) and  $\kappa_L$ , the liquid mixture heat diffusivity (in m<sup>2</sup>/s). Those two last parameters are here approximately equal to the values expected for the water alone, since the solutes are both highly diluted. Furthermore, under the assumption that the stagnant films are identical to the viscous part of the boundary layers at the interface, the above heat and mass transfer coefficients are defined as:

$$k_T^L = \frac{\lambda_L}{\delta_T^L} \quad (\text{B.30})$$

$$k_{O_2}^L = \frac{C_L \mathcal{D}_{O_2;w}^L}{\delta_{O_2}^L} \quad (\text{B.31})$$

$$k_{N_2}^L = \frac{C_L \mathcal{D}_{N_2;w}^L}{\delta_{N_2}^L} \quad (\text{B.32})$$

with  $\lambda_L$ , the liquid mixture heat conductivity (in W/m/K), approximately equal to those of the liquid water alone. The liquid mixture thermal diffusivity being:

$$\kappa_L = \frac{\lambda_L}{C_L \mathcal{C}_p^L} \quad (\text{B.33})$$

this finally yields:

$$\delta_{O_2}^L = \delta_T^L \left( \frac{\mathcal{D}_{O_2:w}^L}{\kappa_L} \right)^{1/3} \quad (\text{B.34})$$

$$\delta_{N_2}^L = \delta_T^L \left( \frac{\mathcal{D}_{N_2:w}^L}{\kappa_L} \right)^{1/3} \quad (\text{B.35})$$

and thus:

$$\frac{\delta_{O_2}^L}{\delta_{N_2}^L} = \left( \frac{\mathcal{D}_{O_2:w}^L}{\mathcal{D}_{N_2:w}^L} \right)^{1/3} \quad (\text{B.36})$$

In Figure B.5 is represented the temperature trend of Equation (B.36), computed by means of the data from [126]. As one can see, the result is almost temperature-independent over the temperature range 10-60°C and close to unity:

$$\left( \frac{\mathcal{D}_{O_2:w}^L}{\mathcal{D}_{N_2:w}^L} \right)^{1/3} \approx 0.95 \quad (\text{B.37})$$

The differences in O<sub>2</sub> and N<sub>2</sub> film thickness being of the order of 5% and smaller than the uncertainty in Equation (B.36), computed from diffusivities which are  $\pm 10\%$  uncertain, one can hence confidently assume:

$$\delta_{O_2}^L \approx \delta_{N_2}^L = \delta_m^L \quad (\text{B.38})$$

with:

$$\delta_m^L = \delta_T^L \left( \frac{\mathcal{D}_{a:w}^L}{\kappa_L} \right)^{1/3} \quad (\text{B.39})$$

an average liquid-side mass transfer film thickness, computed by means of the water-air diffusivity  $\mathcal{D}_{a:w}^L$  provided in [126]. This gives:

$$\delta_m^L = \frac{\lambda_L}{k_T^L} \left( \frac{\mathcal{D}_{a:w}^L}{\kappa_L} \right)^{1/3} \quad (\text{B.40})$$

One may identically wonder if the heat and mass transfer film thicknesses  $\delta_T^L$  and  $\delta_m^L$  are of the same order of magnitude. This point is investigated in Figure B.6. As one can observe, the mass transfer film is 3 to 4 times smaller than the heat transfer film over the temperature range 10-60°C. Nevertheless, the temperature dependence of this *ratio* cannot be neglected.

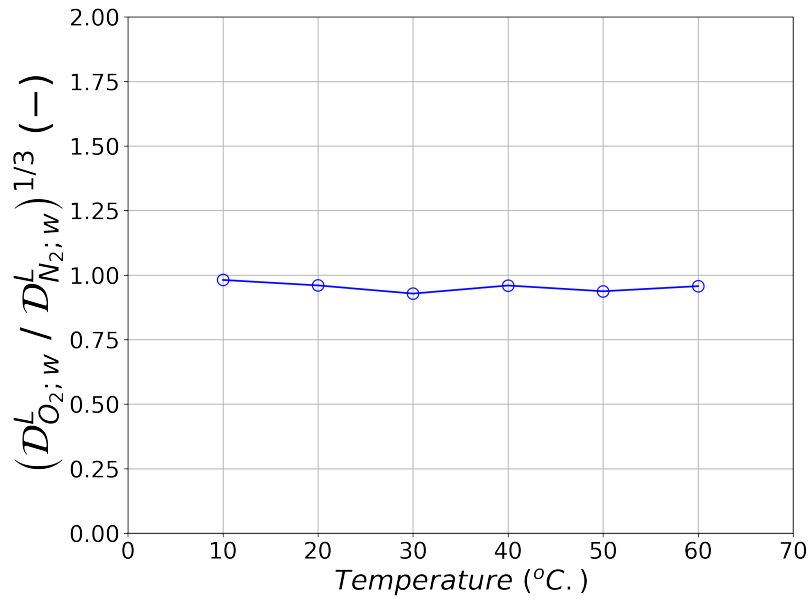


Figure B.5: Temperature dependence of the *ratio* between the  $O_2$  and  $N_2$  film thicknesses. This quantity is almost constant and equal to 0.95 over the temperature range 10-60°C.

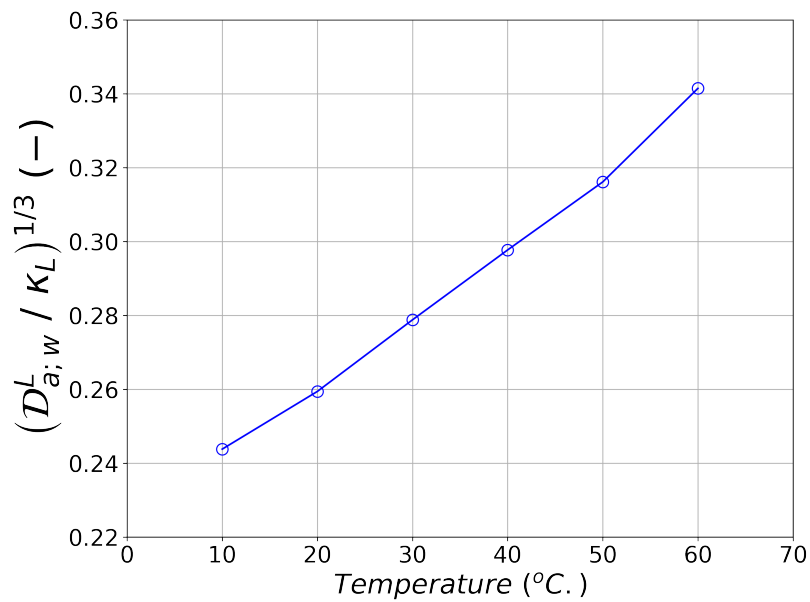


Figure B.6: Temperature dependence of the *ratio* between the mass and heat transfer film thicknesses. The mass transfer film is 3 to 4 times smaller than the heat transfer film over the temperature range 10-60°C.

## B.4 Equivalence between the binary and ternary problems

In some circumstances, it may be more interesting to deal with the simpler air/water binary mixture equations instead of resolving the complete ternary problem. This is done by obviously defining the dissolved air species as a mixture of O<sub>2</sub> and N<sub>2</sub> solutes. As developed in this section, there exists a set of equivalence mathematical relations that allows deducing the analogous binary solution of the problem from its ternary counterpart and *vice versa*. This equivalence is arbitrarily formulated below for the air/O<sub>2</sub> pair of species.

### B.4.1 The liquid-side interfacial composition

At the gas/liquid interface, the gas-side molar fraction of air is defined as:

$$x_a^{Gi} = x_{O_2}^{Gi} + x_{N_2}^{Gi} \quad (\text{B.41})$$

Assuming that the gas and liquid-side molar fractions of air are interrelated by the Henry's law, as for the dissolved O<sub>2</sub> and N<sub>2</sub>, Equation (B.42) can be rewritten as:

$$x_a^{Li} \mathcal{H}_a = x_{O_2}^{Li} \mathcal{H}_{O_2} + x_{N_2}^{Li} \mathcal{H}_{N_2} \quad (\text{B.42})$$

And, with:

$$x_{N_2}^{Li} = x_a^{Li} - x_{O_2}^{Li} \quad (\text{B.43})$$

one gets the following relationship between the liquid-side molar fractions of dissolved air and O<sub>2</sub>:

$$\frac{x_{O_2}^{Li}}{x_a^{Li}} = \frac{\mathcal{H}_a - \mathcal{H}_{N_2}}{\underbrace{\mathcal{H}_{O_2} - \mathcal{H}_{N_2}}_{\mathcal{H}_m^*}} \quad (\text{B.44})$$

with  $\mathcal{H}_m^*$ , the Henry's constants ratio of the dissolved species. On the basis of the available tabulated values for the air, O<sub>2</sub> and N<sub>2</sub> Henry's volatility constants given in Section B.2, we plot in Figure B.7 the temperature trend of  $\mathcal{H}_m^*$  in the range 0-100°C. As one can notice,  $\mathcal{H}_m^*$  exhibits a quasi-constant trend over this temperature range and can be reasonably taken equal to:

$$\mathcal{H}_m^* \approx 0.34 \quad (\text{B.45})$$

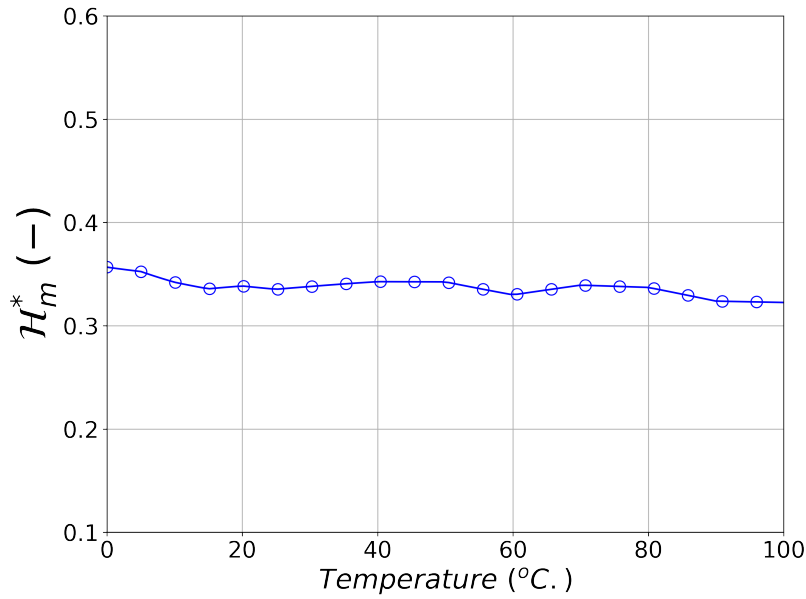


Figure B.7: The temperature dependence of  $\mathcal{H}_m^*$ , the *ratio* of the Henry's constants of the dissolved species, defined in Equation (B.44).

### B.4.2 The liquid bulk composition and degassing fluxes

As already shown in Section B.3 through the simplification of the Maxwell-Stefan equations, there exists a relationship between the  $O_2$  and  $N_2$  degassing fluxes, which reads:

$$\frac{j_{O_2}}{j_{N_2}} = \frac{x_{O_2}^L}{x_{N_2}^L}; \quad \forall z \in \{0, \delta_m^L\} \quad (\text{B.46})$$

Hence, equivalently:

$$\frac{j_a}{j_{O_2}} = 1 + \frac{j_{N_2}}{j_{O_2}} \quad (\text{B.47})$$

$$= 1 + \frac{x_{N_2}^L}{x_{O_2}^L} \quad (\text{B.48})$$

$$= \frac{x_a^L}{x_{O_2}^L} \quad (\text{B.49})$$

This equation being verified for all  $z$  within the mass transfer film thickness  $\delta_m^L$  and the *ratio* between the liquid-side molar fractions of dissolved air and  $O_2$  being equal to  $\mathcal{H}_m^*$  at  $z = 0$ , location of the interface (*cf.* Section B.4.1), this yields:

$$\frac{x_{O_2}^L}{x_a^L} = \frac{j_{O_2}}{j_a} = \mathcal{H}_m^* \quad (\text{B.50})$$

### B.4.3 The dissolved air diffusivity in water

Let us denote as  $\mathcal{D}_{a:w}^L$ , the diffusion coefficient of the dissolved air/liquid water binary mixture (given in  $\text{m}^2/\text{s}$ ). With the dissolved air species assimilated to a mixture of dissolved  $\text{O}_2$  and  $\text{N}_2$  molecules,  $\mathcal{D}_{a:w}^L$  is to be composition-dependent and can be linked to the individual binary diffusion coefficients of the two latter species, *i.e.*  $\mathcal{D}_{\text{O}_2:w}^L$  and  $\mathcal{D}_{\text{N}_2:w}^L$ . As already discussed, the studied ternary mixture is a so-called highly dilute, ideal solution. We show in this section that under those assumptions, one can simply express the dissolved air diffusion coefficient as a combination of the dissolved  $\text{O}_2$  and  $\text{N}_2$  diffusivities which is known in the literature as the *Blanc's law* [73]. Let us start by applying the Maxwell-Stefan Equation (B.9) to the water species. Under the assumptions discussed in Section B.3, this yields:

$$C_L \nabla x_w^L \approx \vec{j}_{\text{O}_2} \frac{1}{\mathcal{D}_{\text{O}_2:w}^L} + \vec{j}_{\text{N}_2} \frac{1}{\mathcal{D}_{\text{N}_2:w}^L} \quad (\text{B.51})$$

By definition:

$$\nabla x_w^L = -\nabla x_a^L \quad (\text{B.52})$$

and since:

$$\vec{j}_{\text{N}_2} x_{\text{O}_2}^L = \vec{j}_{\text{O}_2} x_{\text{N}_2}^L \quad (\text{B.53})$$

(*cf.* Section B.3), Equation (B.51) can be rearranged as:

$$C_L \nabla x_a^L = -\vec{j}_{\text{O}_2} \left( \frac{1}{\mathcal{D}_{\text{O}_2:w}^L} + \frac{x_{\text{O}_2}^L}{x_{\text{N}_2}^L} \frac{1}{\mathcal{D}_{\text{N}_2:w}^L} \right) \quad (\text{B.54})$$

Furthermore, under the retained assumptions, the  $\text{O}_2$  and  $\text{N}_2$  diffusion fluxes being reasonably described by the simple First Fick's law (*cf.* Section B.3), one can expect the constructed dissolved air species to diffuse in water according to a similar law, which reads:

$$\vec{j}_a = -C_L \mathcal{D}_{a:w}^L \nabla x_a^L \quad (\text{B.55})$$

Thus, one gets:

$$\vec{j}_a \frac{1}{\mathcal{D}_{a:w}^L} = \vec{j}_{\text{O}_2} \left( \frac{1}{\mathcal{D}_{\text{O}_2:w}^L} + \frac{x_{\text{O}_2}^L}{x_{\text{N}_2}^L} \frac{1}{\mathcal{D}_{\text{N}_2:w}^L} \right) \quad (\text{B.56})$$

and since:

$$\vec{j}_a x_{\text{O}_2}^L = \vec{j}_{\text{O}_2} x_a^L \quad (\text{B.57})$$

(*cf.* Section B.4.2), therefore by association:

$$\frac{x_a^L}{\mathcal{D}_{a:w}^L} = \frac{x_{\text{O}_2}^L}{\mathcal{D}_{\text{O}_2:w}^L} + \frac{x_{\text{N}_2}^L}{\mathcal{D}_{\text{N}_2:w}^L} \quad (\text{B.58})$$

which is the so-called Blanc's law. At last, with:

$$\frac{x_{\text{O}_2}^L}{x_a^L} = \mathcal{H}_m^* \quad (\text{B.59})$$

then:

$$\frac{1}{\mathcal{D}_{a;w}^L} = \frac{\mathcal{H}_m^*}{\mathcal{D}_{O_2;w}^L} + \frac{1 - \mathcal{H}_m^*}{\mathcal{D}_{N_2;w}^L} \quad (\text{B.60})$$

It is worth questioning the validity of the above equation. At least one study provides enough experimental results for investigating this point [126]. In their paper *Wise and Houghton* empirically determined the  $\mathcal{D}_{a;w}^L$ ,  $\mathcal{D}_{O_2;w}^L$  and  $\mathcal{D}_{N_2;w}^L$  coefficients over the temperature range 10-60°C, by studying the dissolution process of controlled non-condensable bubbles in gas-free water. Their  $O_2$  and  $N_2$  diffusion coefficients are used for computing the predicted dissolved air diffusivity shown in Figure B.8. The authors estimated a  $\pm 10\%$  overall uncertainty associated with the empirical dissolved air diffusion coefficient, corresponding to the magnitude of the error bars visible in this very figure. As one can notice, the Blanc's law behind the estimate of  $\mathcal{D}_{a;w}^L$  is compatible with the reported empirical data for this coefficient.

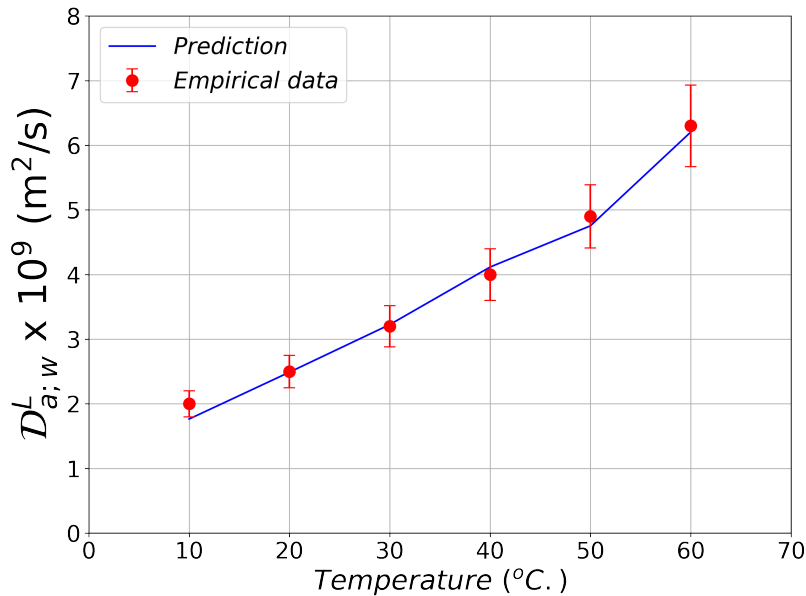


Figure B.8: The comparison between the empirical  $\mathcal{D}_{a;w}^L$ , reported in [126], and its prediction based on Equation (B.60) and on the values of  $\mathcal{D}_{O_2;w}^L$  and  $\mathcal{D}_{N_2;w}^L$  given in [126].

---

## The test data post-processing code in Python 3

```

""" ----- """
""" |      MODULE IMPORTATION      | """
""" ----- """

import numpy as np
import pandas as pd
import scipy.signal as sig

from CoolProp.CoolProp import PropsSI as cp

""" ----- """
""" |      PROPERTIES IMPORTATION      | """
""" ----- """

henry = pd.read_csv('air-water_henrys_constant.csv')
diffu = pd.read_csv('air-water_diffusivity.csv')

""" ----- """
""" |      DATASET PRE-PROCESSING FUNCTION      | """
""" ----- """

def preprocess_dataset(dataset, year, month, day):

    ### Read dataset file
    items = ['hour', 'minute', 'second', 'P140Ap', 'P141Ap', 'I1', 'I2', 'empty0', '
        U', 'Ieff', 'empty1', 'P149Ap', 'P150Ap', 'P151Ap', 'F152', 'empty2', '
        empty3', 'empty4', 'empty5', 'S201o', 'T100W', 'T101W', 'T102W', 'T103W', '
        T104W', 'T105W', 'T106W', 'T107W', 'T108W', 'T109W', 'T120W', 'T121W', '
        T122W', 'T123W', 'T131W', 'T134W', 'T152W', 'T153W', 'T154W', 'pump', '
        heater']

    ds = pd.read_csv(dataset, header=None, sep='\t', decimal=',', na_values=np.
        nan)
    ds.columns = items

    ### Generate time index
    ds.insert(0, 'year', [year] * len(ds.index))

```

```

ds.insert(1, 'month', [month] * len(ds.index))
ds.insert(2, 'day', [day] * len(ds.index))

ds.index = pd.to_datetime(ds[['year', 'month', 'day', 'hour', 'minute', 'second']])

### Clean dataset
list_to_remove = ['year', 'month', 'day', 'hour', 'minute', 'second', 'empty0',
                  'empty1', 'empty2', 'empty3', 'empty4', 'empty5']
ds = ds.drop(columns=list_to_remove)

return ds

def find_imin(dataset, Tl_p='T123W'):

    A = 13.7
    B = 5120.0

    p = dataset['P140Ap']
    psat = 1000 * np.exp(A - B / (dataset[Tl_p] + 273.15))

    dpsat = p - psat

    for i in range(len(dpsat)):

        if dpsat[i] <= 0:
            break

    return i

""" ----- """
""" | DATASET POST-PROCESSING CLASS | """
""" ----- """

class Test:

    def __init__(self, data):

        ### Load test dataset (this is a .csv file)
        self.data = data

    def data_processing(self, period, Tl_p='T122W', Tg_p='T121W', Pg_p='P140Ap'):

        """ Initialization """

        ### Create two resampled and preprocessed datasets
        self.data.insert(0, 't', (self.data.index - self.data.index[0]) / np.
            timedelta64(1, 's'))

        self.drs_mean = self.data.resample(period).mean()
        self.drs_std = self.data.resample(period).std()

        ### Unpack resampled measurements
        self.time = self.data['t'].resample(period).median()
        self.dt = self.time.diff()
        self.period = period

```

```
self.p140 = self.drs_mean['P140Ap']
self.p141 = self.drs_mean['P141Ap']
self.p149 = self.drs_mean['P149Ap']
self.p150 = self.drs_mean['P150Ap']
self.p151 = self.drs_mean['P151Ap']

self.T100 = self.drs_mean['T100W']
self.T101 = self.drs_mean['T101W']
self.T102 = self.drs_mean['T102W']
self.T103 = self.drs_mean['T103W']
self.T104 = self.drs_mean['T104W']
self.T105 = self.drs_mean['T105W']
self.T106 = self.drs_mean['T106W']
self.T107 = self.drs_mean['T107W']
self.T108 = self.drs_mean['T108W']
self.T109 = self.drs_mean['T109W']
self.T120 = self.drs_mean['T120W']
self.T121 = self.drs_mean['T121W']
self.T122 = self.drs_mean['T122W']
self.T123 = self.drs_mean['T123W']
self.T131 = self.drs_mean['T131W']
self.T134 = self.drs_mean['T134W']
self.T152 = self.drs_mean['T152W']
self.T153 = self.drs_mean['T153W']
self.T154 = self.drs_mean['T154W']

self.S201 = self.drs_mean['S201o']

self.I1 = self.drs_mean['I1']
self.I2 = self.drs_mean['I2']
self.Ieff = self.drs_mean['Ieff']
self.U = self.drs_mean['U']

self.F152 = self.drs_mean['F152']

#####

self.std_p140 = self.drs_std['P140Ap']
self.std_p141 = self.drs_std['P141Ap']
self.std_p149 = self.drs_std['P149Ap']
self.std_p150 = self.drs_std['P150Ap']
self.std_p151 = self.drs_std['P151Ap']

self.std_T100 = self.drs_std['T100W']
self.std_T101 = self.drs_std['T101W']
self.std_T102 = self.drs_std['T102W']
self.std_T103 = self.drs_std['T103W']
self.std_T104 = self.drs_std['T104W']
self.std_T105 = self.drs_std['T105W']
self.std_T106 = self.drs_std['T106W']
self.std_T107 = self.drs_std['T107W']
self.std_T108 = self.drs_std['T108W']
self.std_T109 = self.drs_std['T109W']
self.std_T120 = self.drs_std['T120W']
self.std_T121 = self.drs_std['T121W']
self.std_T122 = self.drs_std['T122W']
self.std_T123 = self.drs_std['T123W']
self.std_T131 = self.drs_std['T131W']
self.std_T134 = self.drs_std['T134W']
self.std_T152 = self.drs_std['T152W']
self.std_T153 = self.drs_std['T153W']
```

```

self.std_T154    = self.drs_std['T154W']

self.std_S201    = self.drs_std['S201o']

""" Device parameters """

self.V_p         = 0.0540 # pool vessel total volume (m3)
self.S_p         = 0.135  # pool free surface area (m2)

self.Tw_pos      = {'T100':0.020, 'T101':0.055, 'T102':0.090, 'T103':
                    :0.125, 'T104':0.160, 'T105':0.195, 'T106':0.230, 'T107':0.265, 'T108':
                    :0.300, 'T109':0.335}

""" Physical constants """

A = 13.7
B = 5120.0
R = 8.32

Ma = 29.0
Mv = 18.0
MO2 = 32.0
MN2 = 28.0

k = 1.38e-23
mC_h = 1000.0
mC_p = 7000.0
duldT = 4200.0

""" Pool variables """

### Temperatures
self.Tl_p        = self.drs_mean[Tl_p]
self.Tg_p        = self.drs_mean[Tg_p]

### Pressures
self.Pg_p        = self.drs_mean[Pg_p]
self.Pb_p        = self.p150

### Volumes and mass
self.ml_p        = 1.39 * (self.Pb_p - self.p141) + 0.60

self.rl_p        = pd.Series(cp('D', 'T', (self.Tl_p + 273.15).values.
                               tolist(), 'Q', 0, 'water'), index=self.drs_mean.index)
self.Cw          = self.rl_p / (Mv * 1.0e-3) # Molar density
self.Vl_p        = self.ml_p / self.rl_p
self.Vg_p        = self.V_p - self.Vl_p

self.level       = self.Vl_p / self.S_p

### Thermal saturation
self.Ts_p        = B / (A - np.log(self.Pg_p / 1000)) - 273.15
self.Tsb_p       = B / (A - np.log(self.Pb_p / 1000)) - 273.15
self.DTsat       = self.Tl_p - self.Ts_p

self.Pls_p       = 1000 * np.exp(A - B / (self.Tl_p + 273.15))
self.DPsat       = self.Pls_p - self.Pg_p

```

```

### Flashing length-scale
self.lflash = self.level * (self.DTsat / (self.Tsb_p - self.
    Ts_p)).clip(0)

""" Vessel atmosphere """

### Partial pressures
self.Pv_p = 1000 * np.exp(A - B / (self.Tg_p + 273.15))
self.Pa_p = (self.Pg_p - self.Pv_p).clip(lower=0.01)

### Densities
self.rv_p = pd.Series(cp('D', 'T'), (self.Tg_p + 273.15).values.
    tolist(), 'P', (100 * self.Pv_p).values.tolist(), 'water'), index=
    self.drs_mean.index)
self.ra_p = pd.Series(cp('D', 'T'), (self.Tg_p + 273.15).values.
    tolist(), 'P', (100 * self.Pa_p).values.tolist(), 'air'), index=self
    .drs_mean.index)
self.rg_p = self.ra_p + self.rv_p

### Molar quantities
self.ng_p = 100 * self.Pg_p * self.Vg_p / (R * (self.Tg_p +
    273.15)) # Perfect gas law
self.xa_p = self.Pa_p / self.Pg_p
self.na_p = self.xa_p * self.ng_p
self.nv_p = (1 - self.xa_p) * self.ng_p
self.ma_p = 1.0e-3 * self.na_p * Ma
self.mv_p = 1.0e-3 * self.nv_p * Mv
self.mg_p = self.ma_p + self.mv_p
self.ya_p = self.ma_p / self.mg_p

""" Energies, enthalpies """

self.hls_p = pd.Series(cp('H', 'T'), (self.Ts_p + 273.15).values.
    tolist(), 'Q', 0, 'water'), index=self.drs_mean.index)
self.hgs_p = pd.Series(cp('H', 'T'), (self.Ts_p + 273.15).values.
    tolist(), 'Q', 1, 'water'), index=self.drs_mean.index)
self.Lv_p = self.hgs_p - self.hls_p

self.ha_p = pd.Series(cp('H', 'P'), (100 * self.Pa_p).values.
    tolist(), 'T', (self.Tg_p + 273.15).values.tolist(), 'air'), index=
    self.drs_mean.index)
self.hv_p = pd.Series(cp('H', 'P'), (100 * self.Pv_p).values.
    tolist(), 'T', (self.Tg_p + 273.15).values.tolist(), 'water'), index
    =self.drs_mean.index)
self.hg_p = self.ya_p * self.ha_p + (1 - self.ya_p) * self.
    hv_p

self.uls_p = self.hls_p - (100 * self.Pg_p / self.rl_p)
self.ul_p = self.uls_p + self.DTsat * duldT

self.hl_p = self.ul_p + (100 * self.Pg_p / self.rl_p)
self.ug_p = self.hg_p - (100 * self.Pg_p / self.rg_p)

self.Ul_p = self.ml_p * self.ul_p
self.Ug_p = self.mg_p * self.ug_p

self.lambda_l = pd.Series(cp('L', 'T'), (self.Tl_p + 273.15).values.
    tolist(), 'Q', 0, 'water'), index=self.drs_mean.index)

```

```

self.beta_l      = pd.Series(cp('ISOBARIC_EXPANSION_COEFFICIENT', 'T'
    ,(self.Tl_p + 273.15).values.tolist(), 'Q', 0, 'water'), index=self.
    drs_mean.index)
self.mu_l        = pd.Series(cp('V', 'T', (self.Tl_p + 273.15).values.
    tolist(), 'Q', 0, 'water'), index=self.drs_mean.index)
self.Cpl_p       = pd.Series(cp('C', 'T', (self.Tl_p + 273.15).values.
    tolist(), 'Q', 0, 'water'), index=self.drs_mean.index)
self.kappa_l     = self.lambda_l / (self.rl_p * self.Cpl_p)

""" Unheated wall variables """

self.Tw          = 0.1 * (self.T100 + self.T101 + self.T102 + self.
    T103 + self.T104 + self.T105 + self.T106 + self.T107 + self.T108
    + self.T109)

self.DTs_100     = self.compute_wall_superheat('T100')
self.DTs_101     = self.compute_wall_superheat('T101')
self.DTs_102     = self.compute_wall_superheat('T102')
self.DTs_103     = self.compute_wall_superheat('T103')
self.DTs_104     = self.compute_wall_superheat('T104')
self.DTs_105     = self.compute_wall_superheat('T105')
self.DTs_106     = self.compute_wall_superheat('T106')
self.DTs_107     = self.compute_wall_superheat('T107')
self.DTs_108     = self.compute_wall_superheat('T108')
self.DTs_109     = self.compute_wall_superheat('T109')

self.p_Tw        = [0.02 + i * 0.035 for i in range(10)]
self.m_Tw        = self.drs_mean[['T100W', 'T101W', 'T102W', 'T103W', '
    T104W', 'T105W', 'T106W', 'T107W', 'T108W', 'T109W']].transpose()
self.m_DTsw      = (pd.DataFrame({100: self.DTs_100, 101: self.DTs_101
    , 102: self.DTs_102, 103: self.DTs_103, 104: self.DTs_104,
    105: self.DTs_105, 106: self.DTs_106, 107: self.DTs_107, 108: self.DTs_108
    , 109: self.DTs_109})).transpose()

""" Dissolved gases solubility and transport """

### Liquid-side mass concentrations
self.CO2         = self.S201
self.Ca          = self.CO2 / 0.34
self.CN2         = 0.66 * self.Ca

### Molar fractions
self.xa_gf       = self.Pa_p / self.Pg_p
self.xO2_gf      = 0.21 * self.xa_gf
self.xN2_gf      = 0.79 * self.xa_gf

self.xO2_lf      = (Mv / MO2) * (1.0e-3 * self.CO2 / self.rl_p)
self.xa_lf       = self.xO2_lf / 0.34
self.xN2_lf      = 0.66 * self.xa_lf

### Henry's constants
self.HO2         = np.interp(self.Tg_p, henry['TC'], henry['H_O2']) *
    1.013e5
self.HN2         = np.interp(self.Tg_p, henry['TC'], henry['H_N2']) *
    1.013e5
self.Ha          = np.interp(self.Tg_p, henry['TC'], henry['H_a']) *
    1.013e5

### Dissolved gases diffusion coeff.

```

```

self.Dwa_l      = np.interp(self.Tl_p, diffu['TC'], diffu['Dwa']) *
    1.0e-9
self.DwO2_l     = np.interp(self.Tl_p, diffu['TC'], diffu['DwO2']) *
    1.0e-9
self.DwN2_l     = np.interp(self.Tl_p, diffu['TC'], diffu['DwN2']) *
    1.0e-9
self.Dwa_g      = 1.87e-10 * (self.Tg_p + 273.15)**2.072 / (self.
    Pg_p / 1013)

### Partial pressures
self.Pa_gf      = self.Pa_p
self.PO2_gf     = 0.21 * self.Pa_gf
self.PN2_gf     = 0.79 * self.Pa_gf

self.Pa_lf      = self.Ca * np.interp(self.Tl_p, henry['TC'], henry['
    H_a']) * 1.013e5 / (Ma * 100 * self.Cw)

### Saturation mass concentrations
self.CsO2       = MO2 * self.Cw * 100 * self.PO2_gf / self.HO2

self.CsN2       = MN2 * self.Cw * 100 * self.PN2_gf / self.HN2
self.Csa        = Ma * self.Cw * 100 * self.Pa_gf / self.Ha

self.xO2_li     = 100 * self.PO2_gf / self.HO2
self.xN2_li     = 100 * self.PN2_gf / self.HN2
self.xa_li      = 100 * self.Pa_gf / self.Ha

### Supersaturation indexes
self.DCO2       = self.CO2 - self.CsO2
self.DCN2       = self.CN2 - self.CsN2
self.DCa        = self.Ca - self.Csa

self.DxO2       = self.xO2_lf - self.xO2_li
self.DxN2       = self.xN2_lf - self.xN2_li
self.Dxa        = self.xa_lf - self.xa_li

""" Nucleation """

self.sigma      = pd.Series(cp('I', 'T'), (self.Tl_p + 273.15).values.
    tolist(), 'Q', 0, 'water'), index=self.drs_mean.index)

### radius of curvature of postulated gas nucleus at smooth wall (m)
self.ri_sw      = 2.70e-6

### radius of curvature of postulated gas nucleus at rough wall (m)
self.ri_rw      = 22.0e-6

### Critical superheat for nucleus activation at smooth wall (K)
self.DTsc_sw    = (R * (self.Tsb_p + 273.15)**2.0) * ((2 * self.
    sigma / self.ri_sw) - 100 * self.Pa_lf) / (100 * self.Pb_p * Mv
    * 1.0e-3 * self.Lv_p)

### Critical superheat for nucleus activation at smooth wall (K)
self.DTsc_rw    = (R * (self.Ts_p + 273.15)**2.0) * ((2 * self.
    sigma / self.ri_rw) - 100 * self.Pa_lf) / (100 * self.Pg_p * Mv
    * 1.0e-3 * self.Lv_p)

### Energetic costs
self.Wcr        = (16. * np.pi * (self.sigma)**3 / 3) * (1.0 / (100
    * self.DPsat)**2.0)

```

```

self.Wcra      = (16. * np.pi * (self.sigma)**3 / 3) * (1.0 / (100
    * (self.DPsat + self.Pa_lf))**2.0)

self.Gb       = self.Wcr / (k * (self.Tl_p + 273.15))
self.Gba     = self.Wcra / (k * (self.Tl_p + 273.15))

""" Compute mass and energy fluxes """

### Energy exchanges at boundary walls
self.Q_p      = self.Ieff.clip(0) * self.U.clip(0)

### Time derivatives – pool side
self.dmldt_p  = self.ml_p.diff().div(self.dt.median(), axis=0)
self.dmgdt_p  = self.mg_p.diff().div(self.dt.median(), axis=0)
self.dmadt_p  = self.ma_p.diff().div(self.dt.median(), axis=0)
self.dmvd_t_p = self.mv_p.diff().div(self.dt.median(), axis=0)

self.dUldt_p  = self.Ul_p.diff().div(self.dt.median(), axis=0)
self.dUgdt_p  = self.Ug_p.diff().div(self.dt.median(), axis=0)

### Molar fluxes
self.jO2      = (abs((self.Vl_p * 1.0e-3 * self.CO2).diff()).div(
    self.dt.median(), axis=0) / (1.0e-3 * MO2) / self.S_p).ewm(span
    =15).mean()
self.ja       = self.jO2 / 0.34
self.jN2      = 0.66 * self.ja
self.jw       = (abs(self.dmldt_p) / (1.0e-3 * Mv) / self.S_p).
    ewm(span=15).mean()
self.jg       = self.jw + self.ja

### Heated-wall-to-fluid heat transfer
self.Th       = 0.5 * (self.T131 + self.T134)
self.Tp       = (self.T100+self.T101+self.T102+self.T103+self.
    T104+self.T105+self.T106+self.T107+self.T108+self.T109)/10

self.DThs     = self.Th - self.Tsb_p
self.DTh      = self.Th - self.Tl_p

self.dThdt    = self.Th.diff().div(self.dt.median(), axis=0)
self.dTpdt    = self.Tp.diff().div(self.dt.median(), axis=0)

self.Ih       = mC_h * self.dThdt
self.Ip       = mC_p * self.dTpdt

self.kh       = (self.Q_p - self.Ih) / (0.75 * self.S_p * (self.
    Th - self.Tl_p))

### Dimensionless numbers
self.L        = self.level # characteristic length

self.Nu_l     = self.jw * 1.0e-3 * Mv * self.Lv_p * self.L / (self
    .lambda_l * abs(self.DTsat))
self.Nu_h     = self.kh * self.L / self.lambda_l

self.Ra_l     = (9.81 * self.beta_l * self.rl_p * abs(self.DTsat)
    * self.L**3.0) / (self.mu_l * self.kappa_l)
self.Ra_p     = (9.81 * self.beta_l * self.rl_p * abs(self.Th -
    self.Ts_p) * self.L**3.0) / (self.mu_l * self.kappa_l)
self.Ra_h     = (9.81 * self.beta_l * self.rl_p * abs(self.Th -
    self.Tl_p) * self.L**3.0) / (self.mu_l * self.kappa_l)

```

```

self.Sh_O2      = self.jO2 * self.L / ((self.DCO2 / MO2) * self.
    DwO2_l)
self.Sh_a      = self.ja * self.L / ((self.DCa / Ma ) * self.
    Dwa_l )

self.Ja        = self.Cpl_p * self.DTsat / self.Lv_p

### Heat transfer rate (in W/K)
self.kTS       = (abs(self.dmltd_p * self.Lv_p / self.DTsat)).
    clip(0)
self.phiT      = self.kTS / (0.6 * self.Ra_l**0.33 * self.
    lambda_l * self.S_p / self.L)

### Mass transfer rate (in kg/s)
dmltd         = self.dmltd_p
dCadt         = 1.0e-3 * self.Ca.diff() / self.dt
dTldt        = self.Tl_p.diff() / self.dt

self.kmS       = (abs(dmltd + (self.Vl_p / self.xa_lf) * (Mv / Ma
    ) * dCadt + self.ml_p * self.beta_l * dTldt)).clip(0)
self.phim      = self.kmS / (0.6 * self.Ra_l**0.33 * self.
    lambda_l * self.S_p / self.L / self.Cpl_p * (self.Dwa_l / self.
    kappa_l)**(2./3))

def compute_wall_superheat(self , sensor):

    A  = 13.7
    B  = 5120.0

    Pw = (self.Pg_p + 0.01 * self.rl_p * 9.81 * (self.level - self.
        Tw_pos[sensor])).clip(self.Pg_p)

    Ts = B / (A - np.log(Pw / 1000)) - 273.15
    DTs = self.__dict__[sensor] - Ts

    return DTs

```



---

# Measurement uncertainties analysis

## Introduction

In its recent edition, the reference *Guide to the expression of uncertainty in measurement* - or GUM - recalls that [59]:

*When reporting the result of a measurement of a physical quantity, it is obligatory that some quantitative indication of the quality of the result be given so that those who use it can assess its reliability.*

This very quality can be estimated by means of the concept of *uncertainty*, which quantifies, according to the GUM:

*The doubt about how well the result of the measurement represents the value of the quantity being measured [...] when all of the known or suspected components of error have been evaluated and the appropriate corrections have been applied.*

This uncertainty evaluation is an unmissable stage in the development of an experimental device. The latter was achieved during the presented research and is described in this appendix. Subsection D.0.1 introduces the followed methodology in the quantification of the experimental uncertainties, while Subsections D.0.2 and D.0.3 provide the output of the present analysis. At last, Subsection D.0.4 summarizes the overall uncertainty budget of the Aquarius test device.

### D.0.1 Methodology

The assessment of the uncertainties in the results of the conducted tests is based on the recommendations of the GUM. Before going into details, let us introduce some normalized vocabulary, in use in metrology:

- **Mesurand:** Denoted as  $X$ , this term refers to a “particular quantity subject to measurement” [59];
- **Standard uncertainty:** Denoted as  $u_X$ , this quantity is “the uncertainty of the result of a measurement expressed as a standard deviation” [59];
- **Relative uncertainty:** Denoted as  $\epsilon_X$ , this quantity is the ratio between the standard uncertainty  $u_X$  and the value of the quantity  $X$  being measured;

$$\epsilon_X = \frac{u_X}{X} \quad (\text{D.1})$$

- **Combined uncertainty:** This quantity is “the standard uncertainty of the result of a measurement when that result is obtained from the values of a number of other quantities, equal to the positive square root of a sum of terms, the terms being the variances or covariances of these other quantities weighted according to how the measurement result varies with changes in these quantities” [59];

$$u_X = \sqrt{\sum_{i=1}^N (u_X^i)^2} \quad (\text{D.2})$$

- **Expanded or overall uncertainty:** Denoted as  $U_X$ , this “quantity [defines] an interval about the result of a measurement that may be expected to encompass a large fraction of the distribution of values that could reasonably be attributed to the measurand. The fraction may be viewed as the coverage probability or level of confidence of the interval”, the latter being represented by the so-called *coverage factor*  $k$ , such that:

$$U_X = k \times u_X \quad (\text{D.3})$$

On that basis, let us now develop the followed methodology. First of all, the overall uncertainty affecting any result of the presented experiments is believed as deriving from two distinct, irreducible and unknown sources of errors. Those postulated errors are:

- **In link with the measurements performed throughout a test,** any measuring chain, including those of the present research, being always intrinsically limited and imperfect;
- **In link with the experimental procedure and boundary conditions of the test device, applied throughout an experiment.** In spite of the care taken in setting up and controlling a typical pool flashing test, the initial state and the boundary conditions of the experimental device, together with the actions taken in the course of a test are expected to differ in some limited but irreducible extent, thereby bringing some more uncertainty to the test results.

The uncertainties which derive from the above first type of errors can be estimated by means of any available information about the used measuring chain, such as for instance, a calibration report or a sensor's technical data-sheet. In doing so, the obtained uncertainty estimates are referred to as *Type B uncertainties*, according to [59]. The uncertainties arising from the second type of errors are however better estimated by means of statistical methods, in which case they are referred to as *Type A uncertainties* [59]. In practice, those Type A uncertainties are highlighted by repeating  $N$  times a chosen reference test, by conserving at every trial:

- The same experimental method;
- The same operator;
- The same equipment;
- The same environmental conditions;
- The same location.

All in all, those differing sources of uncertainties combine and alter the quality of the results in a way which is depicted in Figure D.1. They must be evaluated separately as-realistically-as possible. The retained process is illustrated in Figure D.2 and is performed in the present appendix by:

1. Applying the so-called Type B uncertainty evaluation method of the GUM to the primary physical variables that are directly measured throughout an experiment. The details of this methodology will be later introduced in Subsection D.0.2 throughout the Type B evaluation;
- 2.a. Propagating the Type B uncertainties in link with these primary variables into the mathematical expression of some identified relevant physical variables. This stage is developed in Subsection D.0.3, on the basis of the classical uncertainty propagation rules that one may find in every statistics textbook, such as for instance [112];
- 2.b. Evaluating the uncertainties in link with the experimental procedure and boundary conditions affecting the derived physical variables. This stage is detailed in Subsection D.0.3 ;
3. Eventually combining, the uncertainties obtained at stages 2.a. and 2.b. by means of the root-sum-of-squares method introduced above. This yields, for each variable  $X$  of interest, an overall uncertainty  $U_X^c$ , which quantifies its associated quality. This exercise is achieved for each time trend of the variables  $X(t)$ . The obtained results are then time-averaged. The output of this latter stage is given in Subsection D.0.4.

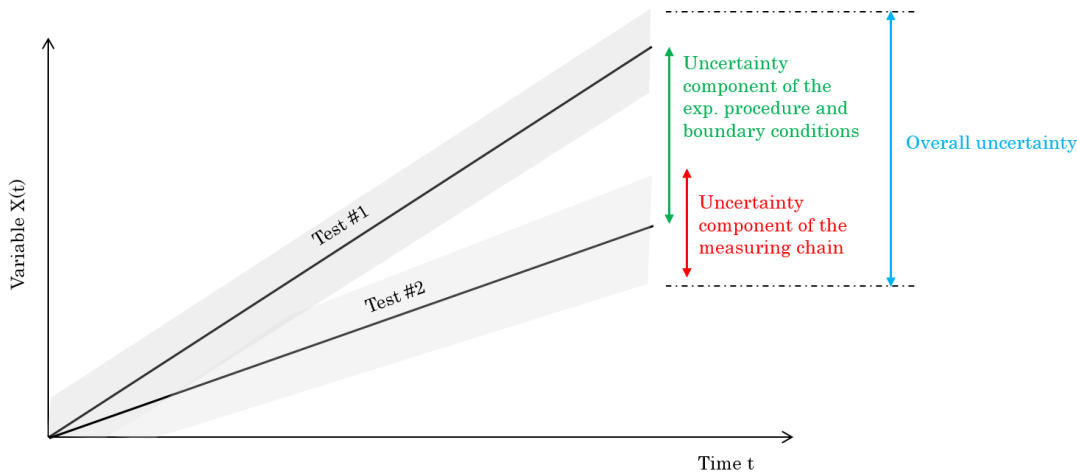


Figure D.1: The uncertainties, respectively in link with the measuring chain and the experimental procedure and boundary conditions, combine and alter the quality of the obtained results. In this example, the depicted overall uncertainty varies arbitrarily with time.

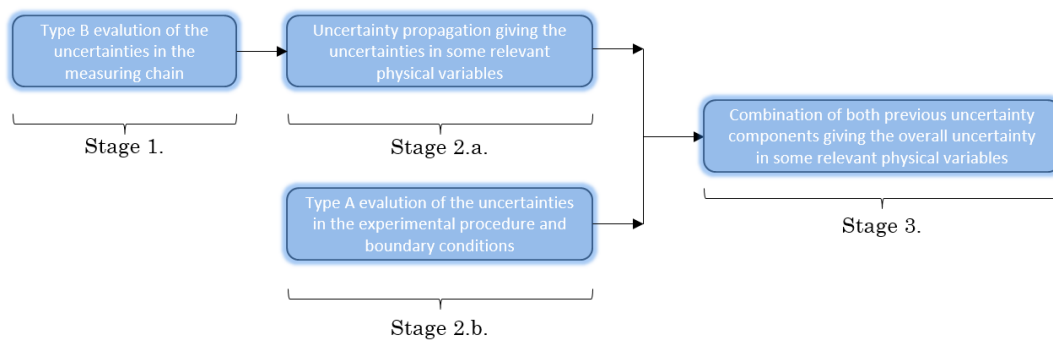


Figure D.2: The followed methodology in the evaluation of the uncertainties affecting the quality of the experimental results, according to the GUM [59].

## D.0.2 The uncertainties in the measured physical variables

### Uncertainties in temperature measurements

The temperature measurements performed within the test device are based on the 19 Pt-100 4-wire platinum resistance thermometers of class A shown in Figure 2.14. The accuracy associated with this latter class is of  $\pm 0.15^\circ\text{C}$  at a reference temperature of  $0^\circ\text{C}$  [118]. In order to improve the accuracy of those measurements, the 19 thermometers were all calibrated. This procedure is described below, together with the uncertainty budget of the temperature measurements.

**Uncertainties estimate prior calibration** Assuming that the errors in the Pt-100 measurements are uniformly distributed, one can compute the standard uncertainty de-

noted  $u_{\text{sensor}}$  as follows:

$$\begin{aligned} u_{\text{sensor}} &= \frac{0.15}{\sqrt{3}} \\ &= 0.0866^{\circ}\text{C} \end{aligned} \quad (\text{D.4})$$

In addition, the temperature measurements are all recorded by means of the NI-9216 cDAQ™ acquisition module equipping the experimental device. Regarding this latter module, the manufacturer reports, in case of a 4-wire cabling, a gain-error of  $\pm 0.007\%$  and an offset error of  $\pm 0.006\ \Omega$ , to account for the errors in the resistance measurements. Over a temperature range of  $50^{\circ}\text{C}$ , the resistance of the Pt-100 sensors is expected to vary by about  $19.73\ \Omega$ , the latter being respectively equal to  $100\ \Omega$  and  $119.73\ \Omega$  at  $0^{\circ}\text{C}$  and  $50^{\circ}\text{C}$ . This yields a conversion factor from resistance to temperature uncertainty of  $50^{\circ}\text{C}/19.73\ \Omega = 2.5340^{\circ}\text{C}/\Omega$ . Hence, the uncertainties related to the gain and offset errors can be estimated as:

$$\begin{aligned} u_{\text{gain}}^{\text{NI9216}} &= \frac{1}{\sqrt{3}} \pm 0.007\% \times 119.73\ \Omega \times 2.5340^{\circ}\text{C}/\Omega \\ &= \pm 0.0122^{\circ}\text{C} \end{aligned} \quad (\text{D.5})$$

and:

$$\begin{aligned} u_{\text{offset}}^{\text{NI9216}} &= \frac{1}{\sqrt{3}} \pm 0.006\ \Omega \times 2.5340^{\circ}\text{C}/\Omega \\ &= \pm 0.0088^{\circ}\text{C} \end{aligned} \quad (\text{D.6})$$

Regarding the ambient temperature effect on the resistance measurements, the manufacturer indicates an offset drift of  $\pm 3.3\ \text{m}\Omega/^{\circ}\text{C}$  and a gain drift of  $\pm 7\ \text{ppm}/^{\circ}\text{C}$ . Assuming a maximum ambient temperature variation of  $10^{\circ}\text{C}$ , this yields the following uncertainties:

$$\begin{aligned} u_{\text{gain drift}}^{\text{NI9216}} &= \frac{1}{\sqrt{3}} \pm 7\ \text{ppm}/^{\circ}\text{C} \times 119.73\ \Omega \times 2.5340^{\circ}\text{C}/\Omega \times 10^{\circ}\text{C} \\ &= \pm 0.012^{\circ}\text{C} \end{aligned} \quad (\text{D.7})$$

and:

$$\begin{aligned} u_{\text{offset drift}}^{\text{NI9216}} &= \frac{1}{\sqrt{3}} \pm 3.3\ \text{m}\Omega/^{\circ}\text{C} \times 2.5340^{\circ}\text{C}/\Omega \times 10^{\circ}\text{C} \\ &= \pm 0.0051^{\circ}\text{C} \end{aligned} \quad (\text{D.8})$$

At last, those uncertainties can be combined as follows thereby leading to an estimate of the overall uncertainty of the Pt-100 measurements, prior calibration, denoted as  $u_{\text{Pt100}}$ :

$$\begin{aligned} u_{\text{Pt100}} &= \sqrt{(u_{\text{sensor}})^2 + (u_{\text{offset}}^{\text{NI9216}})^2 + (u_{\text{gain}}^{\text{NI9216}})^2 + (u_{\text{offset drift}}^{\text{NI9216}})^2 + (u_{\text{gain drift}}^{\text{NI9216}})^2} \\ &= 0.0881^{\circ}\text{C} \end{aligned} \quad (\text{D.9})$$

One may hence notice that the contribution of the measuring chain to the Pt-100 measurement uncertainty is relatively small with respect to the temperature variation scale in the experiment, which is approximately of the order of a few °C.

**The Pt-100 sensors calibration** For calibrating the Pt-100 sensors, the latter were first embedded in a common metallic block that was then immersed in a still water pool during approximately 70 hours. The temperatures given by the 19 thermometers were recorded throughout the test by means of the NI-9216 cDAQ™ temperature acquisition module equipping the experimental device. During the test, the recorded temperature trends were all distant from each other by a constant value, as visible in the below Figure D.3, with an overall dispersion smaller than 0.15°C, in consistency with the expected accuracy of a Pt-100 thermometer of class A.

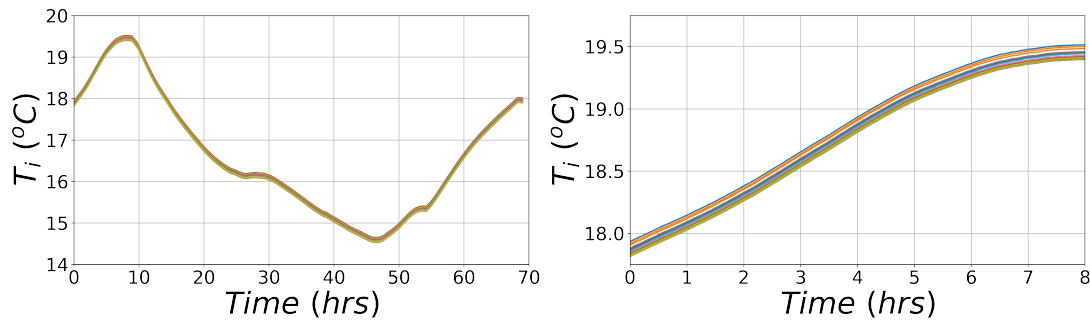


Figure D.3: Calibration test of the Pt-100 probes - temperature records. Left: full time scale. Right: time scale restricted to 8 hours.

From these responses, a reference temperature, denoted  $T_{ref}(t)$  and corresponding to the mean of the 19 Pt-100 recorded outputs, was computed as follows:

$$T_{ref}(t) = \frac{1}{19} \sum_{i=1}^{19} T_i(t) \quad (D.10)$$

where  $T_i(t)$  refers to the temperature record of the  $i$ -th sensor at time  $t$ . This reference temperature is of practical interest. Indeed, let us consider a set of  $n$  Pt-100 thermometers and assume that their characteristic electrical resistances at 0°C are dispersed around the targeted ideal value of 100 Ω according to a normal distribution<sup>1</sup>. In such a case, one can demonstrate that the mean value of  $n$  independent temperature measurements is a best estimate for the true, unknown, temperature  $T_{true}$  of the measured object [112], which reads:

$$T_{true} = \lim_{n \rightarrow \infty} \frac{1}{n} \sum_{i=1}^n T_i \quad (D.11)$$

One can also demonstrate that the uncertainty in  $T_{ref}$  as an estimate of the true unknown value  $T_{true}$  corresponds to the so-called *standard deviation of the mean*, here

<sup>1</sup>This assumption implies that the  $n$  thermometer responses are all independent from each other, *i.e.* that the manufacturing imperfections affecting each Pt-100 electrical resistance were randomly generated.

expressed as:

$$\sigma_{T_{ref}} = \frac{\sigma_{T_i}}{\sqrt{n}} \quad (\text{D.12})$$

Hence, by postulating that the 19 Pt-100 sensors are all independent from each other and by calibrating them against the reference temperature  $T_{ref}$ , their standard uncertainty  $u_{Pt100}$  can be lowered by a factor  $1/\sqrt{19}$ , which yields  $u_{T_{ref}} = 0.0202^\circ\text{C}$ . This calibration was performed by correcting each Pt-100 response by a constant factor denoted as  $C_{T_i}$ , which reads:

$$C_{T_i} = \bar{T}_i(t) - \bar{T}_{ref}(t) \quad (\text{D.13})$$

with  $\bar{\cdot}$  the time-averaging operator. The obtained values, together with their standard uncertainty computed over 70 hours are provided in Table D.1. As a verification, once corrected, the differences between the measurements and the reference temperature were all scattered by less than  $0.006^\circ\text{C}$ , a value which is of the order of the computed standard uncertainties of the correction factors (Figure D.4).

Table D.1: Correction factors applied to the Pt-100 thermometers.

Sensor reference	$C_{T_i}$ ( $^\circ\text{C}$ )	$u_{C_{T_i}}$ ( $^\circ\text{C}$ )
T100W	+0.0757	0.0020
T101W	+0.0459	0.0021
T102W	-0.0139	0.0022
T103W	+0.0110	0.0013
T104W	-0.0378	0.0011
T105W	+0.0196	0.0021
T106W	-0.0279	0.0008
T107W	-0.0430	0.0008
T108W	-0.0389	0.0011
T109W	+0.0055	0.0018
T120W	+0.0221	0.0017
T121W	+0.0614	0.0012
T122W	-0.0289	0.0013
T123W	-0.0223	0.0020
T131W	-0.0097	0.0018
T134W	-0.0281	0.0013
T152W	-0.0119	0.0030
T153W	+0.0211	0.0027
T154W	-0.0262	0.0030

Furthermore, one can note that the computed uncertainty of the correction factors is one order of magnitude smaller than the uncertainty of the reference temperature  $u_{T_{ref}}$ . This uncertainty is at most equal to  $0.003^\circ\text{C}$ , the value retained in the following estimate of the combined uncertainty of the temperature measurements, denoted as  $u_T$ :

$$\begin{aligned} u_T &= \sqrt{u_{T_{ref}}^2 + u_{C_{T_i}}^2} \\ &= 0.0204^\circ\text{C} \end{aligned} \quad (\text{D.14})$$

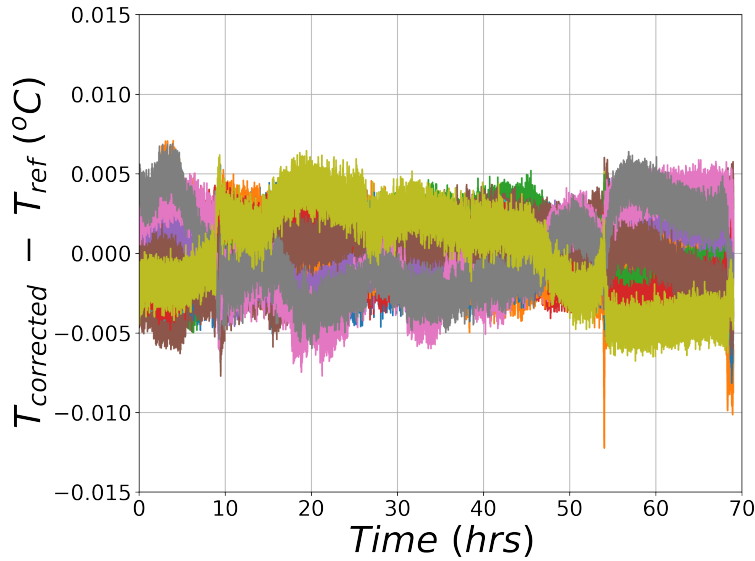


Figure D.4: Calibration test of the Pt-100 probes - differences between the corrected measurements and the reference temperature.

### Uncertainties in pressure measurements

The pressure measurements performed within the test device are based on a set of pressure transducer sensors, as shown in Figure 2.14. Their relative accuracy, defined as a percentage of the measured pressure within the measuring range and specified by the manufacturer after having calibrated those instruments, are given in Table D.2.

Table D.2: The used pressure sensors and their relative accuracy.

Sensor ref.	Model	Measurement range	Relative accuracy
P140Ap	E+H Cerabar PMC21	0-110 mbar	$\pm 0.5\%$
P141Ap	Thermibel AM-510	0-1.6 bar	$\pm 0.5\%$
P150Ap	E+H Cerabar M PMC51	0-150 mbar	$\pm 0.01\%$

As mentioned in Chapter 2, the pressure measurements records are achieved by means of the NI 9205™ acquisition module equipping the test device, in a  $\pm 10$ -V range. Under these conditions, the manufacturer reports an absolute accuracy of  $\pm 6.230 \mu\text{V}$ . By considering a maximum pressure variation range of 1600 mbar over an acquisition voltage range of 2-10 V, one can estimate the maximum uncertainty associated with the acquisition as:

$$\begin{aligned} \text{Max}(u_p^{\text{NI9205}}) &= \frac{1}{\sqrt{3}} \times \pm 6.230 \times 10^{-6} \text{ V} \times 200 \text{ mbar/V} & (\text{D.15}) \\ &= 7.19 \times 10^{-4} \text{ mbar} \end{aligned}$$

At the lower bound of the imposed pressures within the test device, *i.e.* 10 mbar, this envelope uncertainty represents only 0.007% of the measured pressure, a value which is one order of magnitude smaller than the best pressure transducer relative ac-

curacy. Hence, owing to its small magnitude  $u_p^{NI9205}$  can be reasonably neglected in the uncertainty budget of the performed pressure measurements.

### Uncertainties in dissolved oxygen measurements

As mentioned in Chapter 2, the  $O_2$  mass concentration in dissolution within water is measured by means of a Hamilton VisiFerm™ DO Arc 120 optical probe. This instrument was adjusted by the manufacturer which reported a two-point calibration. Another calibration point was checked by means of the ArcAir™ interface software at the laboratory and yielded satisfactory results. The reported accuracy of this sensor represents  $\pm 1\%$  of the measured  $O_2$  mass concentration. In addition, the acquisition of the 4-20 mA signal transmitted by the instrument is performed by means of a NI 9205™ module, in a  $\pm 10$ -V range. Under these conditions, the manufacturer reports an absolute accuracy of  $\pm 6.230 \mu\text{V}$ . With a variation of 20 mg/L of the measured dissolved oxygen concentration over a voltage range of 2-10 V corresponding to the current range of 4-20 mA of the transmitted signal, the conversion factor from voltage to concentration is of 2.5 mg/L/V. In turn, this allows estimating the absolute uncertainty associated with the reading errors, computed as:

$$\begin{aligned} u_{C_{O_2}}^{NI9205} &= \frac{1}{\sqrt{3}} \times \pm 6.230 \times 10^{-6} \text{V} \times 2.5 \text{mg/L/V} \\ &= 9 \times 10^{-6} \text{mg/L} \end{aligned} \quad (\text{D.16})$$

Owing to its small magnitude,  $u_{C_{O_2}}^{NI9205}$  can be reasonably neglected in the uncertainty budget of the performed dissolved oxygen measurements. Hence, the uncertainty of this instrument is best expressed by a relative uncertainty, here denoted as  $\epsilon_{C_{O_2}}$  and taken equal to the value reported by the manufacturer:

$$\epsilon_{C_{O_2}} = 1\% \quad (\text{D.17})$$

## D.0.3 The uncertainties in the computed physical variables

### The propagation of the measuring chain uncertainties

As seen in Chapter 3, a limited set of physical variables does appear relevant for characterizing the performed experiments. Those variables are:

- $\Delta T_{eq}$ : the so-called liquid thermal metastability degree;
- $P_G$ : the vessel's atmosphere pressure;
- $m_L$ : the liquid pool mass;
- $\dot{m}_L$ : the liquid vaporization rate;
- $C_{O_2}$ : the dissolved  $O_2$  concentration;

- $\dot{C}_{O_2}$ : the  $O_2$  degassing rate.

As seen too in Chapter 3, the computation of those quantities rely on some intermediate variables that can be estimated from the available measurements. In what follows, the uncertainties associated with the measuring chain and estimated in Section D.0.2 are propagated through the mathematical expression of the above physical variables and their intermediate components. This is achieved on the basis of the well-known propagation rules that may be found out, for instance, in [112].

**The liquid mean temperature** The liquid mean temperature, denoted as  $T_L$  and expressed in °C, is computed as follows, as the average of two Pt-100 temperature measurements:

$$T_L = \frac{1}{2} (T122W + T123W) \quad (D.18)$$

Hence, the uncertainty  $u_{T_L}^{mes}$  of this mean temperature reads:

$$\begin{aligned} u_{T_L}^{mes} &= \frac{u_T}{\sqrt{2}} \\ &= 0.0142^\circ\text{C} \end{aligned} \quad (D.19)$$

**The pool atmosphere total pressure** The pool atmosphere total pressure, denoted as  $P_G$  and given in mbar, is taken equal to the measured pressure **P140Ap**, in the pressure range 0-110 mbar. Hence:

$$\begin{aligned} \epsilon_{P_G}^{mes} &= \epsilon_{P140Ap} \\ &= 0.5\% \end{aligned} \quad (D.20)$$

**The water saturation temperature and pressure** Those two variables, denoted as  $T_{sat}$  and  $P_{sat}$  and given in °C and mbar, are respectively computed as:

$$T_{sat} = \frac{5120}{13.7 - \text{Log}\left(\frac{P140Ap}{1000}\right)} - 273.15 \quad (D.21)$$

and:

$$P_{sat} = 1000 \times \text{Exp}(13.7 - 5120/(T120W + 273.15)) \quad (D.22)$$

with **P140Ap** and **T120W** respectively given in mbar and °C. The uncertainty of a function  $q(x)$  being [112]:

$$u_q = \left| \frac{dq}{dx} \right| u_x \quad (D.23)$$

the uncertainties  $u_{T_{sat}}^{mes}$  and  $u_{P_{sat}}^{mes}$  thus read:

$$u_{T_{sat}}^{mes} = \frac{5120}{P140Ap(\text{Log}(P140Ap) - 20.61)^2} u_{P140Ap} \quad (D.24)$$

and:

$$u_{P_{sat}}^{mes} = 4.6 \times 10^{12} \frac{\text{Exp}(-5120/(T120W + 273.15))}{(T120W + 273.15)^2} u_{T120W} \quad (D.25)$$

In Figure D.5,  $u_{T_{sat}}^{mes}$  and  $u_{P_{sat}}^{mes}$  are respectively plotted against the expected experimental range for **P140Ap** and **T120W**. Over this range, the maximum value of those two uncertainties is respectively equal to  $0.048^\circ\text{C}$  and  $0.076\text{ mbar}$ . Conservatively, the two propagated uncertainties  $u_{T_{sat}}^{mes}$  and  $u_{P_{sat}}^{mes}$  are thus fixed to:

$$u_{T_{sat}}^{mes} = 0.048^\circ\text{C} \quad (\text{D.26})$$

$$u_{P_{sat}}^{mes} = 0.076\text{ mbar} \quad (\text{D.27})$$

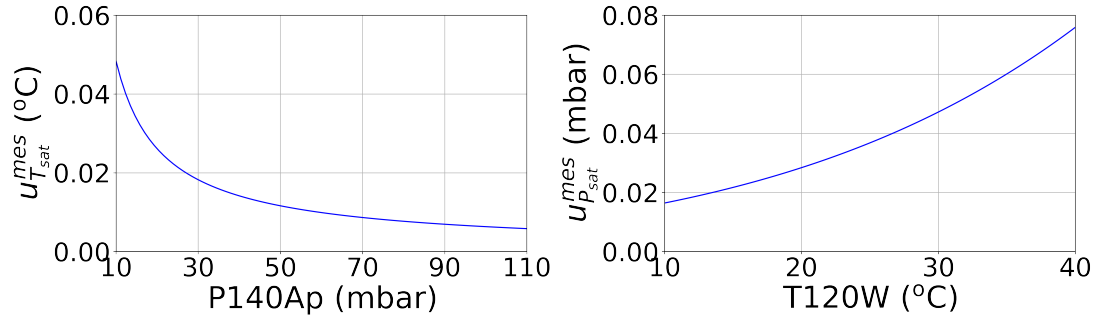


Figure D.5: Left: variation of  $u_{T_{sat}}^{mes}$  against **P140Ap**. Right: variation of  $u_{P_{sat}}^{mes}$  against **T120W**. The maximum value of those two uncertainties is respectively equal to  $0.048^\circ\text{C}$  and  $0.076\text{ mbar}$ .

**The liquid thermal metastability degree** This quantity, denoted as  $\Delta T_{eq}$  and given in  $^\circ\text{C}$ , reads:

$$\Delta T_{eq} = T_L - T_{sat}(P_G) \quad (\text{D.28})$$

Hence, by assuming that  $u_{T_L}^{mes}$  and  $u_{T_{sat}}^{mes}$  are independent, the standard uncertainty  $u_{\Delta T_{eq}}^{mes}$  is equal to:

$$\begin{aligned} u_{\Delta T_{eq}}^{mes} &= \sqrt{(u_{T_L}^{mes})^2 + (u_{T_{sat}}^{mes})^2} \\ &= 0.049^\circ\text{C} \end{aligned} \quad (\text{D.29})$$

**The liquid pool mass** The liquid pool mass, denoted as  $m_L$  and given in kg, is computed from the correlation that was deduced from the tests described in Appendix A. We recall that the correlation giving  $m_L$  reads:

$$\text{P150Ap} - \text{P140Ap} = 0.72 m_L - 0.43 \quad (\text{D.30})$$

or equivalently:

$$m_L = 1.39 (\text{P150Ap} - \text{P140Ap}) + 0.60 \quad (\text{D.31})$$

In Appendix A, the expanded uncertainty related to the filling of the pool with known water volumes and denoted as  $U_{fill}$  is estimated to  $\pm 0.100\text{ kg}$ , a value which

corresponds to one volume graduation of the used 5-L beaker. Assuming that the filling errors are uniformly distributed within an interval of  $\pm 0.100$  kg, this gives:

$$\begin{aligned} u_{fill} &= \frac{U_{fill}}{\sqrt{3}} \\ &= 0.058 \text{ kg} \end{aligned} \quad (\text{D.32})$$

The correspondence between the beaker volume and its contained liquid mass was checked by means of a balance whose indicated precision was of  $\pm 1$  g. This uncertainty is by far much smaller than  $u_{fill}$  and can be neglected. When using the above correlation for predicting  $m_L$  given (P150Ap – P140Ap), one can demonstrate that the expression of the equivalent uncertainty in the prediction is the below combination of the uncertainties in the physical variables  $m_L$ , P150Ap and P140Ap that were used for determining the correlation [37]:

$$u_{m_L}^{mes} = \sqrt{u_{fill}^2 + \mathcal{B}^2((u_{P140Ap})^2 + (u_{P150Ap})^2) + u_{\mathcal{B}}^2(\Delta P_{pool} - \overline{\Delta P_{pool}})^2} \quad (\text{D.33})$$

with  $\mathcal{B}$ , the best-estimate of the slope of the linear relation between  $m_L$  and (P150Ap – P140Ap), here equal to 1.39 kg/mbar, and:

$$\Delta P_{pool} = \text{P150Ap} - \text{P140Ap} \quad (\text{D.34})$$

and  $\overline{\Delta P_{pool}}$  is the arithmetical mean value of the recorded  $\Delta P_{pool}$  during the correlation determination tests. The uncertainty of the slope  $u_{\mathcal{B}}$  reads:

$$u_{\mathcal{B}} = u_{fill} \sqrt{\frac{N}{N \sum_i \Delta P_{pool}^i{}^2 - (\sum_i \Delta P_{pool}^i)^2}} \quad (\text{D.35})$$

where  $N$  is the number of realized individual vessel filling tests.  $u_{\mathcal{B}}$  is equal to 0.0014 kg/mbar. Once applying these expressions to the present case, this yields at most:

$$u_{m_L}^{mes} = 0.080 \text{ kg} \quad (\text{D.36})$$

Interestingly, this result is close to  $u_{fill}$ , thereby indicating that the errors in link with the filling stage of the correlation determination tests, being essentially random, are the main contribution to the overall uncertainty  $u_{m_L}^{mes}$ .

**The liquid vaporization rate** The liquid vaporization rate denoted as  $\dot{m}_L$  and given in g/s, can be approximated by:

$$\dot{m}_L \approx 10^3 \frac{m_L(t + \Delta t) - m_L(t)}{\Delta t} \quad (\text{D.37})$$

In doing so, the estimate of  $\dot{m}_L$  can be greatly affected by the noise associated with  $m_L(t)$ , which may in turn significantly alter the uncertainty in link with this derived variable. One way to cope with this limitation is to smooth out the noisy  $m_L(t)$ , whenever

possible, before computing the numerical estimate of its time derivative. In the performed pool flashing tests, the pool liquid mass typically varies slowly, with a maximum rate of 0.4 g/s at a bounding heat power of 1000 W. If  $m_L(t)$  does not vary significantly over a set of  $n$  consecutive measurements, it is acceptable to divide the whole dataset of  $N$  points by  $n$  and to reduce every obtained set of  $n$  consecutive data points into a single value corresponding to the arithmetical mean of those measurements, thereby smoothing out the signal. In our experiments, the acquisition is performed with a sampling period of 1 s. By a trial and error process, a 3-min smoothing time interval has been identified as a good compromise between accuracy and the minimization of data losses and is systematically applied to each test result. In addition, as seen in the present appendix, the errors contributing to the pool liquid mass determination are most likely mainly random. Hence, whenever  $m_L(t)$  is smoothed out over  $n$  consecutive data points, its uncertainty reduces to  $u_{m_L}^{mes}/\sqrt{n}$ , *i.e.* the standard deviation of its mean. Assuming that the time variable  $t$  is perfectly known, the standard uncertainty  $u_{\dot{m}_L}^{mes}$  is thus equal to:

$$u_{\dot{m}_L}^{mes} = \frac{\sqrt{2} \times 10^3}{\Delta t \sqrt{n}} u_{m_L}^{mes} \quad (\text{D.38})$$

with  $n$  being equal to 180 given a 3-min smoothing interval and a 1-s acquisition period, and  $\Delta t$  being 180 s, this yields:

$$u_{\dot{m}_L}^{mes} = 0.034 \text{ g/s} \quad (\text{D.39})$$

**The dissolved oxygen mass concentration** The dissolved O<sub>2</sub> mass concentration, denoted as  $C_{O_2}$  and given in mg/L, is taken equal to the performed measurement referred to as S201 (*cf.* Figure 2.14). Hence:

$$\begin{aligned} \epsilon_{C_{O_2}}^{mes} &= \epsilon_{S201} \\ &= 1\% \end{aligned} \quad (\text{D.40})$$

**The dissolved oxygen degassing rate** The dissolved O<sub>2</sub> degassing rate, referred to as  $\dot{C}_{O_2}$  and given in mg/L/s, can be approximated by:

$$\dot{C}_{O_2} \approx \frac{C_{O_2}(t + \Delta t) - C_{O_2}(t)}{\Delta t} \quad (\text{D.41})$$

and hence, according to the rule of uncertainties propagation [112]:

$$\begin{aligned} \epsilon_{\dot{C}_{O_2}}^{mes} &= \sqrt{2} \times \epsilon_{C_{O_2}}^{mes} \\ &= 1.4\% \end{aligned} \quad (\text{D.42})$$

**Summary of the propagated uncertainties in link with the measuring chain** The propagated uncertainties in link with the measuring chain, computed within the present section, are all summarized in the below Table D.3. The results obtained at this stage of

the analysis will be later compared with those in link with the experimental procedure and boundary conditions (*cf.* Section D.0.4). Overall, the propagation of the uncertainties, associated with the measurements performed in the test device, yield very low values which comply with the accuracy requirements of this experimental research. Indeed, the propagated uncertainties in the various computed temperatures or temperature differences are all smaller than the uncertainty of a Pt-100 of class A itself (*i.e.* 0.15°C). The uncertainty in the saturation pressure is comparable to those of the pool atmosphere pressure measurement. The uncertainty in the liquid vaporization rate is small when compared with the expected order of magnitude of the latter quantity (*i.e.* 0.4 g/s at a heating power of 1000 W). At last, the standard or relative uncertainties of the remaining computed variables all lie within a reasonable range of values. All these estimates confirm the adequate performance of the measuring chain.

Table D.3: Propagated standard or relative uncertainties  $u_X^{mes}$  or  $\epsilon_X^{mes}$  in link with the measuring chain.

Parameter	Propagated uncertainty $u_X^{mes}$ or $\epsilon_X^{mes}$
Liquid thermal metastability degree $\Delta T_{eq}$	0.049°C
Vessel's atmosphere pressure $P_G$	0.5%
Liquid pool mass $m_L$	0.080 kg
Liquid vaporization rate $\dot{m}_L$	0.034 g/s
Dissolved O <sub>2</sub> concentration $C_{O_2}$	1%
O <sub>2</sub> degassing rate $\dot{C}_{O_2}$	1.4%

### The uncertainties in link with the test procedure and boundary conditions

As discussed above, in spite of the care taken in setting up and controlling a typical test, the initial state and the boundary conditions of the experimental device, together with the actions taken in the course of a test, are expected to differ in some limited but irreducible extent, thereby bringing some more uncertainty to the results. This important contribution to the overall uncertainty budget of the physical variables can be estimated by repeating  $N$  times an identical test. This approach is the so-called Type A uncertainty determination method proposed in [59]. The latter requires, for each repeated test, the conservation of:

- The same experimental method;
- The same operator;
- The same equipment;
- The same environmental conditions;
- The same location.

This assessment process was achieved on the basis of nine repeated identical tests, listed in Table 3.1. Those tests, performed by the same experimentalist (*J. Martin*), at the same location (IRSN's laboratory), only with the Aquarius device, have the following common characteristics:

- Thermal power  $\dot{Q}_p = 1000$  W;
- Operating pressure  $P_G = 22$  mbar;
- Initial liquid temperature  $T_L(0) = 20^\circ\text{C}$ ;
- Initial pool level  $z_p(0) = 30$  cm;
- Initial content in dissolved oxygen  $C_{O_2}(0) = 6.5$  mg/L.

The obtained results are exhibited in Figure D.6. At first, one can notice the overall good repeatability of the already identified physical variables of interest. The observed time trends were all repeatable, with a relatively small level of discrepancy from one test to another. The calculated time-averaged standard deviations, associated with the differences in each variable  $X$  value from test to test, are referred to as  $\bar{\sigma}_X$ . They are further translated into standard or relative uncertainties  $u_X^{rep}$  or  $\epsilon_X^{rep}$  and given in Table D.4. Those values will be later compared with the contribution of the measuring chain to the overall uncertainty budget (Section D.0.4).

Table D.4: Time-averaged standard or relative uncertainties  $u_X^{rep}$  or  $\epsilon_X^{rep}$  of the repeated relevant physical quantities  $X$  of a pool flashing test.

Parameter	Repeatability uncertainty $u_X^{rep}(t)$ or $\epsilon_X^{rep}(t)$
Liquid thermal metastability degree $\Delta T_{eq}$	0.17°C
Vessel's atmosphere pressure $P_G$	2.4%
Liquid pool mass $m_L$	0.32 kg
Liquid vaporization rate $\dot{m}_L$	0.03 g/s
Dissolved $O_2$ concentration $C_{O_2}$	1.5%
$O_2$ degassing rate $\dot{C}_{O_2}$	2.4%

#### D.0.4 The overall uncertainty budget of the computed physical variables

The uncertainties in link with the measuring chain and with the experimental procedure and boundary conditions, respectively estimated in the above Sections D.0.3 and D.0.3, are summed in what follows in order to provide a combined standard uncertainty, denoted as  $U_X^c$ , associated with each physical variable of interest  $X$ . The individual uncertainty components  $u_X^{mes}$  and  $u_X^{rep}$  previously computed are combined according to the root-sum-of-squares method recommended in [59]. The latter reads:

$$U_X^c = \sqrt{(k^{mes}u_X^{mes})^2 + (k^{rep}u_X^{rep})^2} \quad (\text{D.43})$$

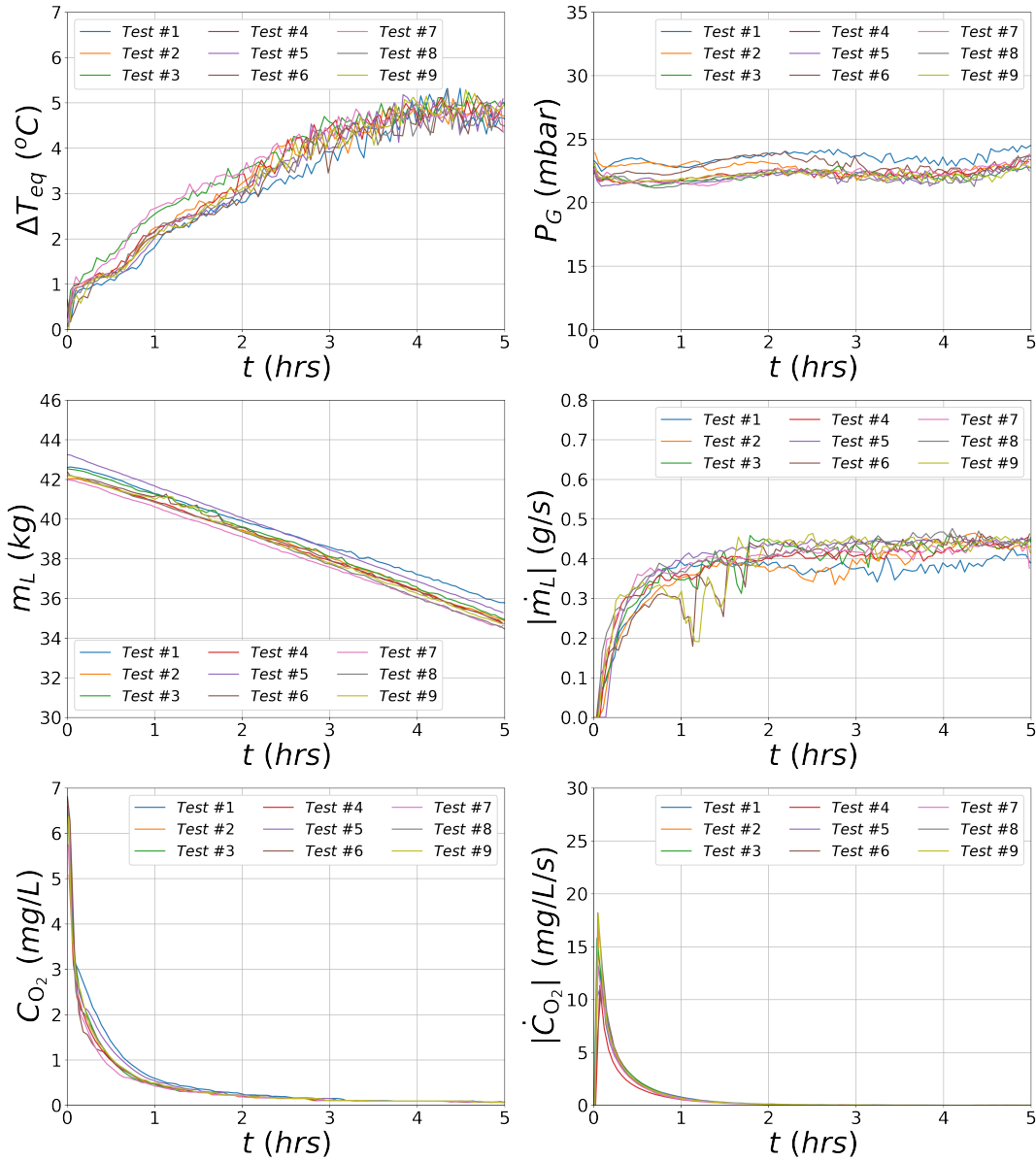


Figure D.6: Main physical variables of the achieved nine identical tests, having parameters as close as possible to those of the so-called reference test. One can notice the overall good repeatability of the considered physical variables.

with  $k^{mes}$  and  $k^{rep}$ , the so-called coverage factors, respectively associated with  $u_X^{mes}$  and  $u_X^{rep}$ . For the uncertainty components in link with the measuring chain, it is chosen that  $k^{mes} = 2$ . Hence,  $(k^{mes} \times u_X^{mes})$  is the range of values that is believed to include the true and unknown value of  $X$ , with a confidence of 95%. However, one must recall that the repeatability components  $u_X^{rep}$  were all estimated by the computation of a standard deviation over only nine repeated tests. In this case, the estimate of the standard deviation is less precise. In order to circumvent this limitation,  $k^{rep}$  must be taken equal to the *Student's coefficient* associated with the required level of confidence in the result and with the number of repeated tests [120]. With the latter variables being respectively

equal to 95% and 9, this gives  $k^{rep} = 2.26$ . The obtained results are provided in Table D.5.

Table D.5: The overall uncertainty budget of the computed physical variables.

Parameter	$U_X^{mes}$ or $\mathcal{E}_X^{mes}$	$U_X^{rep}$ or $\mathcal{E}_X^{rep}$	$U_X^c$ or $\mathcal{E}_X^c$
Liquid thermal metastability degree $\Delta T_{eq}$	0.1°C	0.4°C	0.4°C
Vessel's atmosphere pressure $P_G$	1%	5.4%	5.5%
Liquid pool mass $m_L$	0.16 kg	0.72 kg	0.74 kg
Liquid vaporization rate $\dot{m}_L$	0.07 g/s	0.07 g/s	0.1 g/s
Dissolved $O_2$ concentration $C_{O_2}$	2%	3.4%	3.9%
$O_2$ degassing rate $\dot{C}_{O_2}$	2.8%	5.4%	6.1%

Overall, this table shows that the uncertainties affecting any of the presented physical variables are mainly dominated by the component in link with the experimental procedure and boundary conditions, highlighted by the repeatability tests. Here, with the liquid vaporization rate  $\dot{m}_L$  being a counter-example, the limitations and inaccuracies of the measuring chain play no sensitive role at all, thereby confirming its adequate performance. Taking some height, these combined uncertainties remain acceptable and comply with the accuracy requirements of the present research. Though of a moderate impact, a reduction of the repeatability component of the combined uncertainties  $U_X^c$  or  $\mathcal{E}_X^c$  is still possible by increasing the number of repeated tests. This would lead to a drop in the retained  $k^{rep}$ . For now, with a number of repeated tests of nine, the obtained levels of  $U_X^c$  or  $\mathcal{E}_X^c$  are deemed acceptable and it is not chosen to go any further in the repeatability study, keeping in mind, however, this possibility.



---

## The lumped-parameter model of the Aquarius pool in Python 3

```

""" ----- """
""" |           MODULE IMPORTATION           | """
""" ----- """

from CoolProp.CoolProp import PropsSI as cp

import numpy          as np
import pandas        as pd
import scipy.optimize as so

""" ----- """
""" |   PROPERTIES IMPORTATION   | """
""" ----- """

henry = pd.read_csv('air-water_henrys_constant.csv')
diffu = pd.read_csv('air-water_diffusivity.csv')

""" ----- """
""" |           DEFINE POOL CLASS           | """
""" ----- """

class Pool:

    def __init__(self, S_p):
        self.S_p = S_p          # liquid free surface area (m2)

    def set_BCs(self, Q_p, Pg, Nnuc):

        ### Save the boundary conditions as class attributes
        self.Q_p = Q_p          # heating power (W)
        self.Pg  = Pg           # operating pressure (Pa)
        self.Nnuc = Nnuc        # initial number of nuclei within water (-)

    def compute_state(self, X):

        ### Some constants

```

```

A          = 13.7
B          = 5120.0

Ma         = 29.0          # air molar mass (g/mol)
Mw         = 18.0          # water molar mass (g/mol)

R          = 8.32          # Ideal gas universal constant (J/mol/K)
k          = 1.38e-23      # Boltzmann's constant (J/K)

### Read X
self.ml    = X[0]
self.Tl    = X[1]
self.Ca    = X[2]

### Compute liquid mass and molar densities and liquid volume
self.rl    = cp('D','T',self.Tl,'Q',0,'water')
self.Cl    = self.rl / (Mw * 1.0e-3)
self.Vl    = self.ml / self.rl

### Compute pool collapsed level
self.L     = self.Vl / self.S_p

### Compute dissolved air param.
self.Ha    = np.interp(self.Tl,henry['TK'],henry['H_a']) * 1.013e5
self.Pa_l  = self.Ca * self.Ha / (1.0e-3 * Ma * self.Cl)

self.ma    = self.Ca * self.Vl
self.ya_l  = self.ma / self.ml

### Compute thermal saturation
self.Ts    = B / (A - np.log(self.Pg / 1.0e5))
self.DTsat = self.Tl - self.Ts

self.Pls   = 1e5 * np.exp(A - B / self.Tl)
self.DPsat = self.Pls - self.Pg

### Compute liquid internal energy
if (self.Tl - self.Ts) < 0:
    self.hl = cp('H','Tliquid',self.Tl,'P',self.Pg,'water')
    self.ul = self.hl - (self.Pg / self.rl)
else:
    duldT   = 4200.0
    hls     = cp('H','P',self.Pg,'Q',0,'water')
    self.ul = hls - (self.Pg / self.rl) + (self.Tl - self.Ts) *
        duldT
    self.hl = self.ul + (self.Pg / self.rl)

self.Ul    = self.ml * self.ul

### Compute specific enthalpies
self.hgs   = cp('H','T',self.Ts,'Q',1,'water')
self.hls   = cp('H','T',self.Ts,'Q',0,'water')

self.Lv    = self.hgs - self.hls

### Compute useful properties
self.sigma = cp('I','T',self.Tl,'Q',0,'water')
self.lambda_l = cp('L','T',self.Tl,'Q',0,'water')
self.beta_l = cp('ISOBARIC_EXPANSION_COEFFICIENT','T',self.Tl,'
    Q',0,'water')
self.mu_l   = cp('V','T',self.Tl,'Q',0,'water')

```

```

self.Cp_l      = cp('C', 'T', self.Tl, 'Q', 0, 'water')
self.kappa_l   = self.lambda_l / (self.rl * self.Cp_l)
self.Dwa_l     = np.interp(self.Tl, diffu['TK'], diffu['Dwa']) * 1.0
               e-9

### Compute heater-to-fluid DT, htc and heater temp.
self.DTh      = (self.Q_p / (0.23 * 0.75 * self.S_p * self.lambda_l) *
               (self.kappa_l * self.mu_l / (9.81 * self.beta_l * self.rl))
               **0.33)**(3./4)
self.kw       = self.Q_p / (0.75 * self.S_p * self.DTh)
self.Th       = self.DTh + self.Tl

### Compute dimensionless numbers
self.Ra_l     = (9.81 * self.beta_l * self.rl * abs(self.DTsat) * self
               .L**3.0) / (self.mu_l * self.kappa_l)
self.Ra_p     = (9.81 * self.beta_l * self.rl * abs(self.Th - self.Ts)
               * self.L**3.0) / (self.mu_l * self.kappa_l)

self.Wcra    = (16. * np.pi * (self.sigma)**3 / 3) * (1.0 / (self.
               DPsat + self.Pa_l)**2.0)
self.Gba     = self.Wcra / (k * self.Tl)

### Compute single-phase heat and mass transfer coeffs.
self.kTSo    = 0.6 * self.Ra_l**0.33 * self.lambda_l * self.S_p /
               self.L
self.kmSo    = self.kTSo / self.Cp_l * (self.Dwa_l / self.kappa_l)
               *(2./3)

### Compute two-phase heat and mass transfer coeffs.
self.phi     = (self.Nnuc**(-4.24) * self.Gba**(-0.33) * self.Ra_p
               *(1.5)).clip(1)

self.kTS     = self.phi * self.kTSo
self.kmS     = 2 * self.phi * self.kmSo

### Compute liquid heat and mass transfers
self.Qli     = self.kTS * self.DTsat
self.dmldt  = self.Qli / self.Lv

### Compute dissolved air mass transfer
self.dmadt   = self.kmS * self.ya_l

```

```
def get_Y(self):
```

```

    ### Return conservative vector
    return [self.ml, self.Ul, self.ma]

```

```
def get_fluxes(self):
```

```

    ### Compute state derivatives and return fluxes vector
    dml_dt = - self.dmldt
    dUl_dt = self.Q_p - self.dmldt * self.hgs
    dma_dt = - self.dmadt

    return [dml_dt, dUl_dt, dma_dt]

```

```
""" ----- """
```

```

""" |           DEFINE OUTPUT CLASS           | """
""" |-----| """

class Output:

    def __init__(self, pool):

        """ read 'pool' object """
        self.pool = pool

        """ Create output vectors """
        ### Time (s)
        self.time = [0]
        self.hrs = [0]

        ### Masses (kg)
        self.ml = [self.pool.ml]
        self.ma = [self.pool.ma]

        ### Pool level (m)
        self.level = [pool.L]

        ### Dissolved air concentration (mg/L)
        self.Ca = [1000 * self.pool.Ca]
        self.CO2 = [0.34 * 1000 * self.pool.Ca]

        ### Temperatures (deg.C)
        self.Tl = [self.pool.Tl - 273.15]
        self.Th = [self.pool.Th - 273.15]
        self.Tsat = [self.pool.Ts - 273.15]
        self.DTsat = [0]
        self.DTh = [self.pool.DTh]

        ### Mass fluxes (g/s)
        self.dmldt = [0]
        self.dmadt = [0]

        ### Transfer coeffs.
        self.kw = [self.pool.kw]
        self.kTS = [self.pool.kTS]
        self.kmS = [self.pool.kmS]
        self.kTSo = [self.pool.kTSo]
        self.kmSo = [self.pool.kmSo]
        self.phi = [self.pool.phi]

        ### Dimensionless numbers
        self.Ra_p = [self.pool.Ra_p]
        self.Ra_l = [self.pool.Ra_l]
        self.Gba = [self.pool.Gba]

    def output_update(self, pool):

        ### Masses (kg)
        self.ml.append(pool.ml)
        self.ma.append(pool.ma)

        ### Pool level (m)
        self.level.append(pool.L)

        ### Dissolved air concentration (mg/L)
        self.Ca.append(1000 * pool.Ca)

```

```
self.CO2.append(0.34 * 1000 * pool.Ca)

### Temperatures (deg.C)
self.Tl.append(pool.Tl - 273.15)
self.Th.append(pool.Th - 273.15)
self.Tsat.append(pool.Ts - 273.15)
self.DTsat.append(pool.DTsat)
self.DTh.append(pool.DTh)

### Mass fluxes (g/s)
self.dmltd.append(1000 * pool.dmltd)
self.dmadt.append(1000 * pool.dmadt)

### Transfer coeffs.
self.kw.append(pool.kw)
self.kTS.append(pool.kTS)
self.kmS.append(pool.kmS)
self.kTSo.append(pool.kTSo)
self.kmSo.append(pool.kmSo)
self.phi.append(pool.phi)

### Dimensionless numbers
self.Ra_p.append(pool.Ra_p)
self.Ra_l.append(pool.Ra_l)
self.Gba.append(pool.Gba)
```



---

## An Euler-implicit solver coded in Python 3

```

""" ----- """
""" |   DEFINITION OF AN EULER IMPLICIT SOLVER   | """
""" ----- """

import numpy as np

#####

"""   EULER IMPLICIT SOLVER   """

def solve(X0, clas , step , imax , prec ):

    """
    List of arguments:
    X0      ->      initial value of the iterated state vector
    clas    ->      this is the class from which equations are solved
    step    ->      step
    imax    ->      required maximum iteration number
    prec    ->      required solver precision
    """

    ### Compute Y0, given X0
    clas.compute_state(X0)
    Y0 = clas.get_Y()

    ### First guess for (X,Y)
    X = X0[:]      # the syntax '[:]' allows performing a 'shallow copy' of
                   # list X0, denoted as X
    Y = Y0[:]      # idem, for Y and Y0

    ### Loop while iteration number < imax
    for i in range(imax):

        ### Inertia and Jacobian matrices calculation
        B = compute_B(X,Y0, clas , step)
        A = compute_A(X,Y0, clas , step , prec)

```

```

"""
print("")
print("iter index : ", i)
print("")
print("A = ", A)
print("")
print("B = ", B)
print("")
"""

### Jacobian matrix inversion
Ainv = np.linalg.inv(A)

### Computation of X-increment
dX = np.dot(Ainv,B)

### X vector computation
for k in range(len(dX)):
    X[k] = X[k] + dX[k]

### Compute norm
res = norme(dX,X)

"""
print("")
print("Ainv = ", Ainv)
print("")
print("X = ", X)
print("")
print("dX = ", dX)
print("")
print("inter. res. :", res)
print("")
print("")
"""

if res <= prec:
    clas.compute_state(X)
    print("_")
    print("-----")
    print("|_Successful_convergence_|")
    print("|__Required_niter__", i+1 )
    print("|__Residual__", res )
    print("-----")
    print("_")
    break

if i == imax-1:
    clas.compute_state(X)
    print("_")
    print("-----")
    print("|_Max_iteration_number_is_reached_|")
    print("|__Max_niter__", imax )
    print("|__Residual__", res )
    print("-----")
    print("_")
    break

```

```
#####
```

```

""" COMPUTE INERTIA MATRIX """

def compute_B(X, Y0, clas, step):

    B = []
    clas.compute_state(X)
    F = clas.get_fluxes()
    Y = clas.get_Y()

    for i in range(len(F)):
        B.append(F[i] - (Y[i] - Y0[i])/step)

    return B

#####

""" COMPUTE JACOBIAN MATRIX """

def compute_A(X, Y0, clas, step, prec):

    B0 = compute_B(X, Y0, clas, step)
    A = [[0 for x in range(len(X))] for y in range(len(X))]

    for j in range(len(X)):                # Iteration over column index

        xsave = X[j]
        dx = max(1.0e-10, prec*xsave)

        X[j] = xsave + dx

        Bd = compute_B(X, Y0, clas, step)

        for i in range(len(X)):            # Iteration over line index
            A[i][j] = -(Bd[i] - B0[i])/dx
            X[j] = xsave

    return A

#####

""" COMPUTE A NORM """

def norme(dX, X):

    z = 0
    for j in range(len(X)):
        z = max(z, abs(dX[j]/max(1.0e-10, X[j])))

    return z

```

